Silicon-Based Tandem Solar Cells with Silicon Heterojunction Bottom Cells

by

Zhengshan Yu

A Dissertation Presented in Partial Fulfillment
of the Requirements for the Degree
Doctor of Philosophy

Approved February 2018 by the
Graduate Supervisory Committee:

Zachary Holman, Chair
Yong-Hang Zhang
Stuart Bowden
Richard King

ARIZONA STATE UNIVERSITY

May 2018

ABSTRACT

Silicon photovoltaics (PV) is approaching its theoretical efficiency limit as a single-junction technology. To break this limit and further lower the PV-generated levelized cost of electricity, it is necessary to engineer a silicon-based "tandem" technology in which a solar cell of another material is stacked on top of silicon to make more efficient use of the full solar spectrum.

This dissertation understands and develops four aspects of silicon-based tandem PV technology. First, a new "spectral efficiency" concept is proposed to understand how tandem cells should be designed and to identify the best tandem partners for silicon cells. Using spectral efficiency, a top-cell-design guide is constructed for silicon-based tandems that sets efficiency targets for top cells with various bandgaps to achieve targeted tandem efficiencies.

Second, silicon heterojunction solar cells are tuned to the near-infrared spectrum to enable world-record perovskite/silicon tandems both in two- and four-terminal configurations. In particular, for the 23.6%-efficient two-terminal tandem, a single-side textured silicon bottom cell is fabricated with a low-refractive-index silicon nanoparticle layer as a rear reflector. This design boosts the current density to 18.5 mA/cm^2; this value exceeds that of any other silicon bottom cell and matches that of the top cell.

Third, "PVMirrors" are proposed as a novel tandem architecture to integrate silicon cells with various top cells. A strength of the design is that the PVMirror collects diffuse light as a concentrating technology. With this concept, a gallium-arsenide/silicon PVMirror tandem is demonstrated with an outdoor efficiency of 29.6%, with respect to the *global* irradiance.

Finally, a simple and versatile analytical model is constructed to evaluate the cost competitiveness of an arbitrary tandem against its sub-cell alternatives. It indicates that *tandems will become increasingly attractive in the market*, as the ratio of sub-cell module cost to area-related balance-of-system cost—the key metric that will determine the market success or failure of tandems—is decreasing.

As an evolution of silicon technology, silicon-based tandems are the future of PV. They will allow more people to have access to clean energy at ultra-low cost. This thesis defines both the technological and economic landscape of silicon-based tandems, and makes important contributions to this tandem future.

To my wife, whose endless love, support, and sacrifice for me to take my dream.

And to my Dad who instilled a love of learning from a young age.

ACKNOWLEDGMENTS

Looking back at the enjoyable journey towards my Ph.D. in the past four years, I am truly grateful for the help received from all the people that I have met.

First, I would like to express my sincere gratitude to my advisor Prof. Zachary Holman for the exceptional opportunity of doing photovoltaic research in his group. Also, his dedication and creativity in research, pursuit of perfection in manuscript writing, and encouragement have shaped me to a better researcher.

Besides my advisor, I would like to thank the rest of my committee: Prof. Yong-Hang Zhang, Prof. Stuart Bowden, and Prof. Richard King, not only for their insightful comments and encouragement, but also for the hard but inspiring questions which incented me to widen my research from various perspectives.

My sincere thanks also goes to Dr. Mathieu Boccard and Kathryn Fisher for sharing their knowledge and experience with me; to Jianwei Shi, Mehdi (Ashling) Leilaeioun, Salman Manzoor, Peter Firth, Joe Carpenter, Jonathan Bryan, William Weigand, Nathan Rodkey, and Xiaodong Meng, all have been working together as a great team.

I would like to acknowledge all my project partners for the fruitful collaborations on different kinds of silicon-based tandems: Michael McGehee, Kevin Bush, Axel Palmstrom, Tomas Leijtens, and Hsin-Ping Wang from Stanford University; Jinsong Huang, and Bo Chen from University of Nebraska-Lincoln; Roger Angel, Brian Wheelwright, Justin Hyatt, Lennon Reinhart, Jeffrey Mrkonich, and Wyatt Taylor from University of Arizona; Ray Kostuk, Benjamin Chrysler, and Yuechen Wu also from

University of Arizona; Larry Lee, Michelle Vaisman, and Shizhao Fan from Yale University (now at University of Illinois Urbana Champaign).

I also thank the people at Solar Power Lab for maintaining facilities and share experience: Bill Dauksher, Stas Herasimenka, Mark Bailly, Andre Augusto and many others. And many thanks to Prof. Mariana Bertoni for the access to her lab resources.

I gratefully acknowledge the funding for supporting my research: Advanced Research Projects Agency-Energy (DE-AR0000474), Office of Energy Efficiency and Renewable Energy (DE-EE0007368, DE–EE0006709), National Science Foundation (Award No. 1664669), Engineering Research Center Program of the National Science Foundation and the Office of Energy Efficiency and Renewable Energy of the Department of Energy under NSF Cooperative Agreement (No. EEC–1041895), Research Corporation for Science Advancement through a Scialog Collaborative Innovation Award, and Harold and Lucille Dunn Memorial Scholarship.

TABLE OF CONTENTS

Page

CHAPTER Page

APPENDIX Page

LIST OF TABLES

Table Page

LIST OF FIGURES

Figure Page

Figure Page

CHAPTER 1

INTRODUCTION

Silicon photovoltaic (PV) technology now matures and dominates the PV market with about 320 Giga-watts installed capacity worldwide [1, 2]. Compared to the primitive cell, first invented in 1954, with 6% efficiency [3], 25%-efficient solar cells are rolling out on production lines [4], and the world-record cell efficiency was pushed up to 26.6% in 2016 [5]. This number is approaching the 29.4% theoretical efficiency limit, and is believed to be on par with the 27% practical efficiency limit of silicon cells on device level [6, 7]. As a result of such remarkable development in performance—together with scaling—silicon PV technology now yields a system cost close to $1/W, and becomes one of the cheapest low-carbon power source, which offers the highest technical potential among renewable energy sources that could substantially displace fossil fuels and curb climate change by powering nearly a third of global electricity demand [8-10].

To reach that ambitious goal by 2050, analysis forecasts that the system cost needs to be in the range of $ 0.30-0.70 per watt [9]. Given the already-cheap silicon PV module is no longer a main cost contributor (e.g. less than a third of the total installed system cost in US in 2016 [11, 12]), it is more imperative than ever to further increase the efficiency of silicon PV—exceeding its limit—to discount all the hardware and soft costs.

1.1 Efficiency Limit of Silicon Technology

When considering the principles to overcome the single-junction limit, it is instructive to examine the efficiencies of the individual energy conversion processes, and

thus identify the best opportunities. Figure 1-1 shows the breakdown of the overall conversion into four individual processes, as proposed by Würfel *et al*. [13]. The first process is the absorption of incident photon energy, the absorption efficiency (η_{abs}) is defined as the ratio of absorbed energy current ($j_{E,abs}$) to incident energy current ($j_{E,inc}$), with the absorbed (incident) energy current defined as absorbed (incident) photon current times the mean energy of photons absorbed (incident); the second process is thermalization of electron-hole pairs. In this process, the energy of electron-hole pairs reduced from the mean energy of photons absorbed down to $E_g + 3kT$, its efficiency ($\eta_{thermalization}$) is defined as the ratio of the mean energy of thermalized electron-hole pairs to un-thermalized ones, which equals the mean energy of photons absorbed. The third factor ($\eta_{thermodynamic}$) defines the maximum chemical energy—eV_{oc}—that can be obtained from the thermalized energy of electron-hole pairs. Following that is a fill factor (*FF)* which is the fraction of chemical energy current delivered at maximum power point.

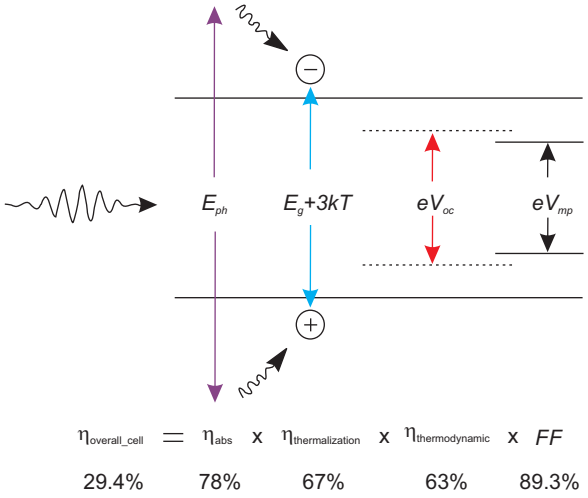

Figure 1-1. Individual processes and their respective efficiency of a silicon cell with limiting efficiency. Achieving the 29.4% overall efficiency, the efficiencies of sequential processes for absorption, thermalization, thermodynamic and FF are 78%, 67%, 63% and 89.3% respectively.

In the calculated 29.4% silicon cell [6], the short-circuit current density (J_{sc}) is 43.31 mA/cm^2, open-circuit voltage is 761.3 mV, *FF* is 89.26%, and the thickness is 110 μm. Therefore, the overall conversion efficiency can break down into absorption efficiency of 78%, thermalization efficiency of 67%, thermodynamic factor of 63% and *FF* of 89.3% ($78\% \times 67\% \times 63\% \times 89.3\% = 29.4\%$). The efficiency breakdown indicated that, compared to *FF*, all other three efficiencies are small and thus need improvement.

At first glance, the bottle-neck process is the third process that is the conversion of the energy of the electron-hole pairs into chemical energy. Therefore, it's tempting to improve that number as the primary goal. However, this efficiency is limited by intrinsic properties of silicon material, which is not of interests to engineer in the scope of my research. For example, in the limiting-efficiency calculation, it models an ideal, un-doped silicon cell with no surface or defect (Shockley-Read-Hall) recombination, perfect anti-reflection coating and perfect rear reflectors, and the quasi-Fermi levels splitting at V_{oc} are determined only by radiative recombination and Auger recombination, both of which are natural properties of silicon material. In fact, Auger recombination is the dominant loss mechanism in this hypothetical device, and this loss on any device made with doped silicon cannot be smaller than this un-doped limit.

1.2 Break the Limit: Silicon Tandem

Since improving $\eta_{thermodynamic}$ is not a viable route, it leaves the thermalization loss as the lowest-hanging fruit. To reduce the thermalization loss, an intuitive approach, first proposed by Ross and Nozik [14], is to prevent carrier thermalization, which means extract the electron-hole pairs while they are "hot" (before they thermalize). The "hot carrier" concept is favorable for narrow-bandgap materials, including silicon, as narrow-bandgap

materials suffer more from thermalization loss. In fact, it has been tried on III-V material systems [13, 15]. Unfortunately, so far, a fully functional hot-carrier solar cell—extract hot carriers from one region of the cell and forming a thermalized distribution in another without losing the thermalization energy to the lattice—has not been demonstrated [16].

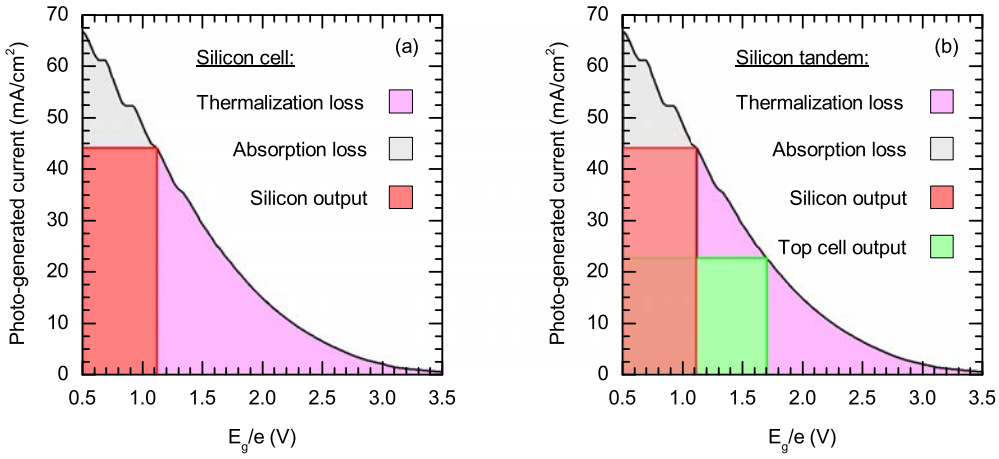

Figure 1-2. Graphical analysis of efficiency of (a) a silicon solar cell, and (b) a tandem solar cell. The area under the black curve represents the total input power of AM1.5 G spectrum. The purple areas represent thermalization loss, the grey areas represent absorption loss, the red areas represent power output by a silicon cell and the green area is power output by a top cell.

Another approach to reduce thermalization is tandem technology—in which a wide-bandgap top cell is coupled with a silicon cell—and Figure 1-2 visualizes how it works (although not accurate). The area under the "$J_{sc}(E_g/e)$" curve is the total input power of AM1.5 G spectrum, and for a single-junction silicon solar cell as shown in Figure 1-2(a), the red shaded rectangle represents the power output by the device, and the grey area above the rectangle, where photon energies are lower than the bandgap of silicon, represents the absorption loss; In contrast, the purple area to the right of the curve, where photon energies are higher than the bandgap of silicon, represents the thermalization loss.

By adding another top-cell material with wider bandgap, e.g. 1.7 eV as shown in Figure 1-2(b), to absorb the high energy photons, the thermalization loss reduces.

1.3 Tandem Efficiency Limit

It is not difficult to conclude that the thermalization loss can be minimized by adding more and more wider-bandgap materials in a cascade fashion in terms of their bandgaps. However, as this thesis limit the scope of research to silicon-based tandem—pairing only *one* top cell with silicon, it's desirable to know which bandgap, in combination with silicon, produces the highest tandem efficiency.

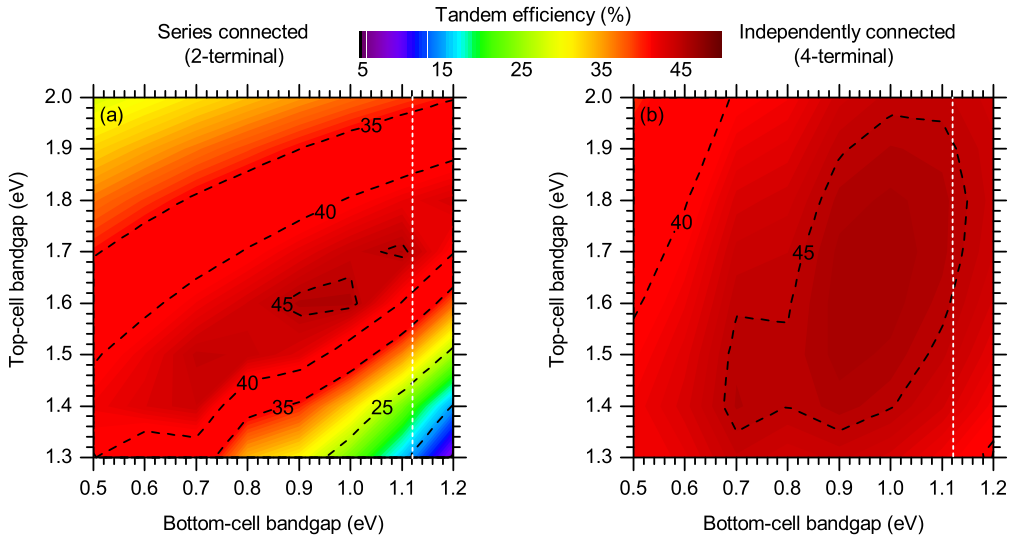

Figure 1-3. Detailed-balance calculation of tandem efficiency for (a) series-connected sub-cells, and (b) independently-operated sub-cells. The white dashed line denotes the bandgap of silicon cell.

A top-down approach to answer this question is the detailed-balance model, often referred as Shockley-Queisser (SQ) limit as originally proposed by Shockley and Queisser to calculate single-junction limit [17]. This model is generalized for all semiconductors that only considers radiative recombination, and can be extended to cover tandem concept

by applying the same approach to multiple materials [18-20]. Figure 1-3 shows the 1-sun tandem efficiency under (ASTM G173-03) AM1.5 G spectrum. For series-connected sub-cells, as shown in Figure 1-3(a), due to the current-matching constraint at maximum power point, the bandgap combinations to yield best tandem efficiency are rather limited. Fortunately, using material with a bandgap of 1.1 eV (silicon) as bottom cell would result close-to-maximum tandem efficiency when pairing with a top cell that has a bandgap of 1.7 eV. When sub-cells are independently connected and thus removed the current-matching constraint, silicon bottom cell can have a wide range of top-cell choice in terms of its bandgap, and still yield maximum tandem efficiency as it would achieve in series-connected situation, as shown in Figure 1-3(b).

1.4 Tandem Assembly Technologies

The essence of a top-cell/silicon tandem is the diversion of high-energy photons to a wide-bandgap material, preventing their absorption in the silicon bottom cell to reduce the thermalization loss. This spectrum filtering process can be achieved by the top cell itself or with help from an additional optical element.

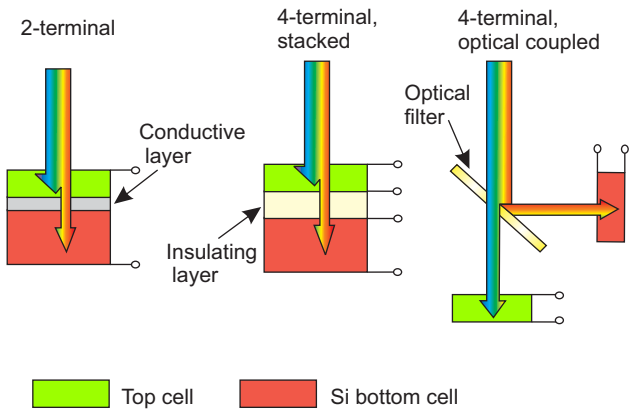

Figure 1-4. Three common coupling configurations [21]. The solored arrows show how the solar spectrum is transmitted and absorbed by the top and bottom cells.

As a semiconductor transmits photons with energies lower than its bandgap energy, stacking a wide-bandgap material on top of silicon results in absorptive filtering. Depending on whether the two sub-cells are electrically connected or not, tandems with absorptive filtering can be subdivided into two categories: monolithic (two-terminal) tandems, and mechanically stacked (four-terminal) tandems, as shown in Figure 1-4 [21, 22]. In a two-terminal configuration, the sub-cells are connected in series, and therefore their currents must be matched at the maximum power points to avoid power loss. In a four-terminal configuration, by contrast, the power output of each sub-cell is measured independently. Removing the current-matching constraint means that precise control of the top-cell bandgap and thickness, front-surface reflection, and parasitic absorption in supporting layers is no longer required. Moreover, four-terminal tandems in the field are expected to have an energy yield a few percent higher than equivalent-efficiency two-terminal tandems because they are insensitive to current mismatch resulting from spectrum variation [23, 24]. Another advantage of four-terminal tandem is that each sub-cell is processed independently, therefore sub-cells fabricated with incompatible processing temperatures or chemistries can still be paired. Also, four-terminal tandem would not suffer any electrical loss from imperfect interfaces, e.g. defects, which people making two-terminal tandems mostly fight with. Recently, to get rid of this interface-defects-induce electrical loss, researchers are investigating wafer bonding technologies, including fusion bonding [25], surface activation bonding [26-30], and transparent conductive oxide (TCO) bonding [31]. However, these bonding technologies require atomic flat surfaces, which imposes the heavy cost of chemical-mechanical polishing, which is not favorable for PV manufacturing. Another “bonding” category is “wiring” sub-cells either with metals

fingers [32], or metal particles [33, 34]. For these technologies, surface roughness requirement may be relaxed, however, optical transparency or electrical conductivity could be the major concern.

Despite these aforementioned advantages, no four-terminal tandem has been commercialized; the III-V multi-junction pioneers as well as thin-film silicon tandems are monolithic two-terminal devices [28, 35-38]. One anticipated stumbling block is the additional wiring that increases the balance-of-system cost, and the jury is out as to whether the value of increased efficiency compared to the two-terminal counterpart will outweigh the cost of increased complexity. Also on the cell level, the four-terminal tandems may suffer more optical losses—mainly parasitic absorption loss—than their two-terminal counterparts, as there are four conductive layers, instead of two, providing lateral transport (two for each sub-cell) that has high carrier concentration and, therefore, notable free-carrier absorption. Another disadvantages of four-terminal tandems compared to two-terminal tandems is the additional metallization that not only increase cost but also induces shading loss from finger misalignment [39]; Also for the same value of resistance in both sub-cells, the resistance-induced power loss in a two-terminal tandem is expected to be less than in a four-terminal counterpart because the former has a higher voltage at the maximum power point [40]. In other words, monolithic tandem can tolerate higher series resistances.

Unlike absorptive filtering in monolithic or mechanically stacked tandems, optically coupled tandems direct high (low) energy photons to wide- (narrow-) bandgap absorbers by an optical element. Depending on the type of optical element, it can be sub-divided into reflective filtering—e.g. using a dichroic mirror [41, 42]—refractive filtering [43], holographic filtering etc. [44, 45]. These optically-coupled tandems are four-terminal

tandems, therefore, their performance are not restricted by issues such as lattice-mismatch or current-mismatch. However, a common challenge for these optically-couple tandems are the spectral fidelity of the optics [46].

Distinct from the oft-discussed two- and four-terminal configuration, three-terminal tandems based on interdigitated-back-contact (IBC) silicon solar cell are gaining attention, which are structurally different from the traditional three-terminal tandems that have been attempted on III-V [47], amorphous silicon [48], and polymer solar cells [49]. In this configuration, one terminal is located on the front surface of the top cell, and the rest two terminals are on the back side—inherited from the IBC silicon cell; these two sub-cells are electrically connected either with a tunnel junction, as in a monolithic tandem, or sharing an electron or hole contact [50]. This tandem, with the additional terminal, decouples the charge collection of the two sub-cells, as in a four-terminal tandem, but eliminates the lateral transport requirement (which causes free-carrier absorption) in the electrical coupling layer, as in a two terminal tandem. A more exotic design even uses back-contact top cell, which further eliminates the front transparent electrode in the top cell [51].

1.5 State of the Art of Silicon-Based Tandems

Coupling configuration aside, there are presently three major top-cell candidates under investigation. III-V materials are predominant due to their earlier success in III-V multi-junctions. (Note that, historically, there was a lot of research of growing III-V solar cell on top of silicon. However, much of this work was aimed to use silicon as an alternative substrate instead of an active bottom cell to form a tandem [27, 52-54], and thus are not the focus of this thesis.) Perovskites are an emerging material that have the potential for

low manufacturing cost. Finally, wide-bandgap II-VI materials are being considered for pairing with silicon—a departure from their historic role as a competitor to silicon in single-junction devices. Other material such as II-IV-V_2 chalcopyrites are also an interesting top-cell absorber candidates, but are still in a pre-cell research stage. [55]

1.5.1 III-V/Si Tandems

III-V is the most successful technology in making tandem or multi-junction solar cells. As shown in Figure 1-5, a tandem efficiency close to 28% was demonstrated both with AlGaAs/GaAs and InGaP/GaAs materials as early as in 1989 [56, 57], and in 1996, Takamoto *et al*. reported a 4 cm^2, 30.3% InGaP/GaAs tandem, which was the first PV device that achieves efficiency greater than 30% measured under 1-sun [58]. The record was pushed up to 31.6% by Alta Devices in 2016 [59]. By tuning the bandgap to 1.1 eV—close to that of silicon—NREL achieved a 32.6% GaInAsP/GaInAs tandem in 2017 [60]. As demonstrated in this device, and predicted by the detailed-balance model, silicon is a better bottom cell than GaAs—in terms of bandgap—for a tandem [61]. With the additional benefits of using silicon substrates such as low cost, high thermal conductivity, and superior mechanical strength [62], direct growth of III-V materials on top of silicon was one of the first approach investigated in III-V/Si tandems. In 1992, Shimizu *et al*. reported the first AlGaAs/Si tandem with an efficiency of 16.3% [63]. By improving the growth sequence and adopting an Al compositionally graded band emitter layer, a 19.9% tandem was reported in 1995 [64]. With further optimization of thermal-cycle annealing and buffer layer, Soga *et al*. reported a 21.4%-efficient $Al_{0.15}Ga_{0.85}As$/Si tandem in 1997, which is the highest-reported III-V/silicon tandem achieved by the direct growth method; however, this device is still limited by the high threading dislocation density (TDD) of the AlGaAs layer

grown on silicon due to the lattice mismatch between the III-V material and silicon [65]. Given the large lattice mismatch between silicon and well-established III-V cells, e.g. GaAs, InGaP, AlGaAs etc., other III-V cells with lattice constant close to silicon are alternative candidates. A GaAsP/Si tandem with GaP as a buffer layer was reported in 1994, with an efficiency of 5.5% [66]. Grassman *et al*. demonstrated a 10.7%-efficient $GaAs_{0.75}P_{0.25}$/Si tandem in 2013 and improved to 13.1% in 2016 [67, 68]. Michelle *et al*. demonstrated a 15.3%-efficient 1.7 eV GaAsP top cell on GaP/Si template with record-low TDD, which paves the way for >25%-efficient monolithic GaAsP/Si tandem [69]. Quaternary compounds such as GaAsNP and InGaNP could match the lattice constant of silicon well, however, the growth control of quaternary compounds is a substantial challenge compared to the well-studied binary or ternary compounds, NREL reported a 5.2% GaNPAs/Si tandem with its top cell being the performance-limiting sub-cell, which indicates the III-V material quality grown on silicon still needs improving [70].

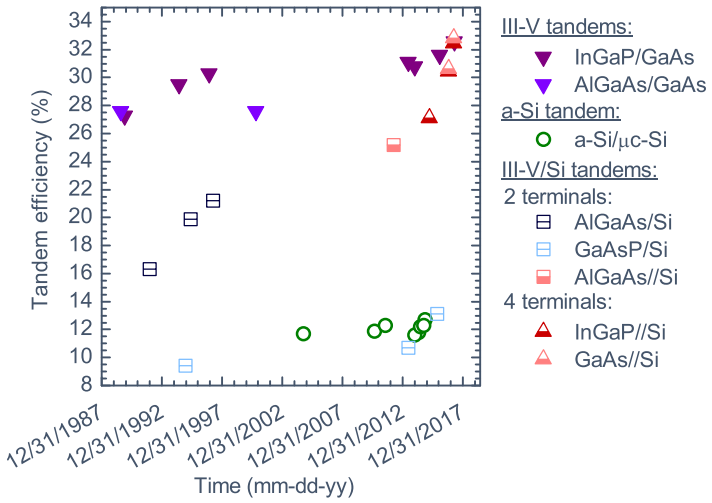

Figure 1-5. Best III-V/silicon tandem efficiencies reported on a time scale. Also shown are efficiencies of III-V tandems and micromorph tandems.

Reducing TDD is a common challenge for direct growth III-V/Si tandem; however, a technology to circumvent it while still making a two-terminal tandem is wafer bonding. In 2012, Tanabe *et al*. first reported a 25.2%-efficient $Al_{0.1}Ga_{0.9}As$/Si tandem, achieved by direct fusion bonding: the GaAs substrate with AlGaAs cell and a silicon diffuse-junction cell were brought into contact with the (011) edges aligned, and annealed at 300–500 °C in ambient air for 3 h under a uniaxial pressure of 0.1 MPa [25]. In 2013, the surface activation bonding technology, developed at Fraunhofer ISE, was applied to bond III-V materials with silicon. In this approach, the Si and GaAs substrates are in contact with 10 kN load at 120°C for 5 minutes right after argon fast-atom-beam treatment [26]. However, only triple-junction (GaInP/GaAs//Si) results were reported with this technology, with the efficiency increased from initial 20.5% to 33% in 2017 [26, 30, 71]. Distinct from using GaAs as a bonding layer, NREL was investigating a bonding technology with transparent-conductive-oxide layers, however, no tandem results were reported [31]. A shared limitation of all the bonding technologies is the necessity of atomic-flat surfaces, usually achieved by chemical-mechanical polishing (CMP), which is cost-prohibitive in PV production.

Four-terminal tandems relax the lattice- and current-matching constraints, and therefore, as expected, III-V/Si tandems in this category have higher efficiencies. With the mechanically stacked configuration, a 31%-efficient GaAs//Si tandem was reported as early as 1988, as measured under a concentration of 347x [72]. As for one-sun application, there were not many reports until in 2015, when NREL/CSEM first reported a 27.1%-efficient GaInP//Si tandem made by epoxying a GaInP cell onto a silicon heterojunction cell [73]. By inserting a glass slide between two sub-cells with additional optical optimization, a 1 cm^2, 29.8%-efficient tandem was report in 2016 [74], this number went

up to 30.5% later in 2016 [75], and improved to 32.5% in 2017 [76]. Using the same configuration but with a GaAs top-cell, a 32.8% GaAs//Si tandem was also reported by CSEM [76].

1.5.2 II-VI/Si Tandems

Cadmium Telluride (CdTe), the dominant II-VI technology, is the only thin-film technology in the market that can compete with silicon in terms of cost [11, 77]. Therefore, most researchers were focused on improving its single-junction efficiency as a "foe" to silicon, instead of being a "friend" of silicon to be used in a tandem. Similar to III-V materials, II-VI materials have a wide range of flexibility in terms of its bandgap (lattice constant is unimportant for polycrystalline cells, but is also tunable), which makes them favorable for top cells to pair with silicon [78, 79]. Notably, unlike III-V materials, the electronic properties of II-VI materials, such as minority-carrier lifetime and mobility, are less sensitive to structural defects such as dislocations due to the more ionic, less covalent nature of the material [78]. This, in principle, enables better II-Vi/Si tandem than III-VI/Si tandems made with direct epitaxial growth, given the TDD challenges. However, experimentally, only one 16.8%-efficient CdZnTe/Si tandem result was reported in the literature, achieved by growing a 1.8-eV-bandgap CdZnTe on top of a diffused-junction silicon cell [80]. The single-junction CdZnTe cell alone was reported to have 16% efficiency. There are very few reports of research progress on high bandgap II-VI cells but, recently, ASU started developing such top cells [81], and a 11.2%-efficient monocrystalline $Mg_{0.13}Cd_{0.87}Te$ solar cell with a bandgap of 1.7 eV was achieved [82]. Polycrystalline MgCdTe and ZnCdTe absorbers with a bandgap of 1.7 eV are also under investigation [83].

1.5.3 Perovskite/Silicon Tandems

Metal halide perovskite solar cells have developed very rapidly, with record single-junction efficiencies now over 22% [75, 84]. Solar cells made with this material are far from commercialization and have several important challenges, such as the need to achieve long-term stability and the development of a manufacturing method for the reproducible fabrication of high-performance devices [85, 86]. Nevertheless, perovskites are receiving considerable attention because of their favorable material properties, such as strong optical absorption, long diffusion lengths, and solution processability enabled by the relatively benign nature of intrinsic defects [87, 88]. Additionally, their wide, tunable bandgap makes perovskites highly attractive for use in silicon to form tandems [89, 90]. Although perovskite/silicon tandems have a relatively short history, progress has been tremendous. As shown in Figure 1-6(a), within about two and half years, tandem efficiencies went from ~13% to 26.4% and 23.6% for mechanical-stacked and monolithic configurations, respectively [91-93]. However, it is important to notice that the cell area of most devices are quite small. Figure 1-6(b) shows the same efficiency data as in Figure 1-6(a) but as a function of device area. Obviously, most of the devices have cell area < 1 cm^2, which is a lab-scale, proof-of-concept device size.

The first two-terminal, monolithic perovskite/silicon tandem was reported in 2015 by Mailoa *et al*. The authors deposited a methylammonium-lead-iodide perovskite ($MAPbI_3$) on a diffused-junction solar cell and achieved a 1-cm^2 tandem cell with an efficiency of 13.7% [94]. Albrecht *et al*. used low-temperature (< 120°C) processing of a perovskite that enabled the use of a silicon heterojunction cell as the bottom cell, and reported a 0.16-cm^2, 18.1%-efficient tandem in the same year [95]. In 2016, with the

utilization of a better transparent conductive oxide (TCO) and anti-reflective foils, a 0.17-cm^2, 21.2%-efficient tandem was achieved by EPFL [96]. Later, employing a nano-crystalline-silicon-based recombination junction, in combination with a cesium-based perovskite ($Cs_{0.19}MA_{0.81}PbI_3$), Sahli *et al*. reported a 0.25-cm^2, 22%-efficient tandem [97]. Due to the low lateral conductivity of its recombination junction, a 12.96-cm^2, 18%-efficient tandem was also reported. Recently, based on diffused-silicon cell, Wu *et al*. reported a 22.5%-efficient perovskite/silicon tandem by employing a rather complicated perovskite top cell ($Cs_{0.07}Rb_{0.03}FA_{0.765}MA_{0.135}PbI_{2.55}Br_{0.45}$), and a low-refractive-index silicon nitride on the rear side of silicon cell to enhance the near-infrared light response in the silicon cell [98]. As the momentum of the research continues, new records are expected to come rapidly.

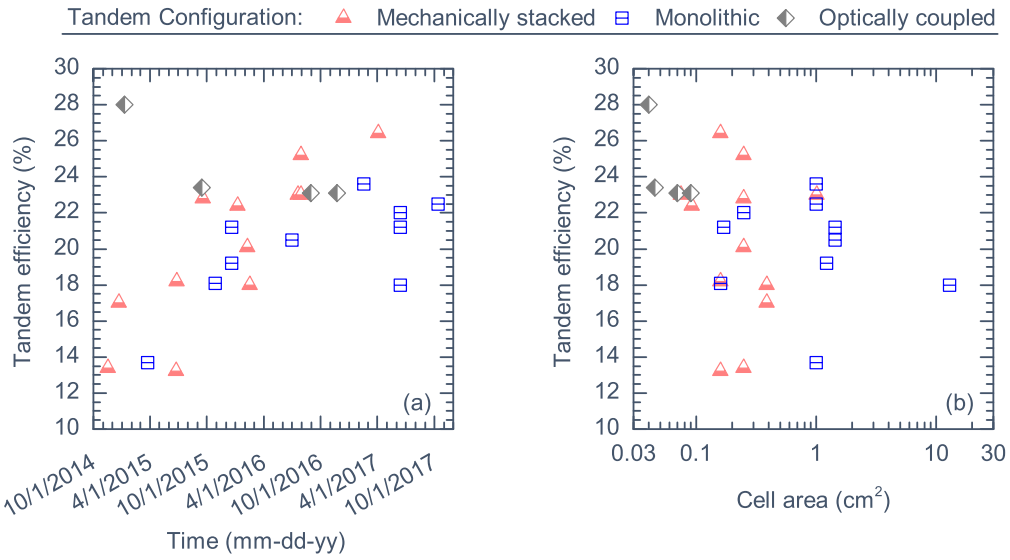

Figure 1-6. Perovskite/silicon tandem efficiency reported (a) on a time scale (b) on a device area scale. Note that the device areas are designated illuminated area during measurement. For four-terminal measurements for which the area of top and bottom cells were different, the smaller one was show on the scale.

Four-terminal, mechanically stacked perovskite/silicon tandems are also improving incredibly. With molybdenum oxide and indium tin oxide (MoOx/ITO) as a semi-transparent hole contact for a perovskite cell, Loper *et al*. reported in 2014 the first mechanically stacked perovskite/silicon tandem with an efficiency of 13.4%, achieved by summing the efficiencies of 6.2% from a 0.25-cm^2 $MAPbI_3$ top cell and 7.2% from a 4-cm^2 silicon heterojunction bottom cell [99]. One month later, Bailie *et al*. reported that using silver nanowire as a semi-transparent electrode for the perovskite cell enabled a 17%-efficient tandem, calculated by summing the efficiencies of 12.7% from a $MAPbI_3$ top cell and 4.3% from a multi-crystalline silicon bottom cell, both 0.39 cm^2 in size [100]. Within the same group, using indium tin oxide (ITO) as a semi-transparent electrode and MgF_2 as an anti-reflection layer, an 18% tandem efficiency was achieved by summing 12.3% from a $MAPbI_3$ top cell and 5.7% from a monocrystalline solar cell [101]. In 2015, with a more transparent indium zinc oxide (IZO) layer to form a MoOx/IZO semi-transparent contact, Werner *et al*. achieved a 18.2%-efficient tandem, summing the efficiencies of 10.4% from a 0.16-cm^2 $MAPbI_3$ top cell and 7.8% from a 4-cm^2 silicon heterojunction bottom cell [102]. This efficiency was quickly pushed up to 22.8%, by improving the top cell to 13.4% on a 0.25-cm^2 size, and by improving the bottom cell to 9.4%, still on a 4-cm^2 device [103]. By further improving the efficiency of the perovskite top cell to 16.4%, Werner *et al*., again, achieved a 25.2%-efficient tandem [104]. All these four-terminal tandems reported were using 1.55-eV $MAPbI_3$ perovskites. With higher-bandgap, mixed-cation perovskites, McMeekin *et al.* first reported a 19.8%-efficient tandem based on a 1.74-eV, formamidinium/cesium-mixed ($FACsPbI_{3-x}Br_x$) perovskite top cell, by summing the efficiencies of 12.5% from the top cell and 7.3% from a silicon heterojunction bottom cell

[105]. Using a 1.63-eV $Cs_{0.05}(MA_{0.17}FA_{0.83})_{0.95}Pb(I_{0.83}Br_{0.17})_3$ perovskite, Peng *et al.* reported a 24.5%-efficiency tandem, by summing the efficiencies of 16.6% from a 0.36-cm^2 top cell, and 7.9% from a 4-cm^2 interdigitated-back-contact (IBC) silicon cell [106]. Recently, a new record of 26.4%-efficient tandem was reported by Duong *et al.,* with 16% from a 1.73-eV, rubidium-incorporated, formamidinium/methylammonium/cesium-mixed perovskite top cell that uses MoOx/ITO as semi-transparent electrode on a 0.3-cm^2 size, and 10.4% from a 4-cm^2 interdigitated-back-contact (IBC) silicon cell [107].

Optically coupled perovskite/silicon tandems have also been investigated, mainly as a demonstration of efficiency potential. As early as 2014, Uzu *et al*. demonstrated the first optically coupled, 28%-efficient perovskite/silicon tandem using a dichroic mirror beamsplitter to couple a 1.6-eV-bandgap, $MAPbI_3$ perovskite and a silicon heterojunction cell [108]. With an aperture of 0.04-cm^2, the 0.2-cm^2 15.3%-efficient top cell generated 7.5% under the reflected light (as the dichroic sends only light < 550 *nm* to the top cell), and the 4-cm^2, 25.2%-efficient Si bottom cell generated 20.5% under the transmitted light, which adds up to 28.0% total efficiency. Similarly, Sheng *et al*. made a 2.3-eV-bandgap, 0.045-cm^2 $MAPbBr_3$ perovskite coupled with a 1-cm^2, 22.7%-efficient passivated-emitter-with-rear-locally-diffused (PERL) cell [109]. The dichroic in this setup sent only light with photon energies higher than 2.5 eV (wavelength < 500 *nm*) to the wide-bandgap perovskite, and the resulting tandem efficiency was 23.4%. Perovskite/silicon tandems that used the band edge of the perovskite as an absorptive filter and reflected sub-bandgap light were demonstrated with 0.09-cm^2 and 0.07-cm^2 perovskite cells by Duong *et al*. and Li *et al*., respectively, and both yielded 23.1%-efficient tandems [110, 111].

CHAPTER 2

SELECTING TANDEM PARTNERS FOR SILICON SOLAR CELLS

This chapter introduces a new "spectral efficiency" concept to understand how tandem cells should be designed and to identify the best tandem partners for silicon cells. "Spectral efficiency" is a bottom-up approach to calculate the limiting tandem efficiency as opposed to the widely known "detailed-balance" top-down approach. It visualizes the efficiency of solar cells at each wavelength and provides a means to assess the efficiency potential of any cell pairing; top cells for silicon can thus be selected among *existing* solar cells, which are different from their idealized counterparts assumed in the detailed-balance model. Using spectral efficiency, the limiting silicon-based tandem efficiency are re-evaluated after taking into account Auger recombination in a silicon bottom cell; and a top-cell-design guide is constructed for silicon-based tandems that sets efficiency targets for top cells with various bandgaps to achieve targeted tandem efficiencies.

2.1 Tandem Efficiency Limits

What efficiency might a silicon-based tandem be expected to reach? A top-down approach to this question begins by calculating the limiting efficiency, which others have done using a detailed-balance model that considers only radiative recombination [18, 19]. A more accurate treatment of the indirect-bandgap silicon bottom cell must also include Auger recombination and incomplete photon absorption [6], however, and thus Figure 2-1 shows the limiting efficiency of a tandem comprised of a radiative-recombination-limited top cell of variable bandgap and an Auger-recombination-limited silicon bottom cell with

Lambertian light trapping [21]. For a two-terminal configuration, a top cell with a bandgap of approximately 1.7 eV is best, and the tandem has a limiting efficiency of 43% under one-sun illumination. For the reasons discussed in Chapter 1, four-terminal configurations are less sensitive to the bandgap of the top cell but also have peak efficiencies near 1.7 eV. Were tandem cells to reach the same level of maturity as monocrystalline single-junction PV technologies such as silicon and GaAs, which have achieved cell efficiencies that are more than 85% of their respective limits, they would operate with over 36% efficiency.

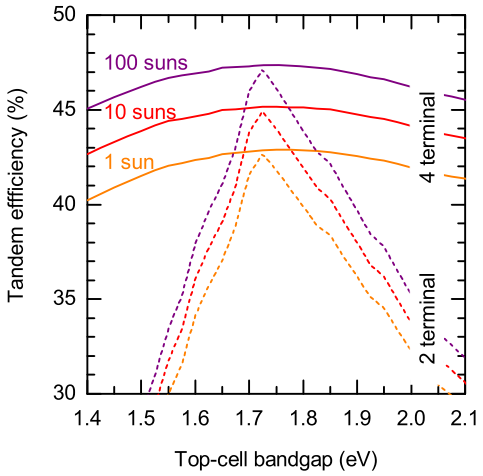

Figure 2-1. Limiting efficiency of a silicon-based tandem PV cell for varying top-cell bandgap. Efficiencies are shown for two- and four-terminal configurations, as well as three illumination intensities. The silicon cell's current–voltage characteristic was calculated with a model that includes Auger recombination and Lambertian light trapping; the top cell's characteristic was calculated with a detailed-balance model that considers radiative recombination only. The efficiency of the four-terminal tandem was calculated by summing the maximum power of the individual sub-cells and normalizing to the input power; the efficiency of the two-terminal tandem was similarly calculated but using the power generated by both sub-cells at the maximum-power current of the limiting sub-cell [21].

2.2 Spectral Efficiency Concept

A different, bottom-up approach to assess the potential of silicon-based tandems is to ask: what would happen if two existing sub-cells were paired? Which cells should one

choose and what efficiency is possible? The limiting efficiency calculations used to generate Figure 2-1, which consider hypothetical, ideal cells, are no help here. Instead, we turn to a little-known concept called spectral efficiency [21, 45], denoted $\eta(\lambda)$ and defined as:

$$\eta(\lambda) = \frac{V_{oc} \cdot FF \cdot J_{sc}(\lambda)}{I(\lambda)} \qquad (2.1)$$

with V_{oc} the open-circuit voltage, FF the fill factor, λ the wavelength, $I(\lambda)$ the spectral irradiance (in $Wm^{-2}nm^{-1}$), and $J_{sc}(\lambda)$ the short-circuit current density per unit wavelength (in $Am^{-2}nm^{-1}$):

$$J_{sc}(\lambda) = q\frac{\lambda}{hc}EQE(\lambda) \cdot I(\lambda) \qquad (2.2)$$

In equation (2.2), q is elementary charge, h is Planck's constant, c is the speed of light, and $EQE(\lambda)$ is the external quantum efficiency. Equation (2.1) looks like the usual definition of PV cell efficiency, but it is spectrally resolved. Spectral efficiency depicts efficiency at each wavelength and—in analogy with EQE and J_{sc}—its spectrum-weighted integral is cell efficiency. To calculate spectral efficiency, one needs only a current–voltage (J–V) characteristic and EQE spectrum, and thus it is possible to find the spectral efficiency of, for example, the record cells in the solar cell efficiency tables [71].

Figure 2-2a displays the spectral efficiencies of several record PV cells, including potential bottom cells such as silicon and CIGS, and potential top cells ranging from GaAs to perovskites. Figure 2-2b displays the limiting spectral efficiencies of cells with a range of bandgaps. Each spectral efficiency curve peaks near the absorber's bandgap wavelength; longer wavelengths are not absorbed and result in zero efficiency, and shorter wavelengths are converted with lower efficiency because of carrier thermalization. The utility of spectral

efficiency in designing tandems is that cells of different technologies can be directly compared, and that the benefit of diverting photons from silicon to a candidate top cell is visually apparent. For example, Figure 2-2a reveals that, even though a-Si:H has the ideal bandgap for a top cell, the best a-Si:H cell converts every wavelength to electricity with poorer efficiency than the best monocrystalline silicon cell, and thus their tandem will necessarily perform less well than the bottom cell alone. Conversely, GaInP, which has a similar bandgap to a-Si:H, can provide a substantial efficiency boost if coupled with silicon so that wavelengths shorter than 650 nm are absorbed in the GaInP cell.

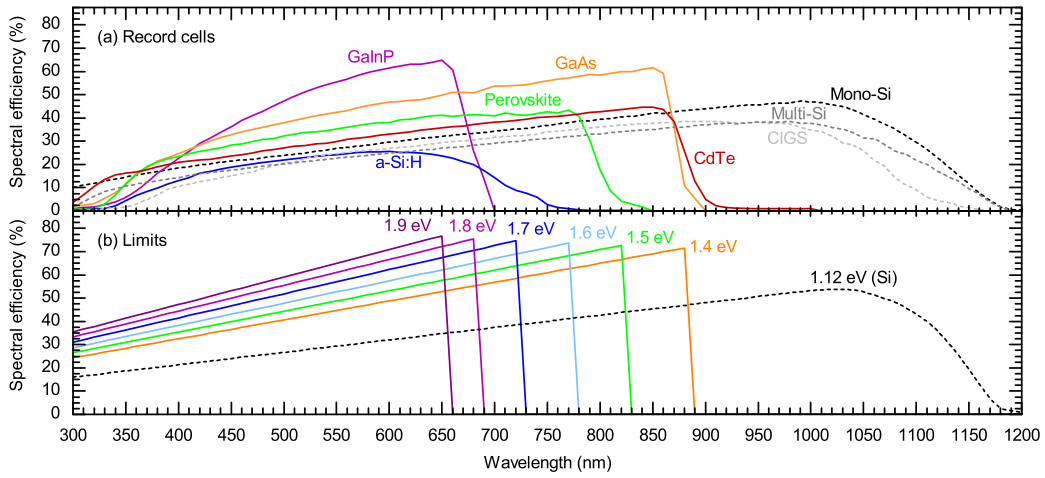

Figure 2-2. Using spectral efficiency to choose tandem pairings. (a) Spectral efficiencies of record PV cells that are candidates for top (solid) and bottom (dashed) cells. Data digitized from the *Solar cell efficiency tables* [112-115]. (b) Limiting spectral efficiencies of ideal top cells—calculated with a detailed-balanced model that considers radiative recombination only—and the ideal silicon bottom cell—calculated with a model that includes Auger recombination and Lambertian light trapping.

2.3 Picking Partners for Silicon

The maximum efficiency of a tandem can be calculated by summing the integrated sub-cell spectral efficiencies, each weighted by the spectra reaching that sub-cell and normalized to the incident photon power:

$$\eta_{tandem} = \frac{\int \eta_{top}(\lambda) f_{top}(\lambda) I(\lambda) d\lambda}{\int I(\lambda)\, d\lambda} + \frac{\int \eta_{bottom}(\lambda) f_{bottom}(\lambda) I(\lambda) d\lambda}{\int I(\lambda)\, d\lambda} \qquad (2.3)$$

with

$$f_{top}(\lambda) = \frac{\Phi_{top}(\lambda)}{\Phi_{incident}(\lambda)} \qquad (2.4)$$

and

$$f_{bottom}(\lambda) = \frac{\Phi_{bottom}(\lambda)}{\Phi_{incident}(\lambda)} \qquad (2.5)$$

In equation (2.4) and (2.5), $f(\lambda)$ is the (wavelength-resolved) spectral fidelity—the fraction of the incident light with wavelength λ that reaches a sub-cell (Φ is photon flux). The efficiency given by equation (2.3) is that of *a tandem composed of two existing cells coupled losslessly*. This means no electrical losses (for example, due to imperfect current matching), and thus implicitly assumes a four-terminal configuration, as well as no optical losses (for example, due to parasitic absorption). All tandems, regardless of their coupling configurations, are subject to the maximum efficiency constraint expressed by equation (2.3). Two-terminal tandems will likely fall below this limit primarily because of electrical losses, whereas four-terminal tandems will likely suffer primarily from optical losses. There are two common assumptions for the limiting spectral fidelities. For a mechanically stacked tandem, $f_{top}(\lambda) = 1$ (all light reaches the top cell) and $f_{bottom}(\lambda) = T_{top}$ (all light transmitted through the top cell reaches the bottom cell). For two cells coupled with a beam splitter, $f_{top}(\lambda) = 1$ for λ shorter than $\lambda_{top=bottom}$ (the wavelength at which the top- and bottom-cell spectral efficiencies are equal) and 0 for longer wavelengths, whereas $f_{bottom}(\lambda) = 0$ for λ shorter than $\lambda_{top=bottom}$ and 1 for longer wavelengths. In other words, the beam splitter is perfect.

Table 2-1. Maximum possible efficiencies of silicon-based tandem PV cells pairing existing record top and bottom cells [21].

Top cell	AM1.5 G Efficiency	Bandgap	Fraction of detailed-balance efficiency	Tandem efficiency with mono-Si cell*		Tandem efficiency with multi-Si cell*	
GaInP	20.8	1.81 eV	77 %	34.5 %	(35.1 %)	32.1 %	(32.6 %)
GaAs	28.8	1.42 eV	87 %	34.9 %	(35.5 %)	33.6 %	(34.2 %)
CdTe	21.5	1.45 eV	66 %	27.3 %	(27.7 %)	26.0 %	(26.4 %)
Perovskite	20.1	1.47 eV	62 %	29.2 %	(30.2 %)	27.4 %	(28.4 %)
Perovskite [105]	17.1	1.75 eV	61 %	29.0 %	(29.7 %)	26.8 %	(27.5 %)

* The efficiencies in parentheses correspond to mechanical stacking; those not in parentheses correspond to coupling with a beam splitter. The V_{oc} of the silicon cell was adjusted to account for filtered illumination.

Table 2-1 lists the maximum efficiencies of tandems made from the cells in Figure 2-2a using the $f(\lambda)$ values corresponding to the two coupling cases described above: mechanical stacking and beam splitter. One surprise is that the best perovskite cell on the best monocrystalline silicon cell results in only a marginal gain in efficiency (approximately 4% absolute) when the two sub-cells are coupled losslessly, yielding a tandem that just reaches 30%. As there will undoubtedly be at least optical losses in their coupling, it will be challenging to significantly exceed the efficiency of the silicon cell alone (25.6%) using present perovskites. An exception is if the sub-cells are coupled optically with an excellent beam splitter—remember the 28.0%-efficiency tandem demonstrated by Uzu *et al*. [108]—but this configuration is usually regarded as a laboratory demonstration that will not be manufactured and that will not collect diffuse light. Note, however, that the best perovskite cell with the best multi-crystalline silicon cell reaches nearly as high an efficiency and offers a substantial boost compared to the inexpensive multi-crystalline silicon cell alone (21.3%). Another surprise is that, of all existing PV cells, GaAs would make the best top cell, even though it has the 'wrong' bandgap according to Figure 2-1. This is because it is much more efficient—that is, closer to its detailed-balance limit—than the other cells.

2.4 Tomorrow's Top Cell

In evaluating new tandem possibilities, we believe that the best approach is to calculate the maximum tandem efficiency using the measured spectral efficiencies of the two cells of interest, as in Table 2-1. It is also possible, however, to construct a top-cell design guide using approximate spectral efficiencies calculated by derating the limiting spectral efficiencies shown in Figure 2-2b. Here, derating indicates that the spectral

efficiency is multiplied by a constant factor less than unity; that is, $\eta_{\text{derated}}(\lambda) = C \cdot \eta_{\text{limiting}}(\lambda)$ with C the 'top-cell fraction of detailed-balance efficiency'. According to equation (2.1), this is equivalent to reducing the V_{oc} or FF of an ideal cell, or reducing its $J_{sc}(\lambda)$ by the same fraction at each wavelength. Figure 2-3 is such a guide and predicts the efficiencies of tandems that pair a 20%- or 25%-efficient silicon bottom cell with top cells of varying bandgap and efficiency derating. The derating is expressed on the x-axis as the fraction of the detailed-balance efficiency, and the one-sun efficiencies of the top cells are given by the gray contours.

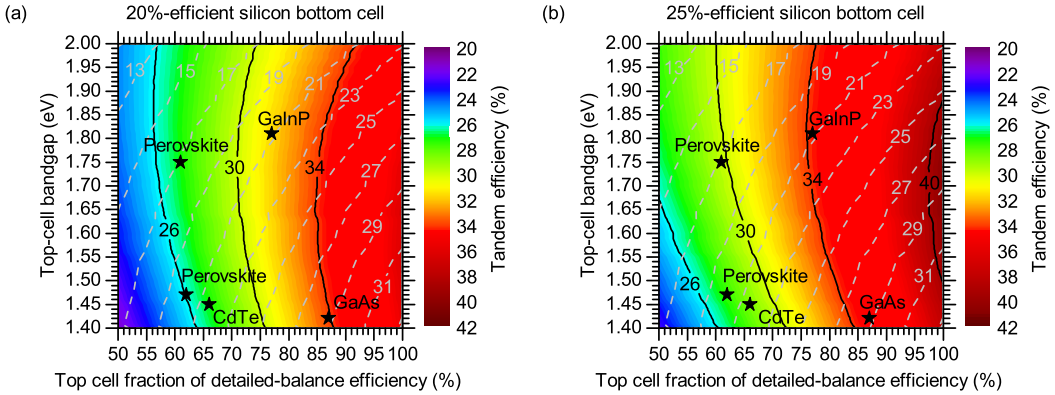

Figure 2-3. Guide for predicting the maximum possible efficiency of a silicon-based tandem as a function of the top-cell bandgap and efficiency. (a) Tandem with a silicon bottom cell that is 20% efficient when measured alone. (b) Tandem with a silicon bottom cell that is 25% efficient when measured alone. In each plot, the color scale and black contour lines indicate the tandem efficiency, and the dashed grey contour lines indicate the efficiency of the top cell when measured alone. To obtain the approximate spectral efficiencies of the sub-cells used to calculate the tandem efficiency, the limiting spectral efficiencies in Figure 2-2b were derated by scaling them by a constant factor.

Although Figure 2-3 is approximate, it successfully reproduces the exact results for existing sub-cells. For example, consider the GaInP cell in Figure 2-3b, which assumes a 25%-efficient silicon bottom cell that is similar to the 25.6%-efficient silicon cell in Table 2-1. The star, which was placed based on the InGaP cell's bandgap and efficiency relative

to the detailed-balance limit, corresponds to both the correct top-cell one-sun efficiency (slightly less than 21%, from the gray contour lines) and the tandem efficiency (slightly over 34%, from the color contours). This indicates how to use this guide to quickly evaluate candidate top cells: Find the cell's bandgap on the *y*-axis and its one-sun efficiency with the gray contours (or its fraction of the detailed-balance limit on the *x*-axis—the result is the same). The color then indicates the maximum tandem efficiency possible if this cell were coupled with a 20%- or 25%-efficient silicon bottom cell.

The future of silicon-based tandems is presently wide open, with several top-cell contenders fighting cost-performance trade-offs, and with new top-cell materials to emerge. Spectral efficiency, which allows cells to be compared at each wavelength on an equal footing, provides a means to assess the efficiency potential of any cell pairing, and thus a methodology for selecting top cells for silicon. At present, only III-V and perovskite top cells have reached efficiencies that justify coupling with the best silicon cells, with the former promising up to 5% higher absolute tandem efficiency than the latter. However, this picture will evolve as wide-bandgap cells continue to develop. Spectral efficiency will serve throughout this process as an unerring arbiter of cell pairings and a tool with which tandem efficiency limits may continually updated.

CHAPTER 3

THE PATH TO MARKET FOR SILICON-BASED TANDEM PHOTOVOLTAIC MODULES

Tandem photovoltaic modules with silicon bottom cells promise to push the efficiency beyond the single-junction limit and further lower the levelized cost of solar electricity. However, it is not clear whether continued improvements in efficiency are sufficient to propel tandems beyond their constituent sub-cell modules in terms of *cost competitiveness*. In this chapter, we ask and answer two questions: Under what conditions, if any, will silicon-based tandems compete in the (flat-plate) photovoltaics market? And, is there any overlap between those favorable conditions and the projected evolution of the market?

We first construct a simple and versatile analytical model to evaluate the cost competitiveness of an arbitrary tandem against its sub-cell alternatives. This model indicates that the ratio of sub-cell module cost to area-related balance-of-system cost is the key metric that will determine the market success or failure of tandems. By analyzing historical U.S. data for silicon module cost and area-related balance-of-system cost, we demonstrate that this ratio is decreasing, which means that *tandems will become increasingly attractive in the market*. With our model, we further predict that top-cell modules that cost up to $\$40/m^2$—which is similar to the projected silicon module cost—will make tandem cost-competitive in the 2020 utility market, and that this breakeven cost is more than $\$100/m^2$ in the 2020 residential market.

3.1 Introduction

In the United States, the levelized cost of electricity (LCOE) generated by photovoltaic (PV) modules in an average utility-scale system dropped from 0.27 $/kWh in 2010 to 0.07 $/kWh in 2016 as the cumulative PV capacity installed in the U.S. skyrocketed from 435 MW to 25 GW [12, 116]. This market growth and electricity cost decline has been driven largely by the rapid fall in the global price for a silicon PV module: over the same period, the average U.S. module price decreased 84%. The balance-of-system (BOS) cost—especially the area-related BOS cost, BOS_A—has not fallen as quickly, however, and now accounts for the majority of the PV system cost [11, 12]. For example, modules were only 34% of the average total utility-scale system cost in 2016, and this fraction is even lower in area-constrained markets such as the residential and commercial markets.

In addition to economies of scale, technological innovation has played a key role in reducing module cost—and thus system cost—and will continue to do so. In particular, higher module efficiency enabled by new cell and module technologies decreases both module costs and BOS_A on a $/W basis by increasing the system power output. Aluminum back-surface field cell manufacturing lines are presently being upgraded to the passivated emitter and rear contact (PERC) cell technology with best cell efficiencies now over 22% [117], and routes have been demonstrated to mass-manufactured cells with efficiencies in excess of 25% using heterojunction or interdigitated-back-contact (IBC) structures [112]. Recently, Kaneka reported a 26.6%-efficient silicon cell, which is approaching the 29.4% theoretical efficiency limit for a silicon cell and is on par with the practical efficiency limit of 27% [5].

As silicon cells and modules approach their terminal efficiency, what will come next for PV? Silicon-based tandems, in which a wide-bandgap top cell is coupled with a silicon cell, are a natural evolution for silicon cells that have the potential to exceed the single-junction efficiency limit. In theory, the limiting one-sun efficiency of a silicon-based tandem with a 1.7-eV top cell is 43% after taking into account Auger recombination in the silicon bottom cell [21]. In practice, top cells with III-V and perovskite absorbers have been paired with silicon cells in a range of coupling configurations and achieved encouraging efficiencies in lab-scale devices [30, 68, 76, 107, 118]. For example, with III-V materials, efficiencies of up to 32.8% were reported recently [76], and with perovskites, the record tandem efficiency has increased from 13% to 26% within just three years [119]. As the research efforts show no sign of slowing, it is plausible that these tandems will approach their limiting efficiencies, just as their sub-cells have.

It is not clear, however, whether continued improvements in efficiency are sufficient to propel tandems beyond their constituent sub-cells in terms of cost competitiveness. Peters *et al*. argued that, for tandems to be cost-competitive, modules composed of their sub-cells should have similar cost—on a $/W basis—at the system level [120]. In other words, a tandem module with expensive top cells and cheap bottom cells would lose out to the corresponding "bottom-cell module" that could be made with the bottom cells alone. After considering present BOS costs, III-V cell costs, and silicon cell costs, Bobela *et al*. found that a hypothetical III-V/silicon tandem would never offer a cost advantage over both single-junction alternatives [121]. Conversely, studies by Werner *et al.* indicated that perovskite/silicon tandems could be competitive in Europe under specific circumstances [119]. A comprehensive analysis is, however, outstanding, and critical

questions remain. For instance: Under what conditions, if any, will silicon-based tandems compete in the (flat-plate) PV market? And, is there any overlap between those favorable conditions and the projected evolution of the market?

3.2 Cost Model

To answer these questions, we constructed a simple and versatile analytical model to compute costs on a system level. The PV system cost (C_{system}), in \$/W, is given by

$$C_{system}\left[\frac{\$}{W}\right] = \frac{C_{module}\left[\frac{\$}{m^2}\right]}{\eta \cdot 1000\left[\frac{W}{m^2}\right]} + \frac{BOS_A\left[\frac{\$}{m^2}\right]}{\eta \cdot 1000\left[\frac{W}{m^2}\right]} + BOS_P\left[\frac{\$}{W}\right] \quad (3.1)$$

where C_{module} is the areal module cost to the system owner, η is the module efficiency, BOS_P is the power-related BOS cost, and the units of each quantity appear in gray in square brackets. Note that, as with most \$/W calculations, this model excludes financial assumptions. The model can be applied to any type of PV system (residential, commercial, or utility) by varying the BOS_A and BOS_P input values, and to any type of PV module by varying the C_{module} and η inputs. In particular, Equation (3.1) can be used to calculate the system cost for an installation with single-junction top-cell modules ($C_{module} = C_{top}$) or bottom-cell modules ($C_{module} = C_{bottom}$), or with tandem modules ($C_{module} = C_{tandem}$).

One way to calculate the cost of a hypothetical tandem module is as a perturbation to the costs of its constituent single-junction modules. Equation (3.2) does this by summing the top-cell and bottom-cell module costs and subtracting the overlap cost ($C_{overlap}$):

$$C_{tandem} = C_{top} + C_{bottom} - C_{overlap} \quad (3.2)$$

Consistent with Equation (3.1), all costs are in \$/m^2. The single-junction module costs include all elements of a standard module—cells, glass, encapsulants, frames, junction boxes, etc.—and the overlap costs might include, for example, double-counted

encapsulants and glass. However, we assume $C_{overlap}$ = 0 hereafter. As shown in APPENDIX A, this turns out to be necessary to "orthogonalize" the contributions of the top-cell and bottom-cell module costs in our model, which simplifies the analysis so that we may draw generally applicable conclusions. Furthermore, while this is a conservative assumption, it is not the worst-case assumption, as tandems can conceivably cost more than the sum of their constituent sub-cells (negative $C_{overlap}$). For example, two-terminal tandems may require extra processing steps during recombination junction formation, and four terminal tandems may require extra layers or spectrum-splitting designs for optimal optical coupling.

Equation (3.1) converts areal costs into power costs by dividing by module output power density, which is the product of module efficiency and the AM1.5G 1000 W/m^2 input power density. Thus, we also need to calculate the tandem module efficiency (η_{tandem}), given by

$$\eta_{tandem} = \left(\eta_{top} + f \cdot \eta_{bottom}\right) \cdot \eta_{coupling} \quad (3.3)$$

In Equation (3.3), η_{top} is the efficiency of the top-cell module, η_{bottom} is the efficiency of the bottom-cell module (both measured alone, under AM1.5G illumination), f is the fraction of η_{bottom} that contributes to the tandem efficiency in the absence of coupling losses, and $\eta_{coupling}$ is the coupling efficiency of the sub-cell modules in the tandem. Equation (3.3) is a simplification of the spectral-efficiency-based tandem coupling model we introduced previously [21]. That model expresses the efficiency of a tandem in which a silicon cell and a hypothetical top cell operating at a fraction of its detailed-balance limit are coupled, and it includes "spectral fidelity" terms that describe how much light at each wavelength reaches the top and bottom cells. To arrive at Equation (3.3), we first assumed

ideal spectral fidelities. This means that all photons with energies below the top-cell bandgap energy reach the bottom cell, and thus f is a function only of the bandgap of the top cell. (f values can be found in APPENDIX A Figure A-1.) We then re-introduced optical losses within the $\eta_{coupling}$ catch-all term, which also includes any electrical losses (or gains) and can be assigned an arbitrary value in accordance with the relative success of the tandem assembly process. Note that, unlike a detailed-balance model, Equation (3.3) can calculate the efficiency of a tandem comprising realistic, imperfect sub-cells. For example, consider a 1.7-eV, 21.7%-efficient top-cell module and a 22.1%-efficient silicon module. From Figure A-1, f = 0.473 and thus the silicon module can contribute 10.4% absolute efficiency to the tandem, assuming unity $\eta_{coupling}$, resulting in a 32.1%-efficient tandem module.

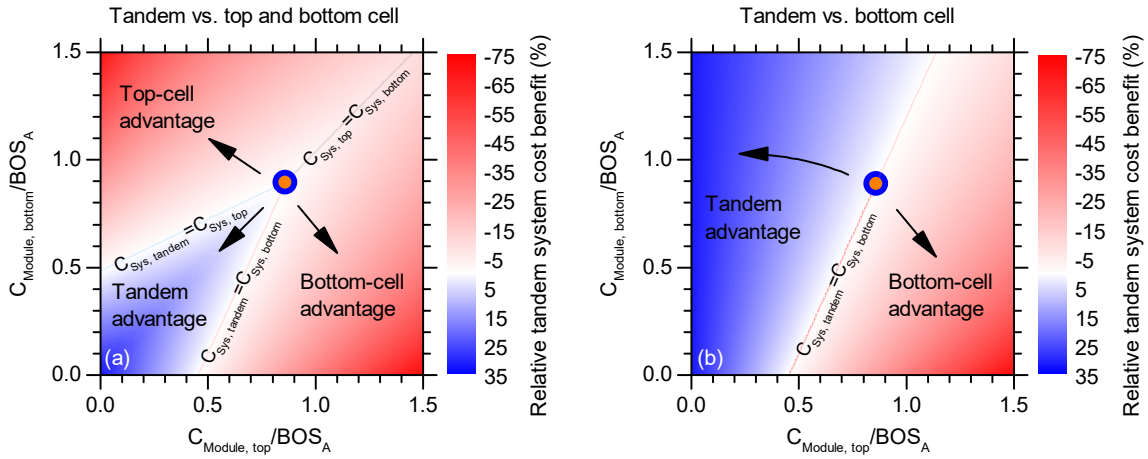

Figure 3-1. Tandem system cost competitiveness plots. (a) A tandem compared to both of its sub-cells. (b) A tandem compared to only its bottom cell. The assumed tandem comprises a 1.7-eV, 21.7%-efficient top cell and a 22.1%-efficient silicon bottom cell, resulting in a tandem efficiency of 32.1%. The blue and orange circle marks the triple point, at which the tandem, top cell, and bottom cell have the same system cost.

Peters *et al.* previously introduced simple plots to visualize the cost competitiveness of tandems. The x- and y-axes of these plots are the ratio of the constituent single-junction

module costs to the "structural" BOS cost, and color contours show the cost benefit of the tandem relative to the cheaper of the two single-junction modules [120]. Figure 3-1a shows such a plot using the aforementioned example efficiencies, but the axes were changed to the ratios of sub-cell module cost to BOS_A, which explicitly scale with area (some costs that scale with power were included in the axes of Peters *et al.*). The relative tandem system cost benefit, ζ, is calculated with Equation (3.4), with each system cost calculated with Equation (3.1).

$$\zeta = \frac{\min(C_{system,top}\,,\, C_{system,bottom}) - C_{system,tandem}}{\min(C_{system,top}\,,\, C_{system,bottom})} \quad (3.4)$$

BOS_P is independent of module type and was set to zero (in Equation (3.1)) throughout this study in order to visualize the maximum possible cost benefits and detriments. Non-zero BOS_P values do not change the sign of the cost benefit shown here but just reduce its absolute value. For example, with BOS_P = \$0.06/W—a typical inverter cost—the maximum cost benefit in Figure 3-1a reduces from 31% to 29%.

Figure 3-1a has three distinct cost-advantage regions, defined by three iso-cost lines. Equations (3.5), (3.6), and (3.7) express, respectively, the conditions for which the tandem system cost equals the bottom-cell system cost, the tandem system cost equals the top-cell system cost, and the top-cell system cost equals the bottom-cell system cost. (Derivations can be found in APPENDIX A.)

$$\frac{C_{top}}{BOS_A} \cdot \eta_{bottom} = (\eta_{tandem} - \eta_{bottom}) \cdot (\frac{C_{bottom}}{BOS_A} + 1) \quad (3.5)$$

$$\frac{C_{bottom}}{BOS_A} \cdot \eta_{top} = (\eta_{tandem} - \eta_{top}) \cdot (\frac{C_{top}}{BOS_A} + 1) \quad (3.6)$$

$$(\frac{C_{top}}{BOS_A} + 1) \cdot \eta_{bottom} = (\frac{C_{bottom}}{BOS_A} + 1) \cdot \eta_{top} \quad (3.7)$$

As first shown by Peters *et al.*, the three iso-cost lines in Figure 3-1a intersect at the "triple point", which is a convenient anchor in the parameter space. To the upper left of the triple point, the top-cell system has the cost advantage; to the lower right, the bottom-cell system has the advantage; and, to the lower left, the tandem system has the advantage. That is, for the efficiency assumptions in Figure 3-1a, this analysis indicates that a tandem would make economic sense only when *both* sub-cell modules are cheap relative to BOS_A. For example, for a tandem system to have a 10% relative cost benefit over the cheaper of the two sub-cell systems, both the top- and bottom-cell module costs should be less than half of BOS_A. The relative tandem system cost benefit peaks at 31% when both sub-cell modules are free, and diminishes towards the triple point as well as the iso-cost boundaries. Note that the maximum benefit depends only on the efficiencies of the three modules, and not on their absolute costs (as it occurs when their costs go to zero) or on BOS_A. In fact, the maximum cost benefit is identical to the relative tandem efficiency advantage. Note as well that a large cost benefit will not necessarily be needed to prefer tandem systems over single-junction systems, as higher efficiencies bring additional perceived benefits like reduced installation area, though it is necessary that the path leading to such a tandem be continuously profitable.

Figure 3-1a suggests that a module comprising excellent single-junction top cells (small values of C_{top}/BOS_A) would likely beat out both silicon and its associated tandem. However, no new absorber technology has been successful in competing again silicon, which now has approximately 80 GW of momentum and exerts extreme price pressure that is most keenly felt by newcomers to the market. For example, thin-film PV technologies such as copper indium gallium selenide (CIGS) and cadmium telluride (CdTe) have lost

market share—from 17% in 2009 to 6% in 2016 [1]. Similarly, thin-film silicon and its "Micromorph" tandem technology were entirely forced out of the market over the last six years as the efficiency of these modules stagnated and the price of crystalline silicon modules dropped [122]. Most companies pursuing (concentrating) III-V terrestrial technologies have faced a similar end [123, 124]. In short, silicon PV has proved itself to be a difficult technology to displace.

Silicon module manufacturers also feel the price pressure they collectively create. They are presently struggling with low margins because the global module selling price is close to or even below the module manufacturing cost [125]. For these manufacturers to progress down the learning curve while remaining profitable (or at least in business), they must decrease the $/W cost of their modules. As most of the margin has been squeezed out of the raw materials (which account for the majority of the manufacturing cost) [11, 126], their most promising route is to increase wattage through efficiency gains. We therefore believe that silicon-based tandem technologies will be adopted first by vertically integrated silicon PV manufacturers seeking to save at the system level via module efficiency enhancements. In this case, tandem modules will enter the market as an evolution of silicon technology and they will compete with their silicon predecessors—PERC and IBC modules, for example—and not with yet-to-be-created single-junction top-cell modules. Figure 3-1b shows the corresponding tandem system cost competitiveness plot, in which the relative cost benefit expressed in Equation (3.4) is instead calculated as

$$\zeta = \frac{C_{system,bottom} - C_{system,tandem}}{C_{system,bottom}} \quad (3.8)$$

Though we expect Figure 3-1b to be most representative of the competitive landscape, for completeness we nevertheless consider both bottom- and top-cell modules as competitors in the remainder of this paper.

3.3 Market Evolution

As evidenced by the axes in Figure 3-1, the ratios of the areal module cost to BOS_A for the top- and bottom-cell modules determine the economic viability of tandems. Although future top-cell module costs are uncertain, the trajectories of the bottom-cell module cost and BOS_A can be estimated. To investigate whether the flat-plate PV market is evolving towards or away from conditions that favor tandems, we constructed one-factor learning curves of both average silicon areal module cost and average BOS_A, as shown in Figure 3-2, with historical data for U.S. PV installations reported by NREL [12].

Figure 3-2a is an unconventional way to show module learning curves—most are displayed on a \$/W basis—but is sensible because module manufacturing costs scale with area and Equations (3.1) and (3.2) take \$/m^2 inputs. Similar or identical silicon modules are used on rooftops and in solar power plants, and thus we used cumulative U.S. PV installation as the metric of experience (x-axis); this also explains why module costs do not vary appreciably across market segments. By contrast, racking for modules on tiled home roofs differs from that on flat commercial roofs, which differs still from that on the desert ground. That is, area-related BOS components are mostly—but not exclusively—particular to the installation type, and thus we used cumulative PV installation *by market segment* as the metric of experience in Figure 3-2b. The learning rates decrease (most for residential and very little for utility) if BOS_A experience is instead assumed not to be segmented. Note as well that the BOS components that are included in BOS_A are different for the different

market segments, as proposed by Bobela *et al.* [121]. In particular, for the utility market, BOS_A includes BOS equipment, installation labor, and land, whereas for the (area-constrained) residential and commercial markets, BOS_A also includes permitting, inspection, and interconnection; installer overhead and profit; and sales tax (i.e., all BOS components except inverters).

Figure 3-2a shows that the silicon module cost decreased from \$320/m^2 in 2009 to \$60/m^2 in 2016. Fitting the historical data with a power-law learning curve using the least-squares method, we find a learning rate of 28%, which means that the areal module cost has decreased by 28% for every doubling of the cumulative PV area installed. The International Technology Roadmap for Photovoltaic reported a comparable, 26.2% per-piece learning rate on a global basis [2]. Figure 3-2b shows that BOS_A for the utility market decreased from \$120/m^2 in 2009 to \$57/m^2 in 2016, resulting in a learning rate of only 10%. The learning rates are similar for the residential and commercial markets, though there have been fewer installations and the absolute BOS_A is higher. The three-fold discrepancy between the module and BOS_A learning rates helps explain the market push towards higher module efficiencies in the last decade and the disappearance of cheap but inefficient modules, like those of thin-film silicon (\$70/m^2 and <10% efficient in 2011) [127]. More importantly, if these learning rates are sustained, tandems will continue to become *increasingly* attractive in the market: Since 2009, C_{bottom}/BOS_A has fallen by a factor of 2.5 for the utility market and approximately 4 for the commercial and residential markets.

To project out to 2020, we first calculated the expected areal annual PV installation in the U.S. using the annual forecast (in Watts) by SEIA and GTM Research [128] and the

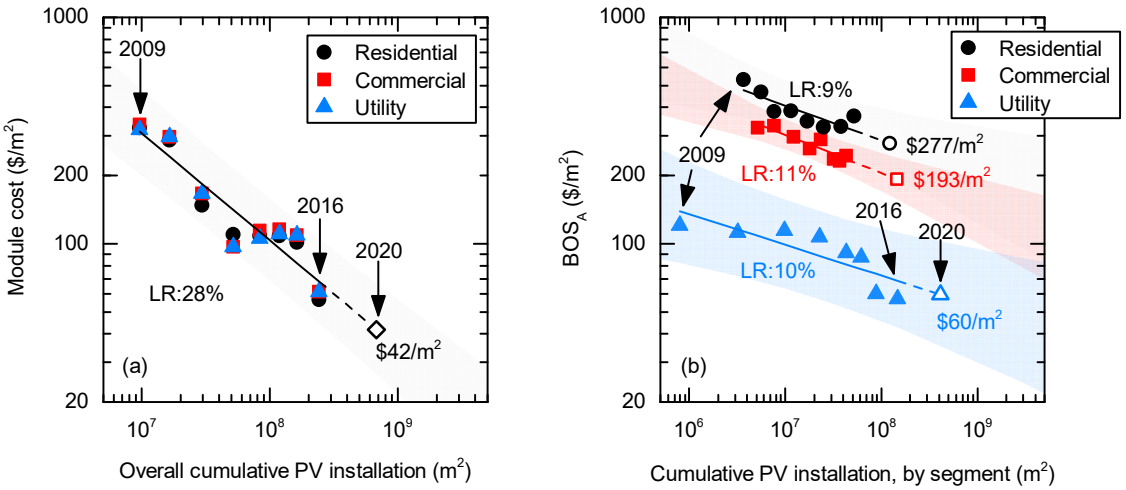

Figure 3-2. PV system learning curves. (a) Silicon module learning. (b) Area-related balance-of-systems learning. Cost data (solid symbols) were reported be NREL for installations in the U.S. [12]. Lines are power-law learning curves fit to the data and are accompanied by learning rates (LR). Open symbols represent predicted values in 2020. The shaded areas represent the 95% prediction intervals for the future values based on the historical data. Reported annual $/W costs were converted into areal costs using the reported average module efficiency in each year. The cumulative installed PV area is the sum of the annual installed PV areas, which were calculated based on the reported annual installation in Watts and the average module efficiency in each year.

compound annual growth rate of module efficiency extracted from NREL data [12]. Extension of the learning curves to the appropriate installation areas then yields the open symbols in Figure 3-2: In 2020, the areal silicon module cost will be $\$42/m^2$ and BOS_A will be $\$277/m^2$, $\$193/m^2$, and $\$60/m^2$ for the residential, commercial, and utility markets, respectively. Note that the 2020 projected utility BOS_A is higher than its current value—it is not yet clear if the present cost is an aberration and a correction will occur or if there has been a true shift off the historical learning curve. To visualize such uncertainties in the projected values, Figure 3-2 also shows the 95% prediction intervals (shaded areas), which account for both the error in the fit based on the existing observations and the random error in the projected BOS_A value [129]. According to this analysis, C_{bottom}/BOS_A is expected to

fall to 0.15, 0.22, and 0.70 in the residential, commercial, and utility markets, respectively, which is up to 1.5 times lower than in 2016.

3.4 Tandem Opportunity

Given these projected values, how expensive and inefficient can the top-cell module be in 2020 and still yield a cost-competitive tandem? Figure 3-3 is a tandem system cost competitiveness plot overlaid with the 2016 and projected 2020 values for C_{bottom}/BOS_A, which appear as horizontal lines. The shaded areas represent the propagated uncertainty from the 95% prediction intervals of the 2020 module and BOS_A values taken from Figure 3-2. As a rule of thumb, if a tandem is to be cost competitive against *both* its corresponding top- and bottom-cell modules, its triple point must be above the C_{bottom}/BOS_A line. Also, for tandems to be competitive over *just* the silicon bottom-cell module, the top-cell module has to be cheaper than the C_{top} value associated with the point at which the (light-red) tandem–silicon iso-cost line intersects the C_{bottom}/BOS_A line.

For example, consider again the blue and orange triple point of the 32.1%-efficient tandem shown in Figure 3-1, which now appears in the middle of Figure 3-3 with the label "$\frac{0.75}{0.75}$, 1.0". This notation indicates that both sub-cells operate at 75% of their respective limiting efficiencies—as mature manufactured PV technologies do—and are coupled with unity efficiency (these quantities, along with the top-cell bandgap, provide enough information to use Equation (3.3)). The triple point for this tandem is below the "Utility 2016" line (C_{bottom} = \$60/m^2, BOS_A = \$57/m^2, and C_{bottom}/BOS_A=1.07) but above the "Utility 2020" line (C_{bottom} = \$42/m^2, BOS_A = \$60/m^2, and C_{bottom}/BOS_A=0.70). Consequently, in 2016, the tandem system could have beaten only the silicon bottom-cell system (never the

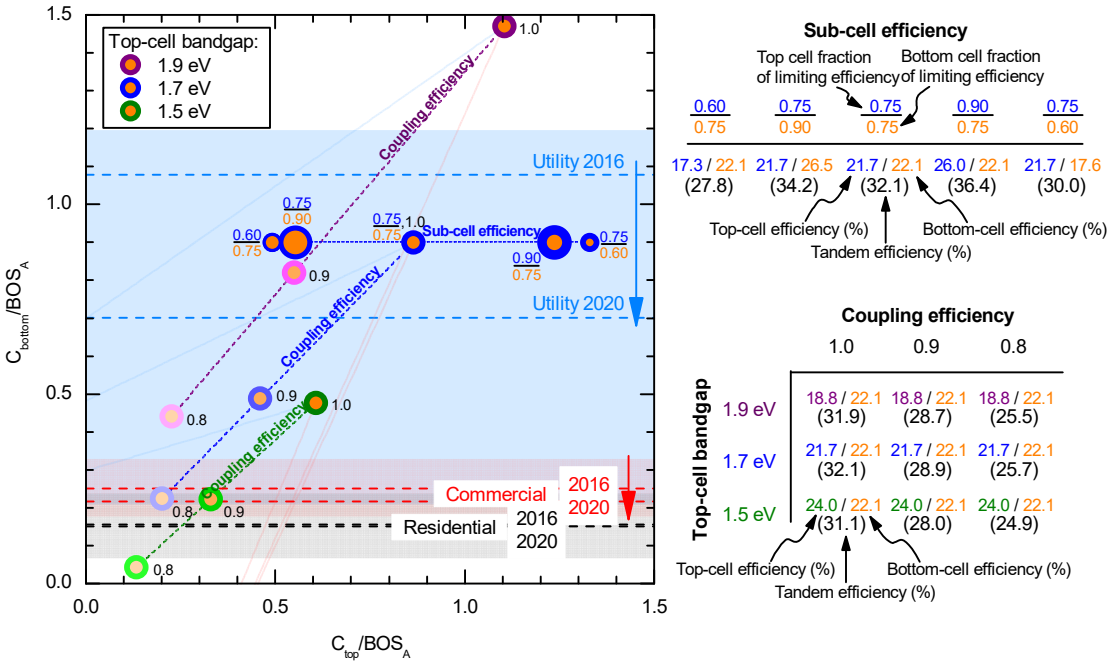

Figure 3-3. Competitive landscape for tandem systems. Tandem system cost competitiveness plot with perturbations in top-cell bandgap, sub-cell efficiency, and coupling efficiency. Dashed horizontal lines are actual (2016) and predicted (2020) ratios of silicon areal module cost to BOS_A, with data from Figure 3-2, and the shaded areas represent the 95% prediction intervals of the 2020 values. The ratios accompanying the blue and orange triple points indicate the efficiencies of the constituent 1.7-eV top cell and silicon bottom cell relative to their respective limiting efficiencies (triple points without ratios all have the default ratio of $\frac{0.75}{0.75}$). This information is also indicated qualitatively by the relative size of the blue and orange areas of the triple points. The absolute efficiencies of these sub-cells, as well as their tandems, appears in the table in the upper right. The color of the outer ring of the triple points corresponds to the top-cell bandgap, per the legend. The saturation of the colors reflects the coupling efficiency, which is also indicated next to triple points with a value between 0.8 and 1.0 (triple points without such numbers all have the default value of 1.0). The table in the lower right shows the sub-cell and tandem absolute efficiencies associated with these variations in top-cell bandgap and coupling efficiency.

top-cell system), and only if the 21.7%-efficient top-cell module had cost less than \$53/m^2. In contrast, in 2020, the tandem will be cost competitive against both single junctions if the top-cell module costs between \$27/m^2 and \$46/m^2. If the top-cell module is less than \$27/m^2, the tandem will lose to the top-cell system; if the top-cell module is greater than

$46/m^2$, the tandem will lose to the bottom-cell system. Even if the utility BOS_A falls to $35/m^2$ at the most aggressive edge of the 2020 prediction interval, Figure 3-3 shows that tandems will be nearly as competitive as they were in the utility market in 2016 (uppermost edge of blue shaded area), and in all other BOS_A scenarios they will be considerably more competitive.

Similarly, in 2020, the top-cell module break-even cost for the commercial market (C_{bottom} = $42/m^2$, BOS_A = $193/m^2$, and C_{bottom}/BOS_A=0.22) will be $107/m^2$, whereas for the residential market (C_{bottom} = $42/m^2$, BOS_A = $277/m^2$, and C_{bottom}/BOS_A=0.15) it will be $145/m^2$. "Break-even cost" is used here to mean the top-cell module cost or tandem module cost—as specified——at which a tandem system reaches cost parity with a system comprising silicon bottom-cell modules. These values are considerably higher than the current areal costs of silicon or thin-film modules, giving appreciable margin for development of these new technologies. Also, the C_{bottom}/BOS_A lines do not intersect the tandem–top-cell iso-cost line for these markets, indicating that silicon will be the only competitor for tandems, even if of our earlier price-pressure argument proves false. High-BOS_A residential and commercial systems thus appear to form a favorable entry market for silicon-based tandems; however, these markets have not historically driven PV innovation because the end customers are insufficiently educated to demand the highest-performance modules. The key to successful introduction of tandems will thus be strong partnerships between module manufacturers and installers who understand that they can offer lower system prices with higher-efficiency modules, or vertical integration between module manufacturers and installers. SunPower, with its premium IBC modules, provides a model for the former route, and the Tesla/Panasonic partnership for the latter.

The "$\frac{0.75}{0.75}$, 1.0" cell in Figure 3-3 represents just one of the many possible future tandems, and the performance of its assumed top cell (21.7% efficiency, 1.7 eV) has not yet been realized. The best reported 1.7-eV top cell, achieved with a perovskite absorber, has an efficiency of approximately 17% [105]. If a 17.3%-efficient, 1.7-eV top cell (60% of its limiting efficiency) is coupled losslessly with the 22.1%-efficient silicon bottom cell (still 75% of its limiting efficiency), the expected tandem efficiency is only 27.8%. As a result, the triple point, labeled "$\frac{0.60}{0.75}$" in Figure 3-3, moves left: the tandem cost-advantage region diminishes whereas the bottom-cell cost-advantage region increases. This 13% relative decrease in tandem efficiency compared to the "$\frac{0.75}{0.75}$, 1.0" tandem causes an outsized effect on cost competitiveness, as the top-cell module break-even cost diminishes by 43%, regardless of the market (i.e., C_{bottom}/BOS_A). On the other hand, if the 1.7-eV top cell reaches 26.0% (90% of its limiting efficiency), the tandem is 36.4% efficient, the triple point, labeled "$\frac{0.90}{0.75}$", moves right, and the top-cell module break-even cost increases by 43%. A similar efficiency perturbation of the silicon bottom cell—refer to the points labeled "$\frac{0.75}{0.90}$" and "$\frac{0.75}{0.60}$"—produces similar outcomes.

1.7 eV is the ideal bandgap for a top cell paired with an ideal silicon cell in a two-terminal tandem due to the current-matching constraint [21]. Four- and three-terminal configurations, however, remove the constraint and can thus tolerate a wider range of bandgaps with minimal sacrifice in tandem efficiency [22, 130]. Varying the bandgap of the top cell changes the efficiency contributions from the top and bottom cells to the tandem, and thus the location of the triple point per Equations (3.5)–(3.7). This is apparent in Figure 3-3, which displays data for top cells with three bandgaps, all of which operate

at 75% of their limiting efficiencies and are paired with the previous 22.1%-efficient silicon cell. Increasing the bandgap of the top cell lifts the triple point (purple and orange point labeled "1.0" near the top of the plot) whereas decreasing the bandgap lowers it (green and orange point labeled "1.0"). However, the bottom-cell cost-advantage region remains similar in all cases, indicating that top-cell bandgap does not affect competitiveness with incumbent silicon technologies. Rather, it trades tandem cost-advantage territory only with top-cell territory. As shown in the first column of the coupling efficiency table in Figure 3-3, the 18.8%-efficient, 1.9-eV top cell yields a 31.9%-efficient tandem. Its triple point is above even the "Utility 2016" line, which means that this tandem system has the largest opportunity to be cost effective compared to *both* of its sub-cell systems. Recall, however, that no matter how far out the triple point of a given system, the largest tandem cost benefit always occurs for C_{bottom}, C_{top}, and BOS_A combinations near the origin.

In addition to varying sub-cell efficiency and bandgap, tandem PV researchers can engineer how sub-cells are coupled. The coupling efficiency of the best reported tandem devices ranges from 0.7 to close to unity (see APPENDIX A Figure A-2), with the majority over 0.9 and thus encouragingly close to the ideal value heretofore assumed. This is important, as decreasing the coupling efficiency proportionally dampens the tandem efficiency (Equation (3.3)) and thus shifts the triple point undesirably towards the origin. For example, as displayed in the coupling efficiency table in Figure 3-3, the efficiency of tandems decreases from 31–32% to 28–29% and then 25–26% as the coupling efficiency is reduced to 0.9 and then to 0.8, and the top-cell module break-even cost shrinks by approximately one-third each time.

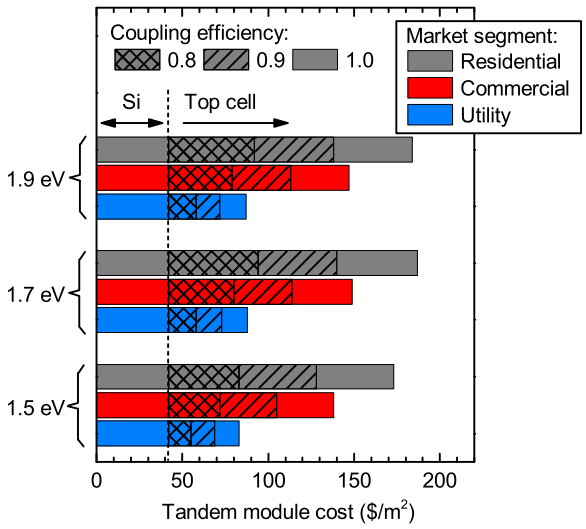

Figure 3-4. Allowable tandem module cost. Maximum tandem module cost to reach system cost parity with a silicon system in 2020 for various U.S. markets, coupling efficiencies, and top-cell bandgaps. All cases assume both sub-cells operate at 75% of their limiting efficiencies ($\frac{0.75}{0.75}$).

Figure 3-4 summarizes the projected 2020 tandem module break-even cost for the range of markets, coupling efficiencies, and top-cell bandgaps explored above. The tandem (and top-cell) module break-even costs are very similar for different top-cell bandgaps, but they depend strongly on the market and coupling efficiency. As coupling efficiencies of 0.9 are realistic, top-cell modules can cost up to approximately \$100/m^2, \$70/m^2, and \$30/m^2 and likely still generate competitive tandems in the 2020 residential, commercial, and utility markets, respectively. With the projected cost of silicon modules at \$42/m^2 in the same year, the top-cell module cost targets for the two area-constrained markets seem like they may be achievable and justify continued research and development of top-cell technologies. The target for the utility market, however, is quite aggressive and thus power plants are unlikely to be the market entry point for tandems.

3.5 Conclusion

The analysis presented here predicts that silicon-based tandem PV modules will become increasingly attractive in the U.S. because of the disparity in the silicon module and area-related balance-of-system learning rates. Tandems are expected to compete only with the incumbent single-junction silicon modules, and are most likely to enter area-constrained markets through vertically integrated silicon module and system manufacturers seeking product differentiation. The critical challenge to realizing this future is the demonstration of a wide-bandgap PV technology with an efficiency above approximately 20%, an areal cost below $\$100/m^2$, the ability to be integrated with silicon PV cells (in at least a four-terminal configuration), and sufficient durability to justify 25-year warranties.

There are several opportunities to learn more from this analytical cost model. The present analysis considered only U.S. data, and, while module costs are similar worldwide, BOS (especially area-related BOS) costs vary dramatically. With appropriate data, it would be valuable to recreate Figure 3-4 for important markets like China, Japan, and India to investigate if particular geographical areas are more likely to adopt tandems than others. The analysis also treated only power densities, assuming an AM1.5G spectrum, and extension to an energy analysis that compared tandem and sub-cell LCOEs would better reflect cost installation drivers. If financial assumptions are still ignored, this can be conveniently accomplished by adapting only Equation 3-3 to account for the spectral variation in a given location, and the spectral efficiency formulation naturally lends itself to this. Such an investigation will begin to separate two-terminal from four-terminal tandem configurations, as the coupling efficiency on an energy basis of the former should be lower in outdoor conditions [131]. Finally, although this analysis focused on silicon

bottom cells, it is trivial to probe other sub-cell combinations—for example, II-VI/CIGS [132], perovskite/CIGS [133], or perovskite/perovskite [134]—by using the appropriate inputs in Equations (3.2) and (3.3).

CHAPTER 4

FOUR-TERMINAL PEROVSKITE/SILICON TANDEM SOLAR CELL

This chapter documents the development of a 23%-efficient, four-terminal perovskite/silicon tandem. The perovskite top cell utilizes a Cu (1 nm)/Au (7 nm) layer stack as a semitransparent back contact, and achieved an efficiency of 16.5%. The double-side textured silicon bottom cell is designed with a high-mobility indium zinc oxide layer that is transparent to infrared light, and the rear side of the cell is engineered with a magnesium fluoride layer to prevent parasitic absorption. Compared to a reference silicon heterojunction cell, this infrared-tuned silicon bottom cell shows 1.6 mA/cm^2 improvement of short-circuit current density in the 700-1200 nm region—where the perovskite top cell is transparent and the silicon cell performance matters—and thus achieved 6.5% with the perovskite top-cell filter on top.

4.1 Introduction

Emerging organic-inorganic hybrid perovskite solar cells (PSCs) distinguish themselves among photovoltaic devices as excellent top cell candidates for high-efficiency silicon-based tandem devices. Due to their excellent light absorption and large electron and hole diffusion lengths, PSCs have reached certified efficiencies as high as 22.1% within six years of research [135-141]. Moreover, perovskite absorbers have bandgaps that may be tuned over a wide range from 1.1 eV to 3.1 eV which facilitates bandgap optimization for high efficiency perovskite/silicon tandem solar cells [142-151]. Another advantage of PSCs is that polycrsytalline perovskite thin films can be made on various substrates by

low-temperature solution processes [152-157]. Perovskite/silicon tandem cells offer an attractive path to increase the efficiency of perovskite and silicon cells beyond the single-junction Shockley–Queisser limit without adding significant cost to silicon solar cells. The perovskite top cell in a perovskite/silicon tandem requires a transparent front electrode that must have both high transparency and good conductivity; in addition, the rear electrode must be transparent to near-infrared light since this light will be converted to electricity with high efficiency in the silicon bottom cell if it is not parasitically absorbed first. Several researches have reported four-terminal and monolithically integrated two-terminal tandem configurations with different types of transparent electrodes for PSCs [94-96, 100-102, 105, 158, 159]. Bailie *et al*. utilized a transparent silver nanowire electrode on PSCs to achieve a 12.7%-efficient semi-transparent perovskite cell [100]. However, the diffusion of silver into the perovskite and charge transport layers leads to device degradation [159, 160]. Transparent conductive oxides (TCOs), such as indium tin oxide (ITO), hydrogen-doped indium oxide (IO:H), aluminum-doped zinc oxide (ZnO:Al), and indium zinc oxide (IZO) deposited by sputtering have also been investigated as transparent electrode for perovskite/silicon tandem cells [95, 96, 101, 102, 105, 158, 159], with efficiencies up to 14.5% for semitransparent perovskite cells and 21.2% for perovskite/silicon tandems [96]. The sputtering process damages the perovskite and charge transport layers, consequently, buffer layers made of inorganic materials such as molybdenum oxide (MoOx), ZnO:Al, and ITO nanoparticles are often inserted before sputtering to protect the perovskite and charge transport layers [95, 96, 101, 102, 105, 158, 159]. Ultrathin metal films (<10 nm thick) deposited by thermal evaporation could be alternative transparent electrodes that would not require buffer layers [161-163], as evaporation causes much less damage than

sputtering. However, such electrodes have not yet been thoroughly exploited in perovskite cells; the highest reported efficiency for a semitransparent PSC utilizing a metal film is 11.5% [161].

4.2 Semitransparent Perovskite Solar Cell

There are three key requirements for a transparent metal electrode in an efficient semitransparent PSC: (1) it should not react with the underlying perovskite layer and charge transport layers, (2) it should have high transmittance for incident sunlight, and (3) it should have good conductivity for charge collection. A challenge is that there is always a trade-off between transparency and conductivity for any transparent electrode. Here, we fixed the thickness of the metal films at 8 nm and evaluated their transparency and conductivity when deposited on glass and perovskite cell. Several metals have been investigated as electrode materials in perovskite solar cells, such as Au, Ag, Al, and Cu [154, 155, 157, 164-169]. In a previous study, we found that Cu and Au had much better stability than Ag and Al when in direct contact with the perovskite films under ambient atmosphere [165], and thus Cu and Au were chosen as the metal electrode candidates in this study. An 8-nm-thick Cu film maintained a decent conductivity of 28 Ω/square; however, as shown in Figure 4-1c, its transmittance is poor in the near infrared range. An 8-nm-thick Au layer, by contrast, displayed low conductivity due to the formation of a discontinuous film on glass and perovskite cell (Figure B-1, APPENDIX B). Au atoms are more strongly coupled to each other than to the substrate, which leads to formation of Au islands via Volmer–Weber growth during thermal evaporation (Figure 4-1a). As Cu has a much higher surface energy of 1790 mJ/m^2 than Au (1506 mJ/m^2) [170], we introduced a

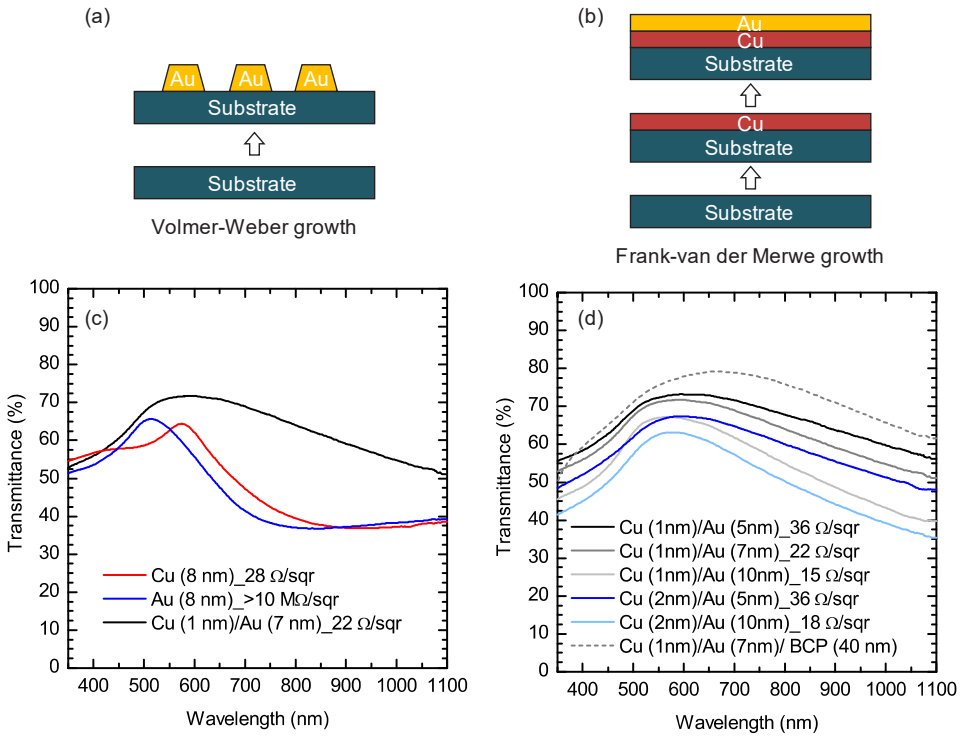

Figure 4-1. Schematic illustration of (a) island growth of Au on a glass substrate and (b) layer-by-layer growth of Au on a Cu-coated glass substrate. (c) Transmittance and conductivity of an 8-nm-thick pristine Cu film, an 8-nm-thick pristine Au film, and a 7-nm-thick Au film with a 1-nm-thick Cu seed layer on glass substrate. (d) Transmittance and conductivity of different Cu-seeded Au films on glass substrate.

1-nm-thick Cu seed layer to improve the Au wettability. As a result, Au atoms attach preferentially to the Cu surface rather than to each other, which leads to Frank—van-der-Merwe growth and the formation of continuous ultrathin Au films (Figure 4-1b). As shown in Figure 4-1c, a 7-nm-thick Au film on a 1-nm-thick Cu seed layer (Cu (1 nm)/Au (7 nm)) demonstrates higher transmittance and better conductivity than pristine 8-nm-thick Au and Cu films. Compared with a Cu (1 nm)/Au (7 nm) electrode, a Cu (1 nm)/Au (5 nm) electrode improved the transparency but un-preferably increased the sheet resistance from 22 Ω/square to 36 Ω/square; on the other hand, a Cu (1 nm)/Au (10 nm) film had better conductivity but significantly sacrificed transparency (Figure 4-1d). Increasing the

thickness of the Cu seed layer from 1 nm to 2 nm did not alter the electrode conductivity but predictably decrease its transparency. Therefore, the Cu (1 nm)/Au (7 nm) layer stack was chosen as the optimum semi-transparent electrode for use in PSCs.

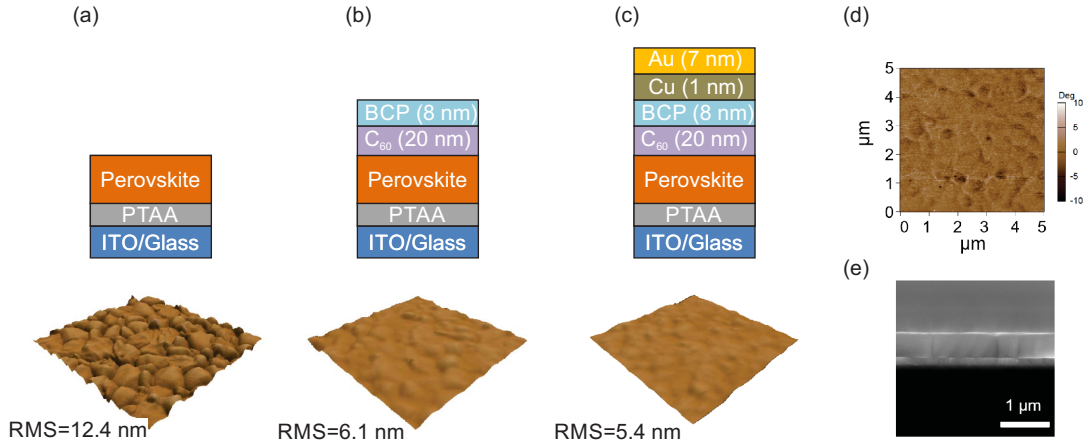

Figure 4-2. Schematic drawing and AFM topography image of a (a) $MAPbI_3$ film on PTAA-coated ITO/glass, (b) PCBM/C_{60}/BCP coated $MAPbI_3$ film, and (c) PCBM/C_{60}/BCP coated $MAPbI_3$ film after deposition of a Cu(1 nm)/Au (7 nm) electrode. The image sizes are 5 μm × 5 μm. The surface roughness is revealed by the root mean square (RMS) value. (d) Corresponding AFM phase image of (c). (e) SEM cross-section image of a $MAPbI_3$ film on PTAA-coated ITO/glass.

When incorporated into a perovskite solar cell, the metal electrode is deposited at last. Because it is only 8 nm thick, the surface roughness of the perovskite absorber and the charge transport layers may dramatically influence its continuity and thus its conductivity and transparency. The roughness of the perovskite layer, in turn, varies with the process used to form the perovskite film. A $MAPbI_3$ film fabricated by the two-step inter-diffusion approach displays a surface roughness of 21.7 nm [156]. Compared to 22 Ω/square on a glass substrate, the sheet resistance of a Cu (1 nm)/Au (7 nm) electrode on two-step $MAPbI_3$ films increases to 40 Ω/square, which is much larger than the 16 Ω/square sheet resistance of ITO-coated glass substrate that normally used for our perovskite cell. In order

to reduce the roughness of the perovskite layer, we utilized a one-step spin extraction approach that is similar to previously reported processes, but the mixed solvents were changed to dimethylformamide (DMF) and dimethyl sulfoxide (DMSO) [155, 171, 172]. While spin-coating the $MAPbI_3$ precursor solution, toluene was dropped to quickly precipitate $MAPbI_3$ so that very smooth films formed, as shown by the scanning electron microscopy (SEM) cross-section image in Figure 4-2e. After thermal annealing at 100 °C for 10 min, the one-step $MAPbI_3$ film had a surface roughness of 12.4 nm, as revealed by the atomic force microscopy (AFM) topography image shown in Figure 4-2a. This is almost half that of two-step $MAPbI_3$ films. Covering the perovskite films with a PCBM/C_{60}/BCP layer stack, which is needed for high device efficiency [166], the surface roughness further reduced to 6.1 nm (Figure 4-2b). The semi-transparent Cu (1 nm)/Au (7 nm) metal electrode on this smooth $MAPbI_3$ perovskite device is continuous (Figure 4-2c and d) and has a sheet resistance of 23 Ω/square, which is close to the ITO top electrode. Finally, a 40-nm-thick BCP layer was added on top of the Cu (1 nm)/Au (7 nm) film to further improve the transmittance of the semitransparent electrode; BCP has been shown to enhance the transparency by around 10% in the near-infrared range (Figure 4-1d).

We fabricated semitransparent perovskite solar cells using 500-nm-thick smooth $MAPbI_3$ films. An opaque control device with an 80-nm-thick Cu electrode displayed a respectable efficiency of 19.4% due to the large crystalline grains (approximately 1 μm) formed with the help of DMSO additives; and due to the excellent passivation of the perovskite surfaces and grain boundaries by the double fullerene layers [155, 173, 174]. Without DMSO in the precursor solution, the $MAPbI_3$ film yields grain size of 300–400 nm, and the surface is much rougher than the mixed solvent of DMF and DMSO (Figure

B-2, APPENDIX B).When illuminated through the glass/ITO side (denoted as front illumination), the semitransparent cell had a short circuit current density (J_{sc}) of 20.6 mA/cm^2 , fill factor (*FF*) of 74.1%, open circuit voltage (V_{oc}) of 1.08 V, and power conversion efficiency (PCE) of 16.5% (Figure 4-3a). The efficiency was confirmed by the stable photocurrent and power output at the maximum power point (0.87 V bias) for 1000s, as shown in Figure 4-3b. The semitransparent perovskite solar cells have excellent stability when stored under the dry inert atmosphere as shown in Figure B-3 in APPENDIX B. When illuminated from the Cu/Au/BCP side (denoted as rear illumination), the device had 12.1% efficiency with a reduced J_{sc} of 15.2 mA/cm^2 because the Cu/Au/BCP layer is less transparent in the visible spectrum than the ITO front electrode. Note that the semitransparent perovskite solar cells had hysteresis-free behavior, as seen by the forward and reverse current-voltage (*J-V*) scans in Figure 4-3a, which is again ascribed to the fullerene passivation effect as we previously reported [173]. A series resistance of 6.4 Ω·cm^2 was calculated from the semitransparent cell under front illumination *J-V* characteristic. This small series resistance and corresponding high *FF* further illustrate that the Cu/Au semitransparent electrodes induce little loss during collection and lateral transport of photo-generated carriers. Semitransparent PSCs under front illumination have lower PCE than opaque control devices mainly because of reduced J_{sc}. As shown in Figure 4-3c, semitransparent perovskite solar cells under front illumination and opaque cells have comparable external quantum efficiency (EQE) values at short wavelengths (300–550 nm), but semitransparent cells have lower EQE at longer wavelengths (600–800 nm). From the extinction coefficient (*k*) [175], more than 500 nm of $MAPbI_3$ film is required to absorb 95% of the photons in the 600–800 nm wavelength range (Figure 4-3d), but the $MAPbI_3$

layer used here is only 500 nm thick. In the opaque PSC, the thick (80 nm) Cu electrode serves as a rear reflector that increases the path length of light inside the perovskite layers, and this benefits the harvesting of long-wavelength photons. In the semitransparent PSC, the transmittance of these non-absorbed photons leads to J_{sc} loss, but they will be absorbed in silicon bottom cell in tandem devices.

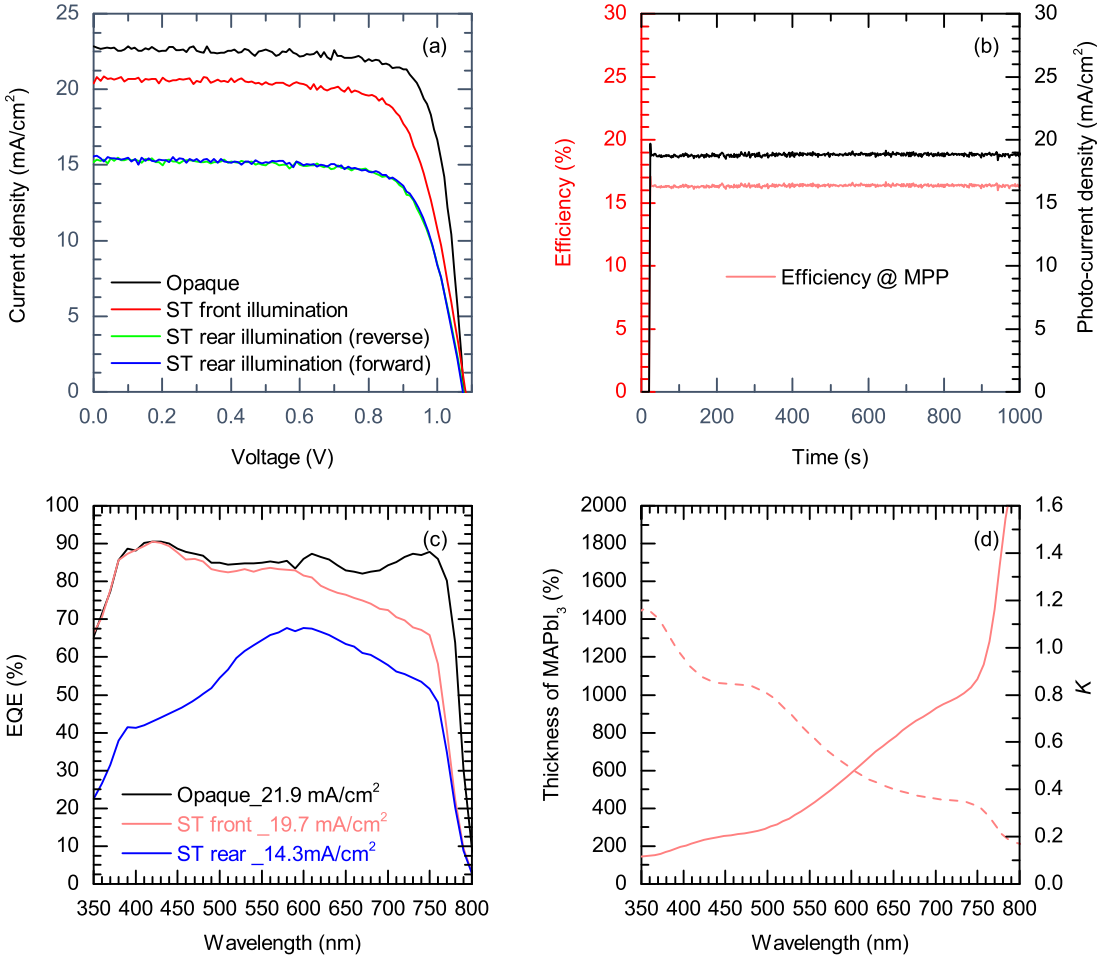

Figure 4-3. (a) *J-V* curves of an opaque PSC and semitransparent (ST) PSC under front illumination and rear illumination with reverse and forward scans. (b) Measured photocurrent density and PCE at the maximum power point (MPP) with 0.87 V bias for semitransparent PSCs under front illumination. (c) EQE curves for opaque and semitransparent PSCs under front and rear illumination. (d) Extinction coefficient to *k* and required thickness for a $MAPbI_3$ film to absorb 95% of light at different wavelengths.

4.3 Infrared-Tuned Silicon Bottom Cell

Amorphous silicon/crystalline silicon heterojunction cells are excellent candidates for silicon-based tandem devices because they have high V_{oc} resulting from the separation of the highly recombination-active (Ohmic) contacts from the silicon absorber bulk [176]. To improve the silicon bottom cell performance for tandem configurations, we fabricated infrared-tuned silicon heterojunction cells (IR cells) by applying a double-layer antireflection coating at the front side and a MgF_2 back reflector layer at the rear side, as illustrated in Figure 4-4a. As in one-sun silicon heterojunction cells [176], intrinsic and doped a-Si:H layers were deposited on a textured n-type monocrystalline wafer. On the front side, conventional ITO was replaced by IZO as a lateral transport layer because IZO has a higher carrier mobility [177]. IZO typically has a lower carrier concentration than ITO and thus higher sheet resistance, but this is desirable in tandems because lower carrier density (and higher mobility) decreases free-carrier absorption that causes parasitic loss of near-infrared light. In addition, the current at the maximum power point (J_{mpp}) in the bottom cell of a perovskite/silicon four-terminal tandem is roughly one-third the one-sun J_{mpp} of the silicon cell, and thus the front TCO layer may be three times more resistive without reducing *FF* [40]. The 50-nm-thick IZO layer was coated with 120 nm of SiO_x; together, they served as a dual-layer anti-reflection coating that better transmits near-infrared light. On the rear side of the cell, a 15-nm-thick ITO layer was deposited over the entire surface, followed by a 300-nm-thick MgF_2 layer that was evaporated through a stainless-steel mesh to define local openings. Finally, a silver layer was sputtered on the rear surface. Because of the MgF_2 patterning, the silver contacts the ITO in the (approximately 5%) area without MgF_2, whereas it remains separated from the ITO and wafer everywhere else. Inserting the

MgF_2 layer between the silver and silicon increases rear internal reflectance by reducing the fraction of light that reaches the lossy silver reflector. It does this by both limiting the transmission cone at the silicon rear surface and suppressing plasmonic absorption of light arriving outside of the cone [178-180].

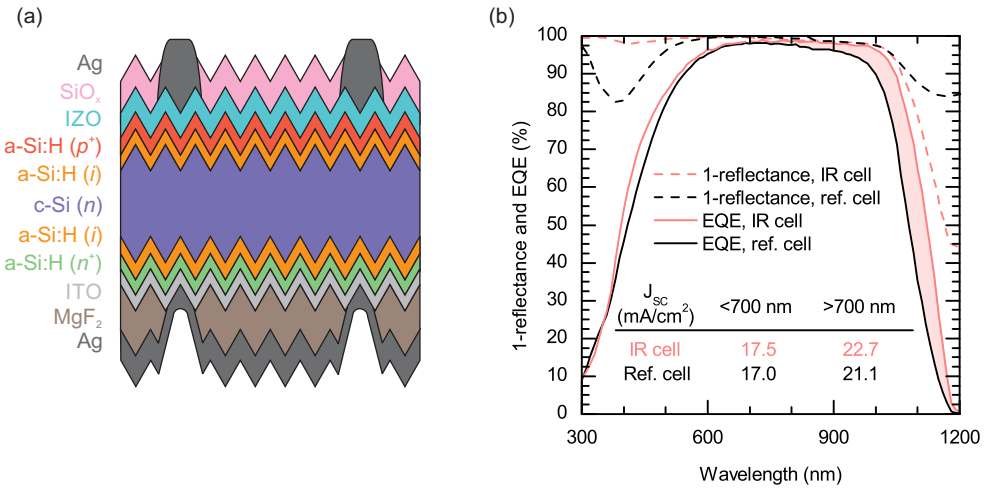

Figure 4-4. (a) Schematic of the infrared-tuned silicon heterojunction cell. (b) Total absorbance (1-reflectance) and EQE spectra of infrared-tuned and reference silicon heterojunction cells. The shaded area indicates the improvement in near-infrared performance resulting from the double-layer antireflection coating and MgF_2 layer.

The performance of a silicon IR cell can be evaluated by the total absorbance (1-reflection) and EQE curves in Figure 4-4b. Compared to the reference cell (which uses only ITO on the front, and no MgF_2 on the back), the IR cell had a J_{sc} only 0.5 mA/cm^2 higher for wavelengths < 700 nm. However, in the near-infrared region of the spectrum (700–1200 nm), where the perovskite top cell is transparent and the silicon cell performance matters, the J_{sc} improvement is considerable: 22.7 mA/cm^2 compared to 21.1 mA/cm^2. This gain results from the aforementioned design alterations that minimize parasitic absorption of near-infrared light. The total absorbance (1-reflection) spectra in Figure 4-4b confirm this: Only 45% of 1200 nm light, which silicon does not absorb, is

absorbed in the IR cell (by, e.g., the TCO and silver). By contrast, 82% is absorbed in the reference cell. As a result of the very small near-infrared parasitic absorption in the IR cell, the gap between the EQE and total absorbance curves is approaching zero, as is expected when all the light absorbed is absorbed within the silicon wafer and thus converted into photo-generated carriers. An IR cell with an area of 4 cm^2, measured alone at one-sun, had a PCE of 21.2% with a V_{oc} of 716 mV and *FF* of 75.6%; the reference cell had a PCE of 20.1%.

4.4 Four-Terminal Perovskite/Silicon Tandem

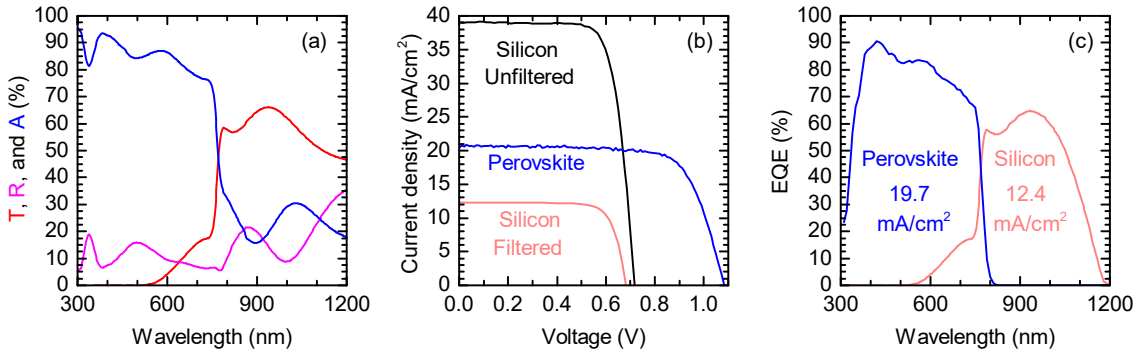

Figure 4-5. (a) Transmittance (T), reflectance (R), and absorbance (A) of a semitransparent PSC under front illumination. (b) *J-V* curves of a semitransparent PSC under front illumination and a silicon IR cell with and without the semitransparent PSC filter. (c) EQE spectra of semitransparent PSC top and filtered silicon IR bottom cells.

Combining the high efficiency semitransparent PSCs and infrared-tuned silicon heterojunction cells, we evaluated the potential for perovskite/silicon tandem cells in the four-terminal configuration by measuring the silicon cell under light filtered with a perovskite cell. The characterization was carried out independently for each sub-cell. Following the results in Figure 4-3, front illumination of the semitransparent PSCs was used for best performance. As shown in Figure 4-5a, most visible light was absorbed by

the perovskite top cell, with 10–20% of red light (600–700 nm) transmitted to the bottom cell. The light absorption around 800 nm and 1020 nm above the bandgap of perovskite film is from the absorption of semitransparent electrode, similar phenomena has also been reported in the sputtered ITO electrode [96]. For near-infrared light, 10-20% light was also reflected by the semitransparent PSC, together with 15-30% absorption, it left approximately 60% of near-infrared light for the silicon IR cell. The *J-V* curves and EQE spectra of the semitransparent PSC and filtered silicon IR cell are shown in Figures 4-5b and 4-5c, and device performance is summarized in Table 4-1. After the light is filtered by the perovskite top cell, the J_{sc} and V_{oc} of the silicon bottom cell are expected to decrease because of the reduced light intensity, and the *FF* is expected to increase because of the reduced effect of series resistance at lower illumination. The filtered silicon IR cell exhibited a V_{oc} of 679 mV, a J_{sc} of 12.3 mA/cm^2, and a *FF* of 77.9% for a PCE of 6.5%. Adding the 16.5% efficiency from the perovskite top cell, this corresponds to a summed efficiency of 23.0%. This is substantially higher than those of both the optimized silicon IR cell and the opaque perovskite cell.

Table 4-1. Summary of *J-V* parameters for a semitransparent perovskite top cell, silicon IR cell, filtered silicon IR cell, and the overall four-terminal perovskite/silicon tandem

Device	V_{oc} (V)	J_{sc} (mA/cm^2)	*FF* (%)	Efficiency (%)
ST-PSC top cell	1.08	20.6	74.1	16.5
Silicon IR cell	0.716	39.0	75.9	21.2
Filtered silicon IR cell	0.679	12.3	77.9	6.5
Sum				23.0

4.5 Conclusion

In summary, we have investigated semitransparent perovskite solar cells and infrared-tuned silicon heterojunction cells for high-efficiency tandem devices. A semitransparent metal electrode with good electrical conductivity and optical transparency has been fabricated by thermal evaporation of 7 nm of Au onto a 1-nm-thick Cu seed layer. For this electrode to reach its full potential, $MAPbI_3$ thin films were formed by a modified one-step spin-coating method, resulting in a smooth layer that allowed the subsequent metal thin film to remain continuous. The semitransparent perovskite solar cells exhibited 16.5% efficiency under one-sun illumination, and were coupled with infrared-tuned silicon heterojunction cells tuned specifically for perovskite/silicon tandem devices. A double-layer antireflection coating at the front side and MgF_2 reflector at rear side of the silicon heterojunction cells reduced parasitic absorption of near-infrared light, leading to 6.5% efficiency after filtering with a perovskite device and 23.0% summed efficiency for the perovskite/silicon tandem device.

CHAPTER 5

TWO-TERMINAL PEROVSKITE/SILICON TANDEM SOLAR CELL

This chapter documents the development of a 23.6%-efficient, two-terminal perovskite/silicon tandem solar cell. This efficiency was certified at NREL, and is recorded in the "Solar Cell Efficiency Table" as the highest monolithic perovskite/silicon tandem.

In this device, the perovskite top cell uses a tin oxide as a buffer layer via atomic layer deposition that prevents shunts, has negligible parasitic absorption, and allows for the sputter deposition of a transparent top electrode; and a single-side textured silicon bottom cell is fabricated with a low-refractive-index silicon nanoparticle layer as a rear reflector. This rear reflector boots the internal reflectance to 99.5% and results in a current density of 18.5 mA/cm^2 in the silicon cell; this value exceeds that of any other silicon bottom cell and matches that of the top cell.

Furthermore, the encapsulated perovskite devices withstand a 1000-hour damp heat test at 85 °C and 85% relative humidity, which paves the way for a stable perovskite/silicon tandem for outdoor application.

5.1 Introduction

The rapid rise of perovskite solar cells with record single-junction efficiencies of over 22% is the result of a unique combination of properties, including strong optical absorption [181], long diffusion lengths [182], and solution processability enabled by the relatively benign nature of intrinsic defects [183]. Additionally, their wide, tunable bandgap makes perovskites highly attractive for use in multijunction solar cells on top of

narrower-bandgap absorbers [142], such as silicon, CIGS, and Sn-containing perovskites [94, 96, 102, 134, 158, 159, 161, 184, 185]. This presents a pathway to achieving industry goals of improving efficiencies to over 30% while maintaining low module cost [186, 187].

The first monolithic perovskite/silicon tandem was made with a diffused silicon *p*-*n* junction, a tunnel junction made of n^{++} hydrogenated amorphous silicon, a titania electron transport layer, a methylammonium lead iodide absorber, and a Spiro-OMeTAD hole transport layer (HTL) [94]. The power conversion efficiency (PCE) was only 13.7% due to excessive parasitic absorption of light in the HTL, limiting the matched current density to 11.5 mA/cm^2. Werner *et al*. raised the PCE to a record 21.2% by switching to a silicon heterojunction bottom cell and carefully tuning layer thicknesses to achieve lower optical loss and a higher current density of 15.9 mA/cm^2 [96]. It is clear from these reports that minimizing parasitic absorption in the window layers is crucial to achieving higher current densities and efficiencies in monolithic tandems. To this end, the window layers through which light first passes before entering the perovskite and silicon absorber materials must be highly transparent. The front electrode must also be conductive to carry current laterally across the top of the device. Indium tin oxide (ITO) is widely utilized as a transparent electrode in optoelectronic devices such as flat-panel displays, smart windows, organic light-emitting diodes, and solar cells due to its high conductivity and broadband transparency. ITO is typically deposited through magnetron sputtering; however, the high kinetic energy of sputtered particles can damage underlying layers [188]. In perovskite solar cells, a sputter buffer layer is required to protect the perovskite and organic carrier extraction layers from damage during sputter deposition. The ideal buffer layer should also be energetically well aligned so as to act as a carrier-selective contact, have a wide bandgap

to enable high optical transmission, and have no reaction with the halides in the perovskite. Additionally, this buffer layer should act as a diffusion barrier layer to prevent both organic cation evolution and moisture penetration to overcome the often-reported thermal and environmental instability of metal halide perovskites [189]. Previous perovskite-containing tandems utilized molybdenum oxide (MoO_x) as a sputter buffer layer [99, 102, 158], but this has raised concerns over long-term stability, as the iodide in the perovskite can chemically react with MoO_x [190].

Mixed-cation perovskite solar cells have consistently outperformed their single-cation counterparts. The first perovskite device to exceed 20% PCE was fabricated with a mixture of methylammonium (MA) and formamidinium (FA) [135]. Recent reports have shown promising results with the introduction of cesium mixtures, enabling high efficiencies with improved photo-, moisture, and thermal stability [105, 191-194]. The increased moisture and thermal stability are especially important as they broaden the parameter space for processing on top of the perovskite, enabling the deposition of metal oxide contacts through atomic layer deposition (ALD) or chemical vapor deposition (CVD) that may require elevated temperatures or water as a counter reagent [195, 196]. Both titanium dioxide (TiO_2) and tin oxide (SnO_2) have consistently proven to be effective electron-selective contacts for perovskite solar cells and both can be deposited via ALD at temperatures below 150 °C [197].

Here, we introduce a bilayer of SnO_2 and zinc tin oxide (ZTO) that can be deposited by either low-temperature ALD or pulsed-CVD as a window layer with minimal parasitic absorption, efficient electron extraction, and sufficient buffer properties to prevent the organic and perovskite layers from damage during the subsequent sputter deposition of a

transparent ITO electrode. We explored pulsed-CVD as a modified ALD process with a continual, rather than purely step-wise, growth component in order to considerably reduce the process time of the SnO_2 deposition process and minimize potential perovskite degradation. These layers, when used in an excellent mixed-cation perovskite solar cell atop a silicon solar cell tuned to the infrared spectrum, enable highly efficient perovskite/silicon tandem solar cells with enhanced thermal and environmental stability.

5.2 Single-Junction Perovskite Solar Cells

We first fabricated single-junction perovskite solar cells on ITO-coated glass in order to develop a transferrable architecture for monolithic tandem solar cells on silicon. We fabricated the $Cs_{0.17}FA_{0.83}Pb\ (Br_{0.17}I_{0.83})_3$ (CsFA) perovskite top cell, with a bandgap of 1.63 eV (Figure C-1, APPENDIX C), in the *p-i-n* architecture, in which the electron-selective contact is deposited on top of the perovskite absorber layer and acts as a window layer. Suitable contacts for this geometry include *n*-type metal oxides such as zinc oxide (ZnO), TiO_2, and SnO_2. Figure 5-1 displays a schematic of the device structure. The perovskite was deposited on top of nickel oxide (NiO_x)—a hole-selective contact—to achieve higher voltage and stability than with the traditional poly (3,4-ethlenedioxythiophene) polystyrene sulfonate (PEDOT:PSS) contact [198, 199]. The CsFA perovskite was deposited from a stoichiometric solution containing CsI, formamidinium iodide (FAI), PbI_2, and $PbBr_2$ in a mixture of dimethylformamide (DMF) and dimethyl sulfoxide (DMSO). This deposition method was modified from that of Yi *et al*. and the full details of device fabrication are provided in APPENDIX C [192].

To deposit an electron-selective contact, we attempted to use phenyl-C_{61}-butyric acid methyl ester (PCBM), and aluminum-doped zinc oxide (AZO) nanoparticles, which

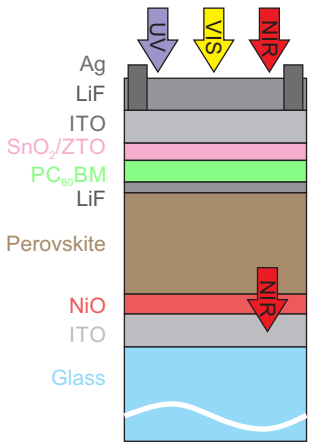

Figure 5-1. Schematic of the single-junction, semi-transparent perovskite solar cell (not to scale).

were previously used successfully in a methylammonium lead iodide ($MAPbI_3$) perovskite solar cell [101]; however, the devices were largely shunted due to the high surface roughness of the CsFA perovskite (Figure C-2, APPENDIX C). Spin coating on rough surfaces requires thick, planarizing layers to be applied to prevent shunt pathways, leading to lower optical transmission. Evaporation, ALD, and CVD enable the fabrication of uniform, conformal, thin films offering high optical transmission, regardless of surface texture. SnO_2 can be deposited by ALD using tetrakis(dimethylamino)tin(IV) (TDMASn) and water at temperatures as low as 30 °C [200], although deposition temperature is known to affect the stoichiometry and electronic properties of metal oxide films [201]. We use this ALD system at 100 °C to deposit SnO_2. Others have shown that a thin layer of PCBM between SnO_2 and the perovskite increases efficiency [105]. We thermally evaporated 1 nm of LiF and 10 nm of PCBM to leverage their good electron extraction properties (Figure C-3, APPENDIX C), while still achieving high optical transmission. We find that LiF acts as a shunt blocking layer similar to how thin, insulating, silicon oxide layers have been employed previously in thin-film silicon solar cells to block shunt pathways and

increase fill factor (*FF*) [202]. We believe LiF helps enable us to fabricate our 1 cm^2 aperture area tandems without a loss in *FF* and a large spread in efficiency (Figure C-11, APPENDIX C). Additionally, we note that PCBM thermally decomposes during evaporation to a more thermally stable isomer with very similar electronic properties [203].

On top of the PCBM layer, we deposited 4 nm of SnO_2 by ALD at 100 °C, followed by 2 nm of ZTO. The X-ray photoelectron spectroscopy (XPS) sputter depth profile of the 4 nm SnO_2/2 nm ZTO stack in APPENDIX C (Figure C-4) shows only partial diffusion of zinc into the tin oxide film, indicating that 4 nm of SnO_2 is sufficient to prevent detectable concentrations of zinc from reaching the perovskite. ZTO was deposited by combining SnO_2 and ZnO ALD processes in a repeating supercycle consisting of three cycles of SnO_2 followed by three cycles of ZnO [204, 205]. The parameters for the individual SnO_2 and ZnO processes used in the ZTO supercycle are described in APPENDIX C (Tables C-4). This process resulted in an effective growth rate of 5.8 Å/supercycle, or 0.1 nm/min. We investigated faster processing methods of our window layer by reducing the purge time from 30 sec to 5 sec between pulses. In doing so, the process approached the pulsed-CVD growth regime, further increasing the deposition rate to 0.5 nm/min, resulting in a total window layer deposition time of approximately 15 min. Current-voltage (*J-V*) and XPS data in Figures C-5 and C-6, in APPENDIX C, illustrate the identical performance and stoichiometry of SnO_2 and ZTO layers deposited via ALD and pulsed-CVD. Pulsed-CVD was used in the fabrication of our champion devices, which is noteworthy as CVD has the potential to reduce processing time compared to ALD and minimize thermal-induced degradation during processing.

A 150-nm-thick ITO electrode with a sheet resistance of 30 Ω/□ was sputtered on top of the cell, as in our previous work [101]. Optical modelling of the device stack indicated that thicker ITO layers introduce significant current losses through parasitic absorption (Figure C-7, APPENDIX C) while thinner layers reduce *FF* due to high series resistance. The 2 nm of ZTO is necessary to achieve low contact resistance with ITO and reach a high *FF*, as shown in APPENDIX C (Figure C-3). Finally, we finished the device stack with an evaporated silver metal electrode around the perimeter of the 1 cm^2 device area to minimize series resistance and a 150-nm-thick, thermally evaporated LiF antireflection coating.

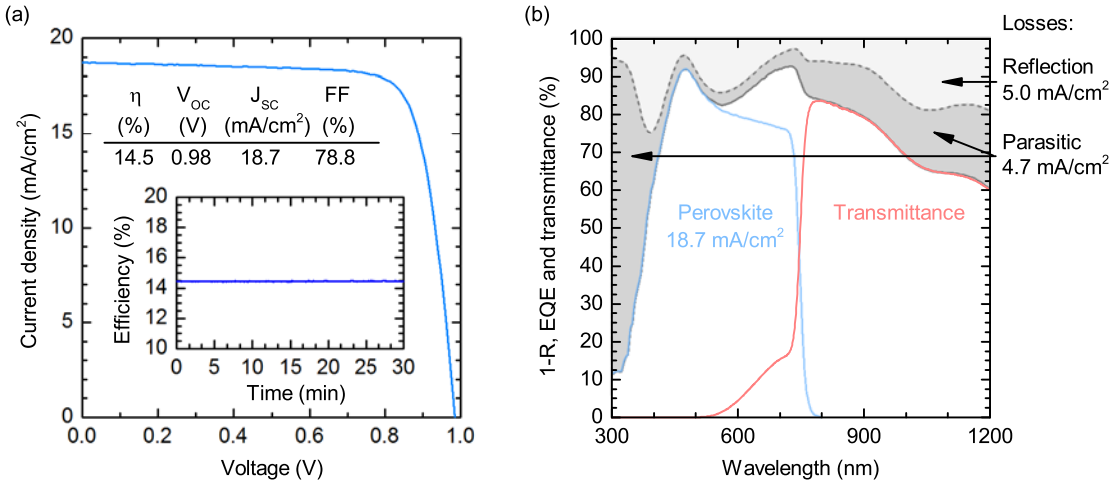

Figure 5-2. (a) *J–V* curve and efficiency at the maximum power point (inset) of the perovskite solar cell with illumination through the SnO_2 side. (b) Total absorbance (1-*R*, where *R* is the reflectance; dashed grey line), EQE (solid blue line), and transmittance (solid red line) of the perovskite solar cell. The sum of the EQE and transmittance (solid grey line) is the total summed current density available to be captured in the final tandem. The light and dark grey shaded areas represent the light lost to reflection and parasitic absorption, respectively, and the associated current density losses are indicated.

Figure C-3, in APPENDIX C, displays the *J-V* curves of a semi-transparent device on glass compared to a reference opaque device, in which an aluminum electrode was

evaporated onto the SnO_2/ZTO bilayer instead of sputtering an ITO electrode. The equivalent efficiency of the semi-transparent and opaque devices speaks to the efficacy of the SnO_2/ZTO bilayer and sputtered ITO layer as an electron-selective contact. Additionally, the high *FF* of 78.8% and lack of an extraction barrier, demonstrated by the *J-V* curve in Figure 5-2a, indicate that the bilayer is a successful sputter buffer layer. Figure 5-2b shows the external quantum efficiency (EQE), transmittance, and 1-reflectance measured from the SnO_2/ZTO bilayer (front) side. The high EQE, with an integrated current density of 18.7 mA/cm^2, and low parasitic losses between 400 and 750 nm showcase the optical properties of the bilayer and sputtered ITO. The AM1.5G-weighted average transmittance of this device between the perovskite bandgap at 765 nm and the silicon bandgap at 1200 nm is 74%. Figure 5-2a indicates that there is still room for open-circuit voltage (V_{oc}) improvement, as the bandgap-voltage offset is over 0.65 V. We believe that the origin of the voltage loss is primarily due to the difficultly in crystallizing the CsFA perovskite in the inverted architecture on a planar surface. Figure C-2, in APPENDIX C, reveals considerable surface roughness, which may cause voids in the LiF and PCBM layers during the evaporation.

5.3 Two-Terminal Perovskite/Silicon Tandem Solar Cells

To form two-terminal perovskite/silicon tandem solar cells, perovskite cells were fabricated directly on top of complete silicon bottom cells, as shown in Figure 5-3a. The perovskite top cells, one of which is shown in cross section in Figure 5-3c, were identical to their single-junction predecessors, except we annealed the NiO_x layer at 190 °C for 10 hours instead of 300 °C for 1 hour to prevent appreciable deterioration of the surface passivation layers in the underlying silicon cell (Figure C-10, APPENDIX C). We chose

an amorphous silicon/crystalline silicon heterojunction solar cell design for the bottom cell because of its high V_{oc}, which results from the separation of the highly recombination-active (ohmic) contacts from the silicon absorber bulk, and because its dominant performance-loss mechanism under the standard solar spectrum—parasitic absorption of blue light in the front amorphous silicon (a-Si:H) layers—is irrelevant in tandems.

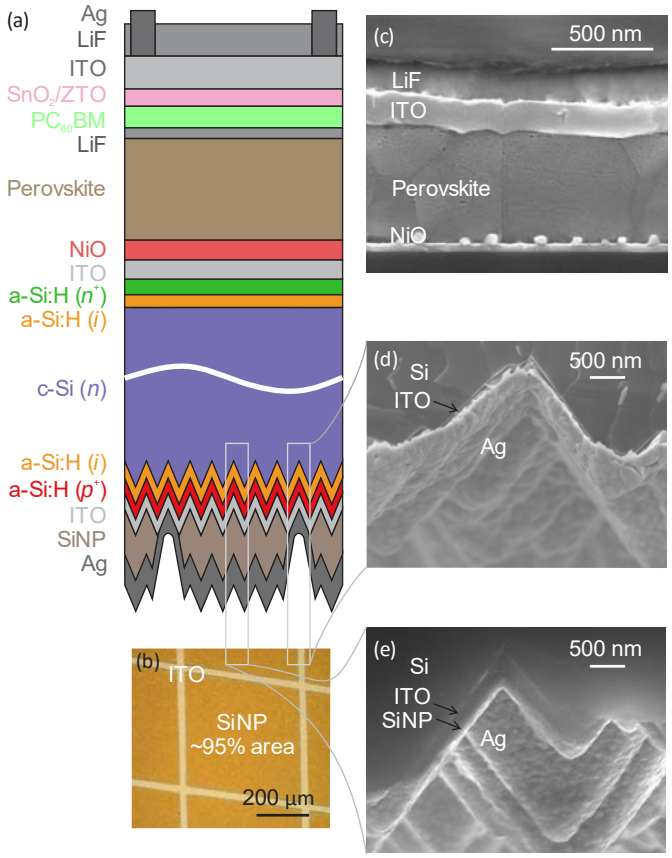

Figure 5-3. (a) Schematic of the perovskite/silicon tandem solar cell (not to scale). (b) Optical microscope image of the silicon-nanoparticle-patterned rear side of the silicon cell before silvering. (c) Cross-sectional SEM image of the perovskite top cell. (d) Cross-sectional SEM image of the rear side of the silicon cell in an area with no silicon nanoparticles. (e) Cross-sectional SEM image of the rear side of the silicon cell in an area with silicon nanoparticles.

The silicon cell fabrication process was adjusted to tune the silicon cells to the infrared spectrum that they receive in the tandem, as well as for compatibility with the spin-

coated perovskite top cells. In particular, the a-Si:H layers on both sides were slightly thickened to enhance passivation and carrier collection (the resulting visible parasitic absorption is not detrimental in tandems) [206]. A wafer with a chemical-mechanical polished front surface was used to allow for top-cell spin coating, but the rear of wafer was textured to form random pyramids. The pyramids scatter weakly absorbed near-bandgap light, elongating its path length through the wafer and enhancing the cell's infrared EQE. An excellent rear reflector comprising a silicon nanoparticle (SiNP)/silver stack was also implemented [207]. The SiNP layer, which is atypical in silicon heterojunction solar cells, is used because of its low refractive index—with a porosity of approximately 60%, its refractive index is 1.4—and high transparency at wavelengths longer than 1000 nm. More details on the use and fabrication of the rear reflector comprising a SiNP/silver stack can be found in [207, 208]. Inserting a thick, low-refractive-index layer between the wafer and metal reflector increases the rear internal reflectance by reducing the fraction of light that reaches the lossy metal layer [180], and a SiNP/silver reflector has a rear internal reflectance of over 99% [178, 207]. Finally, the front ITO layer was thinned to reduce infrared parasitic absorption since it does not need to play the role of antireflection coating in tandems and because, unlike in a single-junction silicon cell, the lateral conductivity of the front electrode need not be high.

In more detail, following the fabrication sequence, an *n*-type, 280-µm-thick, double-side polished, float-zone (FZ) silicon wafer was textured only on its rear side in an alkaline solution, resulting in the formation of random pyramids. Intrinsic and *p*-type a-Si:H films (7 and 15 nm thick, respectively) were first deposited by plasma-enhanced chemical vapor deposition on the textured (rear) side of the wafer, and intrinsic and *n*-type

a-Si:H films (7 and 8 nm thick, respectively) were then deposited on the polished (front) side. A 20-nm-thick, highly transparent ITO layer was next sputtered on the front side through a shadow mask, defining 11 mm x 11 mm square cells, to act as a recombination junction between the silicon and perovskite cells. A 20-nm-thick, highly transparent ITO layer was also deposited over the rear side through the same shadow mask, followed by a 300-nm-thick SiNP layer spray coated through a stainless-steel mesh to define local openings [209], and finally, a 200-nm-thick silver layer. Figure 5-3b shows a plan-view microscope image of the patterned SiNP layer before silver sputtering; the 5% uncoated area allows the silver to make direct electrical contact to the underlying ITO layer (Figure 5-3d), whereas the SiNPs in the remaining area (Figure 5-3e) enhance infrared conversion efficiency.

On its own, the silicon bottom cell has an efficiency well below 10% because of low *FF* caused by the high sheet resistance of the thin front ITO layer and lack of metal fingers, and because of low short-circuit current density (J_{sc}) caused by the high reflectance of the planar front surface and lack of appropriate anti-reflection coating. The best 4 cm^2 silicon heterojunction solar cell fabricated by the same lab with the same—but double-side-textured—wafers, adjusted deposition processes, and screen-printed silver fingers reached an NREL-certified efficiency of 21.4%. A comparable 1 cm^2 cell (as in the tandem) is expected to have an efficiency approximately 0.3% lower because of a 10 mV V_{oc} loss from increased edge recombination, and a comparable cell with a planar front surface (as in the tandem) is expected to reach only 19–20%.

Figure 5-4a displays the *J-V* characteristic of the champion tandem cell, certified at NREL, with a V_{oc} of 1.65 V, J_{sc} of 18.1 mA/cm^2, and *FF* of 79.0%, resulting in an

efficiency of 23.6% with a 1 cm^2 aperture area and no hysteresis, as shown in APPENDIX C (Figure C-9). The tandem was held at its maximum power point for over half an hour, under constant illumination, and maintained 23.6% efficiency. Figure C-11, in APPENDIX C, shows performance metrics for our final batch of devices without IR reflector: V_{oc} = 1.64 ±0.02 V, J_{sc} = 17.5 ±0.2 mA/cm^2, FF = 79.9 ±1.0 %, and η = 22.8 ±0.4 % and with IR reflectors V_{oc} = 1.64 ±0.01 V, J_{sc} = 18.2 ±0.2 mA/cm^2, FF = 78.1 ±1.0 %, and η = 23.3 ±0.4 %. The high performance and narrow statistical distribution for these 1 cm^2 cells—which are large-area amongst present perovskite devices—attests to the ability of the pulsed-CVD process to deposit a window layer that prevents pinholes and shunt pathways.

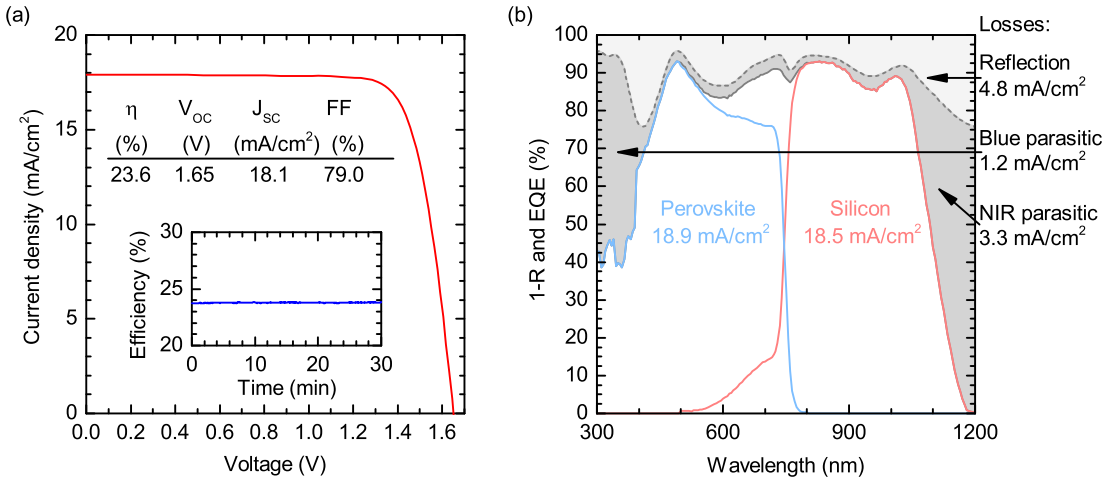

Figure 5-4. (a) *J-V* curve (NREL-certified, see Figure C-8 in APPENDIX C) and efficiency at the maximum power point (inset) of the champion tandem device. (b) Total absorbance (1-*R*, where *R* is the reflectance; dashed grey line), EQE of the perovskite top cell (solid blue line), and EQE of the silicon bottom cell (solid red line). The sum of the EQEs is denoted by the solid grey line. The light and dark grey shaded areas represent the light lost to reflection and parasitic absorption, respectively, and the associated current density losses are indicated.

Figure 5-4b shows the measured total absorbance (1-reflectance) and EQE of both sub-cells in the perovskite/silicon tandem solar cell. The figure has been divided into

several (colored) regions to help visualize the tandem response and loss mechanisms. Integrating the EQE spectra over the AM 1.5G spectrum reveals that the perovskite top cell and silicon bottom cell generate 18.9 mA/cm^2 and 18.5 mA/cm^2, respectively. We note that the silicon cell EQE exceeds 90% between 800 and 875 nm, which is much higher than the measured transmittance of the single-junction perovskite cell in Figure 5-2c. This high EQE results from a thinner ITO electrode (20 nm between the silicon and perovskite in the tandem instead of 170 nm between the perovskite and glass in the single-junction cell) and reduced reflection due to the lack of an air interface in the tandem. Figures C-9 and C-11, in APPENDIX C, illustrate the efficacy of the SiNP rear reflector in increasing infrared absorption within the silicon wafer, corresponding to an increase in J_{sc} of about 1.5 mA/cm^2. Two main current losses are front-surface reflection (area above the total absorbance curve) and parasitic absorption (area between the total absorbance and EQE curves), which account for 4.8 mA/cm^2 and 4.5 mA/cm^2, respectively. To further improve the J_{sc} of the tandem device, the easiest step would be to reduce front-surface reflection. Were it eliminated, the summed J_{sc} would increase by 4.2 mA/cm^2. As parasitic absorption still exists, not all transmitted photons would be converted into electron-hole pairs. The short-wavelength parasitic absorption loss associated with the first pass through the layers at the front of the solar cell is 1.2 mA/cm^2—0.7 mA/cm^2 from the ITO and 0.5 mA/cm^2 from the PCBM and SnO_2/ZTO bilayer, according to our optical simulations—and all of this would be gained as current in the top cell if the parasitic absorption were eliminated. The infrared parasitic absorption, which may occur in any layer in the tandem, appears to be large at 3.3 mA/cm^2, but this “loss” is misleading because not all of this current is available to be gained. Eliminating infrared parasitic absorption will result in a J_{sc} gain (in

the bottom cell) of less than half that value because—even assuming Lambertian light trapping—much of the light will escape out the front of the cell and contribute to the measured reflectance.

5.4 Improved Stability of Perovskite Solar Cells

We have previously shown that, in addition to acting as a highly transparent and conductive electrode, ITO—by virtue of its behavior as a diffusion barrier—can significantly increase the thermal and environmental stability of a perovskite solar cell by essentially trapping the volatile methylammonium cation [210]. The increased thermal stability of the thermodynamically favorable mixed CsFA perovskite compared to the pure methylammonium perovskite [191, 192], along with the dense, pinhole-free ALD SnO_2/ZTO bilayer, should result in perovskite solar cells with even greater stability than previously reported. We tested the stability of single-junction CsFA mixed perovskite solar cells by operating 0.48 cm^2-aperture-area devices at the maximum power point without additional encapsulation under continuous, one-sun-equivalent, visible illumination with a sulfur plasma lamp. The test was performed in ambient conditions with an average room humidity of around 40% and the lamp heating the samples to 35 °C. Remarkably, the devices operated with minimal degradation in performance for over 1000 hours of testing, as shown in Figure 5-5a. In our previous study, small dust particles in the perovskite resulted in pinholes in the ITO encapsulation, creating a pathway for methylammonium evolution and causing eventual efficiency degradation [101]. In the present CsFA devices, however, no such pinhole-based degradation was apparent after 1000 hours of operation, speaking to the efficacy of the conformal ALD process to prevent pinhole formation and to the overall increased stability of the CsFA perovskite.

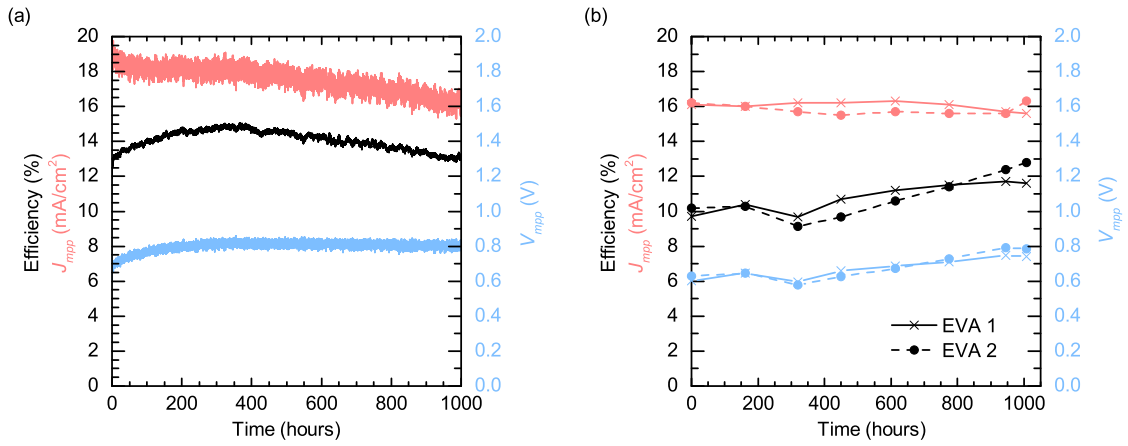

Figure 5-5. (a) Efficiency (black), J_{mpp} (red), and V_{mpp} (blue) of a single-junction perovskite device with no additional encapsulation during 1000 h of continuous maximum-power-point tracking. (b) Efficiency (black), J_{mpp} (red), and V_{mpp} (blue) of a single-junction perovskite device packaged with EVA, glass, and a butyl rubber edge seal during damp heat testing.

Although the cell in Figure 5-5a had the same efficiency after 1000 hours as at the start of the test, this efficiency was not constant over the testing period. As can be seen in Figure 5-5a, the rise in efficiency during the first 400 hours corresponds to an increase in voltage (V_{mpp}), likely indicating the improvement of the NiO/perovskite interface or increased perovskite crystallinity. V_{mpp} started at only a modest value but the lack of V_{mpp} decay during the test is noteworthy. Falling current density (J_{mpp}) is the culprit for the decrease in efficiency over the last 600 hours of the test. The exact cause of this decrease in J_{mpp} is presently being studied, but potential causes are the lack of an edge seal or pinholes in the ITO layer caused by dust particles; either case would lead to evolution of the organic cation. However, both of these potential issues can be solved through proper device encapsulation. The vast majority of commercial silicon solar modules are encapsulated with the elastomeric polymer ethylene-vinyl acetate (EVA) and a glass cover sheet to prevent oxidation and moisture ingress, and thus to enable >25-year lifetimes.

Lamination of EVA is typically performed at 110–150 °C for 30 min under mild vacuum. The increased thermal stability of our perovskite devices with the sputtered ITO electrode enables us to compare the stability of our devices directly to conventional silicon modules by packaging our devices using this industry-standard encapsulation process. We laminated single-junction perovskite devices between two sheets of glass with EVA at a curing temperature of 140 °C for 20 minutes. A butyl rubber edge seal was used to prevent moisture ingress.

In order to test the efficacy of this packaging, we performed the damp heat test described in the International Electrotechnical Commission (IEC) design qualification testing protocol 61215 for "Crystalline Silicon Terrestrial Photovoltaic (PV) Modules." These are accelerated lifetime tests with the goal of rigorously testing modules for the same failure mechanisms observed in the field in a much shorter time. The damp-heat test requires that the module operate at 85 °C and 85% relative humidity for 1000 hours with no more than 10% degradation in performance. We performed this damp heat test on two packaged perovskite devices over the course of 6 weeks (1008 hours). The devices were taken out of the dark damp heat chamber once a week and measured with a maximum-power-tracking program until the efficiency stabilized. Figure 5-5b shows the voltage, current, and efficiency at maximum power each week. Not only do the devices pass the damp heat test, they improve over the course of the test. While the efficiency of the devices is initially limited by poor *FF*, V_{mpp} increases throughout the test, similar to under continuous illumination (Figure 5-5a). However, unlike in the continuous-illumination study, J_{mpp} remains constant throughout the course of the damp-heat test, indicating that

the packaging successfully addressed potential problems such as pinholes in the ITO and an improper edge seal.

5.5 Conclusion

An ALD or pulsed-CVD processed SnO_2/ZTO window layer has enabled the successful fabrication of perovskite solar cells with high efficiency and improved stability. These vapor processes produces a compact, conformal, uniform, and highly transparent SnO_2/ZTO bilayer with efficient hole-blocking ability and sputter buffer layer properties, allowing for 1 cm^2 devices with no pinholes. These devices have the thermal and ambient stability to be further sealed with industry standard encapsulation such as EVA and glass. In addition to being made as single-junction devices on glass, the same devices were fabricated on silicon solar cells with planar front surfaces to form two-terminal tandems. When the perovskite cells were coupled with silicon heterojunction bottom cells with an excellent rear reflector and a-Si:H and ITO layers adjusted for the exclusively infrared spectrum, the resulting tandem reached an efficiency of 23.6% with no hysteresis and stable maximum power over more than 30 minutes under illumination. This efficiency is well beyond that of both sub-cells, beyond that of the record single-junction perovskite cell, and approaching that of the record single-junction silicon cell. Performance-loss simulations suggest the efficiency can be increased further by widening the bandgap of the perovskite and reducing front-surface reflection, which will enable both higher matched current densities and higher voltage. Perovskite/silicon tandems with an ALD SnO_2/ZTO bilayer layer present a promising method to achieving industry standard operational lifetimes with pathways to raising efficiencies over 30%.

CHAPTER 6

PVMIRROR: A NEW CONCEPT FOR TANDEM SOLAR CELLS AND HYBRID SOLAR CONVERTERS

This chapter introduces a new tandem solar collector employing a "PVMirror" that has the potential to both increase energy conversion efficiency and provide thermal storage. A PVMirror is a concentrating mirror, spectrum splitter, and light-to-electricity converter all in one: It consists of a curved arrangement of PV cells that absorb part of the solar spectrum and reflect the remainder to their shared focus, at which a second solar converter is placed. A strength of the design is that the solar converter at the focus can be of a radically different technology than the PV cells in the PVMirror; another is that the PVMirror converts a portion of the diffuse light to electricity in addition to the direct light. We consider two case studies—a PV cell located at the focus of the PVMirror to form a four-terminal PV–PV tandem, and a thermal receiver located at the focus to form a PV–CSP (concentrating solar thermal power) tandem—and compare the outdoor energy outputs to those of competing technologies. PVMirrors can outperform (idealized) monolithic PV–PV tandems that are under concentration, and they can also generate nearly as much energy as silicon flat-plate PV while simultaneously providing the full energy storage benefit of CSP.

6.1 Introduction

Module efficiency is the primary cost driver in the flat-plate photovoltaic (PV) industry because the module cost now accounts for less than half of the total installed

system cost [211, 212]. Consequently, in the past five years, commercial cell and module efficiencies have improved dramatically: In 2014, Panasonic announced a large-area 25.6%-efficient silicon heterojunction cell that broke the 14-year-old record for crystalline silicon [113], and SunPower produced a 25%-efficient interdigitated-back-contact silicon cell on a manufacturing line [4]. These devices are approaching the 29.43% theoretical efficiency limit of a silicon PV cell, as reassessed by Richter et al. in 2012 [6], and are unlikely to exceed 26% as predicted by Swanson in 2005 and re-evaluated by Smith et al. in 2014 [4]. The recent efficiency gains are not limited to silicon; Alta Devices reported a record 28.8%-efficient single-junction cell based on its GaAs technology in 2011 [115]. This device is not far off the 33% detailed-balance radiative limit for a single-junction PV cell with the ideal bandgap of 1.1–1.4 eV [17, 213]. Evidently, regardless of technology, single-junction PV cells are nearing their terminal efficiency plateau. What, then, is the next step for PV? Though many approaches have been proposed to surpass the single-junction limit [214, 215], only multi-junction devices have proven successful thus far.

Theoretical analysis shows that by choosing proper materials with 36 different bandgaps, the limit efficiency of a multi-junction PV cell is as high as 72% [20]. The most developed embodiment of multi-junction PV cells is that of a monolithically integrated two-terminal device in which wider-bandgap cells are stacked directly on top of narrower-bandgap cells, separated by recombination junctions. With three or four junctions of III-V materials arranged in this structure, several groups have successfully produced PV cells that exceed 40% efficiency under concentration [28] [37, 216, 217]. However, due to the expense of the epitaxial growth substrate, III-V precursors, and growth machines, these cells are restricted to high-concentration (and space) applications where their cost is

discounted by the concentration ratio. The penalty of high concentration—in addition to the cost of tracking—is the loss of all diffuse light, which accounts for 25% of annual solar energy even in places as sunny as Phoenix [218]. To reach high efficiencies with respect to the global incident spectrum, it would be nice to reproduce the success of III-V multi-junctions in the much larger flat-plate and low-concentration markets using cheaper materials and growth techniques, as was attempted with thin-film silicon PV [38]. Unfortunately, current mismatch, lattice mismatch, and processing compatibility severely limit material choice and device design.

All multi-junction PV cells split the solar spectrum and send to each sub-cell the wavelengths that it may best use (those above, but near, the absorber bandgap). The monolithically integrated multi-junction cells just discussed (as well as four-terminal stacked cells) achieve this separation through absorptive filtering in which narrow-bandgap cells are illuminated only with light not absorbed by the wide-bandgap cells above. There are, however, four other options to split the spectrum: reflective filtering, refractive filtering, holographic filtering, and luminescent filtering (see Imenes and Mills for a review [219]). These "optically coupled" multi-junction cells have the advantage that current mismatch and cell compatibility are non-issues, but they have traditionally faced other challenges. The reflective method uses a dichroic mirror (also called a Bragg reflector), which is made by stacking high- and low-refractive-index dielectric layers to transmit only certain bands of light; the rest are reflected. Moon et al. reported an outdoor efficiency of 28.5% under 165 suns with two separate PV cells, made of silicon and AlGaAs, coupled with a dichroic mirror [42]. Recently, with a four-junction receiver, Mitchell et al. demonstrated 34% efficiency under one-sun (non-concentrated) outdoor illumination, but

the cells were made of III-V materials and arranged such that the cell area was much larger than the aperture area, so economical operation is expected only under high concentration [220]. The refractive method uses a prism to disperse sunlight to PV cells with different bandgaps spaced laterally, but collimated light is required in order to prevent overlap of spectral bands. The advantage of holographic filtering is that the incident spectrum can be simultaneously concentrated and split with a single optical element, but sufficiently high diffraction efficiencies have yet to be demonstrated and the foci of the beams tend to fall on a curved surface rather than a plane [45, 221]. Luminescent filtering requires a dye with a high photoluminescence quantum yield and a Stokes shift that is large enough to prevent reabsorption of emitted light, but not so large that a substantial fraction of the photon energy is thrown away in the downshift [222, 223].

Here we propose a new two-junction or tandem concept that employs absorptive or reflective filtering to optically couple the sub-cells. This "PVMirror" technology utilizes PV cells as a three-in-one technology—they act as a concentrating mirror, spectrum splitter, and high-efficiency light-to-electricity converter. Distinct from high-concentration multi-junctions, PVMirrors convert part of the diffuse spectrum in addition to the direct beam and can be used to couple two PV cells of wildly different technologies or even one PV cell and a non-PV solar energy converter. Two case studies are presented that show performance improvement with the application of PVMirrors.

6.2 The PVMirror Concept

A PVMirror employs one-sun PV cells as a spectrum splitter that reflects non-absorbed light. This can be realized with a wide-bandgap cell by using the absorber's bandgap as the splitting edge, which is similar to the top cell in a stacked tandem, but a

PVMirror employs a specular rear reflector so that sub-bandgap light is reflected rather than transmitted. Alternatively, a PVMirror can be made using reflective instead of absorptive filtering by putting a spectrum-splitting dichroic mirror on top of the PV cell, which can then have any bandgap, surface morphology, and rear reflector. In either case, by arranging the PV cells so that the specularly reflected light from many cells arrives at a common focus—as with a trough, dish, Fresnel mirror, or heliostat field—the resulting concentrated light can be used to illuminate another PV cell, power a thermal cycle, or drive any other solar energy converter.

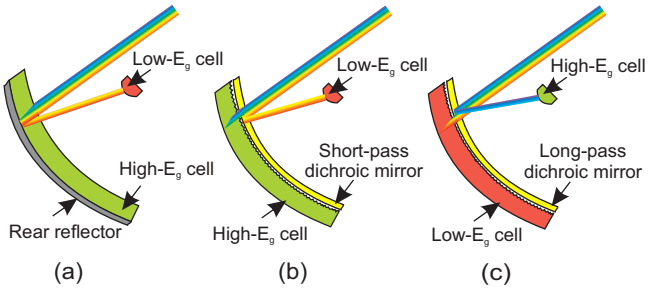

Figure 6-1. Three PVMirror trough configurations illustrating the range of possible embodiments. (a) Smooth, wide-bandgap cell and specular reflector, (b) textured wide-bandgap cell and short-pass dichroic mirror, and (c) textured narrow-bandgap cell and long-pass dichroic mirror. Note that the supporting structures that determine the PVMirror geometry (e.g., curved glass on which the PV cells are affixed) are not shown in this conceptual schematic.

There are three main embodiments of PVMirrors, shown in Figure 6-1 for a PV-PV tandem in the trough geometry. The first (Figure 6-1a) uses smooth (i.e., lacking surface texture that would scatter light) wide-bandgap PV cells with a rear mirror. The PV cell absorbs all super-bandgap wavelengths while specularly reflecting all sub-bandgap light to a common focus, where a narrow-bandgap cell or other receiver sits that is intended to use the concentrated light. The second embodiment, shown in Figure 6-1b, uses the same wide-bandgap PV cell but with a textured rather than smooth surface. In this case, it is

necessary to add a spectrally selective dichroic mirror in front of the cell, which transmits only super-bandgap light while concentrating sub-bandgap light at the focus. The advantage of this design (and the next) is that, for indirect-bandgap cells, the textured surface better traps the near-bandgap light transmitted through the coating. (In a slight modification, the dichroic mirror can be a band-pass design that transmits only near-bandgap light so that both sub-bandgap and very-high-energy photons—which lose most of their energy to thermalization if absorbed in the PV cell—are rejected to the focus. This is appropriate if the converter at the focus is wavelength agnostic—i.e., not another PV cell as in Figure 6-1b.) The third embodiment represented in Figure 6-1c is similar to the second, but switches the PV cell positions so that narrow-bandgap cells (e.g., silicon cells) form the PVMirror and a wide-bandgap cell is positioned at the focus. With an adjusted (long-pass) dichroic mirror, all high-energy photons are reflected to the focus while low-energy photons are absorbed in the PVMirror. In this unusual tandem configuration, sunlight hits the "bottom" cell first rather than the "top" cell. As the per-square-meter cost of silicon PV cells is lower than any comparable-efficiency wide-bandgap PV cell, this configuration can be more quickly adopted by the market.

Manufacturing of PVMirrors should require little, if any, new process and equipment development. For thin-film PV cells, PVMirrors can be made by depositing the cells either on curved glass or on flat glass segments that are then arranged to approximate the desired curvature. In the trough configuration, the latter would look like SunPower or Cogenra's low-concentration silicon PV technology, but with wide-bandgap PVMirrors in the place of silvered mirrors, as illustrated in Figure 6-2. Alternatively, thin-film cells can be deposited on a flexible metal sheet that is then mounted curved, or on plastic or metal

foil that is then laminated to a curved surface. For wafer-based cells, lamination to either curved glass or flat segments is likely the best option. In fact, one can think of a PVMirror as simply a curved (or segmented) PV module with a sophisticated anti-reflection coating (Figure 6-1b and c) or an excellent, specular rear reflector (Figure 6-1a). In the Figure 6-1b and c configurations, commercial cells (thin film or wafer based) with any texture can be used, whereas for the Figure 6-1a configuration, smooth (and parallel) cell surfaces are required to successfully direct reflected light to the focus. In this case, either conformal layers (thin-film cells) or polished wafers are needed. This does not necessarily imply expensive chemical-mechanical polishing that yields atomically flat surfaces; for example, for silicon PV cells, our recent results indicate that inexpensive HF/HNO3 acid-based chemical polishing yields >99% specularity of reflected light [224], [225]. If a dichroic mirror is to be used, it can be sputtered or evaporated onto the inner side of the front glass or plastic sheet, or a polymer optical film like those from 3M can be applied on the inner or outer side of the glass or plastic [226].

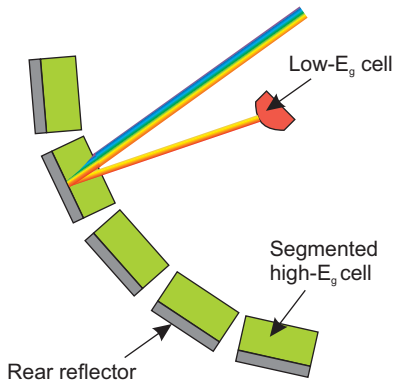

Figure 6-2. The PVMirror configuration of Figure 6-1(a) but with a segmented trough consisting of flat PVMirror strips.

An advantage of PVMirrors for PV-PV tandems is that—like for all optically coupled tandems—the choice of top and bottom cells is free of lattice- and current-

matching restrictions. Furthermore, either the wide- or narrow-bandgap cell can be placed under concentration at the focus depending on their relative costs. Alternatively, a non-PV solar converter can receive the concentrated light, making PVMirrors amenable to hybridization with technologies that offer additional functionality, such as storage with solar thermal systems. An additional advantage is that the PVMirror itself has a lower one-sun operating temperature than a comparable flat-plate PV module as it reflects sub-bandgap light (Figure 6-1a and b), super-bandgap light (Figure 6-1c), or both if using a band-pass dichroic mirror. This reduces infrared parasitic absorption or thermalization of electron-hole pairs generated by high-energy photons, both of which increase the operating temperature of a PV module above the ambient temperature.

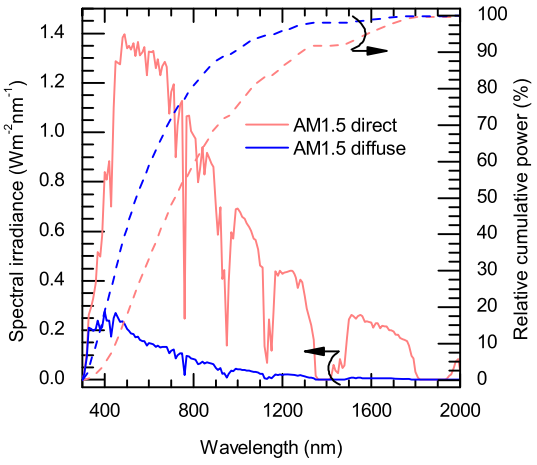

Figure 6-3. AM1.5 direct spectrum and AM1.5 diffuse spectrum, calculated as the difference between the AM1.5 global (not shown) and AM1.5 direct spectra. Also shown is the relative cumulative power (fraction of power below a given wavelength) for the AM1.5 direct and AM1.5 diffuse spectra.

However, the greatest benefit of PVMirrors over most other tandem concepts—and concentrating solar thermal power (CSP) systems, incidentally—is that PVMirrors make use of a portion of the diffuse light whereas concentrator system cannot. This is enabled by

the unusual PVMirror design in which the sub-cell that forms the PVMirror receives one-sun, global irradiation while the sub-cell at its focus receives concentrated direct light. Figure 6-3 shows that, under standard (cloud-free) AM1.5 conditions, diffuse light still accounts for 10% of the global incident power. Furthermore, Rayleigh scattering blue-shifts the spectrum so that about 80% of the diffuse power is at wavelengths below 800 nm; this means that even a relatively wide-bandgap cell can capture most of the blue-sky diffuse light. Figure 6-4 shows the global solar insolation and relative diffuse percentage for various geographic locations in the USA; the most striking feature is that there is much more diffuse light than the 10% attributable to atmospheric scattering under AM1.5 conditions. The additional diffuse light is primarily due to cloud scattering, and—though we are not aware of measured data—we expect the associated spectrum to be relatively white, much like the AM1.5 direct or global spectra.

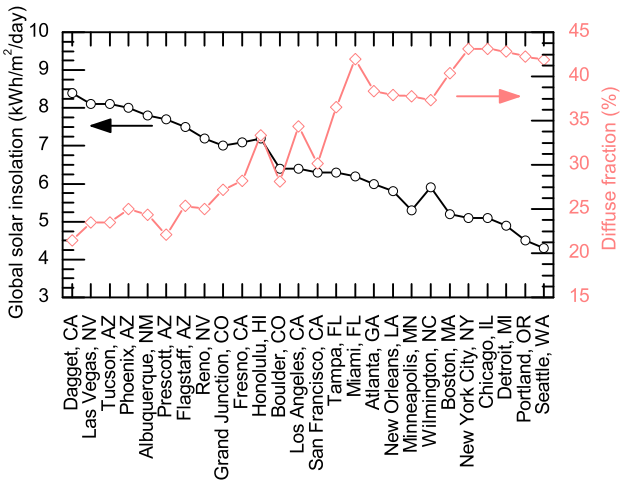

Figure 6-4. Global insolation and fraction of diffuse radiation on a North-South-axis tracking plate for different geographical locations in the U.S [218].

6.3 Case Study I: PV-PV Tandem

Silicon-based tandems are likely to emerge as a successor of flat-plate silicon modules as silicon PV already has GW-scale production capacity and has proved itself a difficult technology to displace in the past [227]. More importantly, the bandgap of silicon is close to ideal for a bottom cell in tandems. The challenge is to find a top cell with the right bandgap and high enough efficiency to produce a tandem that outperforms the (already excellent) silicon cell on its own. A GaInP cell has been demonstrated that would be suitable: the absorber had a bandgap of 1.8 eV and the cell had a record efficiency of 20.8% [228]. Unfortunately, a 4% lattice mismatch limits its application on silicon in the conventional two-terminal monolithically integrated tandem configuration. Wafer-bonding is one route to escape epitaxy and Derendorf *et al.* demonstrated a 20.5%-efficient wafer-bonded multi-junction cell under one-sun illumination [26]. An alternative is to grow epitaxial top cells of other, near-lattice-matched III-V materials such as GaAsP; Connolly *et al.* predicted a GaAsP/Si tandem cell with an efficiency of 32.2% [229]. With the emergence of low-cost halide perovskites PV cells with rapidly improving efficiencies, perovskite/Si tandems have also become an explosive research topic. A theoretical analysis by Loper *et al.* showed that a 35%-efficient tandem is attainable, but will require proper material and device development [89]. Another promising candidate to pair with silicon is CdTe-based II-VI materials, which Garland et al. calculated may result in higher multi-junction cell efficiencies (and with lower cost) than is possible with III-V multi-junction cells [78]. Besides silicon, CdTe is the only competitive technology in the present flat-plate PV market, and ternary alloys of CdTe with Mg, Zn, or Mn have bandgaps that vary from 1.48 eV to 3.5 eV [230], thus spanning the 1.6–1.8 eV range that is required for current

matching with silicon [231]. Xu *et al.* calculated that, using Cd0.5Zn0.5Te with a bandgap of 1.8 eV as a top cell on silicon, a one-sun efficiency of 35.4% is possible [79].

Cell	η (%)	E_g (eV)	V_{OC} (V)	J_{SC} (mA/cm^2)	FF (%)
CdMgTe	21.1	1.8	1.31	20.37	79.0
Silicon	22.4	1.1	0.73	38.74 (20.84)	79.0

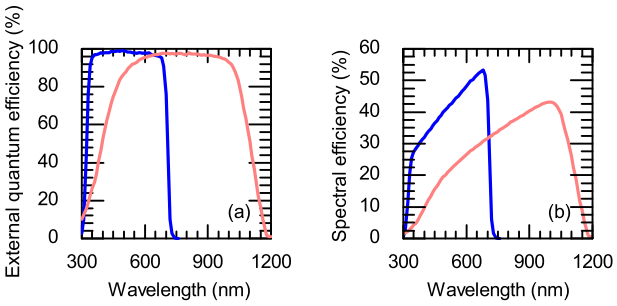

Figure 6-5. Performance of the CdMgTe and silicon heterojunction PVcells used in the tandem simulations. The reported values are those that would be measured for the individual cells with (normally incident) AM1.5 global illumination. The J_{sc} value in parentheses is the calculated current density for the silicon heterojunction cell when used as the bottom cell in a (one-sun) monolithic tandem. (a) *EQE* and (b) photon-to-DC-power spectral efficiency of the CdMgTe (blue) and silicon heterojunction (red) PV cells.

To investigate the potential of PVMirrors for silicon-based tandems, we consider an example in which a hypothetical CdMgTe PV cell with a 1.8 eV bandgap and an efficiency of 21.7% (under one-sun AM1.5 global illumination) is paired with a 22%-efficient silicon heterojunction cell. The external quantum efficiency (*EQE*) and other key one-sun parameters of each cell separately (prior to tandem formation) are shown in Figure 6-5. The short-circuit current density (J_{sc}) values were calculated by integrating the product of the *EQE* and AM1.5 global spectral photon flux. The *EQE* of the silicon heterojunction cell was measured, whereas the *EQE* of the hypothetical CdMgTe cell was obtained by shifting the *EQE* of a record CdTe cell [232]. The resulting J_{sc} of 20.37 mA/cm^2 agrees with that modeled by Xu *et al.* [79]. The open-circuit voltage (V_{oc}) of the silicon

heterojunction cell was assumed to be 730 mV—below what we regularly measure for cells made in our lab—and the V_{oc} of the hypothetical CdMgTe cell was set to 1.31 V, consistent with that demonstrated by Carmody *et al.* [80]. A conservative fill factor (*FF*) of 79% was taken for both cells—Kaneka has demonstrated 84.9% in a silicon heterojunction cell and First Solar reported 80.0% in a CdTe cell [71]. The "spectral efficiency" shown in Figure 6-5b was calculated according to equation (1) and (2) shown in Chapter 2.

To assemble the two sub-cells into a tandem, the CdMgTe top cell is arranged into a segmented parabolic shape to form a PVMirror (Figure 6-2) and the silicon heterojunction bottom cell is placed at the (line) focus. We simulated the performance of this PVMirror tandem system assuming 20X geometric concentration at the focus, and compared the result with that of a monolithic tandem (employing the same sub-cells) both under one-sun illumination and 20X geometric concentration. First, we calculated the efficiencies that would be measured in a laboratory setting with a flash tester that illuminates the cells with the AM1.5 global spectrum at nominally normal angle of incidence (no diffuse light). (This procedure is a compromise between those used to certify the efficiencies of flat-plate and concentrated PV cells.) To do this, the J_{sc} of each sub-cell was calculated from its *EQE* (Figure 6-5) and the specific spectrum and irradiance it receives (e.g., the bottom cell is illuminated only with light not absorbed in the top cell and is under concentration in two of the configurations). Next, the one-sun current-voltage parameters in Figure 6-5 were used to calculate the V_{oc} and *FF* of each sub-cell given the photo-generation just calculated. Finally, the power outputs of the sub-cells were summed and normalized to the incident power. I assumed no efficiency loss in any of the cells during tandem formation; that is, no optical losses for the PVMirror or 20X monolithic tandems, and no current- or lattice-

matching losses in either monolithic tandem. The in-lab efficiencies, therefore, reflect the maximum attainable values given the sub-cells and the chosen tandem configurations.

To compare the tandem configurations in realistic outdoor settings, we also calculated their outdoor efficiencies and annually averaged daily energy outputs when placed on North-South-axis trackers in Phoenix and Miami, which have diffuse light fractions of 25% and 42%, respectively. Direct and diffuse light were treated separately and—in Phoenix—were assumed to have the AM1.5 direct and AM1.5 diffuse (global minus direct) spectra shown in Figure 6-3, normalized to Phoenix's direct and diffuse fractions. Calculations for Miami were the same except the AM1.5 global spectrum was used in place of the AM1.5 diffuse spectrum (for the 42% diffuse fraction). This variation in the assumed spectrum for diffuse light represents our best attempt to approximate the local conditions: most days in Phoenix are cloud-free and thus the diffuse light there should be blue-shifted[1]; many days in Miami are cloudy and we expect cloud scattering to result in a comparatively white spectrum. Independent of location, my calculations assumed that the one-sun monolithic tandem absorbs both direct and diffuse light, the 20X monolithic tandem absorbs only the direct light, and the 20X PVMirror tandem absorbs both in the CdMgTe top cell but only direct light in the silicon heterojunction bottom cell[2]. We did not account for degradation in V_{oc} due to the increased operating temperature of the cells in outdoor environments. The power output of each tandem was normalized to the global input power to arrive at the outdoor efficiency, and the efficiency was multiplied by the

[1] Assuming instead AM1.5 global in Phoenix (cloud scattering dominates Rayleigh scattering) changes the results by less than 5% relative.

[2] Note that, although the geometric concentration ratio is 20, the effective concentration ratio (generation rate multiplier) in the bottom cell is approximately 8 in Phoenix and 6 in Miami because only direct light not absorbed in the top cell reaches the PVMirror focus.

annually averaged daily global insolation on a North-South-axis tracker (given in Table 6-1) to determine the energy output. Table 6-1 displays the results of these calculations, as well as the in-lab efficiencies discussed above and the advantages and drawbacks of each configuration.

Table 6-1. Comparison of CdMgTe/Si monolithic and PVMirror tandems.

	20X PVMirror tandem	One-sun monolithic tandem	20X monolithic tandem
Current matching	Not required	Required	Required
Lattice matching	Not required	Required	Required
Diffuse light collection	300-700 nm	300-1200 nm	None
Material consumption	Full-are CdMgTe, 1/20-area Si	Full-area CdMgTe and Si	1/20-area CdMgTe and Si
In-lab efficiency (AM1.5G, normal)	34.3%	33.4%	35.6%
Solar resource (Phoenix)	Direct light: 6 kWh/m^2/day	Diffuse light: 2 kWh/m^2/day	
Outdoor efficiency	32.5%	33.4%	26.5%
DC energy output	2.60 kWh/m^2/day	2.67 kWh/m^2/day	2.12 kWh/m^2/day
Solar resource (Miami)	Direct light: 3.6 kWh/m^2/day	Diffuse light: 2.8 kWh/m^2/day	
Outdoor efficiency	28.8%	32.4%	20.5%
DC energy output	1.84 kWh/m^2/day	2.07 kWh/m^2/day	1.31 kWh/m^2/day

The 20X monolithic tandem has the highest in-lab efficiency, but has the lowest outdoor energy output as it captures no diffuse light. This discrepancy becomes larger for locations with a higher fraction of diffuse light: For example, in Miami, the 20X monolithic

tandem's average efficiency is only slightly more than half the cell's in-lab efficiency. The 20X PVMirror tandem has higher in-lab efficiency than the one-sun monolithic tandem because the silicon heterojunction bottom cell is under concentration, but lower in-lab efficiency than the 20X monolithic tandem, for which both cells are under concentration. More importantly, the PVMirror tandem has significantly higher outdoor energy output than the 20X monolithic tandem and nearly as high as the one-sun monolithic tandem because it both collects most of the available diffuse light in the CdMgTe top cell, especially in blue-sky Phoenix, and it benefits from the aforementioned concentration in the bottom cell. Although the PVMirror tandem energy output is slightly lower than that of the (current-matched) monolithic tandem, the levelized cost of electricity generated by the PVMirror tandem would be lower (given the same balance-of-systems cost) because it consumes 20 times fewer silicon cells.

The above analysis considered ideal tandems in which two individual sub-cells were coupled without loss. Real PVMirror tandems are expected to approach much closer to this ideal than monolithic tandems. In PVMirror tandems, the sub-cells are fabricated separately and on their own respective substrates (if used), which allows for complete freedom in optimization of each sub-cell; the dominant challenge in monolithic tandems—material and process compatibility—are eliminated. Consequently, PVMirror tandems should be free of, e.g., high recombination currents at defects induced during epitaxy and parasitic absorption in graded buffer layers—common problems in monolithic tandems. In addition, monolithic tandems will frequently experience current mismatch in real meteorological conditions even when designed to be current matched in the lab [233], [234], resulting in power losses not incurred by PVMirror tandems and other four-terminal

designs. The largest anticipated loss in a real PVMirror tandem is parasitic absorption of sub-bandgap light in the top cell, which will reduce the illumination on the bottom cell. Most sub-bandgap absorption is due to free-carrier absorption (e.g., in doped layers, transparent conductive oxides, or metals) and must be carefully controlled for PVMirror configurations that use absorptive filtering (as in Figures 5-1a and 5-2).

Are PVMirror tandems dependent upon the prior development of cheap, efficient, wide-bandgap, thin-film, one-sun top cells like CdMgTe? No. As shown in Figure 6-1c, it is possible to move the wide-bandgap top cell to the focus and use a narrow-bandgap cell with an additional long- or band-pass dichroic mirror to form the PVMirror. This configuration is economically preferred if the top cell is more expensive than the bottom cell, as the cost of the cell at the focus is always discounted by the concentration ratio. An example is a PVMirror with silicon cells directing short wavelengths to a small-area, high-efficiency (and expensive) GaInP cell.

6.4 Case Studay II: PV-CSP Tandem

PVMirrors can also be used with non-PV solar energy converters designed to operate under concentration, including, e.g., CSP receivers. There are four main types of CSP collectors—trough, dish, Fresnel mirror, and heliostat—and PVMirrors can in principle be used in place of all of them by adopting the right curvature. Generally, all three PVMirror configurations introduced in Figure 6-1 suit all four types of collectors; however, heliostats are unique in that they direct light to a fixed central receiver, which means that there is a large variation in the angle of incidence on each heliostat throughout the day. As dichroic mirrors like those in Figures 5-1b and 5-1c tend to be sensitive to angle of

incidence, particularly at grazing angles, the specular-rear-reflector PVMirror configuration shown in Figure 6-1a is preferred for heliostats.

Table 6-2. CSP performance used in Case Study II calculations.

Tracking and trough absorption loss	Receiver optical loss	Receiver thermal loss	Rankine efficiency	Power block parasitic loss	Thermal loss for stored heat	CSP efficiency*
19%	12%	20%	35%	10%	9%	18.0%

* Average system efficiency with respect to direct light only and with no thermal storage.

In this case study, we consider utility-scale trough CSP, which employs a mirrored parabolic trough on a North-South-axis tracker to reflect all wavelengths to a black receiver tube (average concentration on the tube of approximately 27X) filled with a flowing heat-transfer fluid. Trough CSP is the most mature of the CSP technologies but has a low demonstrated average efficiency of 10–15% (with respect to the global insolation) [235]. There are two reasons for this modest efficiency: no diffuse light is intercepted by the receiver tube and the conversion of direct light to electrical power suffers from the many small losses given in Table 6-2 [236]. These are compounded to yield an efficiency of 18.0% with respect to direct light only. By replacing mirrored troughs with PVMirrors, we expect to mitigate both CSP losses: The PV cells will collect diffuse (in addition to direct) light within a particular spectral band, and this light will be converted to electrical power with efficiencies much greater than 18.0%. It is tempting to simply replace the CSP troughs with flat-plate PV modules—SunPower modules on single-axis trackers would yield efficiencies of approximately 21% with respect to the global insolation—but CSP offers the advantages of economical energy storage and thus dispatchable electricity, as well as superior efficiency at converting long and short wavelengths, which are poorly used by PV

cells. A PV-CSP tandem utilizing PVMirrors is expected to match the efficiency of flat-plate PV while retaining the dispatchable-electricity capacity of CSP.

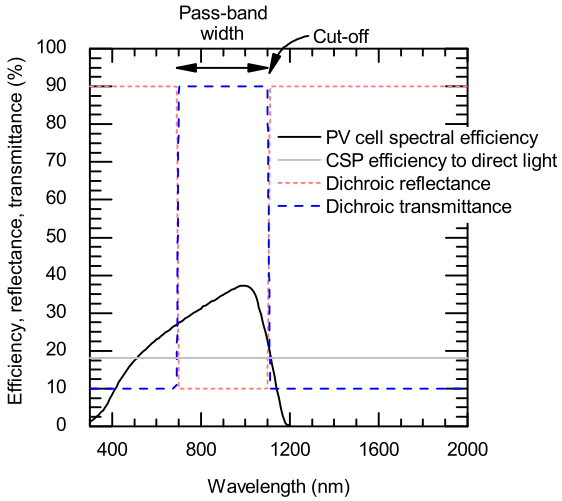

Figure 6-6. Photon-to-AC-power spectral efficiencies of the silicon heterojunction PVMirror and trough CSP system used in calculations for Case Study II. Also shown are the assumed reflectance and transmittance of the band-pass dichroic mirror located in front of the PV cell.

We assumed a trough PVMirror with the same silicon heterojunction PV cells that were used in Case Study I, but with the cells on the glass trough to form the PVMirror rather than at its focus. Figure 6-6 again shows the spectral efficiency of this cell—this time including additional losses described below—as well as the wavelength-agnostic CSP efficiency (to direct light only). Note that wavelengths shorter than 500 nm or longer than 1100 nm are best reflected to the receiver tube, as CSP has a higher conversion efficiency than the silicon heterojunction cell at these wavelengths. We thus included a band-pass dichroic mirror in the PVMirror to arrive at a configuration similar to those depicted in Figures 5-1b and 5-1c. The band-pass mirror was assumed to have 90% transmittance in the pass band and 90% reflectance in the reject bands (shown in Figure 6-6), and the pass-band width and cut-off wavelength (transition from transmitting to reflecting) were varied.

Note that polymer dichroic mirrors with better than the assumed 90%/90% performance are available from, e.g., 3M for ~20 $/m^2. The PVMirror PV-CSP tandem efficiency and energy output was modeled in Phoenix and Miami with the same methodology used in the previous example, but additional PV losses were included to ensure that PV and CSP were equitably compared. In particular, this case study assumed a 10% cell-to-module or cell-to-PVMirror loss and a 4% DC-to-AC inverter loss (all tandems in Case Study I generate DC power and were compared on the cell level for simplicity; thus, these losses were neglected). We assumed that the PV-CSP tandem operates with the same Rankine efficiency of a pure CSP system (given in Table 6-2), which requires that the heat-transfer fluid reach the same outlet temperature despite reduced heat flux (i.e., by a reduced fluid flow).

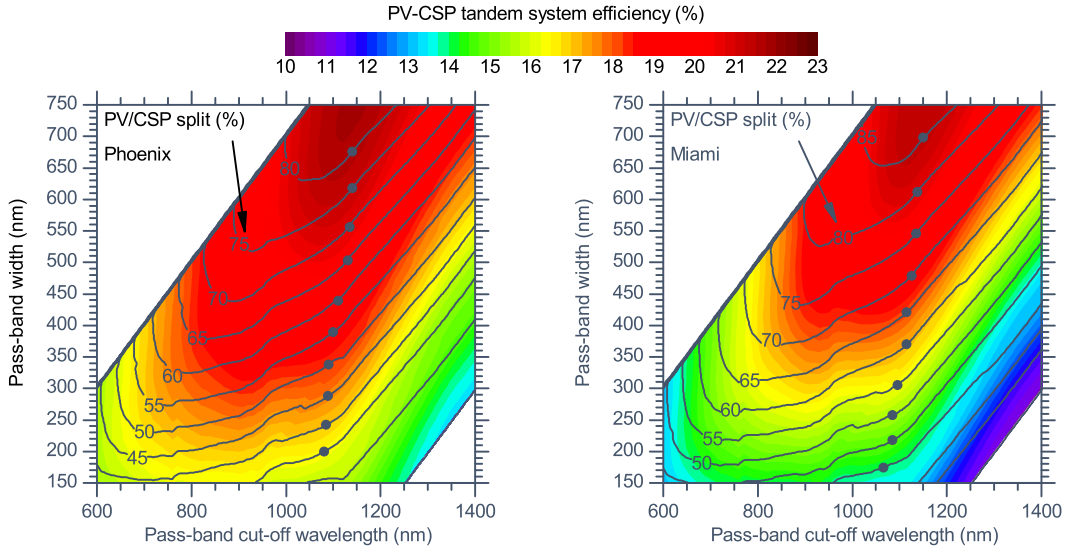

Figure 6-7. Performance of a PV-CSP tandem located in Phoenix or Miami as a function of the pass-band width and cut-off wavelength of the band-pass dichroic mirror. The color contours represent the outdoor system efficiency (with respect to the global insolation) assuming no thermal storage, and the line contours represent the PV/CSP power output split in percentage of PV. The black dots indicate the band-pass mirror characteristics that result in the highest efficiency for a given PV/CSP split.

The first step in modeling the PV-CSP tandem is to determine the optimal band-pass dichroic mirror characteristics for the PVMirror. Figure 6-7 displays color contour plots of the outdoor efficiency of PV-CSP tandems in Phoenix and Miami for a range of mirror pass-band widths and cut-off wavelengths. Also shown with line contours is the PV/CSP split—the fraction of the AC power output that comes from the PV cells. Figure 6-7 assumes no dispatchable electricity; thermal storage is treated separately below. The highest efficiency of approximately 21.8% can be achieved in Phoenix with a wide pass band that sends most of the sunlight to the PV cells (as expected from Figure 6-6). However, this has the consequence that a small fraction of light is sent to the receiver tube, resulting in CSP contributing only 20% of the total output power. It is unlikely that the cost of a CSP system, with the associated thermal energy storage, power block, and collector field, would be justified for this small power output. Although a unique feature of this tandem is that the PV/CSP split can be varied according to the desired plant design, a 50% split is likely a sensible balance between higher efficiency and greater storage capacity. To achieve the highest efficiency with this constraint, Figure 6-7 indicates that the pass band should be 260–340 nm wide, depending on the diffuse fraction, and have a cut-off wavelength of roughly 1100 nm, independent of diffuse fraction (and, in fact, independent of the prescribed PV/CSP split).

Table 6-3 compares the outdoor efficiencies and annually averaged daily energy outputs for a PV-CSP tandem with a 50% split, a flat-plate PV system with the same heterojunction cells on the same North-South-axis tracker, and a trough CSP system. The PV and CSP systems are conceptually like PV-CSP tandems with splits of 100% and 0%, respectively, corresponding to either omitting the dichroic mirror or making it a broadband

Table 6-3. Comparison of a PV-CSP tandem with trough CSP and PV systems.

	PV-CSP tandem system (50% split)	Trough CSP system	PV system
Solar resource (Phoenix)	Direct light: 6 kWh/m^2/day Diffuse light: 2 kWh/m^2/day		
Outdoor efficiency	18.3%	13.5%	19.0%
AC energy output	1.46 kWh/m^2/day	1.08 kWh/m^2/day	1.52 kWh/m^2/day
Solar resource (Miami)	Direct light: 3.6 kWh/m^2/day Diffuse light: 2.8 kWh/m^2/day		
Outdoor efficiency	15.5%	10.5%	19.4%
AC energy output	0.99 kWh/m^2/day	0.67 kWh/m^2/day	1.24 kWh/m^2/day

reflector. As in Figure 6-7, Table 6-3 assumes no dispatchable electricity. The PV-CSP tandem using a PVMirror generates nearly as much energy in Phoenix as the pure PV system and 36% more than the pure CSP system; in Miami it falls short of the PV system[3] but still produces almost as much energy as the pure CSP system in Phoenix. Consequently, PVMirrors may extend the geographical reach of CSP, which has traditionally been limited to the high-direct-insolation Southwest.

At first glance, Table 6-3 appears to indicate that a PV-CSP tandem with a 50% split is inferior to a pure PV system in all locations; however, Table 6-3 ignores the thermal storage capacity of both the PV-CSP tandem and the pure CSP system. Dispatchable electricity is of sufficient value to utility companies—and its value will only increase with increasing PV penetration—that CSP plants continue to be installed when PV plants with the same annual energy output would be cheaper; CSP occupies a different market. Given a 9% loss in energy of stored heat, the outdoor system efficiency is shown in Figure 6-8 as

[3] The efficiency of the PV system is higher in Miami than in Phoenix because the diffuse light in Phoenix was assumed to be bluer and thus poorly matched to silicon's bandgap. Also, the angular dependence of reflection from the front surface of the module was not considered, so the higher diffuse fraction in Miami comes with no penalty.

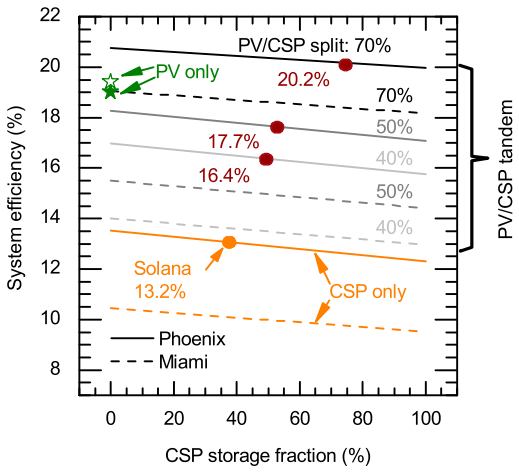

Figure 6-8. Outdoor system efficiency (with respect to the global insolation) of a PV-CSP tandem as a function of the fraction of the CSP AC power output that is dispatchable. Stored heat is assumed to incur a 9% loss. Data are shown for PV/CSP splits of 30–70%, and the product of the PV/CSP split and CSP storage fraction is the fraction of the total system AC power output that is dispatchable. Also plotted are the efficiencies of pure CSP and PV systems. The dots and adjacent system efficiencies correspond to configurations that provide 0.36 kWh/m^2/day of dispatchable electricity.

a function of CSP storage fraction for PV-CSP tandems, a pure CSP system, and a pure PV system. The efficiencies for a storage fraction of zero correspond to those in Table 6-3. On average, storing all of the heat generated in the receiver tube prior to electricity generation (all CSP electricity is dispatchable) results in a 1% absolute decrement in system efficiency. For a typical pure CSP system, roughly one-third of its electricity (0.36 kWh/m^2/day in Phoenix) is dispatchable (e.g., Solana operates for roughly twelve hours a day and is designed for six hours of storage), and it will operate at 13.2% efficiency in Phoenix according to Figure 6-8. For a PV-CSP tandem, the dispatchable electricity is the product of the PV/CSP split, CSP storage fraction, and total system energy output. Thus, PV-CSP tandems in Phoenix with a 40% split and 46% storage fraction, 50% split and 51% storage fraction, and 70% split and 74% storage fraction will all have 0.36 kWh/m^2/day of

dispatchable electricity as well, but will operate with efficiencies of 16.4, 17.7, and 20.2%, respectively (see dots in Figure 6-8). With a properly selected band-pass dichroic mirror, a PVMirror-based PV-CSP tandem can therefore operate—in principle—at higher efficiency than a pure PV system while maintaining the full dispatchability of a pure CSP system. In practice, and as discussed previously, it is likely preferable to operate with a more equitable PV/CSP split and even higher storage capacity to justify the cost of the power block and thermal energy storage.

6.5 Conclusion

The universality of the PVMirror design lies in its ability to turn a narrow- or wide-bandgap PV cell into a tandem with nearly any other solar energy converter. We analyzed two case studies that demonstrate the great flexibility of PVMirrors: In one, a wide-bandgap PV cell was coupled to a second PV cell via absorptive filtering; in the other a narrow-bandgap PV cell was coupled to a thermal absorber via reflective filtering. In both cases, the PVMirror tandems performed well compared to existing technologies. Other hybridizations can also be envisioned; the key is to find converters that "like" input spectra complementary to the spectrum absorbed by the cells in the PVMirror. For example, in solar chemistry, high-energy photons are required to degrade hazardous organic chemical compounds [237]. A possible detoxification process could thus be to flow hazardous chemicals through a pipe located at the focus of a PVMirror employing narrow-bandgap cells and a dichroic mirror. This would particularly make sense if electricity was also required in the detoxification process (or by the plant facilities), since it would be generated on site [238].

This chapter has focused on efficiency and energy output, but the astute reader will also want to know about cost. A good "sanity check" is to compare the installed cost per annual energy yield (equivalent to levelized cost of electricity given similar depreciation times and operating costs) of a PVMirror system and each of its coupled solar energy converters individually. For example, comparing the PV-CSP tandem and pure CSP systems in Case Study II, the tandem saves the cost of the silver on the mirrors but adds the cost of PV cells, a band-pass dichroic mirror, lamination materials, inverters, and field wiring. We estimate that this corresponds to a 30% increase in the cost of the collector field, which itself comprises one-third the cost of a trough CSP power plant [236], leading to a 10% increase in the total installed system cost. For a total dispatchable electricity (or storage) capacity identical to a pure CSP system, we calculated that the tandem has up to a 53% greater annual energy yield, corresponding to a 28% savings in cost per energy. Comparing the PV-CSP tandem and pure PV system in Case Study II, the tandem adds the cost of glass curving and the associated additional support, receiver tubes and fluid, a power block, and thermal energy storage. We estimate that this doubles or triples the installed cost, depending on the size of the power block, for no significant increase in energy output, and a PV-CSP tandem is preferred over a PV system only if the utility company values dispatchable electricity at a substantial premium over variable electricity. This may seem unlikely, but the calculation is even less favorable when comparing pure CSP and pure PV, yet CSP power plants exist. In general, a PVMirror-based tandem is economically competitive when the two constituent solar energy converters have significant overlap in their most expensive components or infrastructure (e.g., glass,

trackers, land); in this case, the marriage of the converters eliminates duplication of the associated costs.

CHAPTER 7

GAAS/SILICON PVMIRROR TANDEM WITH 29.6% EFFICIENCY WITH RESPECT TO THE OUTDOOR GLOBAL IRRADIANCE

This chapter documents the development of a four-terminal, GaAs/Silicon tandem module to prove the PVMirror concept. In this tandem configuration, a curved silicon module, coated with a dichroic mirror, reflects and concentrates visible light onto a GaAs module at the focus. This PVMirror tandem shows a maximum tandem efficiency of 29.6% with respective to the outdoor global irradiance, and, more prominently, demonstrates diffuse light collection as a concentrating technology. As single-axis tracking becomes dominant in the utility market, this proof-of-concept shows that PVMirror tandem technology has the potential to boost the system efficiency >30% and reach the SunShot 2030 target—LCOE of $0.03/kWh with further development of inexpensive top cells.

7.1 Introduction

Silicon photovoltaic (PV) module prices are decreasing faster than balance-of-system costs—especially the area-dependent balance-of-system costs (BOS_A). For example, in the United States, from 2009 to 2016, the module price learning rate was 28% and the BOS_A learning rate was only 10% [239]. As a result, the module cost now accounts for only a third of the total system cost in utility systems [12], and this share will be even smaller in the future if these learning rates continue. With such a cost structure, the annually averaged module efficiency is a primary cost driver: An increase in the annual energy

output per module decreases *both* the $/W module and BOS_A costs, which represent two-thirds of the total system cost.

Single-axis tracking and module efficiency have been proven to be the most effective ways to improve the annual energy output. In 2016, 80% of the newly installed utility-scale PV systems were equipped with trackers, predominantly single-axis trackers [12]. Although a (North-South) single-axis tracking system costs 8% more than a fixed-tilt system when installed, its 10–15% energy insolation gain outweighs the extra cost and warrants its lower levelized cost of electricity (LCOE) [240]. Silicon module efficiency, the multiplier of energy output, has increased to 20% with several technological innovations, including passivated-emitter-rear-contact (PERC) cell structures, and has a clear path to 25% with interdigitated-back-contact (IBC) technology [71]. However, the module efficiency is not expected to exceed 26%, as the practical efficiency limit of its constituent silicon cells is approximately 27% [5]. A possible path to further efficiency gains that leverages the existing silicon PV industry is silicon-based tandems, in which a wide-bandgap top cell is coupled with a silicon cell to raise the limiting efficiency to 43%.

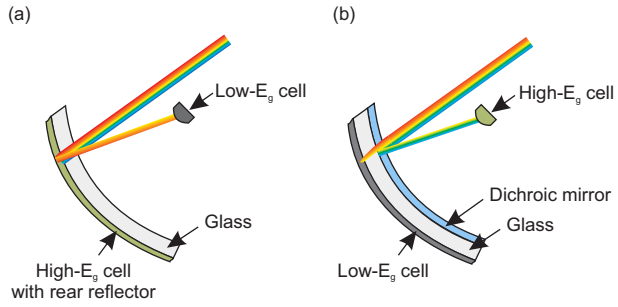

Figure 7-1. Conceptual schematic of PVMirror tandems based on a single-axis tracking system (trackers not shown). (a) Wide-bandgap PV modules reflect and concentrate sub-bandgap light onto narrow-bandgap PV modules, (b) narrow-bandgap PV modules with (long-pass) dichroic mirrors reflect and concentrate super-bandgap light onto wide-bandgap PV modules.

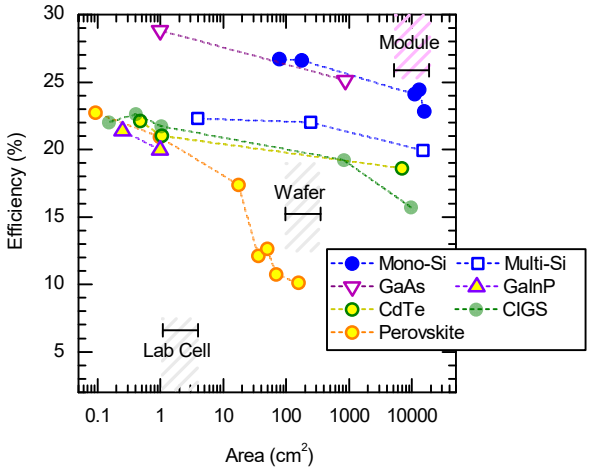

Figure 7-2. Best reported efficiencies of single-junction PV cells with different absorbers.

PVMirrors enable a new tandem concept that we previously proposed [241], in which spatially separate sub-cells mounted on a single-axis tracker are coupled optically. A PVMirror is a one-sun PV module that acts as a concentrating mirror, spectrum splitter, and high-efficiency light-to-electricity converter. By arranging PVMirrors so that specularly reflected light arrives at a common focus—as with a parabolic trough—the resulting concentrated light can be used to illuminate another PV cell with a complementary bandgap (the "receiver"). As illustrated in Figure 7-1a, with the PVMirror absorber's bandgap as the spectrum splitting edge, the PVMirror's rear mirror (rear metal in modern PV technology) reflects sub-bandgap light to the receiver. This is analogous to filtering via transmission in a stacked tandem, but with a double pass through the absorber. PVMirror tandems would look similar to SunPower or Cogenra's low-concentration PV systems but with PV modules in place of silvered mirrors. Unique among concentrating technologies, PVMirror tandems make use of a portion of the diffuse light as the PVMirror intercepts the *global* insolation. By coupling a hypothetical 21%-efficient, 1.8-eV top cell

with 22%-efficient silicon cells, we previously calculated that a PVMirror tandem could achieve 32.5% efficiency under insolation with 25% annually-averaged diffuse light.

The success of PVMirror tandems—like any other tandems—relies on the development of efficient, inexpensive, thin-film type, wide-bandgap PV cells. However, as evident in Figure 7-2, mature technologies such as cadmium telluride (CdTe) and copper indium gallium selenide (CIGS) both have lower efficiencies compared to silicon; emerging technologies such as perovskites, although used to make tandems in PVMirror configurations [110, 111], still need improvement in performance on large areas; efficient wide-bandgap absorbers such as gallium indium phosphide (GaInP) have also been demonstrated only on small devices. In fact, among all the existing cells, our bottom-up analysis indicated that gallium arsenide (GaAs) is presently the best choice for a top cell, even though it has the "wrong" bandgap [21]. Constrained by the current- and lattice-mismatch between GaAs and silicon, GaAs//Silicon tandems were successful only in a 4-terminal configurations. So far, Essig *et al*. demonstrated a record 32.8%-efficient GaAs/Silicon tandem device, 1 cm^2 in size, by mechanically stacking a GaAs cell on top of a silicon heterojunction cell [76]; similarly, Rienacker *et al*. reported a 1.1-cm^2, 31.5%-efficient GaAs//Silicon tandem but with an interdigitated-back-contact (IBC) silicon cell [242]. Substituting GaAs cells with GaInP/GaAs dual-junction cells, both groups reported >35% efficiency. Using dual-junction III-V cells enables a current-matching III-V/Silicon tandem, and Fraunhofer reported a two-terminal, 4-cm^2, 33.3%-efficient GaInP/GaAs/Silicon tandem by wafer bonding [30, 71]. This number is considerably higher than its 19.7%-efficient, direct-growth counterpart, which still suffers from lattice mismatch [71]. Triple-junction III-Vs have been paired with silicon in concentrator

modules, and efficiencies—with respect to direct light—of up to 40.6% were reported [243-245].

Here, we demonstrate a GaAs/Silicon PVMirror tandem on the module level, and report 29.6% outdoor efficiency with respect to the *global* insolation. Despite the fact that GaAs is too expensive to reach the utility market with its present cost, this tandem model can quickly assess the potential of PVMirror tandems as a diffuse-light-collecting concentrating technology.

7.2 Prototype Design

We used silicon and GaAs modules, configured as in Figure 7-1(b), in which a silicon module is coated with a spectrum-splitting dichroic mirror and a GaAs module is at the focus. A 5" silicon IBC cell and a GaAs module (with 7 unit cells connected in series, that almost matches the width of the silicon cell), donated by SunPower and Alta Devices respectively, were used for the prototype. Both the silicon cell and GaAs module have efficiencies greater than 25% at standard test condition (STC), as measured by the donors.

Parabolic trough glass is commercially available. However, for our single-cell silicon PVMirror prototype, a flat, low-iron glass was placed on top of a curved steel mold shaped into a parabolic trough. When heated to approximately 600 °C, the glass conforms to the mold on its own weight, resulting in a curved piece of glass that has a focal length of 1.7 meters, as prescribed by the mold.

To design the dichroic mirror, we first calculated the spectral efficiency of both representative cells, as shown in Figure 7-3, according to [21]:

$$\eta(\lambda) = \frac{V_{OC} \cdot FF \cdot J_{SC}(\lambda)}{I(\lambda)} \qquad (7.1)$$

with V_{OC} the open-circuit voltage, *FF* the fill factor, λ the wavelength, *I(λ)* the spectral irradiance, and $J_{SC}(\lambda)$ the short-circuit current density per unit wavelength:

$$J_{SC}(\lambda) = q\frac{\lambda}{hc}EQE(\lambda)\cdot I(\lambda) \qquad (7.2)$$

with q, h, and c having their usual meanings. The spectral efficiency curves clearly show that, first, GaAs cells have higher efficiency than silicon cells for the light with wavelength < 850 nm; and, second, silicon cells contribute to the tandem by converting the near-infrared light (> 860 nm) with efficiency as high as 45%, which GaAs cells are not able to do. Therefore, an ideal dichroic mirror for this tandem should reflect all the light below 860 nm to the GaAs receiver, transmit all the near-infrared light to the silicon, and have a sharp transition at 860 nm, where the two spectral efficiency curves intersect.

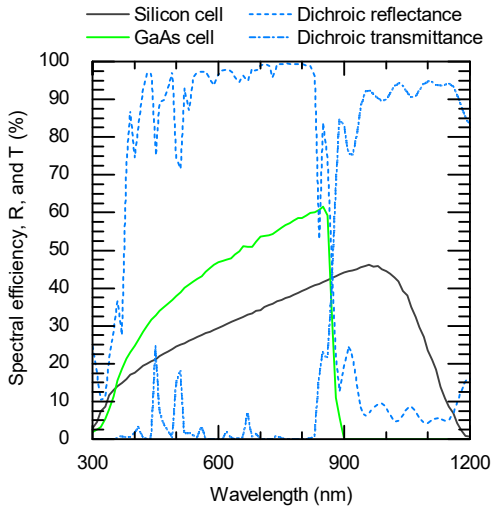

Figure 7-3. Spectral efficiency of representative GaAs (green) and silicon (black) cells. Also shown are the reflectance (dashed blue) and transmittance (dash-dotted blue) of the dichroic-mirror-coated glass.

With these design targets, we designed a 50-layer SiO_2/TiO_2 dielectric stack (on glass) with "Essential Macleod", a thin-film optical software. This design was fabricated with electron-beam (e-beam) evaporation at EMF Corporation, and the performance of the

dichroic mirror is shown in Figure 7-3. As expected, the dichroic coating on glass performs close to the targets but with some non-idealities in the transition region, the reflection- and transmission-bands: the dichroic mirrorhas an AM1.5D-weighted reflectance of 92.2% in the 300–850 nm band, and transmittance of 89.4% in the 860–1100 nm band.

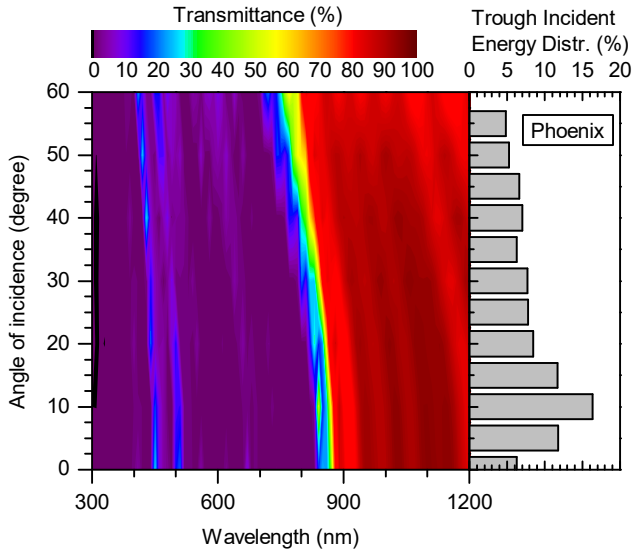

Figure 7-4. Transmittance of the dichroic glass as a function of angle-of-incidence (left panel), and the direct-normal incident energy distribution on a North-South-oriented trough located in Phoenix, USA, throughout a year (right panel).

Figure 7-4 shows the angle-dependent transmittance of the dichroic mirror, characterized by a Perkin Elmer spectrophotometer equipped with an Automated Reflectance/Transmittance Analyzer (ARTA) accessory [246, 247]. This dichroic mirror maintains its fidelity up to a 30-degree angle of incidence (AOI), whereas the splitting edge shifts to 790 nm when the AOI increases to 50 degrees. Note that no lights are lost due to these blue-shifts, they are just sent to the less-efficient silicon cell. Our previous analysis shows that a 50-nm blue shift reduces the tandem efficiency by only 3.2%, relatively [248]. Compared to the direct-normal incident energy distribution on a North-South-oriented trough located in Phoenix, USA, throughout a year, also shown in Figure 7-4, tandems with

this dichroic mirror are expected to capture 70% of incident energy at its best performance (desired splitting edge). Although this e-beam–evaporated dichroic mirror is cost-prohibitive for PV application, it helps prove the concept and assess the potential of this technology. Once proved, PVMirror tandems can use polymer-based dichroic mirrors with similar (or better) performance at very low cost (~\$20/m^2) [249].

7.3 Prototype Assembly and Outdoor Test

Figure 7-5a is a photograph of the assembled PVMirror tandem prototype. The GaAs module, 5 cm × 12 cm in size, was glued to an aluminum heatsink with Arctic Alumina™ thermal adhesive, and then mounted on the tracker located at the University of Arizona, in Tucson, 180 km south of Phoenix. The silicon IBC cell was tabbed and laminated to the dichroic-mirror-coated, curved glass, and mounted on a tip-tilt stage on the tracker. (Note the focal length is 1.7 meters, therefore, the silicon PVMirror looks almost flat). The aperture area of the silicon PVMirror was masked to 12.5 cm × 12.5 cm, the width of the IBC cell. Therefore, this configuration provides 2.5X geometric concentration, and, by tilting the stage, it provides slightly off-axis tracking, so that the receiver does not shade the silicon PVMirror during operation. The distance between the GaAs receiver and silicon PVMirror was adjusted so that the full area of the GaAs cells was illuminated with minimal spillage of light onto the edges.

The tandem prototype was on-sun for three days, and the current-voltage (I-V) data were collected with a Keithley 2640 source-measure unit (SMU) connected to a switch box that alternates which module (silicon PVMirror or GaAs receiver) was measured. Measurements were taken approximately every minute. Weather data, including direct normal irradiance (DNI) and diffuse horizontal irradiance (DHI), were measured with a

one-minute resolution at the NREL OASIS observatory located on the University of Arizona campus 260 meters west of the tracker [250].

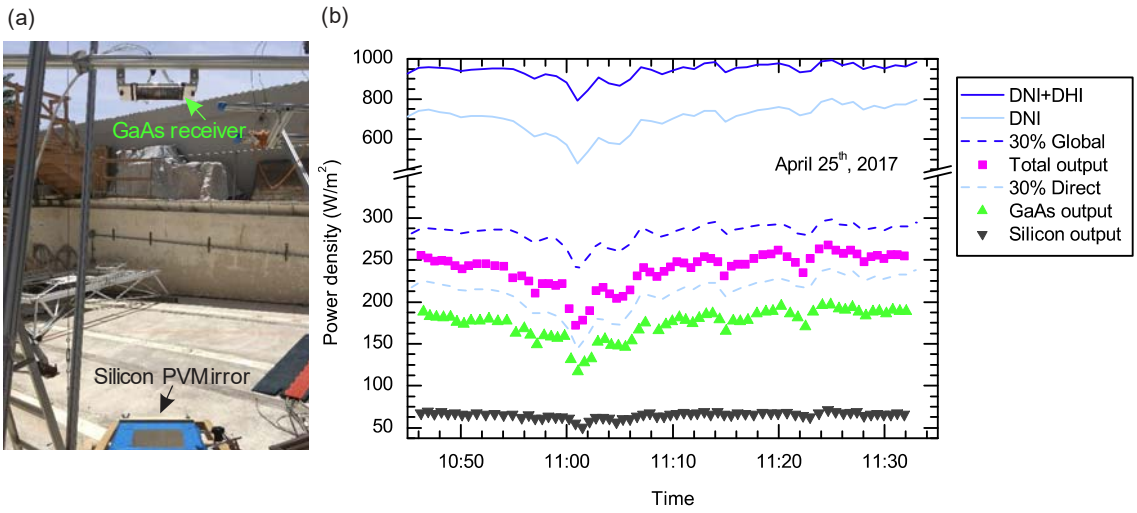

Figure 7-5. (a) Photograph of the GaAs/Silicon PVMirror tandem prototype, mounted on a tracker. (b) Measurement results on the first (cloudy) day: Global (solid blue) irradiance calculated from DNI (solid light blue) plus DHI (not shown), output power density of the GaAs receiver (green) and the silicon PVMirror (black), and summed total (pink). Also shown are 30% of global irradiance (dashed blue), and 30% of DNI (dashed light blue) for reference.

Figure 7-5b shows the outdoor measurement results of the first day (the power output of both the GaAs receiver and the silicon PVMirror were normalized to the aperture area of the silicon PVMirror). On this cloudy day, as noticed from the fluctuation of DNI, the output of both sub-modules follows the swing of DNI (also global irradiance, summed up with DNI and DHI), however, with GaAs being more pronounced as it receives only the direct light. The total power output from this tandem ranges from 170 W/m^2 to 270 W/m^2, corresponding to 20% and 27% efficiency with respect to global irradiance, respectively.

Figure 7-6a shows the tandem efficiency as a function of diffuse fraction for all three days. With less diffuse light (sunny weather) in the other two days, the tandem

efficiencies were higher. Fitting all these data with a least-square method reveals that, first, if there were no diffuse light (as in a STC measurement with a solar simulator), the tandem efficiency would be about 31%; and, second, the PVMirror tandem *does* collect diffuse light, as the fitted line is less steep than the dashed black line, which represents the expected tandem system efficiency with no diffuse-light collection capability.

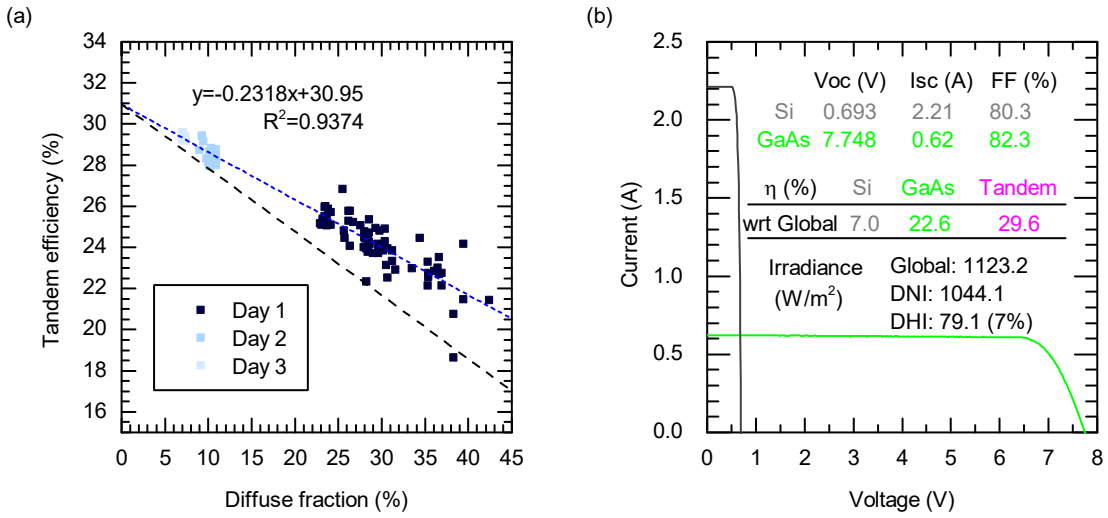

Figure 7-6. (a) Outdoor tandem efficiency as a function of diffuse fraction. The dashed black line is the calculated tandem efficiency if there were no diffuse collection. (b) I-V data and corresponding irradiance condition of the best point.

Among all the collected data, the best I-V curves (measured at the same time) are shown in Figure 7-6b. At this time, the DNI was 1044.1 W/m^2, and the DHI was 79.1 W/m^2, resulting in a calculated global irradiance (DNI+DHI) of 1123.2 W/m^2. The GaAs module, with seven cells connected in series, output a V_{oc} of 7.748 V, short-circuit current (I_{sc}) of 0.62 A, and *FF* of 82.3%, corresponding to an efficiency of 22.6% with respect to the global irradiance (remember that it receives only the reflected direct irradiance); the single-cell PVMirror output a V_{oc} of 0.693 V, I_{sc} of 2.21 A and *FF* of 80.3%, corresponding to an efficiency of 7.0%, again with respect to the global irradiance. By summing these

efficiencies, we find that this prototype tandem hit 29.6% *module* efficiency with respect to the *global* irradiance (31.8% with respect to the DNI) at outdoor conditions with 20.3 °C air temperature. Note that the temperature of the PV modules was not controlled during the measurement.

7.4 Conclusion

Using GaAs and silicon cells, we demonstrated the PVMirror tandem concept with a 29.6% module efficiency, and, more prominently, with diffuse light collection as a concentrating technology. Replacing GaAs with dual-junction cells, e.g. InGaP/GaAs, could further increase the efficiency. As single-axis tracking becomes dominant in the utility market, PVMirror tandem technology has the potential to boost the system efficiency >30% and reach the SunShot 2030 target—LCOE of $0.03/kWh. The jury is still out on whether the annual energy yield gain would outweigh the added top-cell cost—discounted by the concentration.

For this technology—similar to other silicon-based tandem technology—to have a better chance to market, wide-bandgap, thin-film top-cell technology, such as Cd(Mg, Zn)Te and perovskites etc., that can be used as PVMirrors is needed. With such prospective inexpensive PVMirrors, silicon—now the expensive sub-cell—will be placed at the focus. This configuration, shown in Figure 1(a), eliminates the dichroic mirror, which introduces additional cost and angle-of-incidence sensitivity, and the challenge is to ensure that the morphology of these thin-film, wide-bandgap cells to be smooth enough to provide specular reflection of the non-absorbed light.

REFERENCES

[1] Fraunhofer ISE, "Photovoltaics Report 07/12/2016," 2017.

[2] International Technology Roadmap for Photovoltaic (ITRPV): Results 2016, 2017.

[3] D. M. Chapin, C. S. Fuller, and G. L. Pearson, "A New Silicon p-n Junction Photocell for Converting Solar Radiation into Electrical Power," *Journal of Applied Physics,* vol. 25, pp. 676-677, 1954.

[4] D. D. Smith, P. Cousins, S. Westerberg, R. De Jesus-Tabajonda, G. Aniero, and Y. C. Shen, "Toward the Practical Limits of Silicon Solar Cells," *IEEE Journal of Photovoltaics,* vol. 4, pp. 1465-1469, Nov 2014.

[5] K. Yoshikawa, H. Kawasaki, W. Yoshida, T. Irie, K. Konishi, K. Nakano*, et al.*, "Silicon heterojunction solar cell with interdigitated back contacts for a photoconversion efficiency over 26%," *Nature Energy,* vol. 2, p. 17032, 2017.

[6] A. Richter, M. Hermle, and S. W. Glunz, "Reassessment of the Limiting Efficiency for Crystalline Silicon Solar Cells," *IEEE Journal of Photovoltaics,* vol. 3, pp. 1184-1191, 2013.

[7] C. Battaglia, A. Cuevas, and S. De Wolf, "High-efficiency crystalline silicon solar cells: status and perspectives," *Energy & Environmental Science,* 2016.

[8] M. A. Green, "Commercial progress and challenges for photovoltaics," *Nature Energy,* vol. 1, p. 15015, 2016.

[9] V. Sivaram and S. Kann, "Solar power needs a more ambitious cost target," *Nature Energy,* vol. 1, p. 16036, 2016.

[10] M. A. Green, "Silicon solar cells: state of the art," *Philosophical Transactions of the Royal Society a-Mathematical Physical and Engineering Sciences,* vol. 371, 2013.

[11] M. Woodhouse, R. Jones-Albertus, D. Feldman, R. Fu, K. Horowitz, D. Chung*, et al.*, "On the Path to SunShot. The Role of Advancements in Solar Photovoltaic Efficiency, Reliability, and Costs," National Renewable Energy Lab. (NREL), Golden, CO (United States) NREL/TP--6A20-65872 United States 10.2172/1253983 NREL English, 2016.

[12] R. Fu, D. J. Feldman, R. M. Margolis, M. A. Woodhouse, and K. B. Ardani, "US solar photovoltaic system cost benchmark: Q1 2017," National Renewable Energy Laboratory (NREL), Golden, CO (United States), 2017.

[13] P. Würfel and U. Würfel, *Physics of Solar Cells: From Basic Principles to Advanced Concepts*: John Wiley & Sons, 2016.

[14] R. T. Ross and A. J. Nozik, "Efficiency of hot-carrier solar energy converters," *Journal of Applied Physics,* vol. 53, pp. 3813-3818, 1982.

[15] M. A. Green, "Third generation photovoltaics: Ultra-high conversion efficiency at low cost," *Progress in Photovoltaics: Research and Applications,* vol. 9, pp. 123-135, 2001.

[16] J. A. R. Dimmock, S. Day, M. Kauer, K. Smith, and J. Heffernan, "Demonstration of a hot-carrier photovoltaic cell," *Progress in Photovoltaics: Research and Applications,* vol. 22, pp. 151-160, 2014.

[17] W. Shockley and H. J. Queisser, "Detailed Balance Limit of Efficiency of P-N Junction Solar Cells," *Journal of Applied Physics,* vol. 32, pp. 510-519, 1961.

[18] S. Kurtz, D. Myers, W. E. McMahon, J. Geisz, and M. Steiner, "A comparison of theoretical efficiencies of multi-junction concentrator solar cells," *Progress in Photovoltaics: Research and Applications,* vol. 16, pp. 537-546, 2008.

[19] A. D. Vos, "Detailed balance limit of the efficiency of tandem solar cells," *Journal of Physics D: Applied Physics,* vol. 13, p. 839, 1980.

[20] C. H. Henry, "Limiting Efficiencies of Ideal Single and Multiple Energy-Gap Terrestrial Solar-Cells," *Journal of Applied Physics,* vol. 51, pp. 4494-4500, 1980.

[21] Z. Yu, M. Leilaeioun, and Z. Holman, "Selecting tandem partners for silicon solar cells," *Nature Energy,* vol. 1, p. 16137, 2016.

[22] T. Todorov, O. Gunawan, and S. Guha, "A road towards 25% efficiency and beyond: perovskite tandem solar cells," *Molecular Systems Design & Engineering,* vol. 1, pp. 370-376, 2016.

[23] P. Faine, S. R. Kurtz, C. Riordan, and J. M. Olson, "The influence of spectral solar irradiance variations on the performance of selected single-junction and multijunction solar cells," *Solar Cells,* vol. 31, pp. 259-278, 1991.

[24] S. Reynolds and V. Smirnov, "Modelling of two-and four-terminal thin-film silicon tandem solar cells," *Journal of Physics: Conference Series,* vol. 398, p. 012006, 2012.

[25] K. Tanabe, K. Watanabe, and Y. Arakawa, "III-V/Si hybrid photonic devices by direct fusion bonding," *Scientific Reports,* vol. 2, 2012.

[26] K. Derendorf, S. Essig, E. Oliva, V. Klinger, T. Roesener, S. P. Philipps*, et al.*, "Fabrication of GaInP/GaAs//Si Solar Cells by Surface Activated Direct Wafer Bonding," *IEEE Journal of Photovoltaics,* vol. 3, pp. 1423-1428, 2013.

[27] F. Dimroth, T. Roesener, S. Essig, C. Weuffen, A. Wekkeli, E. Oliva*, et al.*, "Comparison of Direct Growth and Wafer Bonding for the Fabrication of GaInP/GaAs Dual-Junction Solar Cells on Silicon," *IEEE Journal of Photovoltaics,* vol. 4, pp. 620-625, 2014.

[28] F. Dimroth, M. Grave, P. Beutel, U. Fiedeler, C. Karcher, T. N. D. Tibbits, *et al.*, "Wafer bonded four-junction GaInP/GaAs//GaInAsP/GaInAs concentrator solar cells with 44.7% efficiency," *Progress in Photovoltaics,* vol. 22, pp. 277-282, 2014.

[29] S. Essig, J. Benick, M. Schachtner, A. Wekkeli, M. Hermle, and F. Dimroth, "Wafer-Bonded GaInP/GaAs//Si Solar Cells With 30% Efficiency Under Concentrated Sunlight," *IEEE Journal of Photovoltaics,* vol. 5, pp. 977-981, 2015.

[30] R. Cariou, J. Benick, P. Beutel, N. Razek, C. Flötgen, M. Hermle, *et al.*, "Monolithic Two-Terminal III-V//Si Triple-Junction Solar Cells With 30.2% Efficiency Under 1-Sun AM1.5g," *IEEE Journal of Photovoltaics,* vol. 7, pp. 367-373, 2017.

[31] A. C. Tamboli, M. F. A. M. van Hest, M. A. Steiner, S. Essig, E. E. Perl, A. G. Norman, *et al.*, "III-V/Si wafer bonding using transparent, conductive oxide interlayers," *Applied Physics Letters,* vol. 106, p. 263904, 2015.

[32] J. Yang, Z. Peng, D. Cheong, and R. Kleiman, "Fabrication of High-Efficiency III–V on Silicon Multijunction Solar Cells by Direct Metal Interconnect," *IEEE journal of photovoltaics,* vol. 4, pp. 1149-1155, 2014.

[33] H. Mizuno, K. Makita, T. Tayagaki, T. Mochizuki, T. Sugaya, and H. Takato, "High-efficiency III–V//Si tandem solar cells enabled by the Pd nanoparticle array-mediated “smart stack” approach," *Applied Physics Express,* vol. 10, p. 072301, 2017.

[34] T. R. Klein, B. G. Lee, M. Schnabel, E. L. Warren, P. Stradins, A. C. Tamboli, *et al.*, "Transparent Conductive Adhesives for Tandem Solar Cells," in *2017 IEEE 44th Photovoltaic Specialist Conference (PVSC)*, 2017.

[35] R. R. King, D. C. Law, K. M. Edmondson, C. M. Fetzer, G. S. Kinsey, H. Yoon, *et al.*, "40% efficient metamorphic GaInP/GaInAs/Ge multijunction solar cells," *Applied Physics Letters,* vol. 90, p. 183516, 2007.

[36] B. M. Kayes, L. Zhang, I. K. Ding, and G. S. Higashi, "Flexible Thin-Film Tandem Solar Cells With > 30% Efficiency," *IEEE Journal of Photovoltaics,* vol. 4, pp. 729-733, Mar 2014.

[37] W. Guter, J. Schone, S. P. Philipps, M. Steiner, G. Siefer, A. Wekkeli, *et al.*, "Current-matched triple-junction solar cell reaching 41.1% conversion efficiency under concentrated sunlight," *Applied Physics Letters,* vol. 94, 2009.

[38] A. V. Shah, H. Schade, M. Vanecek, J. Meier, E. Vallat-Sauvain, N. Wyrsch, *et al.*, "Thin-film silicon solar cell technology," *Progress in Photovoltaics,* vol. 12, pp. 113-142, 2004.

[39] S. E. Sofia, Z. Ren, N. S. Kanghah, L. Zhe, T. Buonassisi, and I. M. Peters, "Metal grid contact design of four-terminal tandem solar cells," in *2016 IEEE 43rd Photovoltaic Specialists Conference (PVSC)*, 2016.

[40] D. L. Meier and D. K. Schroder, "Contact resistance: Its measurement and relative importance to power loss in a solar cell," *IEEE transactions on electron devices,* vol. 31, pp. 647-653, 1984.

[41] S. Ruhle, A. Segal, A. Vilan, S. R. Kurtz, L. Grinis, A. Zaban*, et al.*, "A two junction, four terminal photovoltaic device for enhanced light to electric power conversion using a low-cost dichroic mirror," *Journal of Renewable and Sustainable Energy,* vol. 1, 2009.

[42] R. L. Moon, L. W. James, H. A. Vanderplas, R. O. Yep, G. A. Antypas, and Y. Chai, "Multigap solar cell requirements and the performance of AlGaAs and Si cells in concentrated sunlight," in *13th Photovoltaic Specialists Conference*, Washington, D.C., 1978.

[43] A. K. Converse, "Refractive spectrum splitting optics for use with photovoltaic cells," in *Conference Record of the Twenty Fifth IEEE Photovoltaic Specialists* Conference, 1996.

[44] B. D. Chrysler, Y. Wu, Z. Yu, and R. K. Kostuk, "Volume holographic lens spectrum-splitting photovoltaic system for high energy yield with direct and diffuse solar illumination," in *SPIE Optical Engineering + Applications*, 2017.

[45] J. M. Russo, S. D. Vorndran, D. Zhang, M. Gordon, Y. Wu, and R. K. Kostuk, "Grating-over-Lens Holographic Spectrum Splitting Concentrating Photovoltaics," in *Renewable Energy and the Environment*, Tucson, Arizona, 2013

[46] D. B. Needleman, J. P. Mailoa, R. E. Brandt, N. M. Mangan, and T. Buonassisi, "Sensitivity Analysis of Optical Metrics for Spectral Splitting Photovoltaic Systems: A Case Study," *IEEE Journal of Photovoltaics,* vol. 5, pp. 1380-1388, 2015.

[47] M. Steiner, M. Wanlass, J. Carapella, A. Duda, J. Ward, T. Moriarty*, et al.*, "A monolithic three-terminal GaInAsP/GaInAs tandem solar cell," *Progress in Photovoltaics: Research and Applications,* vol. 17, pp. 587-593, 2009.

[48] C.-H. Tai, C.-H. Lin, C.-M. Wang, and C.-C. Lin, "Three-Terminal Amorphous Silicon Solar Cells," *International Journal of Photoenergy,* vol. 2011, p. 5, 2011.

[49] S. Sista, Z. Hong, M. H. Park, Z. Xu, and Y. Yang, "High-efficiency polymer tandem solar cells with three-terminal structure," *Advanced Materials,* vol. 22, 2010.

[50] T. Nagashima, K. Okumura, K. Murata, and Y. Kimura, "Three-terminal tandem solar cells with a back-contact type bottom cell," in *Conference Record of the Twenty-Eighth IEEE Photovoltaic Specialists Conference*, 2000.

[51] G. W. P. Adhyaksa, E. Johlin, and E. C. Garnett, "Nanoscale Back Contact Perovskite Solar Cell Design for Improved Tandem Efficiency," *Nano Letters,* vol. 17, pp. 5206-5212, 2017.

[52] J. M. Zahler, C.-G. Ahn, S. Zaghi, H. A. Atwater, C. Chu, and P. Iles, "Ge layer transfer to Si for photovoltaic applications," *Thin Solid Films,* vol. 403–404, pp. 558-562, 2002.

[53] M. J. Archer, D. C. Law, S. Mesropian, M. Haddad, C. M. Fetzer, A. C. Ackerman*, et al.*, "GaInP⁄ GaAs dual junction solar cells on Ge⁄ Si epitaxial templates," *Applied Physics Letters,* vol. 92, p. 103503, 2008.

[54] M. J. Griggs, D. C. Law, R. R. King, A. C. Ackerman, J. M. Zahler, and H. A. Atwater, "Design Approaches and Materials Processes for Ultrahigh Efficiency Lattice Mismatched Multi-Junction Solar Cells," in *Photovoltaic Energy Conversion, Conference Record of the 2006 IEEE 4th World Conference on*, 2006

[55] A. D. Martinez, B. R. Ortiz, N. E. Johnson, L. L. Baranowski, L. Krishna, S. Choi*, et al.*, "Development of ZnSiP2 for Si-Based Tandem Solar Cells," *IEEE Journal of Photovoltaics,* vol. 5, pp. 17-21, 2015.

[56] B. C. Chung, G. F. Virshup, S. Hikido, and N. R. Kaminar, "27.6% efficiency (1 sun, air mass 1.5) monolithic Al0.37Ga0.63As/GaAs two-junction cascade solar cell with prismatic cover glass," *Applied Physics Letters,* vol. 55, pp. 1741-1743, 1989.

[57] J. M. Olson, S. R. Kurtz, A. E. Kibbler, and P. Faine, "A 27.3% efficient Ga0.5In0.5P/GaAs tandem solar cell," *Applied Physics Letters,* vol. 56, pp. 623-625, 1990.

[58] T. Takamoto, E. Ikeda, H. Kurita, and M. Ohmori, "Over 30% efficient InGaP/GaAs tandem solar cells," *Applied Physics Letters,* vol. 70, pp. 381-383, 1997.

[59] M. A. Green, K. Emery, Y. Hishikawa, W. Warta, and E. D. Dunlop, "Solar cell efficiency tables (version 48)," *Progress in Photovoltaics,* vol. 24, pp. 905-913, 2016.

[60] N. Jain, K. L. Schulte, J. F. Geisz, R. M. France, and M. Steiner, "GaInAsP/GaInAs Tandem Solar Cell with 32.6% One-Sun Efficiency," in *44th IEEE Photovoltaic Specialists Conference*, Washington D.C., 2017.

[61] I. Almansouri, A. Ho-Baillie, S. P. Bremner, and M. A. Green, "Supercharging Silicon Solar Cell Performance by Means of Multijunction Concept," *Photovoltaics, IEEE Journal of,* vol. PP, pp. 1-9, 2015.

[62] N. Jain and K. Hudait Mantu, "III–V Multijunction Solar Cell Integration with Silicon: Present Status, Challenges and Future Outlook," in *Energy Harvesting and Systems* vol. 1, 2014.

[63] H. Shimizu, T. Egawa, T. Soga, T. Jimbo, and M. Umeno, "First Demonstration of AlxGa1-xAs/Si Monolithic Tandem Solar Cells Grown by Metalorganic Chemical Vapor Deposition," *Japanese journal of applied physics,* vol. 31, p. L1150, 1992.

[64] T. Soga, T. Kato, M. Yang, M. Umeno, and T. Jimbo, "High efficiency AlGaAs/Si monolithic tandem solar cell grown by metalorganic chemical vapor deposition," *Journal of Applied Physics,* vol. 78, pp. 4196-4199, 1995.

[65] T. Soga, K. Baskar, T. Kato, T. Jimbo, and M. Umeno, "MOCVD growth of high efficiency current-matched AlGaAs/Si tandem solar cell," *Journal of Crystal Growth,* vol. 174, pp. 579-584, 1997.

[66] K. Hayashi, T. Soga, H. Nishikawa, T. Jimbo, and M. Umeno, "MOCVD growth of GaAsP on Si for tandem solar cell application," in *Proceedings of 1994 IEEE 1st World Conference on Photovoltaic Energy Conversion - WCPEC (A Joint Conference of PVSC, PVSEC and PSEC)*, 1994.

[67] T. J. Grassman, J. Carlin, C. Ratcliff, D. J. Chmielewski, and S. Ringel, "Epitaxially-grown metamorphic GaAsP/Si dual-junction solar cells," in *Photovoltaic Specialists Conference (PVSC), 2013 IEEE 39th*, 2013.

[68] T. J. Grassman, D. J. Chmielewski, S. D. Carnevale, J. A. Carlin, and S. A. Ringel, "$GaAs_{0.75}P_{0.25}$/Si Dual-Junction Solar Cells Grown by MBE and MOCVD," *IEEE Journal of Photovoltaics,* vol. 6, pp. 326-331, 2016.

[69] M. Vaisman, S. Fan, K. Nay Yaung, E. Perl, D. Martín-Martín, Z. J. Yu*, et al.*, "15.3%-Efficient GaAsP Solar Cells on GaP/Si Templates," *ACS Energy Letters,* vol. 2, pp. 1911-1918, 2017.

[70] J. F. Geisz, J. Olson, D. Friedman, K. Jones, R. Reedy, and M. Romero, "Lattice-matched GaNPAs-on-silicon tandem solar cells," in *Photovoltaic Specialists Conference, 2005. Conference Record of the Thirty-first IEEE*, 2005.

[71] M. A. Green, Y. Hishikawa, E. D. Dunlop, D. H. Levi, J. Hohl-Ebinger, and A. W. Y. Ho-Baillie, "Solar cell efficiency tables (version 51)," *Progress in Photovoltaics: Research and Applications,* vol. 26, pp. 3-12, 2018.

[72] J. M. Gee and G. F. Virshup, "A 31%-efficient GaAs/silicon mechanically stacked, multijunction concentrator solar cell," in *Photovoltaic Specialists Conference, 1988., Conference Record of the Twentieth IEEE*, 1988.

[73] S. Essig, S. Ward, M. A. Steiner, D. J. Friedman, J. F. Geisz, P. Stradins*, et al.*, "Progress Towards a 30% Efficient GaInP/Si Tandem Solar Cell," *Energy Procedia,* vol. 77, pp. 464-469, 2015.

[74] S. Essig, M. A. Steiner, C. Alleb, x00E, J. F. Geisz, B. Paviet-Salomon*, et al.*, "Realization of GaInP/Si Dual-Junction Solar Cells With 29.8%; 1-Sun Efficiency," *IEEE Journal of Photovoltaics,* vol. PP, pp. 1-8, 2016.

[75] M. A. Green, K. Emery, Y. Hishikawa, W. Warta, E. D. Dunlop, D. H. Levi*, et al.*, "Solar cell efficiency tables (version 49)," *Progress in Photovoltaics,* vol. 25, pp. 3-13, 2017.

[76] S. Essig, C. Allebé, T. Remo, J. F. Geisz, M. A. Steiner, K. Horowitz*, et al.*, "Raising the one-sun conversion efficiency of III–V/Si solar cells to 32.8% for two junctions and 35.9% for three junctions," *Nature Energy,* vol. 2, p. 17144, 2017.

[77] R. Jones-Albertus, D. Feldman, R. Fu, K. Horowitz, and M. Woodhouse, "Technology advances needed for photovoltaics to achieve widespread grid price parity," *Progress in Photovoltaics: Research and Applications,* vol. 24, pp. 1272-1283, 2016.

[78] J. W. Garland, T. Biegala, M. Carmody, C. Gilmore, and S. Sivananthan, "Next-generation multijunction solar cells: The promise of II-VI materials," *Journal of Applied Physics,* vol. 109, 2011.

[79] D. Xu, T. Biegala, M. Carmody, J. W. Garland, C. Grein, and S. Sivananthan, "Proposed monolithic triple-junction solar cell structures with the potential for ultrahigh efficiencies using II-VI alloys and silicon substrates," *Applied Physics Letters,* vol. 96, 2010.

[80] M. Carmody, S. Mallick, J. Margetis, R. Kodama, T. Biegala, D. Xu*, et al.*, "Single-crystal II-VI on Si single-junction and tandem solar cells," *Applied Physics Letters,* vol. 96, 2010.

[81] C. M. Campbell, Y. Zhao, E. Suarez, M. Boccard, X. H. Zhao, Z. Y. He*, et al.*, "1.7 eV MgCdTe double-heterostructure solar cells for tandem device applications," in *2016 IEEE 43rd Photovoltaic Specialists Conference (PVSC)*, 2016.

[82] J. Becker, C. Campbell, C.-Y. Tsai, Y. Zhao, M. Lassise, X.-H. Zhao*, et al.*, "11.2%-efficient monocrystalline Mg0.13Cd0.87Te solar cell with 1.7-eV bandgap," Submitted.

[83] D. E. Swanson, C. Reich, A. Abbas, T. Shimpi, H. Liu, F. Ponce*, et al.*, "CdCl2 Passivation of 1.7 eV CdMgTe and CdZnTe Absorbers for II-VI/Si Hybrid Tandem Photovoltaic Cells," Submitted.

[84] W. S. Yang, B.-W. Park, E. H. Jung, N. J. Jeon, Y. C. Kim, D. U. Lee*, et al.*, "Iodide management in formamidinium-lead-halide–based perovskite layers for efficient solar cells," *Science,* vol. 356, pp. 1376-1379, 2017.

[85] N.-G. Park, M. Grätzel, T. Miyasaka, K. Zhu, and K. Emery, "Towards stable and commercially available perovskite solar cells," *Nature Energy,* vol. 1, p. 16152, 2016.

[86] J.-P. Correa-Baena, M. Saliba, T. Buonassisi, M. Grätzel, A. Abate, W. Tress*, et al.*, "Promises and challenges of perovskite solar cells," *Science,* vol. 358, pp. 739-744, 2017.

[87] M. A. Green, A. Ho-Baillie, and H. J. Snaith, "The emergence of perovskite solar cells," *Nature Photonics,* vol. 8, pp. 506-514, 2014.

[88] A. Polman, M. Knight, E. C. Garnett, B. Ehrler, and W. C. Sinke, "Photovoltaic materials: Present efficiencies and future challenges," *Science,* vol. 352, 2016.

[89] P. Loper, B. Niesen, S. J. Moon, S. M. de Nicolas, J. Holovsky, Z. Remes*, et al.*, "Organic-Inorganic Halide Perovskites: Perspectives for Silicon-Based Tandem Solar Cells," *IEEE Journal of Photovoltaics,* vol. 4, pp. 1545-1551, 2014.

[90] B. Chen, X. Zheng, Y. Bai, N. P. Padture, and J. Huang, "Progress in Tandem Solar Cells Based on Hybrid Organic–Inorganic Perovskites," *Advanced Energy Materials,* pp. 1602400, 2017.

[91] J. Werner, B. Niesen, and C. Ballif, "Perovskite/Silicon Tandem Solar Cells: Marriage of Convenience or True Love Story?–An Overview," *Advanced Materials Interfaces,* 2017.

[92] J. Hu, Q. Cheng, R. Fan, and H. Zhou, "Recent Development of Organic–Inorganic Perovskite-Based Tandem Solar Cells," *Solar RRL,* vol. 1, pp. e201700045, 2017.

[93] J.-W. Lee, Y.-T. Hsieh, N. De Marco, S.-H. Bae, Q. Han, and Y. Yang, "Halide Perovskites for Tandem Solar Cells," *The Journal of Physical Chemistry Letters,* vol. 8, pp. 1999-2011, 2017.

[94] J. P. Mailoa, C. D. Bailie, E. C. Johlin, E. T. Hoke, A. J. Akey, W. H. Nguyen*, et al.*, "A 2-terminal perovskite/silicon multijunction solar cell enabled by a silicon tunnel junction," *Applied Physics Letters,* vol. 106, p. 121105, 2015.

[95] S. Albrecht, M. Saliba, J. P. C. Baena, F. Lang, L. Kegelmann, M. Mews*, et al.*, "Monolithic perovskite/silicon-heterojunction tandem solar cells processed at low temperature," *Energy & Environmental Science,* 2016.

[96] J. Werner, C.-H. Weng, A. Walter, L. Fesquet, J. P. Seif, S. De Wolf*, et al.*, "Efficient Monolithic Perovskite/Silicon Tandem Solar Cell with Cell Area >1 cm2," *The Journal of Physical Chemistry Letters,* vol. 7, pp. 161-166, 2016.

[97] F. Sahli, B. A. Kamino, J. Werner, M. Bräuninger, B. Paviet-Salomon, L. Barraud*, et al.*, "Improved Optics in Monolithic Perovskite/Silicon Tandem Solar Cells with a Nanocrystalline Silicon Recombination Junction," *Advanced Energy Materials,* pp. 1701609, 2017.

[98] Y. Wu, D. Yan, J. Peng, T. Duong, Y. Wan, S. P. Phang, *et al.*, "Monolithic perovskite/silicon-homojunction tandem solar cell with over 22% efficiency," *Energy & Environmental Science,* vol. 10, pp. 2472-2479, 2017.

[99] P. Löper, S.-J. Moon, S. M. De Nicolas, B. Niesen, M. Ledinsky, S. Nicolay, *et al.*, "Organic–inorganic halide perovskite/crystalline silicon four-terminal tandem solar cells," *Physical Chemistry Chemical Physics,* vol. 17, pp. 1619-1629, 2015.

[100] C. D. Bailie, M. G. Christoforo, J. P. Mailoa, A. R. Bowring, E. L. Unger, W. H. Nguyen, *et al.*, "Semi-transparent perovskite solar cells for tandems with silicon and CIGS," *Energy & Environmental Science,* vol. 8, pp. 956-963, 2015.

[101] K. A. Bush, C. D. Bailie, Y. Chen, A. R. Bowring, W. Wang, W. Ma, *et al.*, "Thermal and Environmental Stability of Semi-Transparent Perovskite Solar Cells for Tandems Enabled by a Solution-Processed Nanoparticle Buffer Layer and Sputtered ITO Electrode," *Advanced Materials,* 2016.

[102] J. Werner, G. Dubuis, A. Walter, P. Löper, S.-J. Moon, S. Nicolay, *et al.*, "Sputtered rear electrode with broadband transparency for perovskite solar cells," *Solar Energy Materials and Solar Cells,* vol. 141, pp. 407-413, 2015.

[103] J. Werner, G. Dubuis, A. Walter, P. Loper, S. J. Moon, S. Nicolay, *et al.*, "Towards ultra-high efficient phootovoltaics with pervoskite/crystalline silicon tandem devices," presented at the European PV Solar Energy Conference and Exhibition, 31st, Hamburg, 2015.

[104] J. Werner, L. Barraud, A. Walter, M. Bräuninger, F. Sahli, D. Sacchetto, *et al.*, "Efficient Near-Infrared-Transparent Perovskite Solar Cells Enabling Direct Comparison of 4-Terminal and Monolithic Perovskite/Silicon Tandem Cells," *ACS Energy Letters,* vol. 1, pp. 474-480, 2016.

[105] D. P. McMeekin, G. Sadoughi, W. Rehman, G. E. Eperon, M. Saliba, M. T. Hörantner, *et al.*, "A mixed-cation lead mixed-halide perovskite absorber for tandem solar cells," *Science,* vol. 351, pp. 151-155, 2016.

[106] J. Peng, T. Duong, X. Zhou, H. Shen, Y. Wu, H. K. Mulmudi, *et al.*, "Efficient Indium-Doped TiOx Electron Transport Layers for High-Performance Perovskite Solar Cells and Perovskite-Silicon Tandems," *Advanced Energy Materials,* vol. 7, pp. 1601768, 2017.

[107] T. Duong, Y. Wu, H. Shen, J. Peng, X. Fu, D. Jacobs, *et al.*, "Rubidium Multication Perovskite with Optimized Bandgap for Perovskite-Silicon Tandem with over 26% Efficiency," *Advanced Energy Materials,* 2017.

[108] H. Uzu, M. Ichikawa, M. Hino, K. Nakano, T. Meguro, J. L. Hernández, *et al.*, "High efficiency solar cells combining a perovskite and a silicon heterojunction solar cells via an optical splitting system," *Applied Physics Letters,* vol. 106, p. 013506, 2015.

[109] R. Sheng, A. W. Y. Ho-Baillie, S. Huang, M. Keevers, X. Hao, L. Jiang*, et al.*, "Four-Terminal Tandem Solar Cells Using CH3NH3PbBr3 by Spectrum Splitting," *The Journal of Physical Chemistry Letters,* vol. 6, pp. 3931-3934, 2015.

[110] Y. Li, H. Hu, B. Chen, T. Salim, J. Zhang, J. Ding*, et al.*, "Reflective perovskite solar cells for efficient tandem applications," *Journal of Materials Chemistry C,* vol. 5, pp. 134-139, 2017.

[111] T. Duong, D. Grant, S. Rahman, A. Blakers, K. J. Weber, K. R. Catchpole*, et al.*, "Filterless Spectral Splitting Perovskite–Silicon Tandem System With >23% Calculated Efficiency," *IEEE Journal of Photovoltaics,* vol. 6, pp. 1432-1439, 2016.

[112] M. A. Green, Y. Hishikawa, W. Warta, E. D. Dunlop, D. H. Levi, J. Hohl-Ebinger*, et al.*, "Solar cell efficiency tables (version 50)," *Progress in Photovoltaics: Research and Applications,* vol. 25, pp. 668-676, 2017.

[113] M. A. Green, K. Emery, Y. Hishikawa, W. Warta, and E. D. Dunlop, "Solar cell efficiency tables (version 44)," *Progress in Photovoltaics,* vol. 22, pp. 701-710, 2014.

[114] M. A. Green, K. Emery, Y. Hishikawa, W. Warta, and E. D. Dunlop, "Solar cell efficiency tables (version 42)," *Progress in Photovoltaics,* vol. 21, pp. 827-837, 2013.

[115] M. A. Green, K. Emery, Y. Hishikawa, W. Warta, and E. D. Dunlop, "Solar cell efficiency tables (version 40)," *Progress in Photovoltaics,* vol. 20, pp. 606-614, 2012.

[116] SunShot 2030 White Paper, 2016.

[117] F. Ye, W. Deng, W. Guo, R. Liu, D. Chen, Y. Chen*, et al.*, "22.13% Efficient industrial p-type mono PERC solar cell," in *2016 IEEE 43rd Photovoltaic Specialists Conference (PVSC)*, pp. 3360-3365, 2016

[118] K. A. Bush, A. F. Palmstrom, Z. J. Yu, M. Boccard, R. Cheacharoen, J. P. Mailoa*, et al.*, "23.6%-efficient monolithic perovskite/silicon tandem solar cells with improved stability," *Nature Energy,* vol. 2, p. 17009, 2017.

[119] J. Werner, B. Niesen, and C. Ballif, "Perovskite/Silicon Tandem Solar Cells: Marriage of Convenience or True Love Story? – An Overview," *Advanced Materials Interfaces,* pp. 1700731, 2017.

[120] I. M. Peters, S. Sofia, J. Mailoa, and T. Buonassisi, "Techno-economic analysis of tandem photovoltaic systems," *RSC Advances,* vol. 6, pp. 66911-66923, 2016.

[121] D. C. Bobela, L. Gedvilas, M. Woodhouse, K. A. W. Horowitz, and P. A. Basore, "Economic competitiveness of III–V on silicon tandem one-sun

photovoltaic solar modules in favorable future scenarios," *Progress in Photovoltaics: Research and Applications*, 2016.

[122] E. Wesoff. (2014). *The End of Oerlikon's Amorphous Silicon Solar Saga*.

[123] E. Wesoff. (2014). *CPV Hopeful Soitec Latest Victim of the Economics of Silicon Photovoltaics*.

[124] M. Stefancich, M. Chiesa, and H. Apostoleris, "Do we still care about CPV?," in *SPIE Optical Engineering + Applications*, 2017.

[125] Photovoltaic Manufacturer Capacity, Shipments, Price & Revenues, SPV Market Research, 2017.

[126] A. Louwen, W. van Sark, R. Schropp, and A. Faaij, "A cost roadmap for silicon heterojunction solar cells," *Solar Energy Materials and Solar Cells,* vol. 147, pp. 295-314, 2016.

[127] SolarServer. https://www.solarserver.com/service/pvx-spot-market-price index-solar-pvmodules.html, 2017.

[128] Solar Market Insight Report 2017 Q2, Solar Energy Industries Association (SEIA)/GTM Research, 2017.

[129] D. C. Montgomery, E. A. Peck, and G. G. Vining, *Introduction to Linear Regression Analysis*, Fifth ed.: John Wiley & Sons, Inc.

[130] H. Schulte-Huxel, E. L. Warren, M. Schnabel, P. Stradins, D. Friedman, and A. C. Tamboli, "III-V/Si tandem cell to module interconnection-comparison between different operation modes," in *2017 IEEE 44th Photovoltaic Specialist Conference (PVSC)* 2017.

[131] H. Liu, A. G. Aberle, T. Buonassisi, and I. M. Peters, "On the methodology of energy yield assessment for one-Sun tandem solar cells," *Solar Energy,* vol. 135, pp. 598-604, 2016.

[132] J. P. Mailoa, M. Lee, I. M. Peters, T. Buonassisi, A. Panchula, and D. N. Weiss, "Energy-yield prediction for II-VI-based thin-film tandem solar cells," *Energy & Environmental Science,* vol. 9, pp. 2644-2653, 2016.

[133] H. Shen, T. Duong, J. Peng, D. Jacobs, N. Wu, J. Gong*, et al.*, "Mechanically-stacked Perovskite/CIGS Tandem Solar Cells with Efficiency of 23.9% and Reduced Oxygen Sensitivity," *Energy & Environmental Science,* 2018.

[134] G. E. Eperon, T. Leijtens, K. A. Bush, R. Prasanna, T. Green, J. T.-W. Wang*, et al.*, "Perovskite-perovskite tandem photovoltaics with optimized band gaps," *Science,* vol. 354, pp. 861-865, 2016.

[135] W. S. Yang, J. H. Noh, N. J. Jeon, Y. C. Kim, S. Ryu, J. Seo*, et al.*, "High-performance photovoltaic perovskite layers fabricated through intramolecular exchange," *Science,* vol. 348, pp. 1234-1237, 2015.

[136] H. Zhou, Q. Chen, G. Li, S. Luo, T.-b. Song, H.-S. Duan*, et al.*, "Interface engineering of highly efficient perovskite solar cells," *Science,* vol. 345, pp. 542-546, 2014.

[137] W. Chen, Y. Wu, Y. Yue, J. Liu, W. Zhang, X. Yang*, et al.*, "Efficient and stable large-area perovskite solar cells with inorganic charge extraction layers," *Science,* vol. 350, pp. 944-948, 2015.

[138] A. Kojima, K. Teshima, Y. Shirai, and T. Miyasaka, "Organometal halide perovskites as visible-light sensitizers for photovoltaic cells," *Journal of the American Chemical Society,* vol. 131, pp. 6050-6051, 2009.

[139] J. Burschka, N. Pellet, S.-J. Moon, R. Humphry-Baker, P. Gao, M. K. Nazeeruddin*, et al.*, "Sequential deposition as a route to high-performance perovskite-sensitized solar cells," *Nature,* vol. 499, pp. 316-319, 2013.

[140] M. Liu, M. B. Johnston, and H. J. Snaith, "Efficient planar heterojunction perovskite solar cells by vapour deposition," *Nature,* vol. 501, pp. 395-398, 2013.

[141] Q. Dong, Y. Fang, Y. Shao, P. Mulligan, J. Qiu, L. Cao*, et al.*, "Electron-hole diffusion lengths> 175 μm in solution-grown CH3NH3PbI3 single crystals," *Science,* vol. 347, pp. 967-970, 2015.

[142] J. H. Noh, S. H. Im, J. H. Heo, T. N. Mandal, and S. I. Seok, "Chemical management for colorful, efficient, and stable inorganic–organic hybrid nanostructured solar cells," *Nano letters,* vol. 13, pp. 1764-1769, 2013.

[143] E. Edri, S. Kirmayer, D. Cahen, and G. Hodes, "High open-circuit voltage solar cells based on organic–inorganic lead bromide perovskite," *The journal of physical chemistry letters,* vol. 4, pp. 897-902, 2013.

[144] N. K. Noel, S. D. Stranks, A. Abate, C. Wehrenfennig, S. Guarnera, A.-A. Haghighirad*, et al.*, "Lead-free organic–inorganic tin halide perovskites for photovoltaic applications," *Energy & Environmental Science,* vol. 7, pp. 3061-3068, 2014.

[145] Y. Ogomi, A. Morita, S. Tsukamoto, T. Saitho, N. Fujikawa, Q. Shen*, et al.*, "CH3NH3Sn x Pb (1–x) I3 Perovskite solar cells covering up to 1060 nm," *The journal of physical chemistry letters,* vol. 5, pp. 1004-1011, 2014.

[146] F. Hao, C. C. Stoumpos, D. H. Cao, R. P. Chang, and M. G. Kanatzidis, "Lead-free solid-state organic-inorganic halide perovskite solar cells," *Nature Photonics,* vol. 8, pp. 489-494, 2014.

[147] S. Pang, H. Hu, J. Zhang, S. Lv, Y. Yu, F. Wei*, et al.*, "NH2CH□ NH2PbI3: An alternative organolead iodide perovskite sensitizer for mesoscopic solar cells," *Chemistry of Materials,* vol. 26, pp. 1485-1491, 2014.

[148] A. Mei, X. Li, L. Liu, Z. Ku, T. Liu, Y. Rong, *et al.*, "A hole-conductor–free, fully printable mesoscopic perovskite solar cell with high stability," *Science,* vol. 345, pp. 295-298, 2014.

[149] J. W. Lee, D. J. Seol, A. N. Cho, and N. G. Park, "High-Efficiency Perovskite Solar Cells Based on the Black Polymorph of HC (NH2) 2PbI3," *Advanced Materials,* vol. 26, pp. 4991-4998, 2014.

[150] G. E. Eperon, S. D. Stranks, C. Menelaou, M. B. Johnston, L. M. Herz, and H. J. Snaith, "Formamidinium lead trihalide: a broadly tunable perovskite for efficient planar heterojunction solar cells," *Energy & Environmental Science,* vol. 7, pp. 982-988, 2014.

[151] F. C. Hanusch, E. Wiesenmayer, E. Mankel, A. Binek, P. Angloher, C. Fraunhofer, *et al.*, "Efficient planar heterojunction perovskite solar cells based on formamidinium lead bromide," *The journal of physical chemistry letters,* vol. 5, pp. 2791-2795, 2014.

[152] Q. Chen, H. Zhou, Z. Hong, S. Luo, H.-S. Duan, H.-H. Wang, *et al.*, "Planar heterojunction perovskite solar cells via vapor-assisted solution process," *Journal of the American Chemical Society,* vol. 136, pp. 622-625, 2013.

[153] M. Xiao, F. Huang, W. Huang, Y. Dkhissi, Y. Zhu, J. Etheridge, *et al.*, "A fast deposition-crystallization procedure for highly efficient lead iodide perovskite thin-film solar cells," *Angewandte Chemie,* vol. 126, pp. 10056-10061, 2014.

[154] J.-H. Im, I.-H. Jang, N. Pellet, M. Grätzel, and N.-G. Park, "Growth of CH3NH3PbI3 cuboids with controlled size for high-efficiency perovskite solar cells," *Nature nanotechnology,* vol. 9, pp. 927-932, 2014.

[155] N. J. Jeon, J. H. Noh, Y. C. Kim, W. S. Yang, S. Ryu, and S. I. Seok, "Solvent engineering for high-performance inorganic–organic hybrid perovskite solar cells," *Nature materials,* vol. 13, pp. 897-903, 2014.

[156] Z. Xiao, Q. Dong, C. Bi, Y. Shao, Y. Yuan, and J. Huang, "Solvent annealing of perovskite-induced crystal growth for photovoltaic-device efficiency enhancement," *Advanced Materials,* vol. 26, pp. 6503-6509, 2014.

[157] Z. Xiao, C. Bi, Y. Shao, Q. Dong, Q. Wang, Y. Yuan, *et al.*, "Efficient, high yield perovskite photovoltaic devices grown by interdiffusion of solution-processed precursor stacking layers," *Energy & Environmental Science,* vol. 7, pp. 2619-2623, 2014.

[158] L. Kranz, A. Abate, T. Feurer, F. Fu, E. Avancini, J. Löckinger, *et al.*, "High-efficiency polycrystalline thin film tandem solar cells," *The journal of physical chemistry letters,* vol. 6, pp. 2676-2681, 2015.

[159] F. Fu, T. Feurer, T. Jäger, E. Avancini, B. Bissig, S. Yoon, *et al.*, "Low-temperature-processed efficient semi-transparent planar perovskite solar cells for bifacial and tandem applications," *Nature communications,* vol. 6, 2015.

[160] F. Guo, H. Azimi, Y. Hou, T. Przybilla, M. Hu, C. Bronnbauer*, et al.*, "High-performance semitransparent perovskite solar cells with solution-processed silver nanowires as top electrodes," *Nanoscale,* vol. 7, pp. 1642-1649, 2015.

[161] Y. Yang, Q. Chen, Y.-T. Hsieh, T.-B. Song, N. D. Marco, H. Zhou*, et al.*, "Multilayer transparent top electrode for solution processed perovskite/Cu (In, Ga)(Se, S) 2 four terminal tandem solar cells," *ACS nano,* vol. 9, pp. 7714-7721, 2015.

[162] C. Roldán-Carmona, O. Malinkiewicz, R. Betancur, G. Longo, C. Momblona, F. Jaramillo*, et al.*, "High efficiency single-junction semitransparent perovskite solar cells," *Energy & Environmental Science,* vol. 7, pp. 2968-2973, 2014.

[163] G. E. Eperon, V. M. Burlakov, A. Goriely, and H. J. Snaith, "Neutral color semitransparent microstructured perovskite solar cells," *ACS nano,* vol. 8, pp. 591-598, 2013.

[164] Q. Wang, Y. Shao, Q. Dong, Z. Xiao, Y. Yuan, and J. Huang, "Large fill-factor bilayer iodine perovskite solar cells fabricated by a low-temperature solution-process," *Energy & Environmental Science,* vol. 7, pp. 2359-2365, 2014.

[165] Y. Deng, Q. Dong, C. Bi, Y. Yuan, and J. Huang, "Air-stable, efficient mixed-cation perovskite solar cells with Cu electrode by scalable fabrication of active layer," *Advanced Energy Materials,* vol. 6, 2016.

[166] C. Bi, Q. Wang, Y. Shao, Y. Yuan, Z. Xiao, and J. Huang, "Non-wetting surface-driven high-aspect-ratio crystalline grain growth for efficient hybrid perovskite solar cells," *Nature communications,* vol. 6, 2015.

[167] Y. Zhao and K. Zhu, "Efficient planar perovskite solar cells based on 1.8 eV band gap CH3NH3PbI2Br nanosheets via thermal decomposition," *Journal of the American Chemical Society,* vol. 136, pp. 12241-12244, 2014.

[168] L. K. Ono, S. Wang, Y. Kato, S. R. Raga, and Y. Qi, "Fabrication of semi-transparent perovskite films with centimeter-scale superior uniformity by the hybrid deposition method," *Energy & Environmental Science,* vol. 7, pp. 3989-3993, 2014.

[169] J. H. Heo, S. H. Im, J. H. Noh, T. N. Mandal, C.-S. Lim, J. A. Chang*, et al.*, "Efficient inorganic-organic hybrid heterojunction solar cells containing perovskite compound and polymeric hole conductors," *Nature photonics,* vol. 7, pp. 486-491, 2013.

[170] L. Vitos, A. Ruban, H. L. Skriver, and J. Kollar, "The surface energy of metals," *Surface Science,* vol. 411, pp. 186-202, 1998.

[171] Y. Zhou, M. Yang, W. Wu, A. L. Vasiliev, K. Zhu, and N. P. Padture, "Room-temperature crystallization of hybrid-perovskite thin films via solvent–solvent extraction for high-performance solar cells," *Journal of Materials Chemistry A,* vol. 3, pp. 8178-8184, 2015.

[172] N. Ahn, D.-Y. Son, I.-H. Jang, S. M. Kang, M. Choi, and N.-G. Park, "Highly reproducible perovskite solar cells with average efficiency of 18.3% and best efficiency of 19.7% fabricated via Lewis base adduct of lead (II) iodide," *Journal of the American Chemical Society,* vol. 137, pp. 8696-8699, 2015.

[173] Y. Shao, Z. Xiao, C. Bi, Y. Yuan, and J. Huang, "Origin and elimination of photocurrent hysteresis by fullerene passivation in CH3NH3PbI3 planar heterojunction solar cells," *Nature communications,* vol. 5, p. 5784, 2014.

[174] Y. Shao, Y. Fang, T. Li, Q. Wang, Q. Dong, Y. Deng*, et al.*, "Grain boundary dominated ion migration in polycrystalline organic–inorganic halide perovskite films," *Energy & Environmental Science,* vol. 9, pp. 1752-1759, 2016.

[175] J. M. Ball, S. D. Stranks, M. T. Hörantner, S. Hüttner, W. Zhang, E. J. Crossland*, et al.*, "Optical properties and limiting photocurrent of thin-film perovskite solar cells," *Energy & Environmental Science,* vol. 8, pp. 602-609, 2015.

[176] S. De Wolf, A. Descoeudres, Z. C. Holman, and C. Ballif, "High-efficiency silicon heterojunction solar cells: A review," *Green,* vol. 2, pp. 7-24, 2012.

[177] M. Morales-Masis, S. M. De Nicolas, J. Holovsky, S. De Wolf, and C. Ballif, "Low-temperature high-mobility amorphous IZO for silicon heterojunction solar cells," *Photovoltaics, IEEE Journal of,* vol. 5, pp. 1340-1347, 2015.

[178] Z. C. Holman, S. De Wolf, and C. Ballif, "Improving metal reflectors by suppressing surface plasmon polaritons: a priori calculation of the internal reflectance of a solar cell," *Light: Science & Applications,* vol. 2, p. e106, 2013.

[179] Z. C. Holman, A. Descoeudres, S. De Wolf, and C. Ballif, "Record Infrared Internal Quantum Efficiency in Silicon Heterojunction Solar Cells With Dielectric/Metal Rear Reflectors," *IEEE Journal of Photovoltaics,* vol. 3, pp. 1243-1249, 2013.

[180] Z. C. Holman, M. Filipic, A. Descoeudres, S. De Wolf, F. Smole, M. Topic*, et al.*, "Infrared light management in high-efficiency silicon heterojunction and rear-passivated solar cells," *Journal of Applied Physics,* vol. 113, 2013.

[181] S. De Wolf, J. Holovsky, S.-J. Moon, P. Löper, B. Niesen, M. Ledinsky*, et al.*, "Organometallic Halide Perovskites: Sharp Optical Absorption Edge and Its Relation to Photovoltaic Performance," *The Journal of Physical Chemistry Letters,* vol. 5, pp. 1035-1039, 2014.

[182] S. D. Stranks, G. E. Eperon, G. Grancini, C. Menelaou, M. J. Alcocer, T. Leijtens*, et al.*, "Electron-hole diffusion lengths exceeding 1 micrometer in an organometal trihalide perovskite absorber," *Science,* vol. 342, pp. 341-344, 2013.

[183] R. E. Brandt, V. Stevanović, D. S. Ginley, and T. Buonassisi, "Identifying defect-tolerant semiconductors with high minority-carrier lifetimes: beyond

hybrid lead halide perovskites," *Mrs Communications,* vol. 5, pp. 265-275, 2015.

[184] B. Chen, Y. Bai, Z. Yu, T. Li, X. Zheng, Q. Dong*, et al.*, "Efficient Semitransparent Perovskite Solar Cells for 23.0%-Efficiency Perovskite/Silicon Four-Terminal Tandem Cells," *Advanced Energy Materials,* vol. 6, pp. 1601128, 2016.

[185] Z. Yang, A. Rajagopal, C. C. Chueh, S. B. Jo, B. Liu, T. Zhao*, et al.*, "Stable Low-Bandgap Pb–Sn Binary Perovskites for Tandem Solar Cells," *Advanced Materials,* vol. 28, pp. 8990-8997, 2016.

[186] N. N. Lal, T. P. White, and K. R. Catchpole, "Optics and light trapping for tandem solar cells on silicon," *IEEE Journal of Photovoltaics,* vol. 4, pp. 1380-1386, 2014.

[187] C. D. Bailie and M. D. McGehee, "High-efficiency tandem perovskite solar cells," *Mrs Bulletin,* vol. 40, pp. 681-686, 2015.

[188] L. Liao, L. Hung, W. Chan, X. Ding, T. Sham, I. Bello*, et al.*, "Ion-beam-induced surface damages on tris-(8-hydroxyquinoline) aluminum," *Applied physics letters,* vol. 75, pp. 1619-1621, 1999.

[189] T. Leijtens, G. E. Eperon, N. K. Noel, S. N. Habisreutinger, A. Petrozza, and H. J. Snaith, "Stability of metal halide perovskite solar cells," *Advanced Energy Materials,* vol. 5, 2015.

[190] P. Liu, X. Liu, L. Lyu, H. Xie, H. Zhang, D. Niu*, et al.*, "Interfacial electronic structure at the CH3NH3PbI3/MoOx interface," *Applied Physics Letters,* vol. 106, p. 193903, 2015.

[191] J. W. Lee, D. H. Kim, H. S. Kim, S. W. Seo, S. M. Cho, and N. G. Park, "Formamidinium and cesium hybridization for photo-and moisture-stable perovskite solar cell," *Advanced Energy Materials,* vol. 5, 2015.

[192] C. Yi, J. Luo, S. Meloni, A. Boziki, N. Ashari-Astani, C. Grätzel*, et al.*, "Entropic stabilization of mixed A-cation ABX 3 metal halide perovskites for high performance perovskite solar cells," *Energy & Environmental Science,* vol. 9, pp. 656-662, 2016.

[193] X. Xia, W. Wu, H. Li, B. Zheng, Y. Xue, J. Xu*, et al.*, "Spray reaction prepared FA 1− x Cs x PbI 3 solid solution as a light harvester for perovskite solar cells with improved humidity stability," *RSC Advances,* vol. 6, pp. 14792-14798, 2016.

[194] M. Saliba, T. Matsui, J.-Y. Seo, K. Domanski, J.-P. Correa-Baena, M. K. Nazeeruddin*, et al.*, "Cesium-containing triple cation perovskite solar cells: improved stability, reproducibility and high efficiency," *Energy & environmental science,* vol. 9, pp. 1989-1997, 2016.

[195] J. R. Bakke, K. L. Pickrahn, T. P. Brennan, and S. F. Bent, "Nanoengineering and interfacial engineering of photovoltaics by atomic layer deposition," *Nanoscale,* vol. 3, pp. 3482-3508, 2011.

[196] A. F. Palmstrom, P. K. Santra, and S. F. Bent, "Atomic layer deposition in nanostructured photovoltaics: tuning optical, electronic and surface properties," *Nanoscale,* vol. 7, pp. 12266-12283, 2015.

[197] Z. Zhu, Y. Bai, X. Liu, C. C. Chueh, S. Yang, and A. K. Y. Jen, "Enhanced Efficiency and Stability of Inverted Perovskite Solar Cells Using Highly Crystalline SnO2 Nanocrystals as the Robust Electron-Transporting Layer," *Advanced Materials,* vol. 28, pp. 6478-6484, 2016.

[198] J. You, L. Meng, T.-B. Song, T.-F. Guo, Y. M. Yang, W.-H. Chang*, et al.*, "Improved air stability of perovskite solar cells via solution-processed metal oxide transport layers," *Nature nanotechnology,* vol. 11, pp. 75-81, 2016.

[199] J. H. Kim, P. W. Liang, S. T. Williams, N. Cho, C. C. Chueh, M. S. Glaz*, et al.*, "High-Performance and Environmentally Stable Planar Heterojunction Perovskite Solar Cells Based on a Solution-Processed Copper-Doped Nickel Oxide Hole-Transporting Layer," *Advanced Materials,* vol. 27, pp. 695-701, 2015.

[200] M. N. Mullings, C. Hägglund, and S. F. Bent, "Tin oxide atomic layer deposition from tetrakis (dimethylamino) tin and water," *Journal of Vacuum Science & Technology A: Vacuum, Surfaces, and Films,* vol. 31, p. 061503, 2013.

[201] E. Guziewicz, M. Godlewski, L. Wachnicki, T. Krajewski, G. Luka, S. Gieraltowska*, et al.*, "ALD grown zinc oxide with controllable electrical properties," *Semiconductor Science and Technology,* vol. 27, p. 074011, 2012.

[202] M. Despeisse, G. Bugnon, A. Feltrin, M. Stueckelberger, P. Cuony, F. Meillaud*, et al.*, "Resistive interlayer for improved performance of thin film silicon solar cells on highly textured substrate," *Applied Physics Letters,* vol. 96, p. 073507, 2010.

[203] B. W. Larson, J. B. Whitaker, A. A. Popov, N. Kopidakis, G. Rumbles, O. V. Boltalina*, et al.*, "Thermal [6, 6]→[6, 6] isomerization and decomposition of PCBM (phenyl-C61-butyric acid methyl ester)," *Chemistry of Materials,* vol. 26, pp. 2361-2367, 2014.

[204] M. N. Mullings, C. Hägglund, J. T. Tanskanen, Y. Yee, S. Geyer, and S. F. Bent, "Thin film characterization of zinc tin oxide deposited by thermal atomic layer deposition," *Thin Solid Films,* vol. 556, pp. 186-194, 2014.

[205] C. Hägglund, T. Grehl, J. T. Tanskanen, Y. S. Yee, M. N. Mullings, A. J. Mackus*, et al.*, "Growth, intermixing, and surface phase formation for zinc tin oxide nanolaminates produced by atomic layer deposition," *Journal of Vacuum*

Science & Technology A: Vacuum, Surfaces, and Films, vol. 34, p. 021516, 2016.

[206] Z. C. Holman, A. Descoeudres, L. Barraud, F. Z. Fernandez, J. P. Seif, S. De Wolf*, et al.*, "Current losses at the front of silicon heterojunction solar cells," *IEEE Journal of Photovoltaics,* vol. 2, pp. 7-15, 2012.

[207] M. Boccard, P. Firth, Z. J. Yu, K. C. Fisher, M. Leilaeioun, S. Manzoor*, et al.*, "Low-refractive-index nanoparticle interlayers to reduce parasitic absorption in metallic rear reflectors of solar cells," *physica status solidi (a),* p. e201700179, 2017.

[208] S. Qudsia, F. Qazi, M. A. Javed, M. Boccard, Z. J. Yu, P. Firth*, et al.*, "Nanoparticle/metal rear reflectors for low- and high-temperature silicon solar cells," in *2017 IEEE 44th Photovoltaic Specialist Conference (PVSC)*, 2017.

[209] Z. C. Holman and U. R. Kortshagen, "A flexible method for depositing dense nanocrystal thin films: impaction of germanium nanocrystals," *Nanotechnology,* vol. 21, p. 335302, 2010.

[210] I. S. Kim and A. B. Martinson, "Stabilizing hybrid perovskites against moisture and temperature via non-hydrolytic atomic layer deposited overlayers," *Journal of Materials Chemistry A,* vol. 3, pp. 20092-20096, 2015.

[211] D. M. Powell, M. T. Winkler, H. J. Choi, C. B. Simmons, D. B. Needleman, and T. Buonassisi, "Crystalline silicon photovoltaics: a cost analysis framework for determining technology pathways to reach baseload electricity costs," *Energy & Environmental Science,* vol. 5, pp. 5874-5883, 2012.

[212] A. Goodrich, P. Hacke, Q. Wang, B. Sopori, R. Margolis, T. L. James*, et al.*, "A wafer-based monocrystalline silicon photovoltaics road map: Utilizing known technology improvement opportunities for further reductions in manufacturing costs," *Solar Energy Materials and Solar Cells,* vol. 114, pp. 110-135, 2013.

[213] M. A. Green, "Limiting photovoltaic efficiency under new ASTM International G173-based reference spectra," *Progress in Photovoltaics,* vol. 20, pp. 954-959, 2012.

[214] M. A. Green, "Third generation photovoltaics: solar cells for 2020 and beyond," *Physica E-Low-Dimensional Systems & Nanostructures,* vol. 14, pp. 65-70, 2002.

[215] P. Würfel, *Physics of Solar Cells: From Basic Principles to Advanced Concepts*: WILEY-VCH, 2009.

[216] R. R. King, D. C. Law, K. M. Edmondson, C. M. Fetzer, G. S. Kinsey, H. Yoon*, et al.*, "40% efficient metamorphic GaInP/GaInAs/Ge multijunction solar cells," *Applied Physics Letters,* vol. 90, 2007.

[217] S. Corporation. (2012). *Sharp Develops Concentrator Solar Cell with World's Highest Conversion Efficiency of 43.5%.* Available: http://sharp-world.com/corporate/news/120531.html

[218] W. Marion and S. Wilcox, "Solar Radiation Data Manual for Flat-Plate and Concentrating Collectors," 1994.

[219] A. G. Imenes and D. R. Mills, "Spectral beam splitting technology for increased conversion efficiency in solar concentrating systems: a review," *Solar Energy Materials and Solar Cells,* vol. 84, pp. 19-69, 2004.

[220] B. Mitchell, G. Peharz, G. Siefer, M. Peters, T. Gandy, J. C. Goldschmidt*, et al.*, "Four-junction spectral beam-splitting photovoltaic receiver with high optical efficiency," *Progress in Photovoltaics,* vol. 19, pp. 61-72, 2011.

[221] N. Mohammad, P. Wang, D. J. Friedman, and R. Menon, "Enhancing photovoltaic output power by 3-band spectrum-splitting and concentration using a diffractive micro-optic," *Optics Express,* vol. 22, pp. A1519-A1525, 2014.

[222] M. G. Debije and P. P. C. Verbunt, "Thirty Years of Luminescent Solar Concentrator Research: Solar Energy for the Built Environment," *Advanced Energy Materials,* vol. 2, pp. 12-35, 2012.

[223] W. G. J. H. M. van Sark, Z. Krumer, C. De Mello Donega, and R. E. I. Schropp, "Luminescent Solar Concentrators: The route to 10% efficiency," in *Photovoltaic Specialist Conference (PVSC), IEEE 40th*, pp. 2276-2279, 2014,

[224] M. S. Kulkarni and H. F. Erk, "Acid-based etching of silicon wafers: Mass-transfer and kinetic effects," *Journal of the Electrochemical Society,* vol. 147, pp. 176-188, 2000.

[225] Z. J. Yu, B. M. Wheelwright, S. Manzoor, and Z. C. Holman, "Silicon wafers with optically specular surfaces formed by chemical polishing," *Journal of Materials Science: Materials in Electronics,* vol. 27, pp. 10270-10275, 2016.

[226] M. F. Weber, C. A. Stover, L. R. Gilbert, T. J. Nevitt, and A. J. Ouderkirk, "Giant birefringent optics in multilayer polymer mirrors," *Science,* vol. 287, pp. 2451-2456, 2000.

[227] M. A. Green, "The future of crystalline silicon solar cells," *Progress in Photovoltaics,* vol. 8, pp. 127-139, 2000.

[228] J. F. Geisz, M. A. Steiner, I. Garcia, S. R. Kurtz, and D. J. Friedman, "Enhanced external radiative efficiency for 20.8% efficient single-junction GaInP solar cells," *Applied Physics Letters,* vol. 103, 2013.

[229] J. P. Connolly, D. Mencaraglia, C. Renard, and D. Bouchier, "Designing III-V multijunction solar cells on silicon," *Progress in Photovoltaics,* vol. 22, pp. 810-820, 2014.

[230] X. Mathew, J. Drayton, V. Parikh, N. R. Mathews, X. G. Liu, and A. D. Compaan, "Development of a semitransparent CdMgTe/CdS top cell for applications in tandem solar cells," *Semiconductor Science and Technology,* vol. 24, 2009.

[231] T. J. Coutts, J. S. Ward, D. L. Young, K. A. Emery, T. A. Gessert, and R. Noufi, "Critical issues in the design of polycrystalline, thin-film tandem solar cells," *Progress in Photovoltaics,* vol. 11, pp. 359-375, 2003.

[232] M. A. Green, K. Emery, Y. Hishikawa, W. Warta, and E. D. Dunlop, "Solar cell efficiency tables (Version 45)," *Progress in Photovoltaics,* vol. 23, pp. 1-9, 2015.

[233] X. T. Wang and A. Barnett, "The Effect of Spectrum Variation on the Energy Production of Triple-Junction Solar Cells," *IEEE Journal of Photovoltaics,* vol. 2, pp. 417-423, 2012.

[234] A. Nakajima, M. Ichikawa, T. Sawada, M. Yoshimi, and K. Yamamoto, "Spectral characteristics of thin-film stacked-tandem solar modules," *Japanese Journal of Applied Physics Part 1-Regular Papers Short Notes & Review Papers,* vol. 43, pp. 7296-7302, 2004.

[235] T. M. Pavlovic, I. S. Radonjic, D. D. Milosavljevic, and L. S. Pantic, "A review of concentrating solar power plants in the world and their potential use in Serbia," *Renewable & Sustainable Energy Reviews,* vol. 16, pp. 3891-3902, 2012.

[236] ARPA-E, FOA: Full-spectrum Optimized Conversion and Utilization of Sunlight (FOCUS), 2013.

[237] D. Barlev, R. Vidu, and P. Stroeve, "Innovation in concentrated solar power," *Solar Energy Materials and Solar Cells,* vol. 95, pp. 2703-2725, 2011.

[238] J. Blanco, S. Malato, P. Fernandez-Ibanez, D. Alarcon, W. Gernjak, and M. L. Maldonado, "Review of feasible solar energy applications to water processes," *Renewable & Sustainable Energy Reviews,* vol. 13, pp. 1437-1445, 2009.

[239] Z. J. Yu, J. V. Carpenter III, and Z. C. Holman, "The path to market for silicon-based tandem photovoltaic modules," submitted.

[240] NREL. Spectral Solar Radiation Data Base [Online]. Available: http://rredc.nrel.gov/solar/old_data/spectral/

[241] Z. J. Yu, K. C. Fisher, B. M. Wheelwright, R. P. Angel, and Z. C. Holman, "PVMirror: A New Concept for Tandem Solar Cells and Hybrid Solar Converters," *Photovoltaics, IEEE Journal of,* vol. 5, pp. 1791-1799, 2015.

[242] M. Rienacker, M. Schnabel, E. Warren, A. Merkle, H. Schulte-Huxel, T. R. Klein*, et al.*, "Mechanically Stacked Dual-Junction and Triple-Junction III-V/Si-IBC Cells with Efficiencies of 31.5 % and 35.4 %," in *33rd European Photovoltaic Solar Energy Conference and Exhibition*, Amsterdam, 2017.

[243] M. J. Keevers, C. F. J. Lau, I. Thomas, J. Lasich, R. King, and M. Green, "High efficiency spectrum splitting prototype submodule using commercial CPV cells," in *6th World Conf. on PV Energy Conversion, Kyoto*, 2014.

[244] M. A. Green, M. J. Keevers, I. Thomas, J. B. Lasich, K. Emery, and R. R. King, "40% efficient sunlight to electricity conversion," *Progress in Photovoltaics: Research and Applications,* vol. 23, pp. 685-691, 2015.

[245] J. S. Price, A. J. Grede, B. Wang, M. V. Lipski, B. Fisher, K.-T. Lee*, et al.*, "High-concentration planar microtracking photovoltaic system exceeding 30% efficiency," *Nature Energy,* vol. 2, p. 17113, 2017.

[246] Z. J. Yu, Z. C. Holman, and M. O'Neill, "Full-Spectrum, Angle-Resolved Reflectance and Transmittance of Optical Coatings Using the LAMBDA 950/1050 UV/VIS/NIR Spectrophotometer with the ARTA Accessory," 2015.

[247] P. van Nijnatten, J. de Wolf, and I. Schoofs, "Spectrophotometer accessories for thin film characterisation," in *7th ICCG (International Conference on Coatings on Glass & Plastics), Breda, Netherlands*, 2008.

[248] Z. J. Yu, K. C. Fisher, and Z. C. Holman, "Modeling of GaAs/Silicon PVMirror tandem system: A case study," in *Photovoltaic Specialists Conference (PVSC), IEEE 43rd*, pp. 0200-0203, 2016.

[249] Z. J. Yu, K. C. Fisher, and Z. C. Holman, "Evaluation of spectrum-splitting dichroic mirrors for PVMirror tandem solar cells," in *Photovoltaic Specialist Conference (PVSC), IEEE 42nd*, pp. 1-4., 2015

[250] NREL, Observed Atmospheric and Solar Information System (OASIS). Available: http://dx.doi.org/10.5439/1052226

APPENDIX A

SUPPLEMENTARY INFORMATION OF CHAPTER 3

Derivation of expressions for iso-cost conditions:

Tandem system cost equals bottom-cell system cost

$$C_{system,tandem} = C_{system,bottom} \quad (S1)$$

From equation (3.1):

$$\frac{C_{tandem}}{\eta_{tandem} \cdot 1000} + \frac{BOS_A}{\eta_{tandem} \cdot 1000} + BOS_P = \frac{C_{bottom}}{\eta_{bottom} \cdot 1000} + \frac{BOS_A}{\eta_{bottom} \cdot 1000} + BOS_P \quad (S2)$$

Subtracting BOS_P from both sides results:

$$\frac{C_{top} + C_{bottom} - C_{overlap}}{\eta_{tandem} \cdot 1000} + \frac{BOS_A}{\eta_{tandem} \cdot 1000} = \frac{C_{bottom}}{\eta_{bottom} \cdot 1000} + \frac{BOS_A}{\eta_{bottom} \cdot 1000} \quad (S3)$$

Setting $C_{overlap} = 0$ results:

$$\frac{C_{top}}{\eta_{tandem} \cdot 1000} + \frac{C_{bottom}}{\eta_{tandem} \cdot 1000} + \frac{BOS_A}{\eta_{tandem} \cdot 1000} = \frac{C_{bottom}}{\eta_{bottom} \cdot 1000} + \frac{BOS_A}{\eta_{bottom} \cdot 1000} \quad (S4)$$

Simplification:

$$\frac{C_{top}}{\eta_{tandem}} = \frac{C_{bottom}}{\eta_{bottom}} - \frac{C_{bottom}}{\eta_{tandem}} + \frac{BOS_A}{\eta_{bottom}} - \frac{BOS_A}{\eta_{tandem}} \quad (S5)$$

$$\frac{C_{top}}{BOS_A} \cdot \eta_{bottom} = \frac{C_{bottom}}{BOS_A} \cdot \eta_{tandem} - \frac{C_{bottom}}{BOS_A} \cdot \eta_{bottom} + \eta_{tandem} - \eta_{bottom} \quad (S6)$$

$$\frac{C_{top}}{BOS_A} \cdot \eta_{bottom} = (\eta_{tandem} - \eta_{bottom}) \cdot (\frac{C_{bottom}}{BOS_A} + 1) \quad (S7)$$

Note that the ratios of module cost to BOS_A are independent variables. If $C_{overlap} \neq 0$, it is not possible to plot iso-cost contours on a tandem cost competitiveness plot assuming only [efficiencies], as the ratios of module cost to BOS_A do not appear as independent variables. This is what is meant in the text by "orthogonalizing" the problem.

Tandem system cost equals top-cell system cost

Due to symmetry, one can get:

$$\frac{C_{bottom}}{BOS_A} \cdot \eta_{top} = (\eta_{tandem} - \eta_{top}) \cdot (\frac{C_{top}}{BOS_A} + 1) \quad (S8)$$

Top-cell system cost equals bottom-cell system cost

$$C_{system,top} = C_{system,bottom} \quad (S9)$$

Again, from equation (3.1):

$$\frac{C_{top}}{\eta_{top} \cdot 1000} + \frac{BOS_A}{\eta_{top} \cdot 1000} + BOS_P = \frac{C_{bottom}}{\eta_{bottom} \cdot 1000} + \frac{BOS_A}{\eta_{bottom} \cdot 1000} + BOS_P \quad (S10)$$

Subtracting BOS_P from both sides results:

$$\frac{C_{top}}{\eta_{top} \cdot 1000} + \frac{BOS_A}{\eta_{top} \cdot 1000} = \frac{C_{bottom}}{\eta_{bottom} \cdot 1000} + \frac{BOS_A}{\eta_{bottom} \cdot 1000} \quad (S11)$$

Simplification:

$$\frac{C_{top}}{BOS_A} \cdot \eta_{bottom} + \eta_{bottom} = \frac{C_{bottom}}{BOS_A} \cdot \eta_{top} + \eta_{top} \quad (S12)$$

$$(\frac{C_{top}}{BOS_A} + 1) \cdot \eta_{bottom} = (\frac{C_{bottom}}{BOS_A} + 1) \cdot \eta_{top} \quad (S13)$$

Example of calculating tandem efficiency:

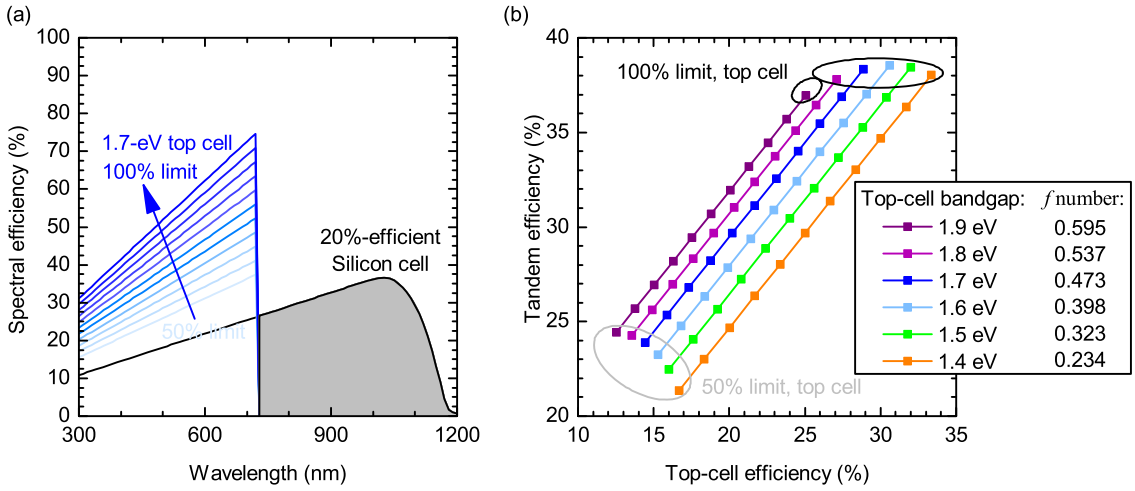

Figure A-1. (a) Spectral efficiency of a 20%-efficient silicon bottom cell and (derated) 1.7-eV top cell. With ideal spectral fidelities[1], scaling the top-cell efficiency doesn't change the contribution from the silicon cell, which is shown as the shaded area. And *f* number is the fraction of the shaded area to the total area under the silicon spectral efficiency curve. (b) Tandem efficiency as a function of top-cell efficiency with different bandgaps, also shown are corresponded *f* numbers.

Coupling efficiency in state-of-the-art devices.

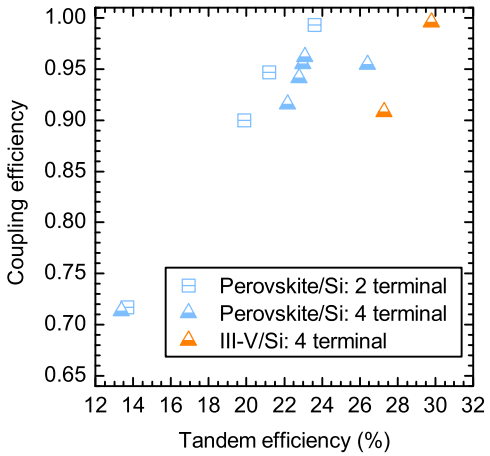

Figure A-2. Estimated coupling efficiency of silicon-based tandem reported in the references[2-12].

References:

1. Yu, Z., Leilaeioun, M. & Holman, Z. Selecting tandem partners for silicon solar cells. Nature Energy 1, 16137, doi:10.1038/nenergy.2016.137 (2016).
2. Bush, K. A. et al. 23.6%-efficient monolithic perovskite/silicon tandem solar cells with improved stability. Nature Energy 2, 17009, doi:10.1038/nenergy.2017.9 (2017).
3. Chen, B. et al. Efficient Semitransparent Perovskite Solar Cells for 23.0%-Efficiency Perovskite/Silicon Four-Terminal Tandem Cells. Adv Energy Mater 6, 1601128-n/a, doi:10.1002/aenm.201601128 (2016).
4. Werner, J. et al. Efficient Monolithic Perovskite/Silicon Tandem Solar Cell with Cell Area >1 cm2. The Journal of Physical Chemistry Letters 7, 161-166, doi:10.1021/acs.jpclett.5b02686 (2016).
5. Albrecht, S. et al. Monolithic perovskite/silicon-heterojunction tandem solar cells processed at low temperature. Energy & Environmental Science (2016).
6. Mailoa, J. P. et al. A 2-terminal perovskite/silicon multijunction solar cell enabled by a silicon tunnel junction. Appl Phys Lett 106, 121105, doi:doi:http://dx.doi.org/10.1063/1.4914179 (2015).
7. Werner, J. et al. Efficient Near-Infrared-Transparent Perovskite Solar Cells Enabling Direct Comparison of 4-Terminal and Monolithic Perovskite/Silicon Tandem Cells. ACS Energy Letters 1, 474-480, doi:10.1021/acsenergylett.6b00254 (2016).
8. Duong, T. et al. Rubidium Multication Perovskite with Optimized Bandgap for Perovskite-Silicon Tandem with over 26% Efficiency. Adv Energy Mater, n/a-n/a, doi:10.1002/aenm.201700228 (2017).
9. Löper, P. et al. Organic–inorganic halide perovskite/crystalline silicon four-terminal tandem solar cells. Physical Chemistry Chemical Physics 17, 1619-1629 (2015).
10. Essig, S. et al. Realization of GaInP/Si Dual-Junction Solar Cells With 29.8% 1-Sun Efficiency. IEEE J Photovolt 6, 1012-1019, doi:10.1109/JPHOTOV.2016.2549746 (2016).
11. Essig, S. et al. Progress Towards a 30% Efficient GaInP/Si Tandem Solar Cell. Energy Procedia 77, 464-469 (2015).
12. Li, Y. et al. Reflective perovskite solar cells for efficient tandem applications. Journal of Materials Chemistry C 5, 134-139, doi:10.1039/C6TC04510C (2017).

APPENDIX B

SUPPLEMENTARY INFORMATION OF CHAPTER 4

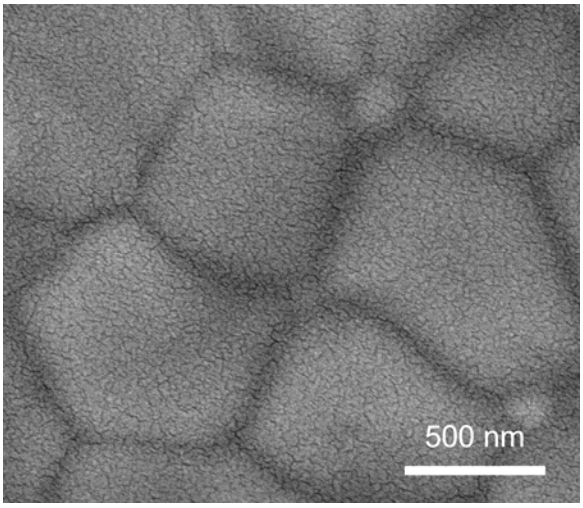

Figure B-1. Scanning electron microscope (SEM) image of 8-nm-thick Au electrode on PCBM/C_{60}/BCP coated $MAPbI_3$ film.

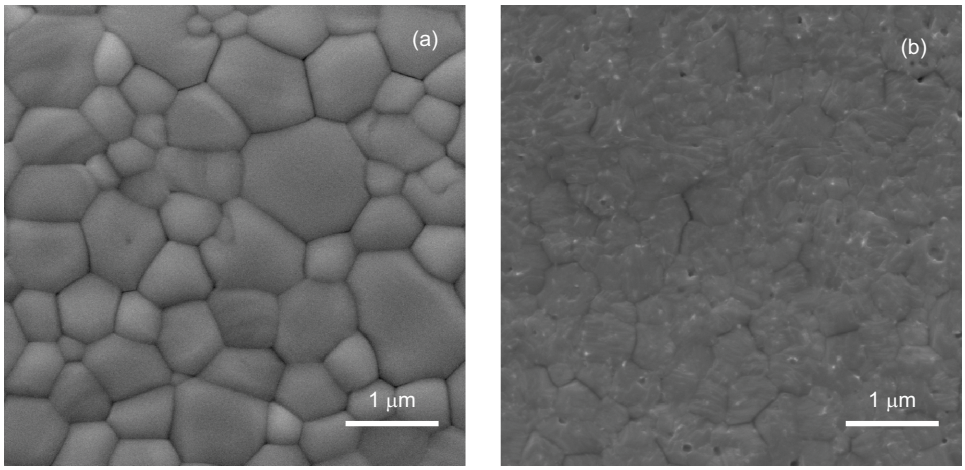

Figure B-2. SEM images of the $MAPbI_3$ perovskite films prepared by anti-solvent extraction approach with (a) mixed solvent of DMF and DMSO, and (b) DMF solvent.

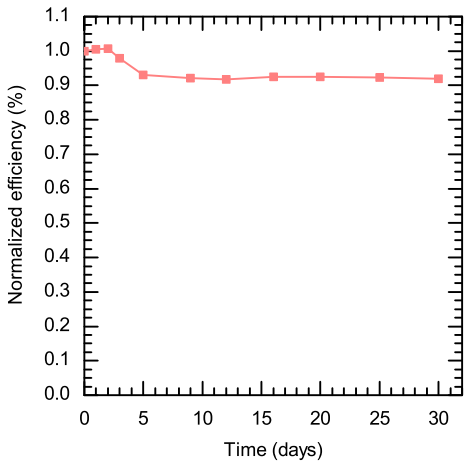

Figure B-3. Normalized efficiency of semitransparent perovskite solar cells, stored in a glovebox.

APPENDIX C

SUPPLEMENTARY INFORMATION OF CHAPTER 5

Perovskite solar cell fabrication:

Semi-transparent perovskite devices were fabricated on patterned, 10 ohms/square glass from Xin Yan Technology. After cleaning with Extran, acetone and isopropanol, the ITO glass was UV ozone cleaned for 15 min. A 1M solution of nickel nitrate hexahydrate (Sigma-Aldrich, puriss) and ethylenediamine (Sigma-Aldrich) in anhydrous ethylene glycol (Sigma-Aldrich) was spun on ITO-coated glass at 5000 r.p.m. for 50 s and annealed at 300 _C for 1 h. The NiOx films were quickly taken into a dry air box where the CsFA perovskite was deposited from a stoichiometric solution containing CsI (Sigma-Aldrich, 99.99% trace metals), formamidinium iodide (Dyesol), PbI2 (TCI) and PbBr2 (Sigma-Aldrich, 96%) in a mixture of N,N-dimethylformamide (Sigma-Aldrich) and dimethyl sulfoxide (Sigma-Aldrich). The solution was deposited through a 0.2 μm PTFE filter and spun at 1000 r.p.m. for 11 s, followed by 6000 r.p.m. for 30 s. During spin-coating, chlorobenzene was quickly dispensed 5 s prior to the end of the spin process as an antisolvent to assist perovskite crystallization. The films were annealed on a hot plate at 50 °C for 1 min and then annealed at 100 °C for 30 min. Next, we thermally evaporated 1nm of LiF and a thin 10nm layer of PCBM. Then, we deposited 4nm of stoichiometric SnO_2 with pulsed-CVD at 100 °C on top of the PCBM, followed by 2nm of zinc tin oxide. Tin oxide and zinc oxide pulsed-CVD processes were developed on an Arradiance GEMStar-6 ALD system at 100 °C. The SnO_2 pulsed-CVD cycle consisted of the processing sequence: 5 s purge (30 sccm N2), 1.5 s TDMASn pulse (30 sccm N2), 5 s purge (90 sccm N_2), 1 s deionized water pulse (90 sccm N_2) and 5 s of purging (90 sccm N_2) (5 s/1.5 s/5 s/1 s/5 s). The door and body temperature was maintained at 100 °C for the hot-wall reactor while the manifold temperature was 115 °C with a precursor temperature of 60 °C. Pulsed-CVD of zinc oxide was grown at 100 °C using diethyl zinc and water with the processing sequence: 100 ms/5 s/1 s/5 s with a constant 90 sccm N_2 flow. The reactor temperatures were the same as the tin oxide process, but the diethyl zinc precursor was unheated. Note that ALD can be performed instead of pulsed-CVD above. See Tables C-4 for details of the ALD and pulsed-CVD process parameters. For the semi-transparent and monolithic tandem devices, 150 nm of ITO was deposited through D.C. sputtering. An ITO witness sample on glass has a mobility of 43 cm^2/Vs and a carrier concentration of $3.5x10^{20}$ cm^{-3}. We finished the device stack with an evaporated or sputtered silver metal electrode around the perimeter of the 1 cm^2 device area to minimize series resistance and subsequently evaporated 150 nm of LiF as a second anti-reflection coating. For the damp heat stability testing, the single-junction solar cells were packaged between top and bottom EVA encapsulants and two sheets of 3-mm-thick glass. The butyl rubber edge seal was placed as a frame on the outer edge of the glass during assembly. The package got pressed with 1000 mbar pressure at 140 °C for 20 min for the edge seal to soften and the encapsulant to cure.

Silicon solar cell fabrication:

An n-type, 280-μm-thick, double-side polished, float-zone wafer was used as the starting substrate. A 250-nm-thick silicon nitride layer was deposited by plasma-enhanced CVD in an AMAT P5000 tool on one side of the wafer as a protective coating, and the wafer was then textured on the uncoated side in potassium hydroxide to reveal random pyramids. After removing the nitride coating in diluted hydrofluoric acid, the wafer was cleaned in piranha and RCA-B solutions, and the oxide was removed in buffered oxide etchant prior to deposition of amorphous silicon (a-Si:H) layers. Intrinsic and p-type a-Si:H films (7 and 15nm thick, respectively) were first deposited by plasma-enhanced CVD on the textured (rear) side of the wafer, and intrinsic and n-type a-Si:H films (7 and 8nm thick, respectively) were then deposited on the polished (front) side. A 20-nm-thick indium tin oxide (ITO) layer was sputtered from a 90/10 In_2O_3/SnO_2 in an MRC 944 tool on the polished side of the wafer through a shadow mask to define square cells 11mm on a side. A 20-nm-thick ITO layer was also sputtered over the textured surface through the same shadow mask. The front ITO layer was deposited using a 2.3:100 oxygen/argon mixture, which results in films with electron densities and mobilities of approximately $5x10^{20}$ cm^{-3} and 25 cm^2/Vs, respectively, after annealing at 200 °C; in contrast, the rear ITO layer was deposited using a 4.1:100 oxygen/argon mixture, which results in films with electron densities and mobilities of approximately $2x10^{20}$ cm^{-3} and 25 cm^2/Vs, respectively, after annealing at 200 °C. The textured surface was subsequently coated with a 300-nm-thick silicon nanoparticle layer that was spray-coated through a stainless-steel mesh (in contact with the wafer) to define local openings occupying approximately 5% of the total area. The nanoparticles were synthesized and deposited in a custom tool that uses a flow-through plasma process to nucleate nanoparticles from silane gas and deposit them via acceleration through a nozzle toward a substrate. The wafer was next annealed at 200 °C for 20 min to partially oxidize the nanoparticles, and a 200-nm-thick silver layer was sputtered through the shadow mask to cover the textured surface, finishing the cell.

Table C-1: Tin oxide growth processes at 100 °C

Process	Purge (s) at 30 sccm N_2	Metal Organic Pulse (s) at 30 sccm N_2	Metal Organic Purge (s) at 90 sccm N_2	Oxidizer Pulse (s) at 90 sccm N_2	Oxidizer Purge (s) at 90 sccm N_2	Growth Rate (Å/cyc)
ALD SnO_2	5	1.5	30	1	30	1.2
Pulsed-CVD SnO_2	5	1.5	5	1	5	1.8*

* Effective growth rate with parasitic CVD contributions.

Table C-2: Zinc oxide growth processes at 100 °C with constant 90 sccm N_2 flow

Process	Metal Organic Pulse (s)	Metal Organic Purge (s)	Oxidizer Pulse (s)	Oxidizer Purge (s)	Growth Rate (Å/cyc)
ALD ZnO	0.1	30	1	30	2.0
Pulsed-CVD ZnO	0.1	5	1	5	1.5

* Effective growth rate with parasitic CVD contributions.

Table C-3: Zinc tin oxide supercycle process

Process	SnO_2 Cycles	ZnO Cycles
ZTO supercycle	3	3

Table C-4: Reactor temperature setpoints

	Chamber Temp	Door Temp	Manifold Temp	TDMASn Bubbler Temp	DEZ Bubbler Temp
Parameter Setpoint	100°C	100°C	115°C	60°C	Unheated

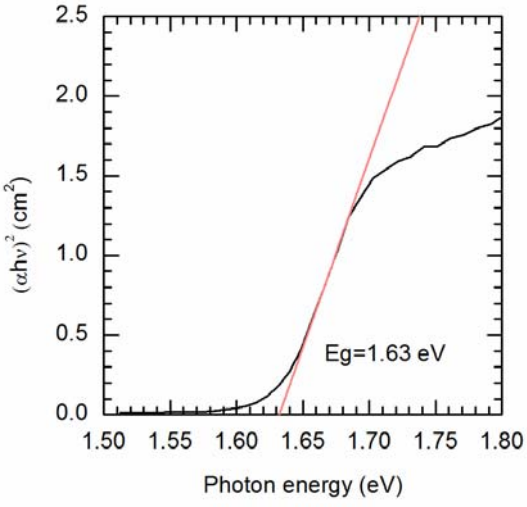

Figure C-1. Tauc plot of $Cs_{0.17}FA_{0.83}Pb(Br_{0.17}I_{0.83})_3$ perovskite top cell showing bandgap of 1.63 eV.

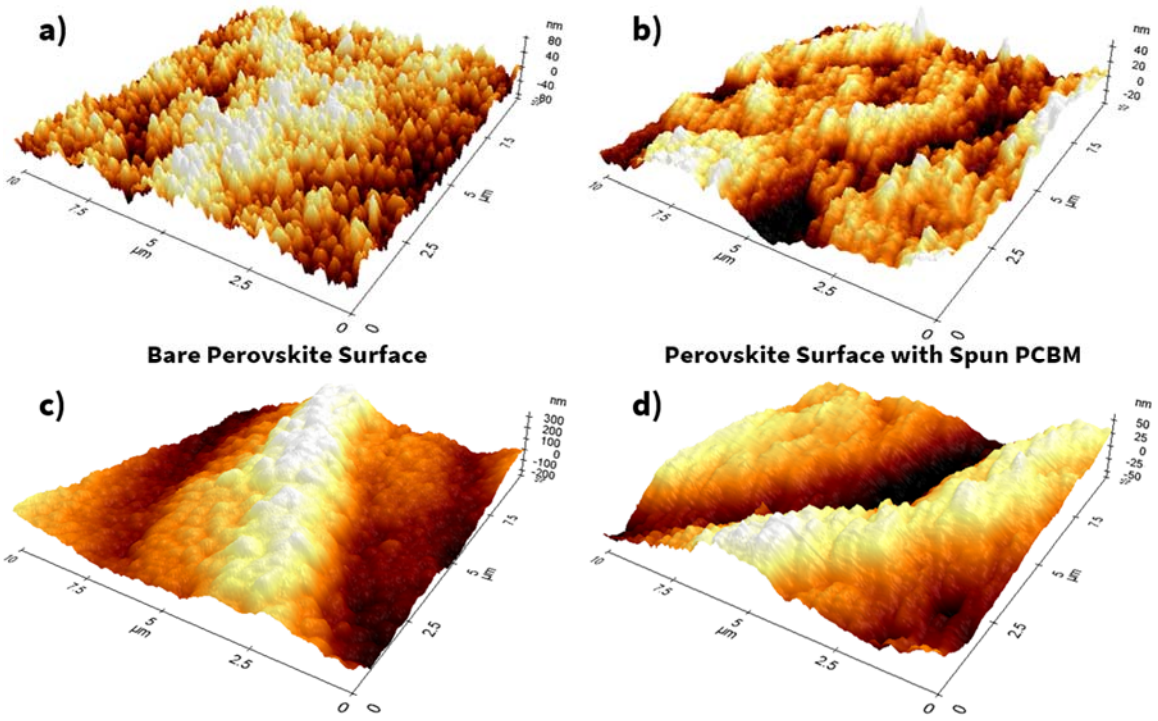

Figure C-2. Atomic force microscopy (AFM) images of CsFA perovskite surface before and after spinning 50 mg/mL PCBM in chlorobenzene onto the perovskite surface. Figures (a) (R_q=23.5 nm, R_z=166.7 nm) and (c) (R_q=132.4 nm, R_z=586.5 nm) show the high degree of surface roughness of the bare perovskite film. Figures (b) (R_q=6.9 nm, R_z=83.2 nm) and (d) (R_q=25.3 nm, R_z=121.2 nm) show how spinning PCBM onto the surface decreases the roughness slightly, but ultimately cannot planarize the surface. The lack of planarization leads to the troughs being filled by a thick layer of PCBM and the peaks being left exposed.

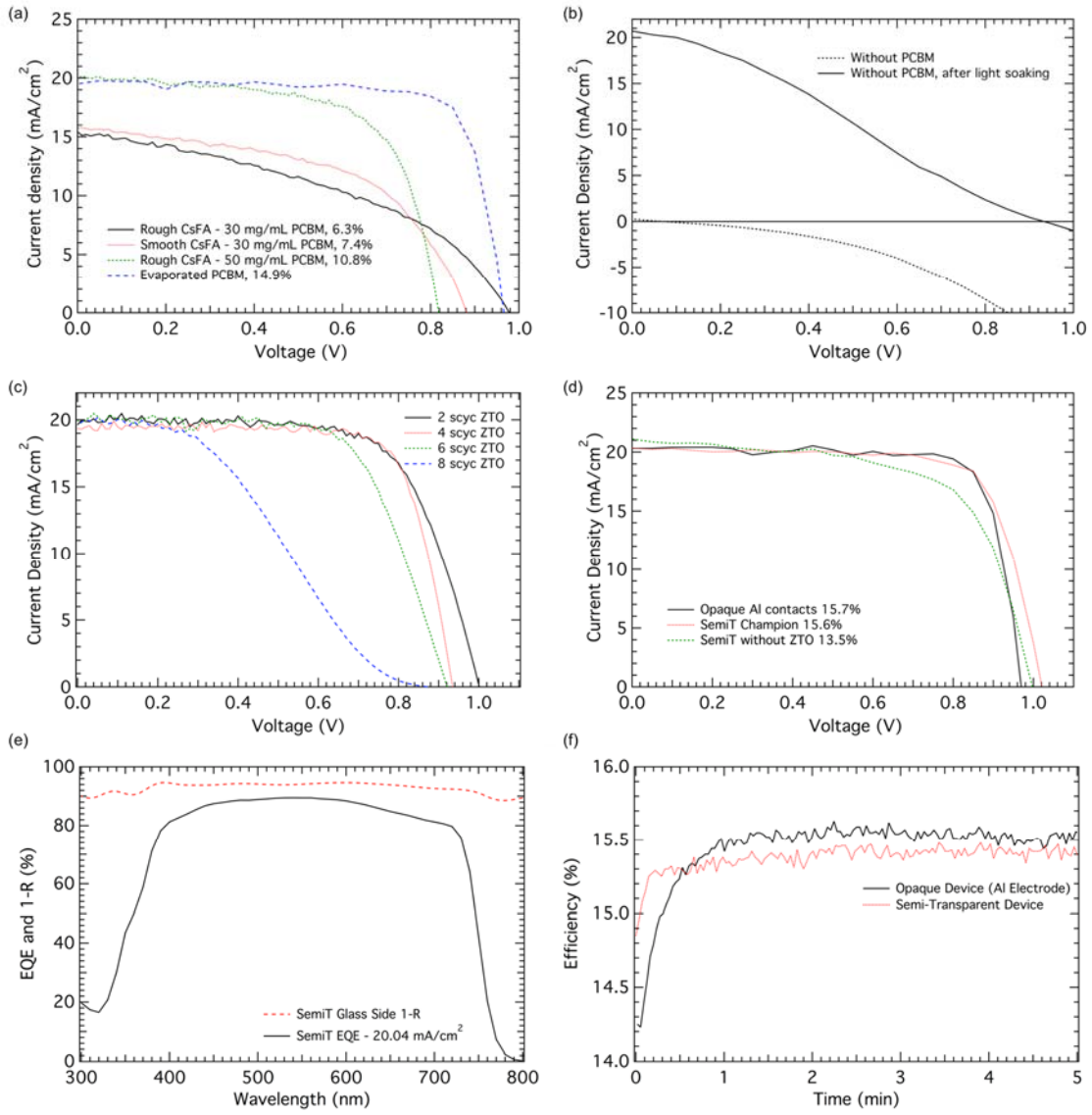

Figure C-3. (a) *J-V* scans of single-junction perovskite devices showing performance is best when heterojunction contacts are deposited through a conformal coating process, such as evaporation. The poor surface coverage from spin coating (Figure C-2) leads to decreased performance in comparison. The "smooth CsFA" refers to a thinner film with slightly decreased surface roughness. The higher concentration of PCBM creates a thicker layer of PCBM and shows improved device performance, but thicker PCBM is not ideal for maximizing transmission. (b) *J-V* scan of device without PCBM layer between perovskite and ALD SnO_2 layers. The large initial extraction barrier can be largely overcome by light soaking for over 30 minutes and holding in forward bias. But regardless of pre-conditioning, the PCBM layer is necessary to enable efficient electron extraction. (c) ZTO thickness, deposited in a repeating supercycle (scyc) on top of 4 nm of SnO_2, was varied in order to achieve the optimal electron extraction properties. While 2 nm consistently led to higher V_{OC}, the higher *FF* of 4 nm of ZTO was selected as the optimal

thickness. (d) *J-V* scans comparing a reference opaque device with evaporated heterojunction *n*-type contacts, the best device without ZTO showing poor *FF*, and the improved *FF* with ZTO (N14). (e) EQE and 1-R of the semi-transparent device in Figure C-2d with illumination through the glass side. Note, Figure 1 in the main text shows *J-V* and EQE taken through the SnO_2/ZTO bilayer side, as this is what is most relevant to the monolithic tandem performance. (f) Continuous maximum power tracking of opaque and semi-transparent devices from Figure C-3d.

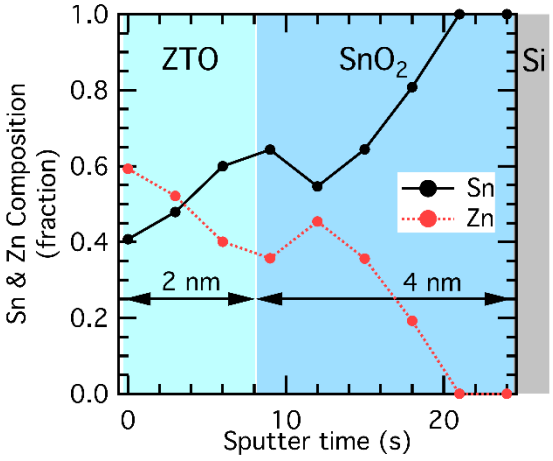

Figure C-4. X-ray photoelectron spectroscopy sputter depth profile showing how the Zn concentration drops off quickly at the ZTO/SnO_2 ALD interface.

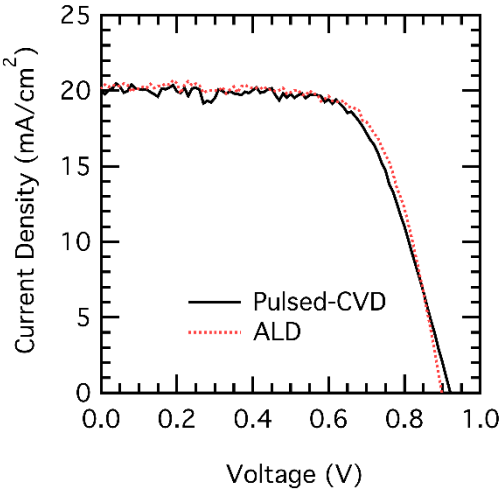

Figure C-5. Comparison of the *J-V* curves for single-junction perovskite devices with ALD *vs*. pulsed-CVD electron contacts.

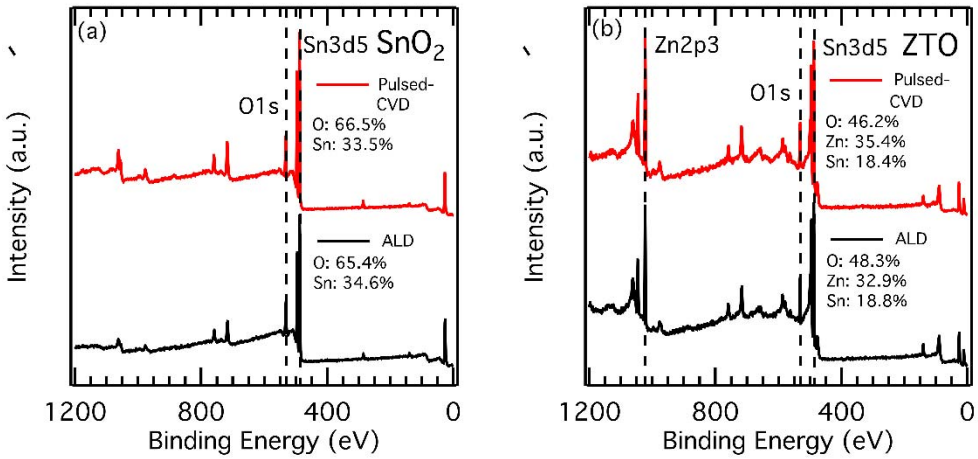

Figure C-6. XPS elemental composition data comparing the (a) SnO_2 and (b) ZTO layers deposited through ALD and pulsed-CVD processes.

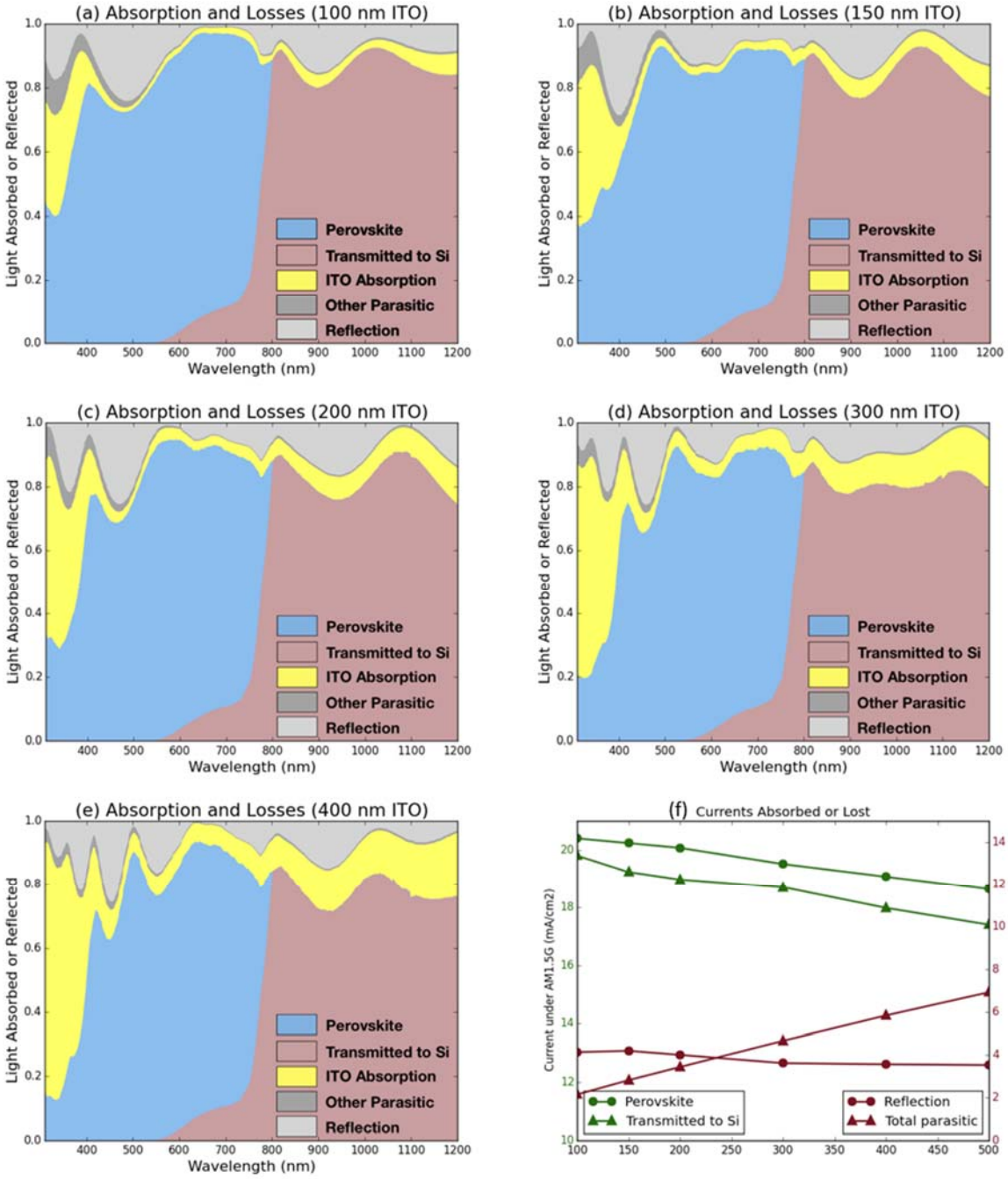

Figure C-7. Optical simulations of the tandem device stack were performed using a one-dimensional transfer matrix formalism[1] implemented in home-built code described previously[2]. Currents corresponding to light reflected, transmitted, or absorbed were computed by integrating over the AM1.5G spectrum. Simulations were performed for a range of top ITO thicknesses of (a) 100nm, (b) 150 nm, (c) 200 nm, (d) 300 nm, and (e) 400 nm. (f) Total integrated current absorbed in the perovskite or lost to parasitic absorption. Differences between theoretical and experimental reflections can be attributed

to thickness variation in our perovskite sample and surface roughness, which will dampen the interference fringes in the measured reflectance.

Stanford

Perovskite/HIT tandem Cell

Device ID: HIT4
2:16 PM 8/9/2016
Spectrum: ASTM G173 global

Device temperature: 25.0 ± 1.0 °C
Device area: 0.990 cm^2 ± 0.1%
Irradiance: 1000.0 W/m^2

NREL NATIONAL RENEWABLE ENERGY LABORATORY
OSMSS IV System
PV Performance Characterization Team

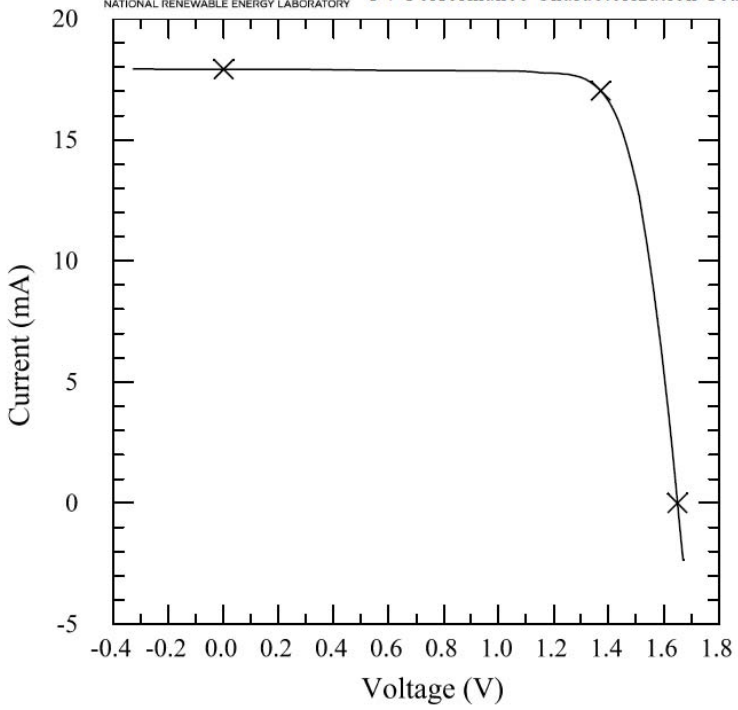

V_{oc} = 1.6506 V ± 0.6%
I_{sc} = 17.910 mA ± 1.3%
J_{sc} = 18.093 mA/cm^2 ± 1.3%
Fill Factor = 79.0 % ± 0.3%

I_{max} = 17.023 mA ± 1.3%
V_{max} = 1.3712 V ± 0.6%
P_{max} = 23.342 mW ± 1.4%
Efficiency = 23.58 % ± 1.4%

10.0 seconds per data point

Figure C-8. NREL certification of 23.6%-efficient perovskite/silicon tandem device.

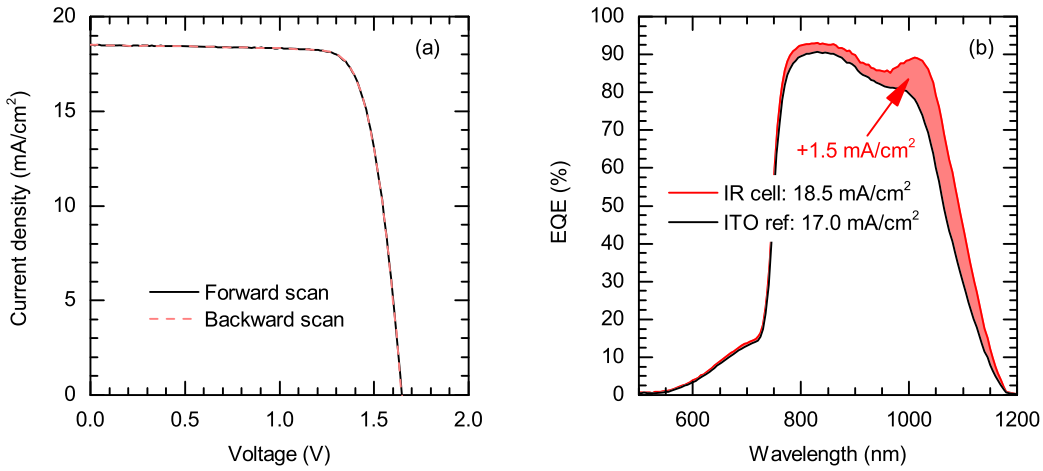

Figure C-9. (a) *J-V* scans of the perovskite/silicon tandem device sweeping forward (negative-to-positive bias) and backward (positive-to-negative bias) showing negligable hysteresis. (b) EQE of silicon bottom cells with and without SiNP rear reflectors, showing a 1.5 mA/cm^2 increase in J_{sc} in the IR-tuned cell.

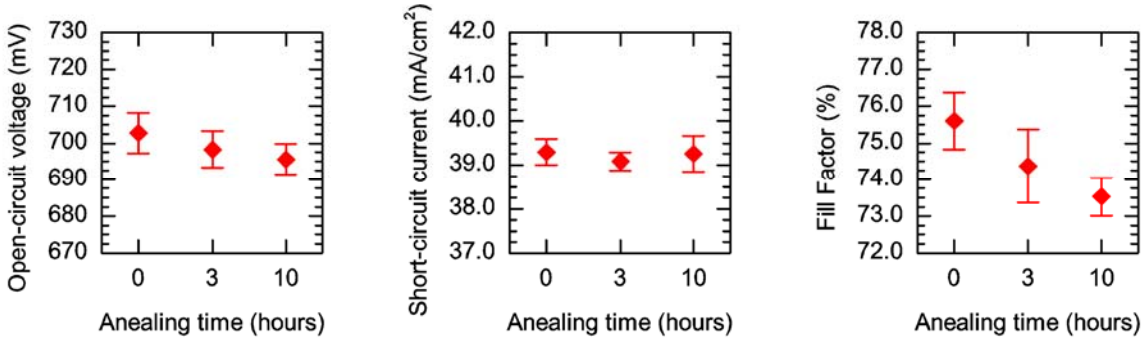

Figure C-10. In order to determine the annealing temperature window for our solution-processed NiO_x layer, we tested the thermal stability of silicon heterojunction solar cells. The devices were ramped to 190 °C in 30 minutes, held at 190 °C for 3–10 hours, and then ramped down to room temperature over 30 minutes. We observed a nearly 3% relative drop in the *FF* of the silicon solar cells after thermal stressing, but minimal degradation of the V_{oc} and J_{sc}. We conclude from this experiment that the NiO_x can be processed at 190 °C on top of the silicon heterojunction cells with minimal concern for a-Si:H degradation. The error bars designate the standard deviation of the measured results with a sample size of 3.

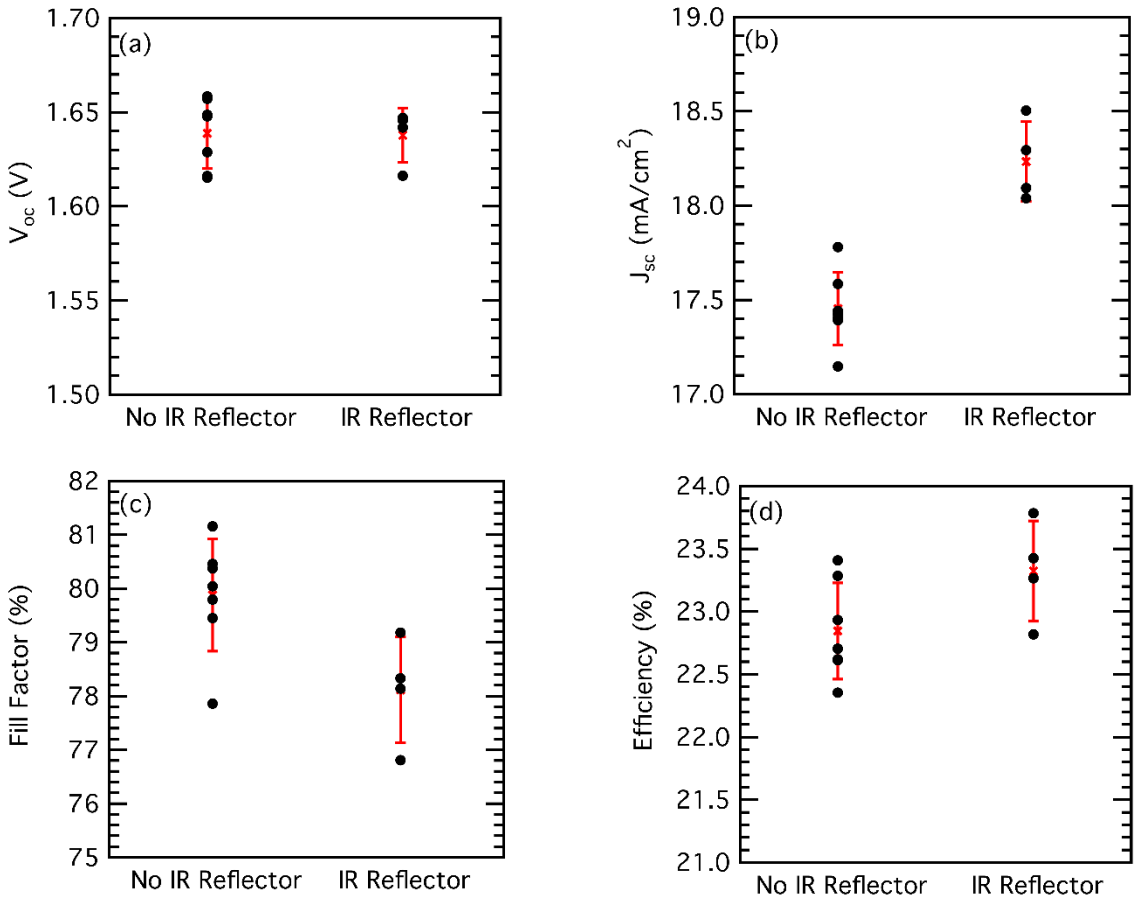

Figure C-11. Performance of the full batch of 12 of perovskite/silicon tandem solar cells (4 with IR reflectors and 8 with no IR reflector) that yielded the record device. The batch included silicon bottom cells with and without SiNP IR rear reflectors; these are compared. Individual device performances (black dots) as well as batch average (red cross) and standard deviation are shown (red lines).

References

1. Pettersson, L. A. A., Roman, L. S. & Inganas, O. Modeling photocurrent action spectra of photovoltaic devices based on organic thin films. J. Appl. Phys. 86, 487–496 (1999).

2. Burkhard, G. F., Hoke, E. T. & McGehee, M. D. Accounting for interference, scattering, and electrode absorption to make accurate internal quantum efficiency measurements in organic and other thin solar cells. Adv. Mater. 22, 3293–3297 (2010).

APPENDIX D

PREDICTING THE EFFICIENCY OF THE SILICON BOTTOM CELL IN A TWO-TERMINAL TANDEM SOLAR CELL

PREDICTING THE EFFICIENCY OF THE SILICON BOTTOM CELL IN A TWO-TERMINAL TANDEM SOLAR CELL

Abstract — In two-terminal top-cell/silicon tandem solar cells, such as perovskite/silicon tandems, the efficiency of the silicon bottom cell is unknown, as individual sub-cell characterization is inaccessible after tandem formation. Here, using the "spectral efficiency" concept, we propose a simple model that determines the silicon bottom cell efficiency in a tandem device, as well as predicts the efficiency potential of a silicon bottom cell before completing a tandem device. The model relies on the characterization of a silicon cell before tandem formation, and specifically takes as input data from external quantum efficiency, reflectance, and *Suns-Voc* measurements, as well as the absorption coefficient of the top cell. By applying this model, we find that the silicon bottom cell contributes 10.2% efficiency to the recent 23.6%-efficient, record monolithic perovskite/silicon tandem.

I. INTRODUCTION

Efficiency is a key driver of levelized cost of electricity (LCOE) in the photovoltaic (PV) market. The dominant technology in the market—silicon—increased its record cell efficiency to 26.6% last year, and record silicon module efficiencies are now near 25% [1]. This is approaching the 29.4% theoretical efficiency limit and is on a par with the oft-claimed 26% practical efficiency limit of a real silicon device [2, 3]. To push the efficiency still higher, and thus further reduce LCOE, silicon PV needs to transition to the only device structure that has successfully surpassed the single-junction limit: multi-junctions.

Silicon has excellent characteristics for a bottom cell in a tandem: It's abundant, efficient, inexpensive, and has the near-optimum bandgap for maximum tandem efficiency [4]. The challenge is to identify and develop a similarly efficient and inexpensive top cell, as well as a suitable configuration to couple it with the silicon bottom cell [5, 6].

Among top-cell candidates, perovskite solar cells stand out. Due to their wide, tunable bandgap and low-cost solution processability, perovskites are becoming increasingly attractive for achieving 30% tandem efficiency while maintaining low module cost [7]. Following the unprecedented rapid development of single-junction perovskites, the efficiency of perovskite/silicon tandems in the four-terminal configuration has increased from 13.4%, first reported in 2014, to 26.4% this year [8-13]. Similarly, two-terminal tandems, first reported in 2015 with an efficiency of 13.7%, have improved to 23.6% [14-17].

Unlike four-terminal tandems, in which each sub-cell is measured independently so that the efficiency contribution of each sub-cell—especially the silicon bottom cell—can be

unambiguously identified, two-terminal tandems make the performance of the sub-cells hard to deconvolute. The individual sub-cells are inaccessible upon the completion of the tandem device, and the performance of the silicon cell measured before tandem formation is not in general representative of that after tandem formation. For example, a silicon heterojunction bottom cell lacks front metallization and has resistive ITO on the front, leading to large series resistance losses that disappear upon deposition of a top cell that has a front electrode designed for lateral transport.

Here, we propose a model that evaluates the efficiency of a silicon bottom cell in a two-terminal tandem by characterizing a reference silicon cell, and that determines the efficiency potential of such a bottom cell before completing a tandem device.

II. Model Development and Demonstration

A reference silicon cell with the same structure as the one used in the 23.6%-efficient perovskite/silicon tandem was used as an example to develop and test the model [17]. As shown in Figure 1a, it comprises a planar front surface with a 20-nm-thick indium tin oxide (ITO) layer and a textured rear surface with silicon nanoparticle (SiNP) and silver layers as a rear reflector. Details of the structure and fabrication process can be found in [17, 18].

As previously mentioned, the current-voltage (*I-V*) characteristic of the reference silicon cell alone is not representative of its performance in a tandem because of the low fill factor (*FF*) caused by high sheet resistance due to the thin front ITO and lack of metal fingers, and because of the low short-circuit current density (J_{sc}) due to the reflective planar front surface. Consequently, the external quantum efficiency (*EQE*) and reflectance (*R*) of the reference silicon cell were first characterized, and then the internal quantum efficiency (*IQE*) was calculated with Equation (1). The front-surface reflectance, shown in Figure 1b, is approximately constant at ~32% from 700 to 1000 nm, as the 20-nm-thick ITO on the front is too thin to serve as an anti-reflection coating. As a result of such a big reflection loss, the *EQE* of the reference silicon cell, also shown in Figure 1b, is very low. The J_{sc} of the reference silicon cell, calculated by integrating the product of the *EQE* and the AM1.5 global photon flux, is thus only 27.8 mA/cm^2. Fortunately, the *EQE* curve meets the 1-*R* curve from 700 to 900 nm, which indicates near-unity *IQE* in this range, as shown in Figure 1c. With the *IQE*, one could calculate the *EQE* of the silicon bottom cell in a tandem by multiplying by the transmittance through the top cell.

$$IQE(\lambda) = \frac{EQE(\lambda)}{1 - R(\lambda)} \quad (1)$$

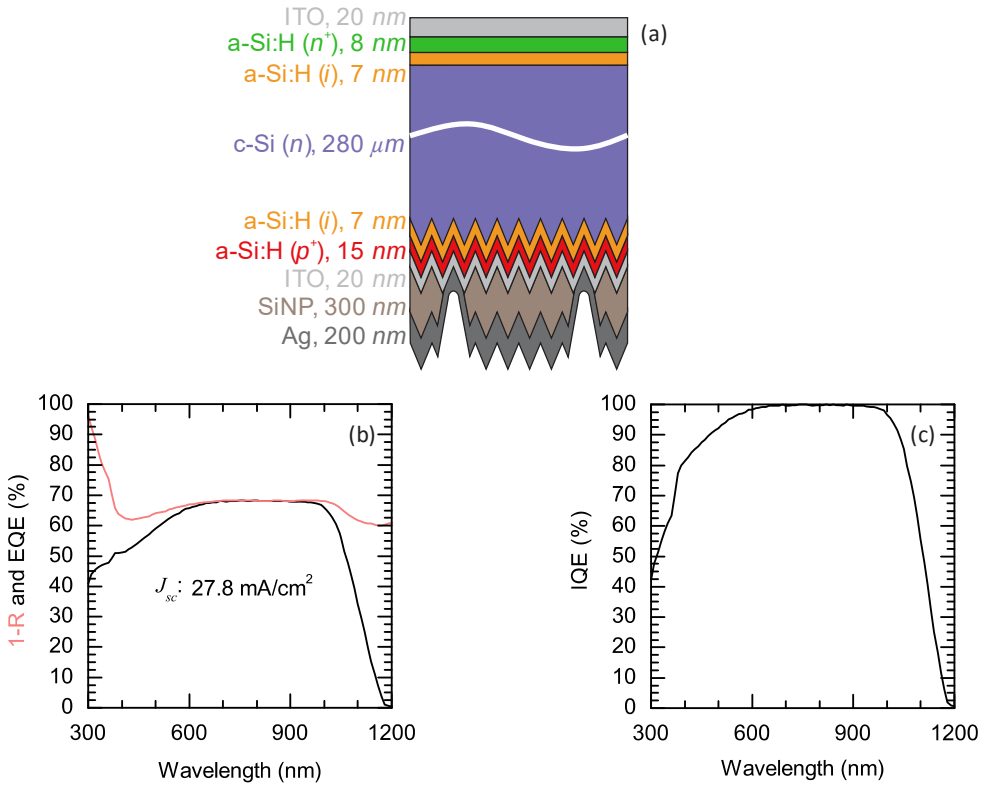

Fig. 1 (a) Schematic of the reference silicon cell (not to scale), (b) total absorbance (1-*R*) and *EQE* curves of the reference silicon cell, and (c) *IQE* of the reference silicon cell, calculated from 1-*R* and *EQE*.

The transmittance through the top cell, however, is difficult to obtain experimentally because the transmittance from the perovskite to silicon is different from that of glass to air, as one would measure when fabricating semi-transparent perovskites in the substrate configuration. Comprehensive optical modeling could access the transmittance [19-21]; however, characterizing optical constants accurately for each layer in a perovskite top cell is not trivial. To obtain the transmittance of a top cell without comprehensive optical modeling, we use Equation (2) as a first-order approximation:

$$T(\lambda) = f(\lambda) \cdot T_{ideal}(\lambda) = f(\lambda) \cdot e^{-\alpha(\lambda) \cdot d} \quad (2)$$

Here, f is the top-cell effective transparency, α is the absorption coefficient, d is the thickness of the perovskite absorber, λ is the wavelength, and T_{ideal} is the maximum possible transmittance to a silicon cell through a perovskite cell. Figure 2 shows example transmittance curves with constant effective transparencies of 1 and 0.91, with a 500-nm-thick perovskite absorber (the absorption coefficient of the perovskite was adapted from PV Lighthouse, initially reported by Loper et al [22]). Figure 2 also displays the *EQE* of a silicon bottom cell in a tandem, calculated with the *IQE* of the reference silicon cell shown in Figure 1c and a top-cell effective transparency of 0.91. The *EQE* curve overlaps with

the transmittance curve for wavelengths < 900 nm because the *IQE* is close to unity. The resulting J_{sc} is 18.5 mA/cm^2, which is the same as the value reported for the 23.6%-efficient perovskite/silicon tandem (in fact, the effective transparency was chosen to yield the same J_{sc}) [17].

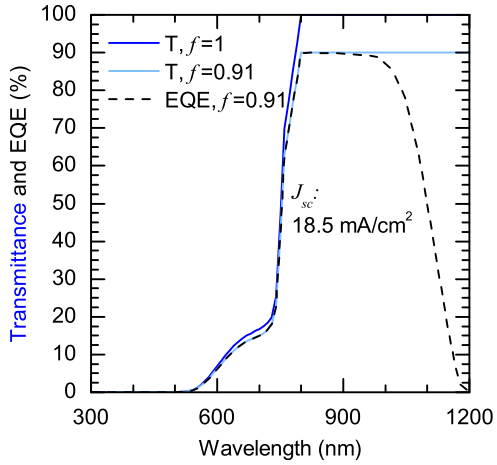

Fig. 2 Transmittance curves assuming effective transparencies *f* of 1 (dark blue) and 0.91 (light blue). Also shown is an example *EQE* (black) of a silicon cell in a tandem, calculated with the *IQE* shown in Fig. 1c and $f = 0.91$.

The injection-dependent open-circuit voltage (V_{oc}) of the reference silicon cell was obtained by *Suns*-V_{oc} measurements (not shown) [23]. At one-sun illumination, the V_{oc} of the reference silicon cell is 713 mV, and, for a photo-generated current density of 18.5 mA/cm^2, the expected open-circuit voltage of the silicon bottom cell in a tandem ($V_{oc,\text{Si-2T}}$) is 701 mV. The fill factor of the silicon bottom cell in a tandem (FF_{2T}) cannot accurately be extracted from the bottom cell alone since it is sensitive to both sub-cells and their coupling (e.g., current mismatch). However, were FF_{2T} known, the efficiency of the silicon bottom cell in a tandem ($\eta_{Si\text{-}2T}$), relative to the total incident irradiance, could now be calculated with Equation (3), which is adapted from the "spectral efficiency" concept [6]:

$$\eta_{Si-2T} = \frac{\int J_{sc}(\lambda) \cdot V_{oc,Si-2T} \cdot FF_{2T} \cdot d\lambda}{\int I(\lambda) \cdot d\lambda} \quad (3)$$

In this equation, I is the spectral irradiance and J_{sc} is given by

$$J_{sc}(\lambda) = q \cdot \frac{\lambda}{hc} \cdot IQE(\lambda) \cdot f(\lambda) \cdot e^{-\alpha(\lambda) \cdot d} \cdot I(\lambda) \quad (4)$$

where q is the elementary charge, h is Planck's constant, and c is the speed of light.

For the 23.6%-efficient perovskite/silicon tandem, FF_{2T} = 79% [17], and therefore the efficiency contribution to the tandem from the silicon bottom cell is calculated to be 10.2%, as indicated by the star in Figure 3. Figure 3 also shows the silicon bottom cell efficiency

potential as a function of the effective transparency of the top cell and *FF* of the tandem device. Given the *IQE* and the injection-dependent V_{oc} of the reference silicon cell, with an ideal effective transparency (f = 1) and excellent *FF* (FF_{2T} = 85%, as most two-junction III-V tandems have), the efficiency potential of our silicon bottom cell is as high as 12.4%. This figure also provides a guide for semi-transparent perovskite development when a certain tandem efficiency is targeted. For example, to make a 30%-efficient perovskite/silicon tandem with FF_{2T} = 80%, a 20%-efficient perovskite must have an effective transparency of ~0.9 in order for the bottom cell to contribute the remaining 10%, and a 21%-efficient perovskite must have an effective transparency of at least 0.8.

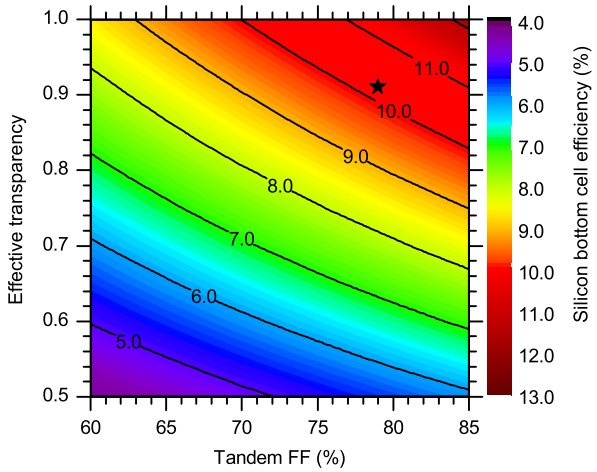

Fig. 3 Calculated silicon bottom cell efficiency as a function of top-cell effective transparency and FF_{2T}. The star indicates the bottom cell efficiency contribution to the 23.6%-efficient perovskite/silicon tandem.

III. Conclusion

In this paper, we developed a model that evaluates the efficiency of a bottom cell in a two-terminal tandem and demonstrated the model's use with the 23.6%-efficient silicon/perovskite tandem. Using the absorption coefficient of the perovskite top cell and the *EQE*, reflectance and *Suns*-V_{oc} of a reference silicon cell, we calculated that the bottom cell contributed 10.2% efficiency to that tandem. The model can be used to guide future perovskite top cell or silicon bottom cell development since it predicts the efficiency of the bottom cell in the tandem using measurements prior to top-cell deposition, and it can also be used in other two-terminal tandem systems if the absorption coefficient of the top-cell material is known.

References

1. K. Yoshikawa, H. Kawasaki, W. Yoshida, T. Irie, K. Konishi, K. Nakano, et al., "Silicon heterojunction solar cell with interdigitated back contacts for a photoconversion efficiency over 26%," Nature Energy, vol. 2, p. 17032, 2017.

2. A. Richter, M. Hermle, and S. W. Glunz, "Reassessment of the Limiting Efficiency for Crystalline Silicon Solar Cells," IEEE Journal of Photovoltaics, vol. 3, pp. 1184-1191, 2013.

3. D. D. Smith, P. Cousins, S. Westerberg, R. De Jesus-Tabajonda, G. Aniero, and Y. C. Shen, "Toward the Practical Limits of Silicon Solar Cells," IEEE Journal of Photovoltaics, vol. 4, pp. 1465-1469, 2014.

4. M. A. Green, "Commercial progress and challenges for photovoltaics," Nature Energy, vol. 1, p. 15015, 2016.

5. I. M. Peters, S. Sofia, J. Mailoa, and T. Buonassisi, "Techno-economic analysis of tandem photovoltaic systems," RSC Advances, vol. 6, pp. 66911-66923, 2016.

6. Z. Yu, M. Leilaeioun, and Z. Holman, "Selecting tandem partners for silicon solar cells," Nature Energy, vol. 1, p. 16137, 2016.

7. B. Chen, X. Zheng, Y. Bai, N. P. Padture, and J. Huang, "Progress in Tandem Solar Cells Based on Hybrid Organic–Inorganic Perovskites," Advanced Energy Materials, pp. 1602400, 2017.

8. P. Löper, S.-J. Moon, S. M. De Nicolas, B. Niesen, M. Ledinsky, S. Nicolay, et al., "Organic–inorganic halide perovskite/crystalline silicon four-terminal tandem solar cells," Physical Chemistry Chemical Physics, vol. 17, pp. 1619-1629, 2015.

9. C. D. Bailie, M. G. Christoforo, J. P. Mailoa, A. R. Bowring, E. L. Unger, W. H. Nguyen, et al., "Semi-transparent perovskite solar cells for tandems with silicon and CIGS," Energy & Environmental Science, vol. 8, pp. 956-963, 2015.

10. K. A. Bush, C. D. Bailie, Y. Chen, A. R. Bowring, W. Wang, W. Ma, et al., "Thermal and Environmental Stability of Semi‐Transparent Perovskite Solar Cells for Tandems Enabled by a Solution‐Processed Nanoparticle Buffer Layer and Sputtered ITO Electrode," Advanced Materials, 2016.

11. J. Werner, L. Barraud, A. Walter, M. Bräuninger, F. Sahli, D. Sacchetto, et al., "Efficient Near-Infrared-Transparent Perovskite Solar Cells Enabling Direct Comparison of 4-Terminal and Monolithic Perovskite/Silicon Tandem Cells," ACS Energy Letters, vol. 1, pp. 474-480, 2016.

12. B. Chen, Y. Bai, Z. Yu, T. Li, X. Zheng, Q. Dong, et al., "Efficient Semitransparent Perovskite Solar Cells for 23.0%-Efficiency Perovskite/Silicon Four-Terminal Tandem Cells," Advanced Energy Materials, vol. 6, pp. 1601128,2016.

13. T. Duong, Y. Wu, H. Shen, J. Peng, X. Fu, D. Jacobs, et al., "Rubidium Multication Perovskite with Optimized Bandgap for Perovskite-Silicon Tandem with over 26% Efficiency," Advanced Energy Materials, 2017.

14. J. P. Mailoa, C. D. Bailie, E. C. Johlin, E. T. Hoke, A. J. Akey, W. H. Nguyen, et al., "A 2-terminal perovskite/silicon multijunction solar cell enabled by a silicon tunnel junction," Applied Physics Letters, vol. 106, p. 121105, 2015.

15. S. Albrecht, M. Saliba, J. P. C. Baena, F. Lang, L. Kegelmann, M. Mews, et al., "Monolithic perovskite/silicon-heterojunction tandem solar cells processed at low temperature," Energy & Environmental Science, 2016.

16. J. Werner, C.-H. Weng, A. Walter, L. Fesquet, J. P. Seif, S. De Wolf, et al., "Efficient Monolithic Perovskite/Silicon Tandem Solar Cell with Cell Area >1 cm2," The Journal of Physical Chemistry Letters, vol. 7, pp. 161-166, 2016.

17. K. A. Bush, A. F. Palmstrom, Z. J. Yu, M. Boccard, R. Cheacharoen, J. P. Mailoa, et al., "23.6%-efficient monolithic perovskite/silicon tandem solar cells with improved stability," Nature Energy, vol. 2, p. 17009, 2017.

18. M. Boccard, P. Firth, Z. J. Yu, K. C. Fisher, M. Leilaeioun, S. Manzoor, et al., "Low-refractive-index nanoparticle interlayers to reduce parasitic absorption in metallic rear reflectors of solar cells," physica status solidi (a), pp. e201700179, 2017

19. R. Santbergen, A. H. M. Smets, and M. Zeman, "Optical model for multilayer structures with coherent, partly coherent and incoherent layers," Optics Express, vol. 21, pp. A262-A267, 2013.

20. R. Santbergen, R. Mishima, T. Meguro, M. Hino, H. Uzu, J. Blanker, et al., "Minimizing optical losses in monolithic perovskite/c-Si tandem solar cells with a flat top cell," Optics Express, vol. 24, pp. A1288-A1299, 2016.

21. K. Jäger, L. Korte, B. Rech, and S. Albrecht, "Numerical optical optimization of monolithic planar perovskite-silicon tandem solar cells with regular and inverted device architectures," Optics Express, vol. 25, pp. A473-A482, 2017.

22. P. Löper, M. Stuckelberger, B. Niesen, J. Werner, M. Filipič, S.-J. Moon, et al., "Complex Refractive Index Spectra of CH3NH3PbI3 Perovskite Thin Films Determined by Spectroscopic Ellipsometry and Spectrophotometry," The Journal of Physical Chemistry Letters, vol. 6, pp. 66-71, 2015.

23. R. Sinton and A. Cuevas, "A quasi-steady-state open-circuit voltage method for solar cell characterization," in Proceedings of the 16th European Photovoltaic Solar Energy Conference, 2000.

APPENDIX E

EVALUATION OF SPECTRUM-SPLITTING DICHROIC MIRRORS FOR PVMIRROR TANDEM SOLAR CELLS

EVALUATION OF SPECTRUM-SPLITTING DICHROIC MIRRORS FOR PVMIRROR TANDEM SOLAR CELLS

Abstract — Single-junction solar cells are approaching their theoretical efficiency limit, and tandem or multi-junction architectures provide a route for further increasing efficiency. However, due to high material cost, these technologies have traditionally been restricted to high concentrations with the penalty of the loss of diffuse light in outdoor applications. We propose a new tandem concept called a "PVMirror" that makes use of the global spectrum. It utilizes PV cells as a three-in-one technology—they act as a concentrating mirror, spectrum splitter, and high-efficiency light-to-electricity converter. A key element of this technology is an effective spectrum-splitting dichroic mirror, and this paper evaluates three dichroic mirror designs. Prototype PVMirrors with these mirrors and silicon heterojunction solar cells were made, and their reflection and transmission spectra confirm the spectrum-splitting capability of the dichroic mirrors. Outdoor testing shows that reflected light is successfully concentrated to a focus at which the second sub-cell in the tandem is to be located.

I. INTRODUCTION

Single-junction solar cells are approaching their theoretical efficiency limit. The best GaAs solar cell, fabricated by Alta Devices, has achieved an efficiency of 28.8% which is not far off the Shockley-Queisser limit [1, 2]. Similarly, the record 25.6%-efficient silicon cell announced by Panasonic in 2014 [3] is very close to the 29.4% theoretical limit for a silicon cell [4]. Multi-junction cells are the only technology that has been proven to surpass the single-junction efficiency limit: three- or four-junction III-V cells that exceed 40% efficiency under concentration have been produced by several companies [5-8]. However, the market share of this technology is still small, even for high-concentration applications in which the III-V materials cost is not dominant. One reason is the expense of the two-axis trackers needed to reach these concentrations; another is the loss of all diffuse light, which cannot be concentrated. The high efficiency reported for multi-junctions is usually with respect to only the direct fraction of the incident light, so that in outdoor applications the annually averaged efficiency with respect to the global irradiance is discounted by a location-dependent diffuse fraction. This often neglected factor is significant: even in sunny places such as Phoenix the annual diffuse fraction is as high as 25% [9].

In a recent paper, we introduced a new tandem concept called a "PVMirror" which collects diffuse light [10]. It utilizes PV cells as a three-in-one technology—they act as a concentrating mirror, spectrum splitter, and high-efficiency light-to-electricity converter. A PVMirror intercepts the global spectrum and reflects select wavelengths to a second solar cell or even a non-PV solar converter locates at a focus; together, the PVMirror and

second converter form a spatially separated 4-terminal tandem solar collector. Here we evaluate three spectrum-splitting dichroic mirror architectures and report progress on PVMirror prototypes using these mirrors and silicon heterojunction solar cells.

II. Silicon PVMirror Concept

A silicon PVMirror is composed of a silicon solar cell, a curved substrate, and a dichroic mirror (Figure 1). Near-bandgap light is transmitted by the dichroic mirror into the silicon solar cell, and for these wavelengths the silicon solar cell can have an efficiency as high as 40%. Light not transmitted by the dichroic mirror is reflected to a common focus; this focusing occurs because the dichroic mirror has the curvature of the substrate. Depending on the solar converter at the focus, a long-pass or band-pass dichroic mirror can be used so that the silicon PVMirror reflects only high-energy photons to the focus or both high-energy and infrared photons (only near-infrared photons are transmitted). The former configuration would be ideal to power a wide-bandgap solar cell at the focus, which makes use of high-energy photons only, whereas the latter configuration can be used to power a non-PV solar converter, e.g., a concentrating solar power (CSP) receiver, which is a wavelength-agnostic technology that converts photon energy into thermal energy.

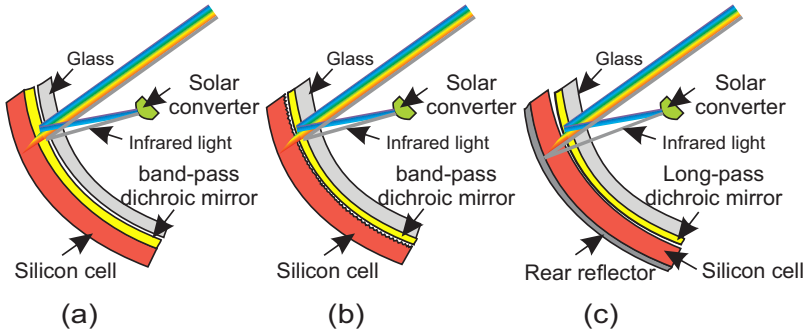

Fig. 1. Three silicon PVMirror trough configurations. (a) Planar cell with a band-pass dichroic mirror deposited on top of the solar cell, (b) textured cell laminated to glass coated with a band-pass dichroic mirror, and (c) planar cell with a rear reflector and a free-standing long-pass dichroic mirror included in the laminate.

There are three embodiments of the PVMirror concept depending on how we arrange the solar cell and dichroic mirror, as shown in Figure 1. The first embodiment uses a planar solar cell (smooth surfaces formed by cheap chemical polishing) and dielectric layers are deposited right on top of the planar solar cell to get the desired band-pass dichroic mirror. The cells are then laminated to a curved glass substrate, as shown in Figure 1a. As an alternative, Figure 1b shows a band-pass coating deposited directly on the glass, to which regular textured silicon solar cells are laminated. Finally, dielectric dichroic mirrors can be replaced with a free-standing long-pass polymer film from 3M [11], and the film can be included in the laminate between the silicon solar cell and glass. (Note that 3M does not presently manufacture a band-pass film with desired pass band.) This configuration will lose all of the infrared light since it will enter the solar cell and be scattered away from the

focus, unless using a planar solar cell with a specular rear reflector on the back, as shown in Figure 1c.

III. Prototype Manufacturing and Testing

Dichroic mirror design is a key component to the success of the PVMirror concept. For the embodiments shown in Figure 1a and 1b, dielectrics stacks of SiO_2/TiO_2 were used as dichroic mirrors, and the software Essential Macleod was used to design the mirrors. By stacking SiO_2 and TiO_2 periodically and tuning each layer thickness, 48-layer band-pass dichroic mirrors were successfully designed on a planar silicon solar cell (Figure 1a) and on glass (Figure 1b). The pass band was designed to be between 700-1000 nm in both cases. The dichroic mirrors were deposited at EMF Corp by e-beam evaporation.

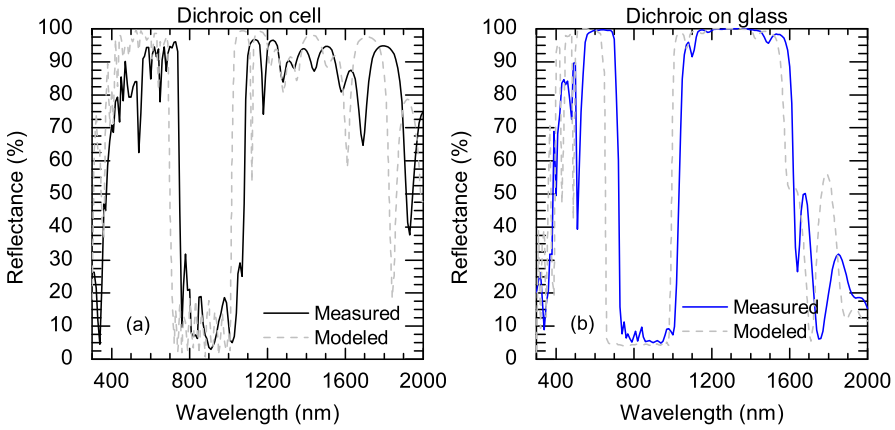

Fig. 2. Measured and modeled reflectance of (a) a 48-layer SiO_2/TiO_2 dichroic mirror deposited on a silicon cell, and (b) a 48-layer SiO_2/TiO_2 dichroic mirror deposited on glass.

Reflectance spectra of the dielectric dichroic mirrors were measured using a Lambda 950 spectrophotometer from PerkinElmer and were compared with the modeled spectra; the results are shown in Figure 2. Both dichroic mirrors behave well as band-pass filters: they are highly transmitting in the pass band and reflecting in both rejection bands. The spectra are very close to the models except for a slight redshift of the pass band, which could be caused by a difference in refractive index between the deposited material and the modeled material from the database of the design software.

Figure 2 shows the reflectance at near-normal incidence, but dichroic mirrors in trough PVMirrors will see a wide range of incidence over the course of a year due to the changing declination angle of the earth. To investigate the sensitivity of the dichroic mirrors to angle, the angular-resolved transmittance was measured on the dichroic mirror deposited on glass with an "Automated Reflectance/Transmittance Analyzer (ARTA)" accessory, and the results are shown in Figure 3. The measured and modeled performance is similar in that, when the angle of incidence increases, the pass band blueshifts but maintains its band-pass property. However, the transmittance in the transmission band is about 5% lower than in the model because the glass used is not as transparent as the glass modeled. Angular-

resolved reflectance measurements were also done on both dichroic mirrors (on glass and on cell), and the results are similar to the model as well. The observed blueshifts with increasing angle will not cause a substantial degradation of a PVMirror, but the efficiency is expected to decrease slightly as the band that is transmitted is shifted to less ideal wavelengths for the silicon solar cell.

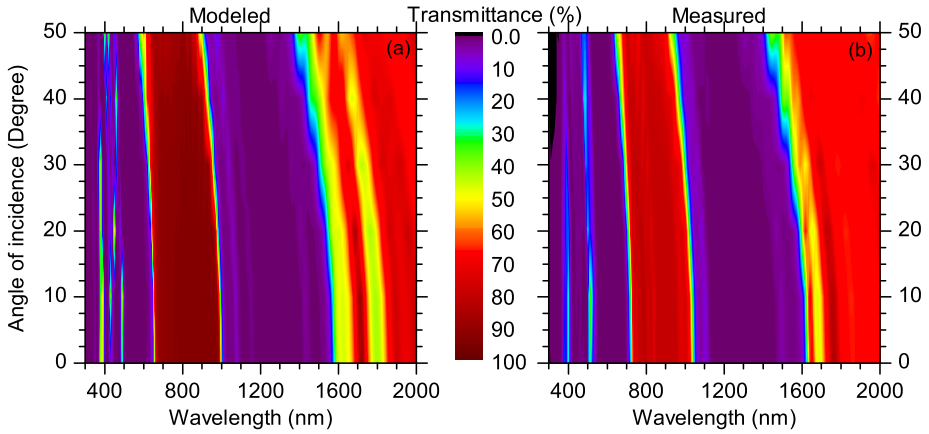

Fig. 3. Angular-resolved transmittance contour map of a 48-layer SiO_2/TiO_2 dichroic mirror deposited on glass. (a) Modeled performance, (b) measured performance.

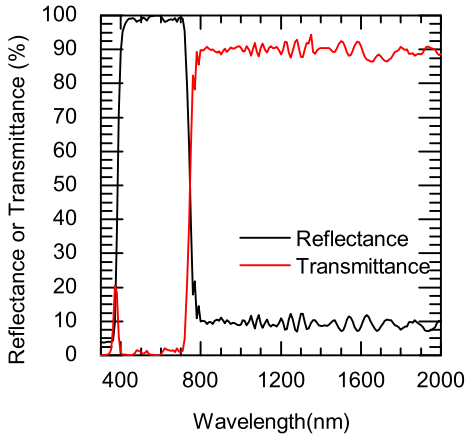

Fig. 4. Measured reflectance and transmittance of a long-pass dichroic mirror from 3M.

The free-standing long-pass dichroic mirror shown in Figure 1c was purchased from 3M. The reflectance and transmittance were measured and are shown in Figure 4. The transmission cut-on is around 750 nm with 90% transmittance at longer wavelengths, the reflectance is near perfect in the 400–750 nm band, and the light below 400 nm is absorbed by the film itself.

Silicon heterojunction solar cells were fabricated on planar and textured wafers and were laminated to parabolic curved glass with each of the three dichroic mirrors to form prototypes of the three PVMirror configurations shown in Figure 1. The cells had a full-area silver layer as a back contact; the silver layer also acts as a rear reflector for sub-bandgap light (important for the configuration in Figure 1c). Reflectance measurements were performed on the three PVMirror prototypes and the 1-R curves are plotted in Figure 5.

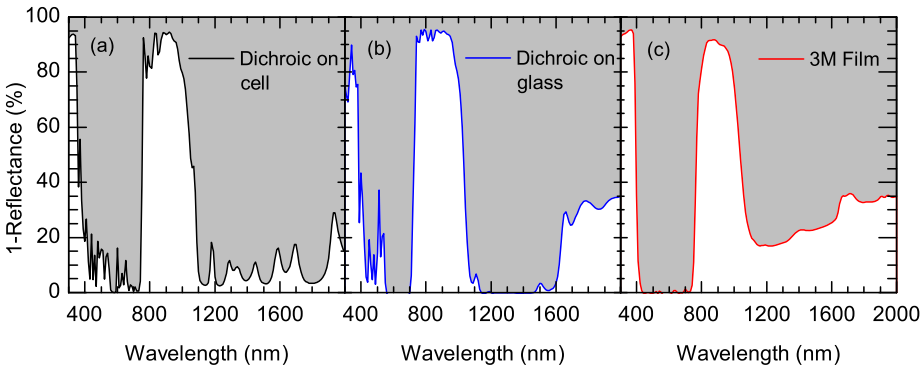

Fig. 5. 1-Reflectance curves of three PVMirror trough configurations, all of which have the general structure of (from the sunward side) glass/dichroic mirror/silicon heterojunction solar cell. (a) Planar cell with a band-pass dichroic mirror deposited on top of the solar cell, (b) textured cell and glass coated with a band-pass dichroic mirror, and (c) planar cell and a free-standing, long-pass dichroic mirror.

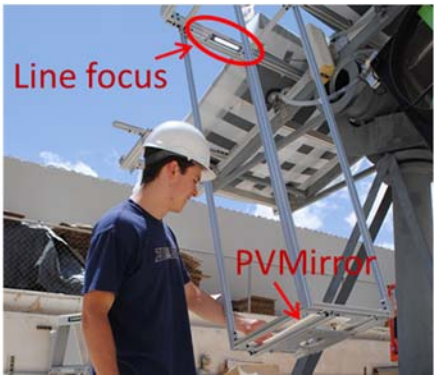

Fig. 6. Photograph of an outdoor test of a PVMirror. The PVMirror is mounted on the tracker and a clear line of visible light is produced at the focus, indicating that the PVMirror performs as a concentrating optic.

The white area below the 1-Reflectance curves represents the light that is absorbed somewhere in the PVMirror (no light is transmitted through the whole structure because of the silver reflector), whereas the grey area represents the light reflected to the focus by the PVMirror. The white area in the pass band is absorbed by the silicon cell and is converted

into electricity; however, the white areas below 400 nm and above 1200 nm correspond to parasitic absorption. The parasitic absorption in Figures 5b and c is quite high in the long-wavelength region and is caused by free-carrier absorption in the ITO layers of the solar cells. Infrared parasitic absorption is particularly severe in Figure 5c because, in this configuration (Figure 1c), all of the long-wavelength light transmits through the long-pass dichroic mirror into the cell and is reflected back by the silver on the back side of the polished cell. The resulting double pass through the ITO layers increases absorption; a less absorbing transparent conductive oxide would mitigate this issue and reflect more infrared light back.

We have begun outdoor testing of PVMirrors: the prototype made with the 3M long-pass dichroic mirror was mounted on a tracker at the University of Arizona. Figure 6 shows that the PVMirror nicely concentrates the reflected light at the line focus.

IV. Conclusion

We presented a new technology—a "PVMirror"—that is a tandem solar collector that makes use of diffuse light. Prototype PVMirrors based on silicon heterojunction solar cells were built with three different dichroic mirrors, and all of them function as spectrum splitters. Outdoor optical measurements confirm that the PVMirror also performs as a concentrating mirror. Each PVMirror presented has advantages and challenges: the configuration with the dichroic mirror deposited on the solar cell (Figure 1a) can be thought of as a polished cell with a sophisticated anti-reflection coating, but the micron-thick dichroic mirror introduces stress to the cell; the second configuration (Figure 1b) with the dichroic mirror deposited on glass can use commercial textured solar cells, but there are not presently tools to deposit dichroic mirrors on large curved substrates; and the configuration with the 3M long-pass dichroic mirror offers an economic solution with excellent optical properties at visible and near-infrared wavelengths, but parasitic absorption of infrared light within the silicon solar cell reduces the reflected energy, which is not favorable for a broadband solar converter at the focus.

Acknowledgment

We thank Brian Wheelwright and Justin Hyatt at University of Arizona for performing the outdoor testing.

The information, data, or work presented herein was funded in part by the Advanced Research Projects Agency-Energy (ARPA-E), U.S. Department of Energy, under Award Number DE-AR0000474.

References

1. M. A. Green, K. Emery, Y. Hishikawa, W. Warta, and E. D. Dunlop, "Solar cell efficiency tables (version 40)," Progress in Photovoltaics, vol. 20, pp. 606-614, Aug 2012.

2. W. Shockley and H. J. Queisser, "Detailed Balance Limit of Efficiency of P-N Junction Solar Cells," Journal of Applied Physics, vol. 32, pp. 510, 1961.

3. M. A. Green, K. Emery, Y. Hishikawa, W. Warta, and E. D. Dunlop, "Solar cell efficiency tables (version 44)," Progress in Photovoltaics, vol. 22, pp. 701-710, Jul 2014.

4. A. Richter, M. Hermle, and S. W. Glunz, "Reassessment of the Limiting Efficiency for Crystalline Silicon Solar Cells," Ieee Journal of Photovoltaics, vol. 3, pp. 1184-1191, Oct 2013.

5. R. R. King, D. C. Law, K. M. Edmondson, C. M. Fetzer, G. S. Kinsey, H. Yoon, et al., "40% efficient metamorphic GaInP/GaInAs/Ge multijunction solar cells," Applied Physics Letters, vol. 90, Apr 30 2007.

6. F. Dimroth, M. Grave, P. Beutel, U. Fiedeler, C. Karcher, T. N. D. Tibbits, et al., "Wafer bonded four-junction GaInP/GaAs//GaInAsP/GaInAs concentrator solar cells with 44.7% efficiency," Progress in Photovoltaics, vol. 22, pp. 277-282, Mar 2014.

7. S. Corporation. (2012). Sharp Develops Concentrator Solar Cell with World's Highest Conversion Efficiency of 43.5%. Available: http://sharp-world.com/corporate/news /120531.html

8. W. Guter, J. Schone, S. P. Philipps, M. Steiner, G. Siefer, A. Wekkeli, et al., "Current-matched triple-junction solar cell reaching 41.1% conversion efficiency under concentrated sunlight," Applied Physics Letters, vol. 94, Jun 1 2009.

9. W. Marion and S. Wilcox, "Solar Radiation Data Manual for Flat-Plate and Concentrating Collectors," 1994.

10. Z. J. Yu, K. C. Fisher, B. M. Wheelwright, R. P. Angel, and Z. C. Holman, "PVMirror: A New Concept for Tandem Solar Cells and Hybrid Solar Converters," Photovoltaics, IEEE Journal of, vol. 5, pp. 1791-1799, 2015.

11. M. F. Weber, C. A. Stover, L. R. Gilbert, T. J. Nevitt, and A. J. Ouderkirk, "Giant birefringent optics in multilayer polymer mirrors," Science, vol. 287, pp. 2451-2456, Mar 31 2000.

APPENDIX F

MODELING OF GAAS/SILICON PVMIRROR TANDEM SYSTEM:

A CASE STUDY

MODELING OF GAAS/SILICON PVMIRROR TANDEM SYSTEM: A CASE STUDY

Abstract — We propose a new, optically coupled tandem architecture with a silicon "PVMirror" as the bottom cell. A silicon PVMirror is a curved silicon module with an integrated dichroic mirror that transmits near-infrared light to the silicon cells and reflects and focuses visible light onto a GaAs receiver. Simulating such a system with record GaAs and silicon cells and an ideal dichroic mirror shows the tandem efficiency can reach over 36% with no diffuse light and over 30% with 20% diffuse light. A sensitivity analysis indicates that the PVMirror tandem is most sensitive to the GaAs cell performance and dichroic mirror cut-off wavelength but relatively insensitive to the silicon cell performance.

I. INTRODUCTION

Several companies and institutions have successfully made >25%-efficient silicon cells, many of them even with large-area (> 150 cm2) substrates [1]. These efficiencies are not far from the 29.4% maximum theoretical efficiency limit of silicon cells, and they are bumping up against the oft-claimed 26% practical efficiency limit [2, 3]. Though many routes have been proposed to go beyond the single-junction efficiency limit, only tandem technology offers the success witnessed in III-V field.

Silicon is an excellent bottom cell for use in tandem cells: It is abundant, efficient, inexpensive, and, fortunately, it has the near-optimum bandgap [4, 5]. To achieve a successful silicon-based tandem requires that, first, an efficient top cell to pair with silicon is developed, and, second, a cost-effective way to assemble it with a silicon bottom cell is devised that has high energy yield with respect to the global insolation.

Detailed-balance limit calculations indicate that the optimum bandgap for a top cell paired with silicon is around 1.7 eV [6]. Consequently, many top cells with bandgaps of 1.6—1.8 eV have been used in silicon-based tandems. With III-V materials, NREL demonstrated a 29.8%-efficient tandem by mechanically stacking a GaInP cell on top of a silicon cell [7]; with II-VI materials, EPIR technologies demonstrated a 16.8%-efficient tandem by direct growth of a wide-bandgap CdZnTe cell on silicon [8]; with perovskites, efficiencies of 19.2% and 28.0% were demonstrated with two- and four-terminal tandems, respectively [9, 10]. All of these efficiencies are far from the theoretical maximum tandem efficiency, and the reason is that none of the top (or bottom) cells operates near its detailed-balance limit. Using a concept called "spectral efficiency", we recently calculated that, of all *existing* cells, GaAs would offer the highest achievable efficiency when paired with silicon [5].

Direct growth of III-V materials on silicon is one of the earliest methods used to couple the sub-cells; however, the large lattice mismatch between silicon and GaAs or 1.7-ev-bandgap III-V absorbers degrades material quality and thus device performance. Four-terminal

configurations circumvent the lattice-mismatch challenge and thus yields higher tandem efficiencies. However, due to the high cost of the III-V sub-cells, particularly in four-terminal configurations that utilize a costly growth substrate, the tandems must be operated under concentration if they are to reach competitive costs. Unfortunately, the associated penalty is the loss of all diffuse light, thus reducing the annual energy yield of tandem systems.

In a recent paper, we introduced a new tandem concept based on a "PVMirror" that collects diffuse light [11]. It utilizes PV cells as a three-in-one technology—they act as a concentrating mirror, spectrum splitter, and high-efficiency light-to-electricity converter. A PVMirror is full aperture and thus intercepts the global spectrum, and it reflects select wavelengths to a second solar cell or even a non-PV solar converter located at a focus. Together, the PVMirror and second converter ("receiver") form a spatially separated four-terminal tandem solar collector. Here, we model the performance a PVMirror tandem system comprising a silicon PVMirror and a GaAs receiver at its focus, and we conduct a sensitivity analysis of this system. In so doing, we explore the performance upper bounds of a tandem formed by coupling existing cells with the PVMirror technology.

II. PVMirror Tandem

A silicon PVMirror is composed of a silicon solar cell, a curved or segmented glass substrate, and a dichroic mirror, as shown in Figure 1. Light is incident upon a full-aperture dichroic mirror that reflects visible (VIS, 300–870 nm) light and transmits infrared (IR, 870–1200 nm) light. The transmitted light is absorbed in the silicon solar cell that is placed behind the dichroic mirror and that converts IR photons to electricity with high efficiency. The dichroic mirror and silicon cell are affixed to a curved glass trough that tracks the sun about a single, North-South axis such that the reflected VIS light is concentrated at a common line focus, at which is placed a second, wider-bandgap GaAs cell having high efficiency at shorter wavelengths. The GaAs cell receives concentrated direct light, whereas the silicon cell receives part of the direct and diffuse light.

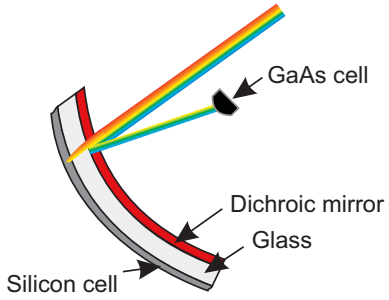

Fig 1. Schematic of a GaAs/silicon PVMirror tandem system.

III. Results and Discussion

To investigate the potential performance of such a tandem system, we modeled it using an ideal dichroic mirror as well as record silicon and GaAs cells. The dichroic mirror has unity reflectance in the VIS region of the spectrum, and unity transmittance in the IR region. The

key one-sun parameters (obtained from the solar cell efficiency tables [12]) of both cells (prior to tandem formation) that we used in simulation are shown in Figure 2. The short-circuit current densities (J_{sc}) were calculated by integrating the product of the AM1.5 global spectral photon flux and published external quantum efficiency (*EQE*) spectra, which are shown in Figure 2a. The spectral efficiencies of both cells, shown in Figure 2b, were calculated according to [5]:

$$\eta(\lambda) = \frac{V_{OC} \cdot FF \cdot J_{SC}(\lambda)}{I(\lambda)} \quad (1)$$

with V_{oc} the open-circuit voltage, *FF* the fill factor, $I(\lambda)$ the spectral irradiance (in $Wm^{-2}nm^{-1}$), and $J_{sc}(\lambda)$ the short-circuit current density at each wavelength:

$$J_{SC}(\lambda) = q\frac{\lambda}{hc} EQE(\lambda) \cdot I(\lambda) \quad (2)$$

With the spectral efficiency curves of both cells, it is straightforward to compare cell efficiency at each wavelength and determine the preferred cut-off wavelength of the dichroic mirror from the wavelength at which the cross over (870 nm).

Cell	η (%)	E_g (eV)	V_{OC} (V)	J_{SC} (mA/cm^2)	FF (%)
GaAs	28.8	1.4	1.12	29.68	86.5
Silicon	25.6	1.1	0.74	41.80	82.7

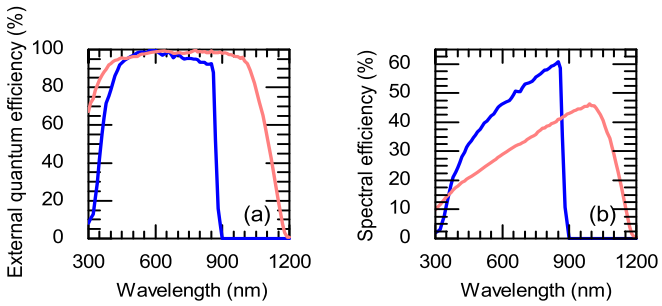

Fig 2. Performance of the individual record GaAs (blue) and silicon (red) cells used in the tandem simulations. (a) *EQE* and (b) spectral efficiency.

We simulated the performance of this PVMirror tandem system assuming 7x geometric concentration at the focus and different diffuse light fractions. To do this, the J_{sc} of each sub-cell was first calculated from its *EQE* and the spectrum and irradiance it receives. Then, the V_{oc} was calculated according to the one-sun V_{oc} and the photo-generated current just calculated. *FF* was assumed to be the same as its one-sun value for simplicity. Finally, the power outputs of the sub-cells were summed and normalized to the incident power to arrive at the tandem efficiency. In this calculation, direct and diffuse light were treated separately, with the AM 1.5 direct and AM 1.5 diffuse spectra normalized to their respective fractions.

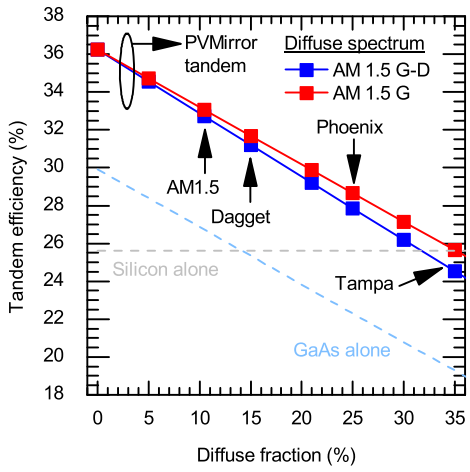

Fig. 3 PVMirror tandem performance under different diffuse fractions. The red curve assumes the AM 1.5 global spectrum for the diffuse light, whereas the blue curve assumes the AM 1.5 diffuse spectrum (global minors direct). Also shown is the efficiency of the GaAs cell alone operating under 7x concentration with a perfect reflector, and the efficiency of the silicon cell alone operating at one sun.

Figure 3 shows the PVMirror tandem efficiency as a function of diffuse fraction. For no diffuse light, as one would measure in a lab, the simulated efficiency is as high as 36.2%. As diffuse fraction increases, however, the system efficiency drops because the silicon PVMirror captures only part of the diffuse light and the GaAs receiver captures none. Two diffuse spectra were used in the simulations: the AM 1.5 global spectrum, and the AM 1.5 diffuse spectrum, which is calculated as the difference between the AM 1.5 global and direct spectra. Using the AM 1.5 global spectrum for diffuse light results in slightly higher tandem efficiency because it has more photons in the IR region, for which the dichroic mirror transmits and the silicon cell operates with over 40% efficiency. For locations that have lower diffuse fractions, e.g. Dagget or Phoenix, most days are cloud-free and thus the diffuse light should be "blue-shifted"; using the AM 1.5 diffuse spectrum is more representative than using the AM 1.5 global spectrum. In contrast, for locations such as Tampa in Florida, where cloud scattering is often the source of diffuse light, the converse is more appropriate. Compared to a conventional (7x) concentrating system with a perfect, broadband parabolic mirror and a GaAs receiver (similar to SunPower's C7 technology), the PVMirror tandem reaches an efficiency that is 6% (absolute) higher at each diffuse fraction. Compared to flat-plate silicon alone, which captures all diffuse light, the PVMirror tandem is preferred at locations with diffuse fractions below approximately 30%.

So far, the simulation results represent the maximum achievable tandem efficiency by using existing record cells and an ideal dichroic mirror. To further investigate a more realistic PVMirror tandem system and determine how much deviation from ideal can be tolerated, we conducted a sensitivity analysis of the main components in the system; the results are shown in Figure 4. The tandem system is most sensitive to the GaAs cell: By

decreasing the GaAs cell's performance by 5% relative, the system efficiency drops by about 4% relative. This is expected as the GaAs cell receives most of the light. The cut-off wavelength of the dichroic mirror is the next most important parameter: A 50 nm redshift results in a 3.6% decrease in tandem efficiency, whereas a 50 nm blueshift results in a 3.2% loss. The reason why a redshift matters more than a blueshift can be understood from the spectral efficiencies in Figure 2: For wavelengths > 870 nm, the silicon cell is more efficient than the GaAs cell, and directing wavelengths > 900 nm to the GaAs cell is a complete waste; directing wavelengths < 870 nm to the silicon cell instead of to the GaAs cell, however, is not a total loss but still decreases the tandem efficiency since the silicon cell still converts these photons less efficiently than the GaAs cell. Using a dichroic mirror with 95% reflectance and 5% transmittance (no parasitic loss) before the cutoff, instead of 100% and 0%, results in a 1.6% efficiency loss. By contrast, applying this change after the cutoff causes an efficiency drop of less than 1%. Dichroic mirrors with a soft, 100-nm-wide cutoff reduces the system efficiency by about 1.6%. Finally, a 5% decrease in the silicon cell performance results in less than a 1% drop in system efficiency, which indicates that for this tandem system, less efficient but cheap silicon cells may be favorable.

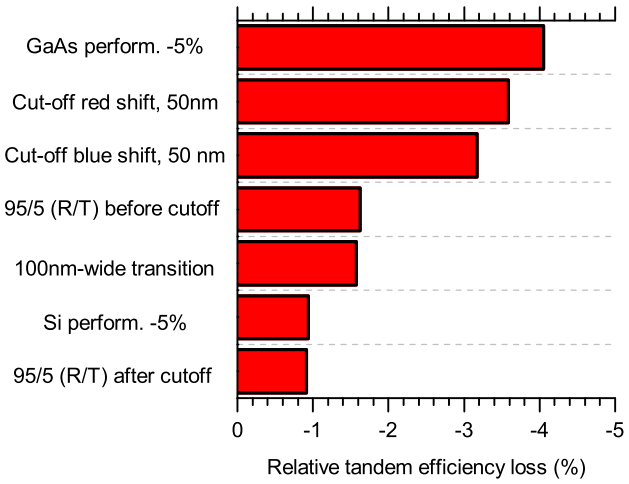

Fig. 4 Sensitivity analysis of a PVMirror tandem system.

IV. Conclusion

Silicon and GaAs are the most mature technologies in the PV market, and, by using inexpensive silicon cells in a full-aperture PVMirror with a relatively expensive GaAs cell at its focus, efficiencies well in excess of 30% are possible today. More importantly, as perovskite or other cheap, wide-bandgap top cells mature, PVMirror tandems can act as a drop-in platform in which the inexpensive top cell is used in the PVMirror and silicon cells are placed at the focus. In this configuration, PVMirror tandems become more powerful, as the wide-bandgap PVMirror captures all above-bandgap diffuse light and thus reaches higher outdoor system efficiency. In this configuration, the silicon cell now becomes the "expensive" sub-cell and its cost can be discounted by the concentration. In addition, the

dichroic mirror can be omitted if the top cell has a specular rear reflector; the bandgap of top cell then serves as an absorptive filter that has precisely the right “cutoff”.

ACKNOWLEDGMENT

The information, data, or work presented herein was funded in part by the Advanced Research Projects Agency-Energy (ARPA-E), U.S. Department of Energy, under Award Number DE-AR0000474, and NSF/DOE and QESST under grant Number EEC-1041895.

REFERENCES

1. C. Battaglia, A. Cuevas, and S. De Wolf, "High-efficiency crystalline silicon solar cells: status and perspectives," Energy & Environmental Science, 2016.
2. A. Richter, M. Hermle, and S. W. Glunz, "Reassessment of the Limiting Efficiency for Crystalline Silicon Solar Cells," IEEE Journal of Photovoltaics, vol. 3, pp. 1184-1191, Oct 2013.
3. D. D. Smith, P. Cousins, S. Westerberg, R. De Jesus-Tabajonda, G. Aniero, and Y. C. Shen, "Toward the Practical Limits of Silicon Solar Cells," IEEE Journal of Photovoltaics, vol. 4, pp. 1465-1469, Nov 2014.
4. M. A. Green, "Commercial progress and challenges for photovoltaics," Nature Energy, vol. 1, p. 15015, 2016.
5. Z. Yu, M. Leilaeioun, and Z. Holman, "Selecting tandem partners for silicon solar cells," Nature Energy, vol. 1, p. 16137, 2016.
6. S. Kurtz, D. Myers, W. E. McMahon, J. Geisz, and M. Steiner, "A comparison of theoretical efficiencies of multi-junction concentrator solar cells," Progress in Photovoltaics: Research and Applications, vol. 16, pp. 537-546, 2008.
7. S. Essig, M. A. Steiner, C. Alleb, x00E, J. F. Geisz, B. Paviet-Salomon, et al., "Realization of GaInP/Si Dual-Junction Solar Cells With 29.8%; 1-Sun Efficiency," IEEE Journal of Photovoltaics, vol. PP, pp. 1-8, 2016.
8. J. W. Garland, T. Biegala, M. Carmody, C. Gilmore, and S. Sivananthan, "Next-generation multijunction solar cells: The promise of II-VI materials," Journal of Applied Physics, vol. 109, May 15 2011.
9. J. Werner, C.-H. Weng, A. Walter, L. Fesquet, J. P. Seif, S. De Wolf, et al., "Efficient Monolithic Perovskite/Silicon Tandem Solar Cell with Cell Area >1 cm2," The Journal of Physical Chemistry Letters, vol. 7, pp. 161-166, 2016/01/07 2016.
10. H. Uzu, M. Ichikawa, M. Hino, K. Nakano, T. Meguro, J. L. Hernández, et al., "High efficiency solar cells combining a perovskite and a silicon heterojunction solar cells via an optical splitting system," Applied Physics Letters, vol. 106, p. 013506, 2015.
11. Z. J. Yu, K. C. Fisher, B. M. Wheelwright, R. P. Angel, and Z. C. Holman, "PVMirror: A New Concept for Tandem Solar Cells and Hybrid Solar Converters," Photovoltaics, IEEE Journal of, vol. 5, pp. 1791-1799, 2015.

12. M. A. Green, K. Emery, Y. Hishikawa, W. Warta, and E. D. Dunlop, "Solar cell efficiency tables (version 47)," Progress in Photovoltaics: Research and Applications, vol. 24, pp. 3-11, 2016.

APPENDIX G

SILICON WAFER WITH OPTICALLY SPECULAR FURFACES FORMED BY CHEMICAL POLISHING

SILICON WAFERS WITH OPTICALLY SPECULAR SURFACES FORMED BY CHEMICAL POLISHING

This letter investigates chemical polishing with a hydrofluoric acid, nitric acid, and acetic acid (HNA) mixture as an alternative to chemical mechanical polishing (CMP) to produce smooth surfaces on both slurry- and diamond-cut silicon solar wafers. With 30 μm of silicon etched from each side, as-cut wafers appear mirror-like to the naked eye. A quantitative analysis of the specularity of HNA-polished wafers indicates that 97% of light reflected from slurry-cut wafers falls within ±10 mrad of the specular beam and is isotropically distributed. Conversely, HNA-polished diamond-cut wafers retain a history of the wafer-sawing process: the reflected light is anisotropic with 99.4% of light within ±10 mrad of the specular beam in the sawing direction but only 89.1% within ±10 mrad in the perpendicular direction. Topographical characterization by optical profilometry and atomic force microscopy measurements reveals that HNA-polished slurry-cut wafers are spatially uniform with a surface roughness of 45 nm. Diamond-cut wafers have a roughness of only 18 nm but also have residual sawing grooves tens of micrometers across—these are responsible for the anisotropic scattering of light. The HNA-polished wafers are appropriate alternatives to CMP wafers for high-efficiency solar cells, including interdigitated-back-contact and tandem cells that require single-side polished wafers, as well as for other optical applications such as process monitoring with characterization techniques that require planar substrates.

Silicon wafer polishing or planarization is most often performed with chemical mechanical polishing (CMP).[1,2] In the integrated circuit industry, CMP is used to planarize bare and coated silicon surfaces both for initial wafer polishing and between process steps.[2] The resulting surfaces can have atomic-scale planarity over their full area,[3,4,5] which makes the wafers suitable for, e.g., epitaxial growth and fabrication of nanometric electronic devices. However, the cost of a (single-side) CMP step is in the tens of dollars per wafer,[6,7] depending on wafer size, because the consumables (slurry and polishing pads) are expensive and the polishing process is slow. Consequently, CMP has not been adopted by other technology areas that demand less expensive polished substrates but that also have less stringent surface planarity requirements.

For example, in silicon photovoltaics, cell structures that are now being commercialized—such as passivated-emitter-and-rear-contact cells and interdigitated-back-contact cells—feature rear wafer surfaces that are chemically polished.[8,9,10] The polished rear surfaces reduce feature spreading during patterning of, e.g., interdigitated fingers, and they also result in lower surface recombination velocity compared to rough surfaces with the same passivation layers.[11,12] For these applications, a surface roughness of up to 300 nm can be

tolerated,[13,14] but the polishing process must cost well under $0.10 per wafer since the selling price of completed cells is less than $1.50 per cell.[15] During fabrication of photovoltaic cells, polished wafers may also be used to monitor deposition processes, as many thin-film characterization techniques require or benefit from planar surfaces (e.g., ellipsometry, secondary ion mass spectrometry, Rutherford backscattering).[16] Future photovoltaic structures may rely even more heavily on planar surfaces and have more stringent cost and planarity requirements: For example, two-terminal tandem solar cells with silicon as the bottom cell have top cells formed either by direct (e.g., epitaxial) growth or wafer bonding, and both processes require polished surfaces. In addition, a new optically coupled "PVMirror" tandem concept uses a polished solar cell to specularly reflect select wavelengths of light to a second solar collector.[17]

Mixtures of hydrofluoric acid (HF), nitric acid (HNO_3), and acetic acid (CH_3COOH)—commonly referred to as HNA—were first used to etch polysilicon and were studied extensively for the integrated circuit industry.[18,19] Schwartz and Robbins investigated the effect of the HNA mixing ratio on the surface geometry of silicon after etching, and reported that mixtures with high concentrations of HNO_3, medium-to-low concentrations of HF, and low concentrations of CH_3COOH produce smooth surfaces, as viewed under an optical microscope.[20] In this regime, the etching behavior is HF limited: the abundant HNO_3 molecules oxidize the silicon surface and form a film of SiO_2, CH_3COOH functions as a diluent that prevents excessive dissociation of HNO_3, and the reaction between HF and the SiO_2 film controls the etching rate and surface morphology. Researchers studying microelectromechanical systems (MEMS) have further tuned the etching process to achieve three-dimensional structures such as silicon microneedles that maintain their shape as their surfaces become smooth.[21,22] However, (electron) microscope images are still most frequently used as evidence of smoothness after HNA etching; we are unaware of a quantitative analysis that evaluates the surfaces in light of the aforementioned potential applications of chemically polished wafers.

In this letter, we report on the surface roughness and specularity of as-cut solar-grade monocrystalline silicon wafers after HNA polishing. Polishing was performed on n-type (3 ohm·cm) Czochralski wafers with both diamond-cut and slurry-cut surfaces.[23] Three wafers cut with each technology were chemically polished at room temperature with a 10:73:17 $HF:HNO_3:CH_3COOH$ mixture using a stirring bar. This HNA ratio is in the region identified by Schwartz and Robbins as being effective at polishing,[20] and was found to give optimal results in our previous experiments. Etching times of 1.5, 3.0, and 6.0 minutes were used, resulting in measured wafer thickness removals of 10, 17, and 30 μm per side, respectively. Another six wafers—three diamond-cut and three slurry-cut—were etched in a 30% potassium hydroxide (KOH) solution at 85 °C and served as references. In these experiments, the etching time was tuned to achieve the same per-side material removal as in the HNA experiments. All etched wafers were put through an RCA-2 cleaning sequence and subsequent HF dip prior to measurement to remove any surface contamination. A CMP wafer was used as a reference for an optically specular surface.

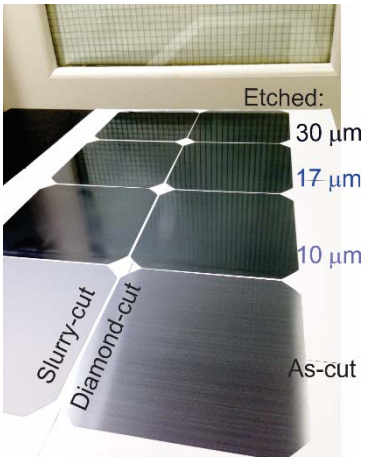

FIG 1. Photograph of slurry- and diamond-cut wafers after polishing with HNA for 0–6 minutes. The reflection of the square mesh grid of the window can be seen in the wafers.

Figure 1 shows a photograph of as-cut and HNA-polished wafers. The surface finishes of the as-cut wafers cut with different technologies are quite different: the slurry-cut wafer looks uniform but diffuse, while the diamond-cut wafer looks shiny but has visible grooves.[23] As the HNA etching time increases (wafer thickness reduces, as indicated) the haziness of the wafers diminishes and mirror-like polished surfaces begin to emerge. After 30 μm of silicon removal from each side, the slurry- and diamond-cut wafers at first appear to be optically similar. However, upon closer inspection, the polished diamond-cut wafer shows anisotropic scattering resulting from the original grooves; this is visible in Figure 1 as an absence of horizontal lines in the reflected image of the mesh grid in the window. In contrast, both the horizontal and vertical lines of the mesh grid are visible from the polished slurry-cut wafers.

The specularity of these wafers was first characterized by measuring the angular distribution of reflected light with a PerkinElmer Lambda 950 UV/VIS/NIR spectrophotometer equipped with an Automated Reflectance/Transmittance Analyzer (ARTA) accessory.[24,25] Wafer pieces mounted on a goniometer were tilted 15° with respect to the incident beam of 600 nm light, so that the specular beam should have reflected from the samples at 30° (again with respect to the incident beam). An integrating sphere detector with an entrance aperture 7.5 mm wide—corresponding to an acceptance angle of 5°—was swept on a second goniometer from 25° to 35° (with respect to the incident beam) in 1° increments.

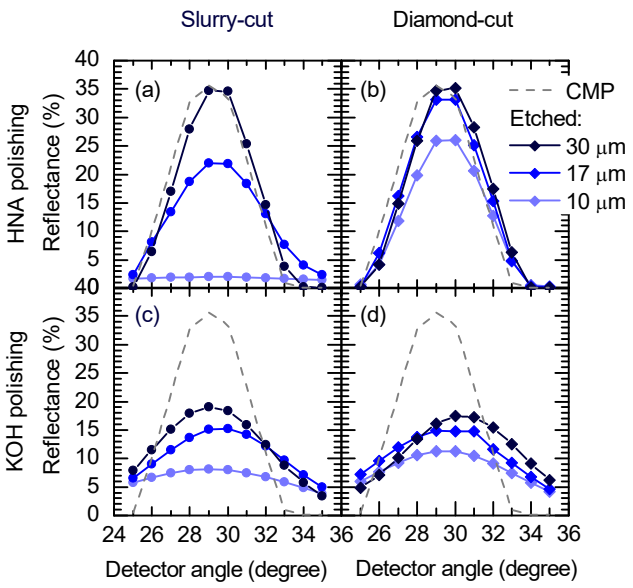

FIG 2. Angular distribution of reflected light from (a) slurry-cut wafers with HNA polishing, (b) diamond-cut wafers with HNA polishing, (c) slurry-cut wafers with KOH polishing and (d) diamond-cut wafers with KOH polishing. Each plot shows a CMP reference wafer and as-cut wafers etched for varying time. The samples were tilted 15° with respect to the 600-nm-wavelength incident beam; a detector angle of 30° therefore corresponds to the specular beam. The detector aperture was 5°.

Figure 2 shows the reflectance, resolved by detector angle, of HNA- and KOH-polished wafers, as well as a CMP reference wafer. The reflectance increases as the detector scans from 25° towards 30°—the specular angle—and then decreases for higher angles, resulting in a peak. The peak is not delta-function-like, as might be expected, but bell-like instead because of a combination of the acceptance angle of the detector (which limits the minimum possible peak width to 5°) and the spot size of the incident beam (which broadens the minimum peak to about 8° as seen from the CMP reference). The peak is not at exactly 30° for every sample because it is challenging to place the wafer pieces on the goniometer with better than 1° precision. The peak reflectance increases with HNA etching time for both slurry- and diamond-cut wafers, and tops out at 35.6%, which is the same value measured on the CMP reference wafer. Further, the reflectance curves of the best HNA polished samples (30 μm etched per side) overlap with that of the CMP wafer, which indicates that—as seen by this detector—the HNA polished surfaces are as flat as the CMP surface. The reflectance at shorter etching times reveals that diamond-cut wafers become specular more quickly than slurry-cut wafers: After removal of 10 μm per side, the diamond-cut wafer has a peak reflectance of 26% whereas the slurry-cut wafer has only 2%. KOH etching is frequently used in solar cell and micromachining processes[26]—often to smooth surfaces—but Figure 2 indicates that it is not nearly as effective as HNA polishing, at least for the conditions used here. The KOH-polished samples have much

lower peak reflectance and broader peaks, even after 30 μm has been etched from each side, indicating that light is scattered outside of the 10° scanned by the detector.

To probe the specularity of the best HNA-polished wafers beyond the angular resolution limit of the ARTA's detector, we imaged their reflected beams with a Thorlabs BP209-IR two-dimensional Beam Profiler with a 2*f* imaging optical setup. The wafers were coated with 200 nm of sputtered silver on one side. A 1310 nm laser was focused into the aperture of the beam profiler after a 45° reflection from the wafer under test. In most measurements, the laser was incident on the silvered side of the wafer and reflection only from this surface was recorded. However, in select measurements, the wafer was reversed and the beam profiler recorded the specularity of light that had reflected from the rear surface and traversed the wafer thickness twice (this is why a wavelength of 1310 nm was used). In this configuration, Snell's Law indicates that any scattering will be amplified by a factor of the refractive index of the wafer (n = 3.5) as light returns to air from the silicon.

The solid lines in Figure 3 show the normalized reflectance of the (front surface of the) best HNA-polished diamond-cut and slurry-cut wafers, as well as a CMP reference wafer, as a function of the angular deviation from specular. As the profiled beams were either circularly symmetric (slurry-cut and CMP) or approximately symmetric about the wafer sawing direction (diamond-cut), we have displayed the average profiles of each beam in the x- (perpendicular to sawing wire) and y-directions (parallel to sawing wire). The diamond-cut sample exhibits anisotropic scattering: the scattering in the x-direction is within ±20 mrad whereas in the y-direction it is within ±5 mrad. This anisotropy is caused by the persistent sawing grooves and explains the disappearance of the horizontal lines observed in Figure 1. In contrast, the scattering of the slurry-cut sample is isotropic, like the CMP reference but much broader. (The width of the beam reflected from the CMP wafer reveals the angular uncertainty of the beam profiler, which is approximately 0.5 mrad.) For the diamond-cut sample, 89.1% of the reflected light is within ±10 mrad in the x-direction while 99.4% is within this specification in the y-direction. For the slurry-cut sample, 97% of reflected light is within ±10 mrad in both directions.

The wafers from Figure 3a and b were also subjected to surface profiling using a ZeScope optical profilometer and a Dimension 3000 atomic force microscope (AFM). The 1 mm × 1 mm optical profilometry maps in Figure 4a and the line scans in Figure 4c expose the persistent sawing grooves (diamond-cut) and random roughness (slurry-cut) on the wafer surfaces that result in the scattering seen in Figure 3. The power spectral density functions (PSDFs) of the maps in Figure 4a (not shown) confirm that the slurry-cut wafer is isotropically rough (same PSDF in the x- and y-directions)—consistent with the isotropic scattering in Figure 3a. The PSDFs also indicate that the grooves in the diamond-cut wafer along the y-direction have wavelengths of 5–100 μm, corresponding to approximately 1–1/20 the diamond wire diameter.

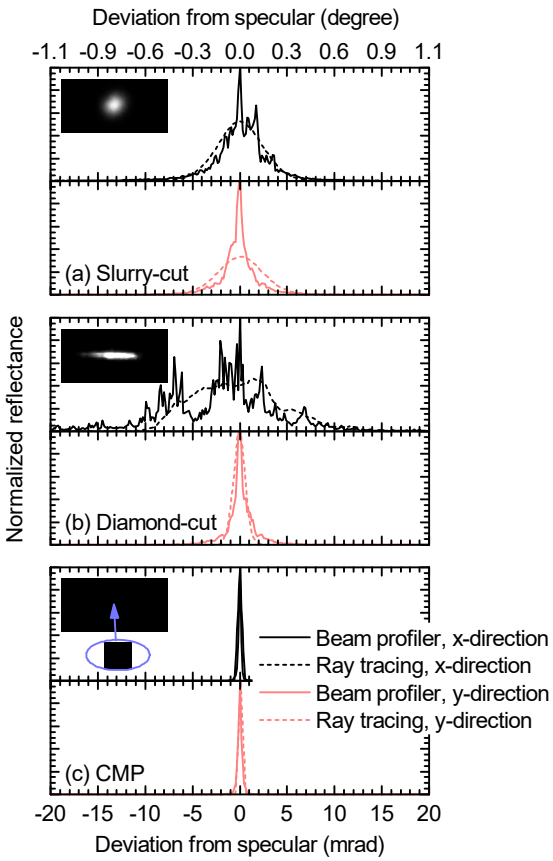

FIG 3. Measured and ray-traced average profiles in the x- and y-directions of a laser beam reflected from (a) a HNA-polished slurry-cut wafer, (b) a HNA-polished diamond-cut wafer, and (c) a CMP reference wafer. The HNA polished wafers are the same as those shown in Figures 1 and 2 with 30 μm of silicon etched per side (6 minutes of etching). The measured and ray-traced profiles were normalized to have the same total area, corresponding to the same number of photons at the detector. The insets are images of the beams generated from ray tracing using the optical profilometry maps in Figure 4; the ray-traced beam profiles in the figure were generated by averaging the intensities at all y-values for a given x-value (x-direction profile) or at all x-values for a given y-value (y-direction profile).

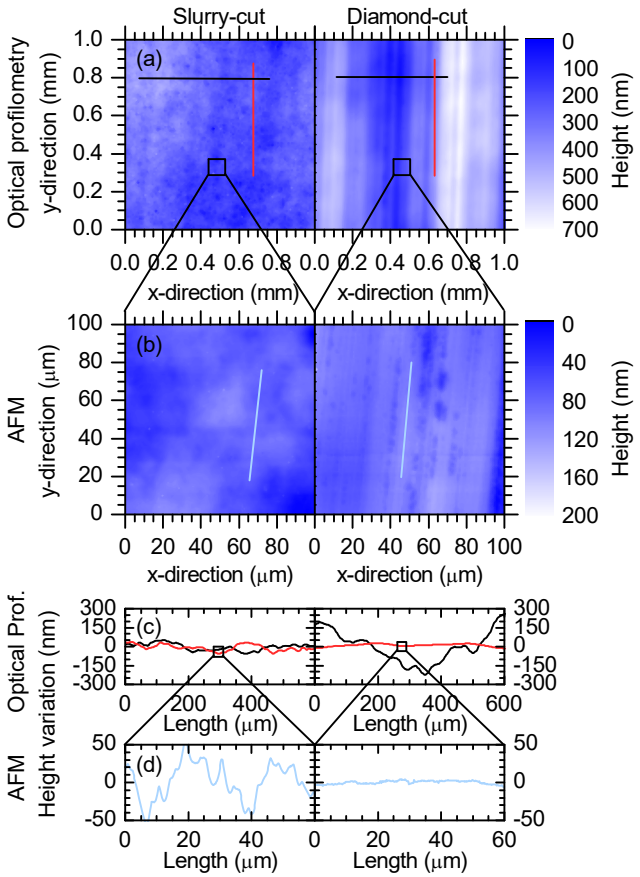

FIG 4. (a) Optical profilometery height maps, (b) AFM height maps, (c) optical profilometry line scans, and (d) AFM line scans of HNA-polished slurry- and diamond-cut wafers. The wafers are the same as those shown in Figures 1–3 with 30 μm of silicon etched per side (6 minutes of etching). The line scans in (c) were extracted from the maps in (a) along the indicated perpendicular lines; similarly, the lines scans in (d) were extracted from the maps in (b).

The AFM height maps in Figure 4b and line scans in Figure 4d, which span 1/100 the area and length of the maps and line scans from optical profilometry, show that the variation in height with position is substantially dampened at shorter length scales. In particular, the acute waviness of the diamond-cut wafer surface disappears in the AFM map because the map lays almost entirely on a "step" of a residual sawing groove. The root-mean-square (RMS) surface roughness across the AFM map of the diamond-cut wafer is only 17.8 nm; in comparison, the RMS roughness of the slurry-cut wafer across the same area is 45.2 nm. Figure 4b also reveals particles on the slurry-cut surface—these appear as white dots—of unknown origin. The diamond-cut wafers were etched and cleaned in the same solutions as the slurry-cut wafers and yet do not have particulate residue, and subsequent experiments with both wafer types yielded similar results. It may be that the higher-frequency roughness of the slurry-cut surface is more effective at trapping particles

generated in solution (see Figure 4d) and that more vigorous cleaning is required to remove them.

As a consistency check, the optical profilometry maps in Figure 4a were used to simulate the beam profiling experiments in Figure 3 by ray tracing in ZEMAX. Rays emitted normal to the local surface from each point of the maps were focused through a simulated lens onto a screen; the beam images on the screen are shown in Figure 3 as insets. As with the experimental data, the average profiles of the beams in the x- and y-directions are plotted in Figure 3. Ray tracing reproduces many of the features of the measured beams, including their approximate full width in both directions. It also tends to blur sharp features, however, perhaps because ZEMAX interpolates between grid points and because much of the remaining roughness after polishing is sub-wavelength in size yet is treated with geometric optics when ray tracing. Additionally, Figure 3a implies that the particles on the slurry-cut wafer do not contribute overwhelmingly to the measured scatter. The particles are absent from the map used in ray tracing (refer to the optical profilometry map in Figure 4a) but the simulated beam profiles still roughly overlap the measured profiles.

Our quantitative analysis of the specularity and roughness of HNA-polished wafers indicates that they should be suitable for many applications in silicon photovoltaics, and likely other technology areas too. Slurry-cut wafers with 30 μm of silicon etched per side are approximately six times smoother than the roughness upper limit identified by Richter et al. and Horzel et al. for optimal passivated-emitter-and-rear-contact cell performance,[13,14] and diamond-cur wafers with the same degree of polishing are even smoother in one direction. Furthermore, the measurements presented here were all from the same six wafers (shown in Figure 1) and subsequent experiments with longer etching times and minor optimization further reduced roughness (e.g., to 21.1 nm RMS for slurry-cut wafers).

In looking beyond this work, we have begun preliminary tests to explore whether HNA-polished wafers can be successfully used as more than just specular reflectors. For example, we deposited intrinsic amorphous silicon passivation layers on both sides of a HNA-polished diamond-cut wafer and measured effective lifetimes of over 6 ms, indicating that the etched surfaces are free of defects and contamination in addition to being planar. We are in the process of attempting homo- and hetero-epitaxial growth on these surfaces, and we have begun making tandem cells with silicon wafers that have HNA-polished top surfaces and alkaline-textured rear surfaces. We have also made PVMirrors with silicon solar cells on HNA-polished wafers; in this case, a Bragg reflector was deposited on the front surface to reflect visible light and the cells look like a mirror to the naked eye.[27] Finally, we have investigated the use of HNA-polished wafers as cheap monitor wafers during deposition processes when, e.g., the deposited layers are to be characterized with techniques requiring or benefitting from planar surfaces. For example, we found that 110-nm-thick indium oxide layers sputtered on HNA-polished and CMP wafers yield indistinguishable ellipsometry spectra. HNA-polishing is not without drawbacks—60 μm of silicon is dissolved and the resulting wafers can be thin and brittle—but the high degree

of specularity achieved after polishing makes the wafers useful for many optical and device applications.

The authors thank Mathieu Boccard for valuable discussions.

The information, data, or work presented herein was funded in part by the Advanced Research Projects Agency-Energy (ARPA-E), U.S. Department of Energy, under Award Number DE-AR0000474.

REFERENCES

1. W. J. Patrick, W. L. Guthrie, C. L. Standley, and P. M. Schiable, J. Electrochem. Soc. 138, 1778 (1991).
2. P. B. Zantye, A. Kumar, and A. K. Sikder, Mater. Sci. Eng. R. 45, 89 (2004).
3. G. J. Pietsch, Y. J. Chabal, and G. S. Higashi, Surf. Sci. 331, 395 (1995).
4. T. Kasai, K. Horio, and A. Kobayashi, CIRP Annals - Manufacturing Technology 39, 321 (1990).
5. J. L. Yuan, P. Zhao, J. Ruan, Z. X. Cao, W. H. Zhao, and T. Xing, J. Mater. Process. Technol. 138, 116 (2003).
6. A. S. Brown, IEEE Spectrum, 42, 40 (2005).
7. S. C. Wood, IEEE Trans. Semicond. Manuf. 10, 98 (1997).
8. Martin A. Green, Sol. Energy Mater. Sol. Cells 143, 190 (2015).
9. T. Desrues, S. de Vecchi, F. Souche, D. Munoz, and P. J. Ribeyron, in Proceedings of the 38th IEEE Photovoltaic Specialists Conference (PVSC), Austin TX (2012).
10. N. Mingirulli, J. Haschke, R. Gogolin, R. Ferré, T. F. Schulze, J. Düsterhöft, N. P. Harder, L. Korte, R. Brendel, and B. Rech, physica. status solidi. (RRL) – Rapid Research Letters 5, 159 (2011).
11. S. De Wolf, G. Agostinelli, G. Beaucarne, and P. Vitanov, J Appl. Phys. 97, (2005).
12. C. Kranz, S. Wyczanowski, S. Dorn, K. Weise, C. Klein, K. Bothe, T. Dullweber, and R. Brendel, in Proceedings of the 27th European Photovoltaic Solar Energy Conference, Frankfurt, Germany, (2012).
13. M. Richter, P. Saint-Cast, T. Dannenberg, M. Zimmer, and J. Rentsch, Energy Procedia 77, 832 (2015).
14. J. Horzel, A. Lorenz, E. Cornagliotti, A. Uruena, J. John, M. Izaaryene, D. Habermann, P. Jaffrennou, and J. Penaud, in Proceedings of the 26th European Photovoltaic Solar Energy Conference, Hamburg, Germany,(2011).
15. M. A. Green, Philos. T. R. Soc. A 371 (2013).

16. K. R. McIntosh, T. C. Kho, K. C. Fong, S. C. Baker-Finch, Y. Wan, N. Zin, E. T. Franklin, D. Wang, M. D. Abbott, N. E. Grant, E. Wang, M. Stocks, and A. W. Blakers, in Proceedings of the 40th IEEE Photovoltaic Specialist Conference (PVSC), Denver CO (2014).

17. Z. J. Yu, K. C. Fisher, B. M. Wheelwright, R. P. Angel, and Z. C. Holman, IEEE J. Photovoltaics, 5, 1791 (2015).

18. M. J. Madou, Fundamentals of microfabrication: the science of miniaturization. (CRC press, 2002).

19. H. Robbins and B. Schwartz, J. Electrochem. Soc. 107, 108 (1960).

20. B. Schwartz and H. Robbins, J. Electrochem. Soc. 123, 1903 (1976).

21. E. Koukharenko, W. Tudor, and S. P. Beeby, Mater. Lett. 62, 651 (2008).

22. A. A. Hamzah, N. Abd Aziz, B. Y. Majlis, J. Yunas, C. F. Dee, and B. Bais, J. Micromech. Microeng. 22, (2012).

23. B. Meinel, T. Koschwitz, C. Blocks, and J. Acker, Mater. Sci. Semicond. Process. 26, 93 (2014).

24. PA van Nijnatten, JMC de Wolf, and IJE Schoofs, presented at the 7th ICCG (International Conference on Coatings on Glass & Plastics), Breda, Netherlands, (2008).

25. Z. J. Yu, Z. C. Holman, and Mark O'Neill, PerkinElmer Application Note (2015).

26. Theo Baum and David J Schiffrin, J. Micromec.h Microeng. 7, 338 (1997).

27. Z. J. Yu, K. C. Fisher, and Z. C. Holman, in Proceedings of the 42nd IEEE Photovoltaic Specialist Conference (PVSC), New Orleans LA, (2015).